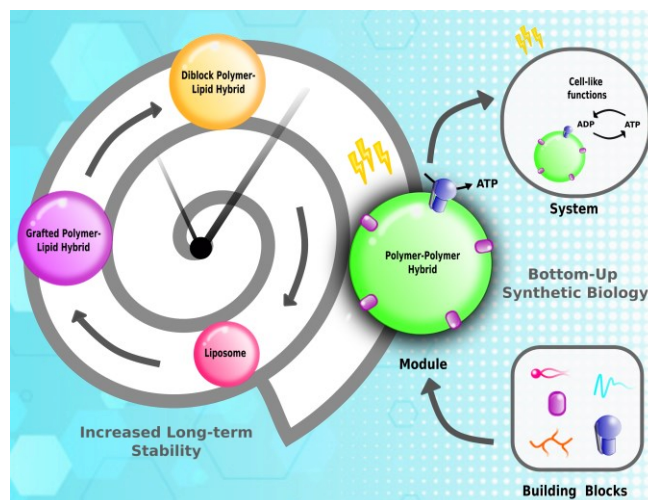


Bottom-up Assembly of a Light-driven ATP Regeneration Module in Lipid, Polymer and Hybrid Vesicles

Bottom-up Konstruktion eines lichtgetriebenen ATP
Regenerationsmoduls in Lipid-, Polymer- und Hybrid-Vesikeln



Dissertation

zur Erlangung des akademischen Grades

Doctor rerum naturalium

(Dr. rer. nat.)

von: M.Sc. Christin Kleineberg
geb. am 22.02.1987 in Paderborn

genehmigt durch die Fakultät für Verfahrens- und Systemtechnik der Otto-von-Guericke-Universität Magdeburg

Promotionskommission: Prof. Dr. rer. nat. Franziska Scheffler (Vorsitz)
Prof. Dr. rer. nat. Seraphine V. Wegner (Gutachter)
Prof. Dr. rer. nat. Katharina Landfester (Gutachter)
Prof. Dr.-Ing. Kai Sundmacher (Mitglied)

eingereicht am: 29. Oktober 2020
Promotionskolloquium am: 09. Juli 2021

Abstract

The ability to design artificial protocells from modular building blocks, holds among others great promise for biotechnological application as well as for solving the origin of life puzzle. One of the major components of a minimal biological system is energy regeneration to carry out activities, such as growth, movement or reproduction.

This thesis comprises the construction of a light-driven ATP regeneration module from molecular building blocks. Therefore, two proteins, Bacteriorhodopsin and ATP synthase are integrated in suitable compartments. Both enzymes are first investigated separately and are afterwards combined to form a light-driven ATP regeneration module. Optimization of different factors that influence synthesis rates, enabled the generation of ATP production rates up to 4.5 μM ATP (mg ATP synthase)⁻¹(min⁻¹).

Keeping the bioactivity of energy converting proteins high for longer is of high relevance in biotechnology applications as well as when planning to create a minimal cell from bottom-up. Therefore, a detailed study of membrane protein functionality over time in different hybrid compartments made of graft polymer PDMS-g-PEO and diblock copolymer PBd-PEO is presented. Activity of more than 90% in lipid/polymer hybrid vesicles compared to conventional liposomes proves an excellent biocompatibility. A significant enhancement of long-term stability (80% remaining activity after 42 days) is demonstrated in polymer/polymer-based hybrids.

The combination with other functional modules confirmed the capability of the ATP module to serve as energy supply to efficiently power metabolic pathways or movement in artificial protocells.

Zusammenfassung

Künstliche Protozellen aus modularen Bausteinen zusammen zu setzen, eröffnet vielversprechende Möglichkeiten im Bereich der Biotechnologie und könnte darüber hinaus neue Rückschlüsse über den Ursprung des Lebens zulassen. Eine der wichtigsten Komponenten einer "Minimalzelle" ist die Energieregeneration, welche Aktivitäten wie Wachstum, Bewegung oder Reproduktion ermöglicht.

Inhalt dieser Arbeit ist die Konstruktion eines lichtgetriebenen ATP Regenerationsmoduls aus kleinsten molekularen Bausteinen. Dazu werden zwei Proteine, Bacteriorhodopsin (bR) und ATP Synthase, in geeignete Kompartimente integriert. Beide Enzyme werden zunächst getrennt voneinander analysiert und anschließend durch Ko-Rekonstitution zu einem lichtgetriebenen ATP Regenerationsmodul kombiniert. Die ATP Syntheseleistung wird durch Analyse verschiedener Einflussfaktoren optimiert. Hierdurch können Produktionsraten von bis zu $4.5 \mu\text{M ATP (mg ATP synthase)}^{-1}(\text{min}^{-1})$ erreicht werden.

Für biotechnologische Anwendungen, sowie für die Absicht eine künstliche Zelle aus Einzelbausteinen zusammensetzen, ist es besonders wichtig die Aktivität der energieumsetzenden Proteine über einen längeren Zeitraum zu erhalten. Daher wird eine detaillierte Langzeitstudie über die Funktionalität der Membranproteinen in unterschiedlichen Hybrid-Kompartimenten durchgeführt. Diese beinhalten eine Mischung aus konventionellem Lipid und zwei Polymeren: PDMS-g-PEO und PBd-PEO. Durch Aktivitäten von mehr als 90% in Polymer/Lipid Vesikeln im Vergleich zu konventionellen Liposomen, kann zunächst eine hervorragende Biokompatibilität beider Polymere nachgewiesen werden. Sowohl die Lipid/Polymer-Hybride, als auch reine Polymer/Polymer-Hybride erhöhen die Langzeitstabilität der Membranproteine signifikant. Die maximal verbleibende Aktivität von etwa 80% nach 42 Tagen, kann jedoch in Polymer/Polymer-Hybriden, die aus jeweils 50% PDMS-g-PEO und 50% PBd-PEO bestehen, gezeigt werden.

Dass sich das ATP Modul tatsächlich zur Energieversorgung einer minimalen künstlichen Zelle eignet, kann durch erfolgreiche Kombination mit einer metabolischen Reaktion sowie durch Kopplung mit Elementen des motorischen Apparats der Zelle, bestätigt werden.

Table of contents

Abstract	i
Zusammenfassung	ii
Table of contents	iv
Nomenclature.....	x
1 Introduction.....	1
1.1 Motivation	1
1.2 Aim of this work	2
2 Theoretical Background.....	5
2.1 Synthetic Biology	5
2.1.1 Bottom-up synthetic Biology.....	6
2.1.2 Design of Biosystems from Functional Modules.....	7
2.2 Light Energy Conversion to ATP.....	9
2.2.1 EF_0F_1 ATP synthase	13
2.2.2 Bacteriorhodopsin.....	15
3 Material and Methods.....	17
3.1 Chemicals and Materials	17
3.2 EF_0F_1 ATP synthase expression, purification and characterization	17
3.2.1 Non his-tagged ATP synthase	18
3.2.1.1 <i>E. coli</i> cell growth	18
3.2.1.2 Isolation of EF_0F_1	19
3.2.1.3 Purification of EF_0F_1	20
3.2.2 His-tagged ATP synthase	21
3.2.2.1 <i>E. coli</i> cell growth	21
3.2.2.2 Isolation of EF_0F_1	21

3.2.2.3	Purification of EF _o F ₁	21
3.2.3	SDS-PAGE Analysis	22
3.2.4	Determination of ATP synthase concentration	22
3.2.5	Preparation of dialysis liposomes	22
3.2.6	ATP synthase reconstitution.....	23
3.2.7	Measurement of ATP synthesis.....	23
3.2.7.1	Calculation of ATP concentration and determination of k_{cat}	24
3.2.7.2	Vesicle preparation for determination of ATP synthase ΔpH and $\Delta\Psi$ dependency.....	25
3.2.8	Measurement of ATP hydrolysis	26
3.2.8.1	Determination of $k_{cat,H}$	26
3.2.9	Characterization of ATP synthase with AFM and cryo-TEM.....	27
3.2.9.1	Atomic Force Microscopy (AFM).....	27
3.2.9.2	Sample preparation for cryo-Transmission Electron Microscopy (cryo-TEM).....	28
3.3	Bacteriorhodopsin expression, isolation and characterization	28
3.3.1	<i>Halobacterium salinarium</i> cell growth.....	28
3.3.2	Isolation of purple membrane	28
3.3.3	Determination of bR concentration.....	29
3.3.4	Solubilization of bR patches	29
3.3.5	Preparation of vesicles for bR proton pumping	30
3.3.6	bR reconstitution and determination of reconstitution efficiency	31
3.3.6.1	Calculation of reconstitution efficiency	32
3.3.6.2	Proton pumping experiments	33
3.3.6.3	pH calculation from absorption change of encapsulated pyranine.....	33
3.3.7	Determination of bR orientation by proteolytic cleavage.....	34
3.4	Characterization of the ATP module	35
3.4.1	Preparation of vesicles for light-driven ATP production	35
3.4.1.1	Determination of destabilization points	35
3.4.1.2	Vesicle size and dispersity by Dynamic Light Scattering (DLS)	35
3.4.1.3	Estimation of liposome concentration and number of reconstituted enzymes	35
3.4.2	Co-reconstitution of ATP synthase and bR	36
3.4.3	Light-driven ATP production	37
3.4.3.1	Calculation of ATP concentration.....	37
3.4.4	Proton Permeability Measurements.....	37
3.4.4.1	Preparation of vesicles.....	37
3.4.4.2	Permeability measurements in PIPES buffer	38
3.4.4.3	Permeability measurements in HEPES buffer	38
3.4.4.4	Determination of pyranine calibration curves for different membrane compositions	38

Table of contents

3.5	IMV isolation and measurement	39
3.5.1	<i>Purification of Inverted Membrane Vesicles (IMVs)</i>	39
3.5.2	<i>Measurement of ATP production</i>	40
3.5.2.1	Calculation of ATP and determination of the initial reaction velocity	40
3.5.3	<i>Measurement of NADH consumption</i>	40
3.5.3.1	Calculation of NADH and determination of the initial reaction velocity	41
3.6	Coupling of the ATP module	41
3.6.1	<i>Multistimuli sensing adhesion unit for self-positioning of minimal synthetic cells</i>	41
3.6.1.1	Preparation of Ni ²⁺ -NTA liposomes	41
3.6.1.2	Co-reconstitution of EF ₀ F ₁ -ATP synthase and bR into Ni ²⁺ -NTA liposomes	41
3.6.1.3	ATP production and determination in reconstituted liposomes	41
3.6.1.4	QCM-D measurement	42
3.6.2	<i>Reactivation of isolated flagella via light-driven ATP regeneration</i>	42
3.6.2.1	Co-reconstitution and measurement of ATP production	42
3.6.2.2	Isolation and reactivation of flagella via light-driven ATP production	43
3.6.2.3	Axoneme counter tracking	43
3.6.3	<i>Measurement of light-triggered glucose consumption</i>	44
3.6.4	<i>Light-triggered actin-myosin contraction</i>	44
3.6.4.1	Actin preparation and labeling (Actin mix)	44
3.6.4.2	Myosin preparation and labeling (Myosin mix)	44
3.6.4.3	Preparation of ATP synthase-Actin/Myosin Droplets	45
3.6.4.4	Detection of Actin/Myosin contraction	45
4	Results and Discussion	47
4.1	ATP synthase	47
4.1.1	<i>Isolation of ATP synthase</i>	47
4.1.1.1	Isolation of his-tagged ATP synthase	51
4.1.2	<i>ATP synthase characterization in liposomes</i>	54
4.1.2.1	ATP synthesis as a function of ΔpH	54
4.1.2.2	ATP synthesis depending on ΔΨ	56
4.1.2.3	Long-term measurements of ATP synthesis	58
4.1.2.4	Characterization of ATP synthase with AFM and Cryo-TEM	59
4.2	Bacteriorhodopsin	61
4.2.1	<i>Isolation of bacteriorhodopsin</i>	62
4.2.2	<i>Characterization of bacteriorhodopsin in liposomes</i>	63
4.2.2.1	Pyranine as internal probe	63

4.2.2.2	Proton pumping using bR patches - Dependence on the number of pumping units	65
4.2.2.3	Bacteriorhodopsin solubilization	67
4.3	Light-driven ATP regeneration	68
4.3.1	<i>The ATP module in liposomes</i>	69
4.3.1.1	ATP synthesis rates as a function of bR concentration	71
4.3.1.2	ATP synthesis rates – bR patches vs. solubilized bR	72
4.3.1.3	ATP synthesis rates as a function of EF _o F ₁ concentration.....	73
4.3.1.4	Influence of the light source on the ATP synthesis rate.....	75
4.3.1.5	Influence of valinomycin on the ATP production rate.....	76
4.3.1.6	Influence of the ADP concentration on the ATP production rate	77
4.3.1.7	Influence of the liposome preparation method on the ATP synthesis rate	79
4.3.1.8	Influence of different buffers on the ATP synthesis rates	80
4.3.1.9	Freezing and storing of the ATP module	81
4.3.2	<i>The ATP module in lipid, polymer and hybrid vesicles with solubilized bR</i>	82
4.3.2.1	Membrane composition	84
4.3.2.2	Reconstitution procedure	86
4.3.2.3	Performance.....	89
4.3.2.4	bR reconstitution efficiency and proton pumping activity	91
4.3.2.5	bR orientation in different membranes	93
4.3.2.6	Passive proton permeability	95
4.3.2.7	Long-term stability	100
4.3.3	<i>The ATP module in lipid, polymer and hybrid vesicles with bR patches</i>	104
4.3.3.1	Membrane composition	104
4.3.3.2	Reconstitution procedure	105
4.3.3.3	Performance.....	110
4.3.3.4	bR reconstitution efficiency and proton pumping activity	112
4.3.3.5	bR orientation in different membranes	114
4.3.3.6	Passive proton permeability	115
4.3.3.7	Long-term stability	120
4.4	ATP production in IMVs	121
4.4.1	ATP production in Wildtype IMVs.....	122
4.4.2	ATP production in overexpressed IMVs.....	124
4.4.3	Comparison of kinetic data in bulk and droplets.....	125
4.5	Combining the ATP module with other functional modules	127
4.5.1	<i>Multistimuli sensing adhesion unit for the self-positioning of minimal synthetic cells</i>	127
4.5.2	<i>Reactivation of isolated flagella via light-driven ATP regeneration module</i>	132

Table of contents

4.5.3	<i>Light-triggered glucose consumption</i>	137
4.5.4	<i>Light-triggered actin-myosin contraction</i>	140
5	Conclusion and Outlook	143
A	Appendix	147
A.1	Chemicals & Devices	147
A.1.1	<i>Chemicals, Dyes, Enzymes and Kits</i>	147
A.1.2	<i>Materials and Devices</i>	150
A.2	Buffer and Media	151
A.3	Models for calculation of permeability coefficients.....	161
A.4	Supporting Figures.....	168
	References	171
	List of figures	183
	List of tables	187
	Publications and list of authorship	189

Nomenclature

ADP	Adenosine-5'-Disphosphate
ATP	Adenosine-5'-Triphosphate
DDM	Dodecyl- β -D-maltoside
DGS-NTA	1,2 Dioleoyl-sn-Glycero-3-[(N-(5-Amino-1-Carboxypentyl) iminodiacetic acid) succinyl (Nickel salt)
DMPC	1,2-Dimyristoyl-sn-Glycero-3-Phosphocholine,
DMPG	1,2-Dimyristoyl-sn-Glycero-3-Phosphoglycerol,
DOTAP	1,2-Dioleoyl-3-Trimethylammonium-Propane
DTT	Dithiothreitol
NADH	Nicotinamide Adenine Dinucleotide Hydride
OG	n-Octyl- β -D-Glucoside, Octyl glucoside
PA	Phosphatic Acid
PBd/PBd-PEO	Polybutadiene-b-Poly(ethylene oxide)
PC	Phosphatidylcholine
PDMS/PDMS-g-PEO	Polydimethylsiloxane-graft-Poly(ethylene oxide)
PEG	Polyethylene Glycol
P _i	Inorganic Phosphate
PMSF	Phenylmethanesulfonylfluoride
POPC	1-Palmitoyl-2-Oleoyl-sn-Glycero-3-Phosphocholine,
POPE	1-Palmitoyl-2-Oleoyl-sn-Glycero-3-Phosphoethanolamine
POPG	1-Palmitoyl-2-Oleoyl-sn-Glycero-3-Phosphoglycerol,
SDS	Sodium Dodecyl Sulfate
Triton	Triton X-100
CMC	Critical Micelle Concentration
<i>E. coli</i>	<i>Escherichia coli</i>
HPTS	Pyranine/8-Hydroxyprone-1,3,6-Trisulfonic acid
IMVs	Inverted Membrane Vesicles

kDa	kilo Daltons
ns	non-significant
*	significant
MT	Microtubule
P	Permeability coefficient
PDI	Polydispersity Index
PMF	Proton Motive Force
SDS-PAGE	Sodium Dodecyl Sulfate Polyacrylamide Gel Electrophoresis
SEM	Standard Error of the Mean
SLB	Supported Lipid Bilayers
Z_{ave}	Average size
bR	Bacteriorhodopsin
pR	Proteorhodopsin
CF ₀ F ₁ ATP synthase	F-type ATP synthase from chloroplasts
EF ₀ F ₁ ATP synthase	F-type ATP synthase from E. coli
MF ₀ F ₁ ATP synthase	F-type ATP synthase from beef heart mitochondria
TF ₀ F ₁ ATP synthase	F-type ATP synthase from thermophilic bacillus PS3
NDH	NADH Dehydrogenase
Q	Ubiquinone
cybd	Terminal Oxidase
ILD	Improved Light-induced Dimer
LOV2 domain	Light Oxygen Voltage sensing domain
GUVs	Giant Unilamellar Vesicles
LUVs	Large Unilamellar Vesicles
SUVs	Small Unilamellar Vesicles
AFM	Atomic Force Microscopy
DLS	Dynamic Light Scattering
TEM	Transmission Electron Microscopy
TIRF	Total Internal Reflection Fluorescence
QCM	Quartz Crystal Microbalance
R_{eff}	Reconstitution Efficiency
RLU	Relative Light Units
Δ pH	pH difference
pH _{in}	pH inside the vesicle

Nomenclature

pH_{out}	pH outside of the vesicle
pH_{mean}	middle value of pH courses
pH_0	pH at $t_0=0$
$\Delta\mu_{\text{H}}$	Electrochemical Potential Difference
$\Delta\psi$	Electrical potential difference
$c(\Delta\text{K}^+)$	Difference in K^+ concentration
$c(\text{K}^+_{\text{in}})$	K^+ concentration inside the vesicle
$c(\text{K}^+_{\text{out}})$	K^+ concentration outside the vesicle
A_{PC}	Lipid surface area of PC
A_x	Absorption at x nm
c_x	concentration of x
ε_x	extinction coefficient at x nm
l	thickness of the bilayer
I_x	Luminescence signal of x
N_{A}	Avogadro constant
N_{tot}	total number of lipids per vesicle
n_x	amount of substance x
N_x	Number of x per ml
M_x	Molar mass of x
V_x	Volume of x
$[\text{E}]$	Enzyme concentration
k_{cat}	catalytic constant of ATP synthesis
$k_{\text{cat,H}}$	catalytic constant of ATP hydrolysis
c_{ATP}	ATP concentration change
$c_{\text{ATP,mean}}$	middle value of ATP concentration changes
$c_{\text{ATP,cor}}$	corrected ATP concentration changes ($t_0=0$)
v_0	initial reaction velocity

1 Introduction

*Every brilliant experiment, like every great work of art,
starts with an act of imagination.*

Jonah Lehrer

1.1 Motivation

This work has been prepared in the framework of the MaxSynBio project (<https://www.maxsynbio.mpg.de/13480/maxsynbio>). Long-term goal of MaxSynBio is to create minimal protocells from bottom-up.

Natural systems are very complex, and it is far from evident whether life as such could not be implemented and maintained in much simpler predictable systems. In this regard, minimal systems could represent more efficient machineries for energy conversion or drug production compared to traditional host organisms like microbes. Therefore, minimal cells could potentially allow maximal efficiency in biotechnology processes.

A lot of research has been done in order to define a minimal host chassis using the top-down approach. Anyway, these studies have so far not attempted to define the minimal set of functional elements required to build a living system from scratch.

These fundamental questions, namely, what is life and how could it be integrated in a minimal system are addressed in the recently founded MaxSynBio initiative. Within MaxSynBio synthetic biology is approached from a fundamental perspective of basic research. This means the primary goal is a true bottom-up synthesis of minimal living systems through modular synthesis from well-characterized functional molecular entities, parts, and modules.

In order to reduce the complexity of living organisms, MaxSynBio focuses on the following selected life processes:

1 Introduction

- Energy Supply
- Metabolism
- Growth
- Replication and Division
- Signalling and Motility

At the MPI for Dynamics and Complex Systems in Magdeburg, one main focus is the energy supply of the minimal synthetic cell. Energy supply is a unique feature of living cells which have the ability to extract energy from their environment and use this energy to carry out activities such as growth, movement, or reproduction. Energy from nutrients (in cellular respiration) or light (in photosynthesis) is converted through respiratory or photosynthetic electron-transfer chains into a proton gradient across the membrane. This gradient is finally utilized for adenosine triphosphate (ATP) generation. To sustain life-mimicking processes in a synthetic cell, continuous supply of energy is required. Therefore, the aim of this thesis is to design and construct a light-driven module that is specified to continuously supply energy in form of ATP.

1.2 Aim of this work

The goal of this thesis is to construct a well-defined and characterized ATP regeneration module that uses solar energy to convert adenosine diphosphate (ADP) to ATP. This module consists of the light-driven proton pump bacteriorhodopsin (bR) and the EF_0F_1 ATP synthase. The electrochemical gradient generated by bR is used by the ATP synthase to synthesize ATP. The light-driven ATP module shall serve as energy supply for a minimal protocell.

To assemble the ATP module, the first step was to isolate and characterize both utilized enzymes (or parts) separately (Figure 2.1). After protein expression and purification, activity measurements proofed the functionality of the proteins. For ATP synthase, kinetic analysis was performed in order to clarify the contribution of the potential and pH gradient to the ATP production rate.

The next step was the co-reconstitution of both proteins in a suitable compartment. First, liposomes were used for co-reconstitution as lipids are the natural and therefore optimal surrounding of membrane proteins. The functionality of the assembled module was proven by light-triggered ATP production. Different factors that might influence the performance of the module were investigated to find the optimal conditions for maximal ATP production. A well-defined procedure for membrane protein co-reconstitution and measurement of ATP production rates were established.

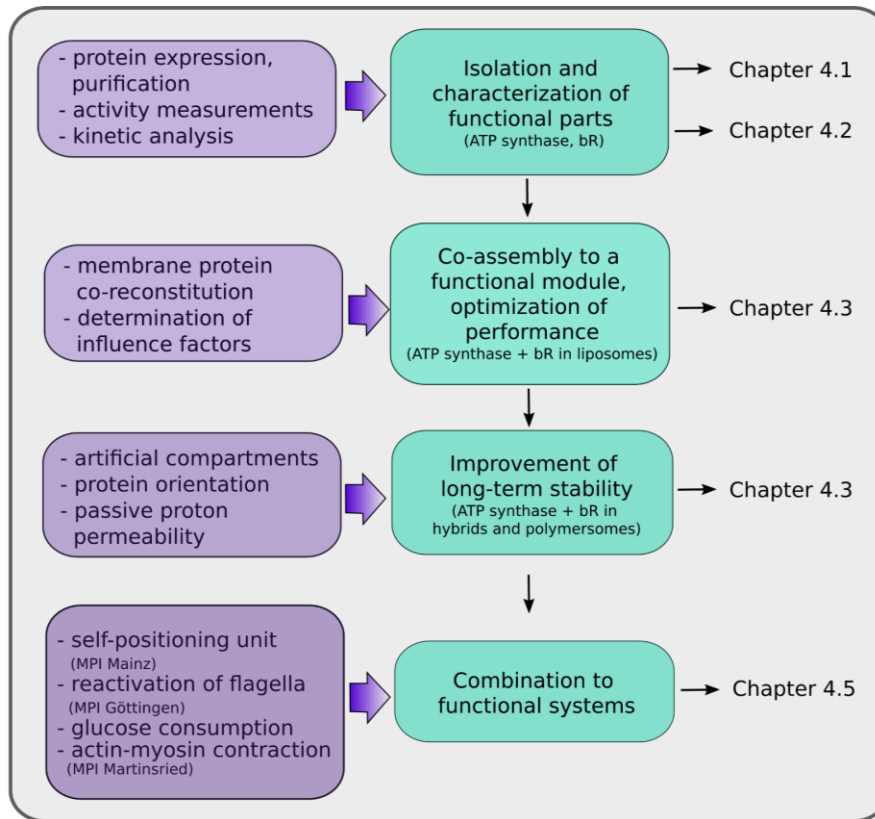


Figure 2.1 Overview of the thesis.

Afterwards, the main focus was to increase the long-term stability of the module. This is especially relevant when combining the module with other functional modules or for the usage in biotechnology applications. Polymers were reported to increase the durability of membrane proteins. Therefore, suitable hybrid and polymer compartments were used for membrane incorporation. A detailed study of the performance, protein orientation and permeability of different hybrid and polymer vesicles were conducted and compared with the results yielded for natural lipid membranes.

The ultimate goal of the project is to build a minimal protocell from functional modules and systems. Consequently, the light-driven ATP module was combined with other functional modules. First, as a proof of concept a combination with a trivial metabolic cascade, the conversion of glucose to glucose-6-phosphate was investigated. Afterwards, the module was coupled to a self-positioning unit in cooperation with the group of Prof. Dr. Seraphine Wegner at the MPI Mainz, was applied as energy supply for the reactivation of isolated flagella together with

1 Introduction

the group of Dr. Azam Gholami at the MPI Göttingen and was coupled to actin-myosin contraction in collaboration with Dr. Sven Vogel at the MPI Martinsried.

Another project was realized with our cooperation partners in Bordeaux. In this study, the ATP production kinetics of inverted membrane vesicles (IMVs) was analysed.

Following parts of the thesis are already published and are cited according to the corresponding journal article:

- Chapter 2.2 L. Otrin, **C. Kleineberg**, L. Caire da Silva, I. Ivanov, M. Wang, C. Bednarz, K. Sundmacher, T. Vidakovic-Koch (2019) Artificial Organelles for Energy Regeneration. *Adv. Biosyst.* 3 (6).
- Chapter 4.3.2 **C. Kleineberg**, C. Wölfer, A. Abbasnia, D. Pischel, C. Bednarz, I. Ivanov, T. Heitkamp, K. Sundmacher, T. Vidakovic-Koch (2020) Light-Driven ATP Regeneration in Diblock/Grafted Hybrid Vesicles. *ChemBioChem.* 21 (15), 2149-2160.
- Chapter 4.4 T. Beneyton, D. Krafft, C. Bednarz, **C. Kleineberg**, C. Woelfer, I. Ivanov, T. Vidakovic-Koch, K. Sundmacher, J.-C. Baret (2018) Out-of-equilibrium microcompartments for the bottom-up integration of metabolic functions. *Nat. Commun.* 9 (1).
- Chapter 4.5.1 D. Xu, **C. Kleineberg**, T. Vidakovic-Koch, S. V. Wegner (2020) Multistimuli sensing adhesion unit for the self-positioning of minimal synthetic cells. *Small* 16 (35), 2002440-2002448.
- Chapter 4.5.2 R. Ahmad[†], **C. Kleineberg[†]**, V. Nasirimarekani, Y. Su, S. Goli Pozveh, A. J. Bae, K. Sundmacher, E. Bodenschatz, I. Guido, T. Vidakovic-Koch, A. Gholami (2021) Light-Powered Reactivation of Flagella: and Contraction of Microtubule Networks: Toward Building an Artificial Cell. *ACS Synth. Biol.* 10, 6, 1490-1504.

2 Theoretical Background

*Nature doesn't have a design problem.
People do.*

William McDonough, Michael Braungart

2.1 Synthetic Biology

This section introduces the emerging field of synthetic biology and reviews the recent advances in this field. A particular focus is on bottom-up synthetic biology, which is the main focus of MaxSynBio.

In the past 60 years huge advances in biology, especially molecular biology, have been made. Thereby, genetic and biological information such as gene sequences or protein structures has been rapidly accumulated. Besides decoding many microbial genomes as well as the human genome, great progress has been made in the technologies that allow us to analyse small molecules or manipulate genetic material (1). One important technology is genetic engineering, which can be used to design new gene circuits from scratch and create desired properties in a predictable manner (2). This progress led to the birth of a new field called synthetic biology. Synthetic biology has been established as an engineering discipline with the goal to design and construct novel biologically based parts, devices and systems, as well as the redesign of existing natural biological systems, for useful purposes (3).

The scientists of the engineering field of synthetic biology like quoting the phrase Richard Feynman had written on his blackboard: 'What I cannot create I do not understand'. This phrase comprises both a warning about the limitations of analysis in understanding complex systems as well as the endorsement of the value of design in the quest for discovery (4).

2 Theoretical Background

Analysis, modelling and simulation focus on the details of individual elements and components, whereby the pure nature of design deals with the compromises to enable system function. This suggests as well that the redesign is a promising route to understand the fundamental principles. Rewriting efforts of synthetic biology have usually followed a strategy of constructing simplified systems to get an understanding of cellular regulatory processes from the bottom-up (5; 6; 7; 8).

The synthetic biology field itself is diverse, but can broadly be divided into two main areas. One area is the bottom-up approach which has the goal to truly create artificial life *de novo*. The top-down approach focuses on the design of systems based on known biology, which involves designing metabolic and signalling pathways inside cells to achieve a specific purpose. Within the top-down approach, biological elements such as promoters or gene products can be defined as parts being assembled into a system. The big advantage of the top-down approach is that the use of a host cell enables the possibility to take co-factors, metabolites, transcription pathways or other components that already exists in the cell. On the other hand, this holds the risk of potential crosstalk between the endogenous system and the introduced synthetic system (3).

2.1.1 *Bottom-up synthetic Biology*

Bottom-up synthetic biology takes the challenge to construct cell-like systems starting from molecular building blocks, with the goal to recreate living organisms. As living organisms are highly complex, the aim is to understand the fundamental principles underlying the life processes by reducing the complexity of the systems to be investigated drastically. Minimization is an important strategy in synthetic biology. The bottom-up approach has the big advantage that the complexity of the objects of investigations, particularly the number of system components and the number of interactions, is much better controllable than in experiments performed in the top-down manner. The bottom-up approach moreover opens the door for the new combination of natural and non-natural molecules and parts. Thereby, one could not only mimic essential processes of life, but could possibly obtain new bio machines featuring totally new behaviours (9). One major focus of bottom-up synthetic biology is the creation and manipulation of synthetic compartments for encapsulation and/or reconstitution of active modules that support lifelike properties. The generation of synthetic compartments with defined sizes, chemical and material properties is therefore essential. One possibility to achieve this, is for example microfluidics which is becoming a more and more important tool for the generation, handling, manipulation and analysis of synthetic compartments. One recent example is presented by Krafft et al. (10) to produce giant unilamellar vesicles (GUVs) from double emulsion templates. Using osmotic

pressure complete separation of the undesired oil-phase from the liposomes could be achieved. Robinson and Dittrich in contrast, showed the capture of single GUVs by microfluidics and how to manipulate and shape them using an integrated micro-stamp (11). Further work on the formation, growth and division of membrane vesicles (12), the replication of nucleic acids inside protocells, (13) and primitive bio catalysis was pioneered by origin-of-life researchers who followed the bottom-up approach (14).

The most rewarding model systems with regard to quantitative description of biological structure formation and self-organization are on the one hand successful reconstitution of molecular motor systems, as well as the creation of membrane model systems with reduced complexity or the encapsulation of biological information in minimal systems (15). The *in vitro* reconstitution of 'functional modules' of the cytoskeleton such as motor proteins or interactions between them can be seen as a way of balancing mutually conflicting demands for simplicity. This is essential for systematic and quantitative studies, and for a sufficient degree of complexity that allows an appropriate representation of biological functions (16).

Other recent examples for bottom-up synthetic biology addresses further important aspects of living systems such as energy production and regeneration as described by Ma et al. (17). Ma et al. showed a polymer-based module capable of nicotinamide adenine dinucleotide (NAD⁺) coenzyme regeneration by light-triggered photocatalysis. Hürtgen et al. demonstrated a further essential feature for the design of a minimal synthetic cell. He and his group used simple T7 bacteriophage system and the plasmid-derived ParMRC segregation to successfully replicate and segregate genetic material (18).

2.1.2 Design of Biosystems from Functional Modules

In the future, great progress in the bottom-up design of biosystems is expected, which goes along with an increasing number of functional building blocks. In this way, libraries of molecules, parts and modules will be established. Defined parts and modules are one of the major prerequisites for systematic synthesis of artificial life-like systems (19; 20).

One of the critical steps in sustaining life-mimicking processes in synthetic cells, is the energy regeneration. Metabolism, cell division and motility are examples for cell-like functions that are dependent on continuous supply of energy in form of adenosine triphosphate (ATP). As previous studies have shown that simple addition of ATP or ATP regeneration systems which do not regenerate ATP directly from ADP and P_i, have no or only limited success due to accumulation of ATP hydrolysis products (21), an ATP regeneration system that produces ATP from ADP is

2 Theoretical Background

essential. A scheme of the engineering perspective of basic principles of energy regeneration is shown in Figure 2.2. Different functional parts are defined as proteins or compartments. Compartments consist either of lipids or amphiphilic polymers that are assembled to vesicles. Proteins have to be first isolated and then characterized due to performance and orientation. In a next step, proteins are embedded into a suitable container using an appropriate reconstitution method. The assemble of various functional parts creates a functional module. This can be for example a transport module, a metabolic conversion module or an energy regeneration module. The energy regeneration module can be subdivided in a 'Chemical energy to ATP module' and a 'Solar energy to ATP module' depending on the source of energy (chemical energy and light respectively). At the end, an artificial life-like system is built by assembly of functional modules. The computer-aided support is a big vision from the bioengineer's point of view. This can be realized by simulations and optimizations that in the end allow for correct assembly of functional modules or systems.

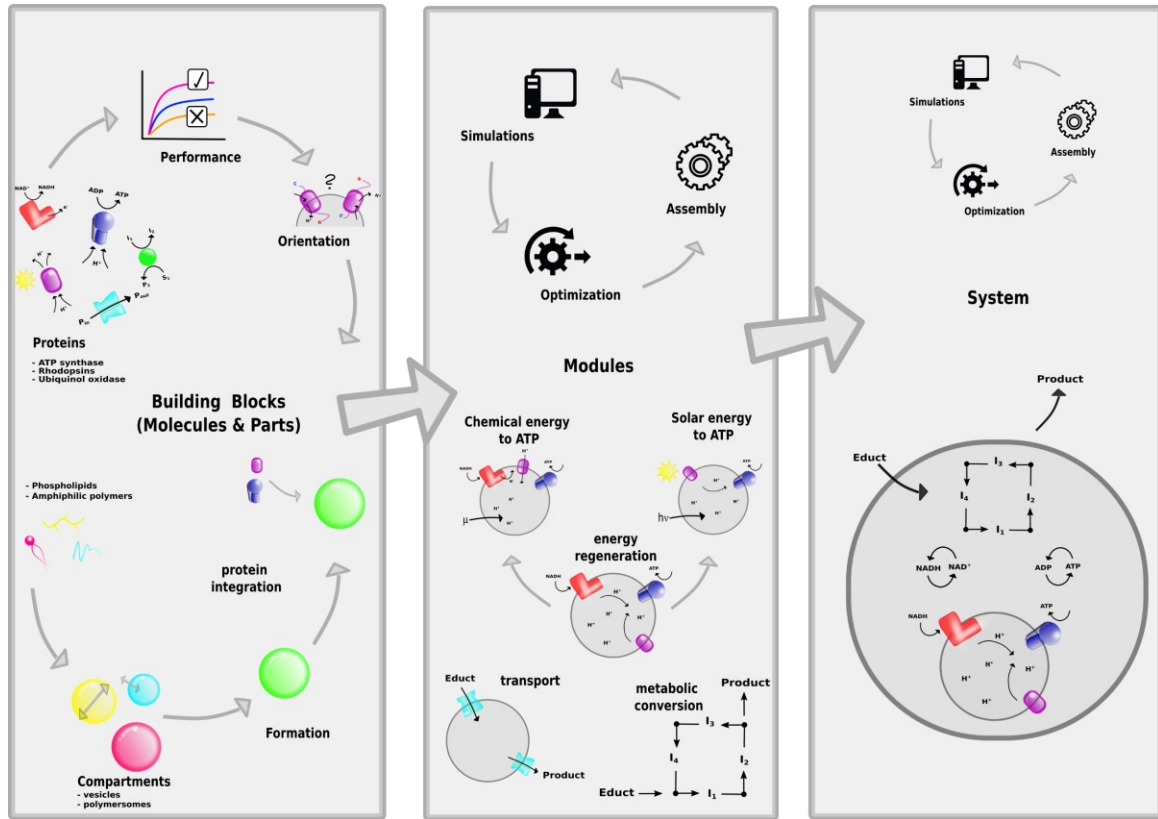


Figure 2.2 Scheme of the engineering perspective of the basic principles of energy and co-factor regeneration as well as the assembly to a functional system.

2.2 Light Energy Conversion to ATP

A unique feature of living cells is the ability to extract energy from their environment and to use this energy to carry out essential activities such as movement, growth or reproduction. This energy can either come from nutrients in the case of cellular respiration or from light in the case of photosynthesis. In general, energy is transformed through respiratory or photosynthetic electron-transfer chains into a proton gradient across the membrane, which is utilized for ATP synthesis (19).

In nature, ATP regeneration is coupled to the recycling of nicotinamide cofactors (NADH or NADPH). These processes can be decoupled when the necessary proton gradient for ATP synthesis is generated by a light-driven proton pump such as bacteriorhodopsin (bR).

The use of light as a source to produce energy in form of ATP confers this system several advantages. The usage of sunlight makes it a free and unlimited energy source, drawing parallels with solar cells or other photovoltaic devices with respect to their potential applications. Up to

2 Theoretical Background

date, different attempts to mimic energy regeneration processes under *in vitro* conditions have been reported. So far, the combination of ATP synthase with a light-driven proton pump attracted most attention. This is mainly due to the fact that this assembly is “less” complex compared to oxidative or photo-phosphorylation and produces energy in form of ATP which is required in all life mimicking processes.

The first reports for simple prototypes of these modules combining light-driven proton pumps and ATP synthase in liposomes have been published already in the early 70's. In 1974, Racker and Stoeckenius (5) could give the first experimental proof of the Mitchells chemiosmosis theory by co-reconstitution of bacteriorhodopsin and ATP synthase. Mitchell's chemiosmosis theory suggested that the ATP synthase is driven by the so-called proton motive force (PMF) compounded by the proton gradient and the potential gradient over the membrane. By variation of different types of ATP synthases and lipid compositions the stability and productivity of the bR-ATP synthase co-assembly could be constantly improved (22; 23; 24; 25). *In vitro* assemblies of bR and ATP synthase from chloroplasts (CF_0F_1) (22; 23), beef heart mitochondria (MF_0F_1) (24), and thermophilic *bacillus* PS3 (TF_0F_1) (25; 26) have been reported. A summary of existing light-driven ATP regeneration systems is reviewed in Table 2.1 (27).

Table 2.1 Overview of light-driven ATP regeneration modules.

Reference	Compartment	ATP synthase	Gradient generator	Performance
Matuschka 1995 (24)	PC	Beef heart mitochondria (MF ₀ F ₁)	Bacteriorhodopsin, <i>H. salinarium</i> , 150 µg ml ⁻¹	58 nmol ATP min ⁻¹ mg ⁻¹ FoF ₁
Richard 1992 (23)	PC/PA mixture	Spinach chloroplasts (CF ₀ F ₁)	Bacteriorhodopsin, <i>H. salinarium</i> , 12 x 10 ⁻⁶ M	204 nmol ATP min ⁻¹ mg ⁻¹ FoF ₁
Racker 1974 (28)	Soybean phospholipids	Beef heart mitochondria (MF ₀ F ₁)	Bacteriorhodopsin, <i>H. salinarium</i> , 4.2 mg ml ⁻¹	312 nmol Glucose-6-P min ⁻¹ mg ⁻¹ FoF ₁
Pitard 1996 (25)	PC/PA mixture	<i>Bacillus PS3</i> (TF ₀ F ₁)	Bacteriorhodopsin, <i>H. salinarium</i> , 0.8 mg ml ⁻¹	200 nmol ATP min ⁻¹ mg ⁻¹ FoF ₁
Wagner 1987 (29)	Soybean lecithin	<i>Rhodospirillum rubrum</i> (EF ₀ F ₁)	Bacteriorhodopsin, <i>H. salinarium</i> , 0.1 mg ml ⁻¹	280 nmol ATP min ⁻¹ mg ⁻¹ FoF ₁
Choi 2005 (30)	ABA triblock copolymer	<i>Bacillus PS3</i> (TF ₀ F ₁)	Bacteriorhodopsin, <i>H. salinarium</i> , 4.8 mg ml ⁻¹	~120 nmol ATP min ⁻¹ mg ⁻¹ FoF ₁
Feng 2016 (31)	Liposome (DMPC and DMPG mixture)-coated PSII-based microspheres	Spinach chloroplasts (CF ₀ F ₁)	Photosystem II, spinach, 0.2 mg ml ⁻¹	15 nmol ATP min ⁻¹ mg ⁻¹ FoF ₁
Lee 2018 (32)	POPC/POPE/POPG/Chloroform mixture	<i>Bacillus pseudofirmus</i> (TF ₀ F ₁)	Photosystem II, spinach 2.2x10 ² /100 nm liposome and proteorhodopsin Proteobacterium, 4.3x10 ² /100nm liposome	150 mol ATP (1 mol chromophores) ⁻¹
Steinberg-Yfrach 1998 (33)	PC/PA/Chloroform mixture	Spinach chloroplasts (CF ₀ F ₁)	Lipophilic quinone Qs, 1x10 ³ /150nm liposome	35 nmol ATP h ⁻¹ or 7 s ⁻¹ FoF ₁ ⁻¹
Li 2019 (34)	DMPC/DOTAP mixture	Spinach chloroplasts (CF ₀ F ₁)	Photoacid, 10 mg ml ⁻¹	250 nmol ATP min ⁻¹ mg ⁻¹ FoF ₁
Xu 2017 (35)	DMPC/DMPG mixture	Spinach chloroplasts (CF ₀ F ₁)	Assembled membrane containing photoacid, 10 mg ml ⁻¹ and proton conductor	20 nmol ATP min ⁻¹ mg ⁻¹ FoF ₁
Li 2019 (36)	DMPC/DMPG mixture	Spinach chloroplasts (CF ₀ F ₁)	Photobase, 0.5x10 ⁻³ M	0.7 nmol ATP min ⁻¹ mg ⁻¹ FoF ₁

PC: Phosphatidylcholine, PA: Phosphatic Acid, POPC: 1-palmitoyl-2-oleoyl-sn-glycero-3-phosphocholine, POPG: 1-palmitoyl-2-oleoyl-sn-glycero-3-phosphoglycerol, DMPC: 1,2-dimyristoyl-sn-glycero-3-phosphocholine, DMPG: 1,2-Dimyristoyl-sn-glycero-3-phosphoglycerol, POPE: 1-palmitoyl-2-oleoyl-sn-glycero-3-phosphoethanolamine, DOTAP: 1,2-dioleoyl-3-trimethylammonium-propane

2 Theoretical Background

To construct such an energy conversion apparatus in a well-defined and controllable way, both enzymes have to be isolated independently and reincorporated into a membrane. During co-reconstitution procedure it's difficult to match experimental requirements for each protein. In practice, this often leads to problems with the unidirectional orientation of bacteriorhodopsin and therefore to a suboptimal performance of the synthesized module (27).

Another critical point for the performance of these co-assemblies is the bR/ATP synthase ratio per liposome. Different bR/ATP synthase ratios ranging from 1/1 (29; 24) to 170/1 (23) have been reported. Various methods to analyse the activity of both building blocks in the membrane have been established. For example, the generated proton motive force (PMF) is usually measured by light-induced changes in pH using the pH-sensitive probe pyranine (26; 30). The activity of ATP synthase can be determined in an acid-base transition experiment, measuring the ATP production with the luciferin/luciferase assay (22; 23; 24; 25).

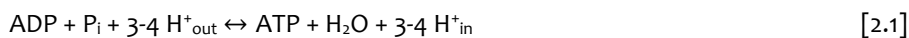
Besides the commonly used rhodopsin's as proton pump, application of other PMF generators was reported. Altamura et al. (37) for example extracted a transmembrane protein, called the photosynthetic reaction center (RC) and reconstituted the proton pump in a highly orientated manner into giant vesicles capable of generating a photoinduced proton gradient over the membrane. In purple photosynthetic bacteria a simple version of this photoenzyme catalyses the reduction of a quinone molecule, accompanied by the uptake of two protons from the cytoplasm. In the presence of an electron donor (reduced cytochrome c_2) and an electron acceptor (ubiquinone), RC absorbs a photon and generates an electron-hole. While reduced cytochrome c_2 transfer electrons to RC from the external pool, protons are taken up from the cytoplasm by ubiquinone. This leads to the formation of ubiquinol, thus establishing a proton gradient over the membrane. Li's group (31) co-assembled photosystem II and ATP synthase and showed light-driven ATP production in these artificial chloroplasts. Only recently, a switchable photosynthetic organelle has been designed by co-assembly of ATP synthase and two types of proton pumps, a plant-derived photosystem II (PSII) and a bacteria-derived proteorhodopsin, respectively (32). In this assembly blue and red light activates electron transport chains in the PSII reaction center, whereas green light initiates direct proton pumping in proteorhodopsin. Proteorhodopsin exhibits pH-dependent bidirectional proton-pumping. At higher pH both proton pumps are working in conjunction to increase the PMF, but at lower pH proteorhodopsin is changing pumping direction, counteracting the action of PSII. Thus, ATP synthesis can be dynamically facilitated or impeded by stimulation of PSII and PR with red or green light.

Although most studies reporting on light to ATP conversion devices that rely on biological building blocks, there are some examples where chemical building blocks were implemented. The first incorporation of light energy conversion building blocks into artificial environment was reported by Choi and Montemagno (30) who demonstrated functional integration of bR and TF₀F₁ ATP synthase into polymersomes consisting of ABA triblock copolymer as chemical building blocks. In other approaches biochemical proton pumps were replaced by biomimetic analogues. Steinberg-Yfracht (33) successfully co-assembled ATP synthase with an artificial photosynthetic membrane containing components of the proton-pumping photocycle. The proton pump is driven by vectoral photoinduced electron transfer in a carotene-porphyrin-naphthoquinone molecular triad.

Besides the above described biological proton pumps, there are also some chemical analogues reported for proton gradient establishment. Junbai Li's group (35; 34) recently used a light-driven photoacid generator to drive ATP synthesis. Another example reported by Guangle Li et al. (36) established a proton gradient for ATP synthase by scavenging protons present in the external medium by hydroxyl ions, produced by partially photo-induced splitting of photobase generator. In this study, bacteriorhodopsin and EF₀F₁ ATP synthase were used for light-driven ATP synthesis and are therefore explained in the following.

2.2.1 EF₀F₁ ATP synthase

F-type ATP synthases are ubiquitous membrane-bound enzymes. In bacteria, ATP synthases are located in the plasma membrane and are called EF₀F₁ ATP synthases. F-type ATP synthases are producing ATP from adenosine diphosphate (ADP) and inorganic phosphate (P_i). The general reaction scheme is as follows:



To drive the energetically unfavoured formation of ATP, ATP synthase uses an electrochemical gradient which is produced by differences in H⁺ concentrations on both sides of the membrane. F-type ATP synthases consists of two main subunits, F₀ and F₁, which have a rotational motor mechanism allowing for ATP production (Figure 2.3) (38).

2 Theoretical Background

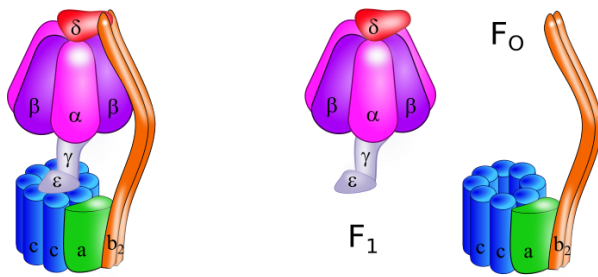


Figure 2.3 Schematic presentation of bacterial ATP synthase (EF₀F₁).

Own representation based on Okuno et al. (39).

F₁ region

The F₁ part is made of subunits α , β , γ , δ , ϵ and has a predominant hydrophilic character. Therefore, this part sticks out of the membrane and is responsible for hydrolysis/synthesis of ATP. The group of J. E. Walker showed in 1994 (40) that the F₁ part is comprised of three $\alpha\beta$ -pairs that form a hexagonal barrel with 6 binding sites. Three of them are catalytically inactive and bind ADP, while the other three catalyse ATP synthesis. The other subunits of the F₁ region (γ , δ , ϵ) are part of the rotational motor mechanism (39).

F₀ region

The F₀ part is the membrane-spanning part of the enzyme. It has a hydrophobic character and acts as proton pore. F₀ causes the rotation of the F₁ part and contains the c-ring as well as subunit a and subunit b₂. The c-ring has a tetramer shape with a helix-loop-helix protein that changes its conformation upon binding or deliver of a proton. This conformation change pushes neighbouring subunits to rotate (39). The number of c subunits forming the ring can vary between different species and is crucial for the H⁺ to ATP stoichiometry. Recently determined cryo-TEM structures of the EF₀F₁ ATP synthase confirms a stoichiometry of c10 (38). Therefore, the conversion of 3.5 protons to one ATP can be expected.

In the 1960s Paul Boyer postulated the binding change mechanisms for ATP synthase. This mechanism indicates that ATP synthesis depends on conformational changes in the enzyme generated by the rotation of γ subunit. The active sites of the β subunits are cycling between three states (Figure 2.4). In the 'loose' (L) state, ADP and phosphate enter which causes a conformational change in shape. This forces ADP and P_i molecules together, with the active site resulting in the 'tight' (T) state. In the T state new produced ATP can be bound with high affinity.

The produced ATP is released when the protein changes into the 'open' (O) state. New ADP and P_i for the next cycle can enter (41).

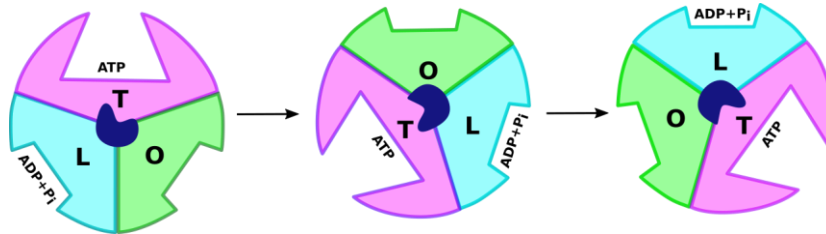


Figure 2.4 Schematic illustration of Boyer's binding change mechanism for ATP synthase.

Own representation based on Gresser et al. (41).

2.2.2 Bacteriorhodopsin

Bacteriorhodopsin (bR) is a light-induced proton pump found in the purple membrane of the archaeal bacterium *Halobacterium Halobium*. The protein is usually present in a two-dimensional crystalline lattice. Each repeating element is formed by 3 monomers of the enzyme and each monomer is assembled by 7 transmembrane alpha helices with one molecule retinal buried deep within. The light-sensitive chromophore retinal is covalently linked to Lys216 by Schiff base action and absorbs green light with a broad absorption maximum at 570 nm. Upon irradiation, isomerization of the chromophore from *all-trans* to *13-cis* conformation is induced. The photocycle of bR is divided in the time dependent intermediates J_{260} , K_{590} , L_{550} , M_{412} , N_{530} and O_{640} that have different charge- or configuration states and can be distinguished by their changing absorption maxima (Figure 2.5) (42).

In the absence of light bR is in the dark-adapted state in which the retinal is to 65% present in the *13-cis* conformation. Upon light irradiation all retinal turns into the *all-trans* conformation. Upon the absorption of a photon, the photocycle starts and isomerization from *all-trans* to *13 cis* conformation (J_{620}) occurs. In this conformation the retinal is present in a highly tensioned form. In the K_{590} state retinal has already transferred to the *13-cis* conformation, but is still strongly twisted. The relaxed *13-cis* conformation is reached (L Intermediate) and upon degradation of the L intermediate the Schiff base releases its proton to aspartate D85, resulting in a strong blue shift in the absorption spectra. The intermediate N_{530} marks the state in which the Schiff base gets reprotonated by a proton from the extracellular side. The retinal returns in the *all-trans* conformation (O intermediate) and a proton is released from D85 to the intracellular space (42).

2 Theoretical Background

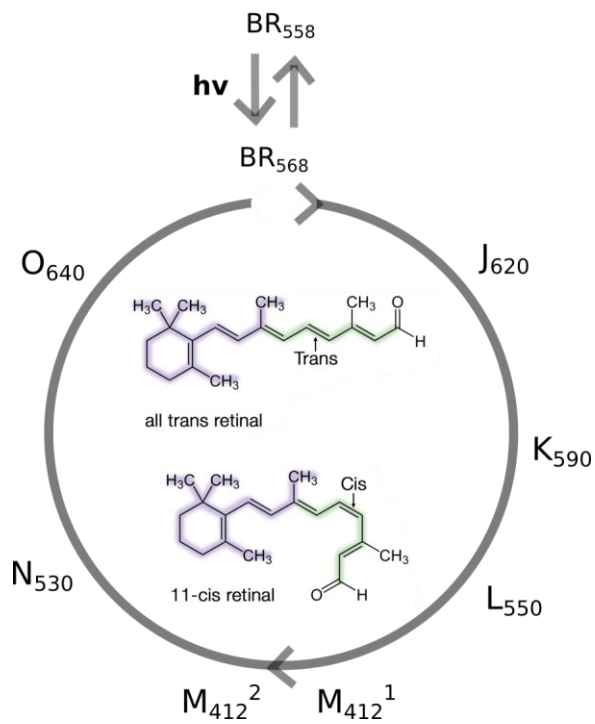


Figure 2.5 Schematic presentation of the intermediates of the photocycle of bR.

The transport of a proton from the intracellular to the extracellular space occurs between M_{412}^1 and M_{412}^2 . Own representation based on Havashi et al. (42).

3 Material and Methods

*Above all, don't fear difficult moments.
The best comes from them.*

Rita Levi-Montalcini

3.1 Chemicals and Materials

Lipids were purchased from Avanti Polar Lipids. Polymer PDMS-g-PEO was a kind gift from Dow Corning. Poly(butadiene-b-ethylene oxide) (PBd22-b-PEO14) was purchased from Polymer Source (P9089-BdEO). Luciferin/Luciferase reagent CLSII from Roche was prepared as a 10 times concentrated solution. Ultra-pure ADP was purchased from Cell Technology. Most of the other reagents were obtained from Sigma Aldrich. All buffers and solutions were strictly prepared using MilliQ water, which was purified by the Integral Water Purification System from Merck. A detailed listing of all chemicals and devices can be found in the appendix (A.1 Chemical and Devices, A.2 Buffer and Media).

3.2 EF_0F_1 ATP synthase expression, purification and characterization

EF_0F_1 ATP synthase was expressed as non his-tagged ATP synthase in the labs of Prof. Michael Börsch (University Jena) (chapter 3.2.1). The adaption of the procedure to our labs was quite difficult and the isolation of ATP synthase time consuming. Therefore, we implemented his-tagged ATP synthase isolation in *E. coli* which was conducted in our labs at MPI Magdeburg (chapter 3.2.2).

3 Material and Methods

3.2.1 Non his-tagged ATP synthase

Non his-tagged ATP synthase was expressed from the plasmid pBWU13 (*atpI*'BEFHAGDC, Ap^R) (43) in the *E. coli* strain DK8 (*bg/R*, *thil*, *rell*, *Hfr*801, Δ *atpB-C ilv::Tn10*) (44) according to Fischer et al. (45). The ratio of ATP synthase to the overall membrane proteins using this strain and plasmid was around 25% (46). In contrast, the ratio in *E. coli* wildtype is only 1-2%.

3.2.1.1 *E. coli* cell growth

The bacteria cultivation was performed by plating, followed by two precultures and a cultivation step in a fermenter. The steps are explained in the following.

Plating

Bacteria from the long-term culture were used to inoculate agar plates which were incubated overnight at 37 °C.

Precultures

Preculture I: A bacteria colony from the agar plate was inoculated in 200 ml Luria media (Table A.1) supplemented with 100 mg/l Ampicillin and was incubated for 7 hours in a shaker at 250 rpm and 37°C.

Preculture II: 60 ml of preculture I was inoculated in 2 l culture medium (Table A.2) and incubated for 6 hours at 250 rpm and 37°C.

Fermentation

The main culture was grown in a fermenter (Bioengineering, Laborpilot LP351) at 37°C, 1 bar and 250-450 rpm. 22 l Milli-Q water, 2.8 l T1 (Table A.3) and 560 ml glycerine solution (3.75 M) were sterilized for 20 min at 121°C. 2 l of preculture II was supplemented with 4 ml amino acid solution (Table A.5), 4.2 ml thiamine solution (20 g/l) and 14 ml Ampicillin (200 g/l). The cell growth was checked each hour by measuring the optical density at 578 nm and by monitoring the oxygen content of the media. The fermenter was equipped with an oxygen sensor and an oxygen inlet. Oxygen content could be regulated by adjusting the flow of oxygen from an external gas bottle. Oxygen is the limiting factor for the bacteria growth. If the oxygen content is lower than 5%, the bacteria growth switches from the exponential phase to the stationary phase (47). Therefore, the fermentation was stopped at an oxygen content of 5% after approximately 12 hours with an optical density of around 1.6.

Cell harvesting

The cell growth was stopped by cooling the fermenter down to 5°C. The cells were collected by centrifugation (Beckmann Instruments, 9.000 rpm, 4°C), frozen in liquid nitrogen and stored in 20-25 g portions at -80°C.

3.2.1.2 Isolation of EF₀F₁

Isolation of EF₀F₁ was conducted according to Starke et al. (48). Figure 3.1 shows the schematic procedure.

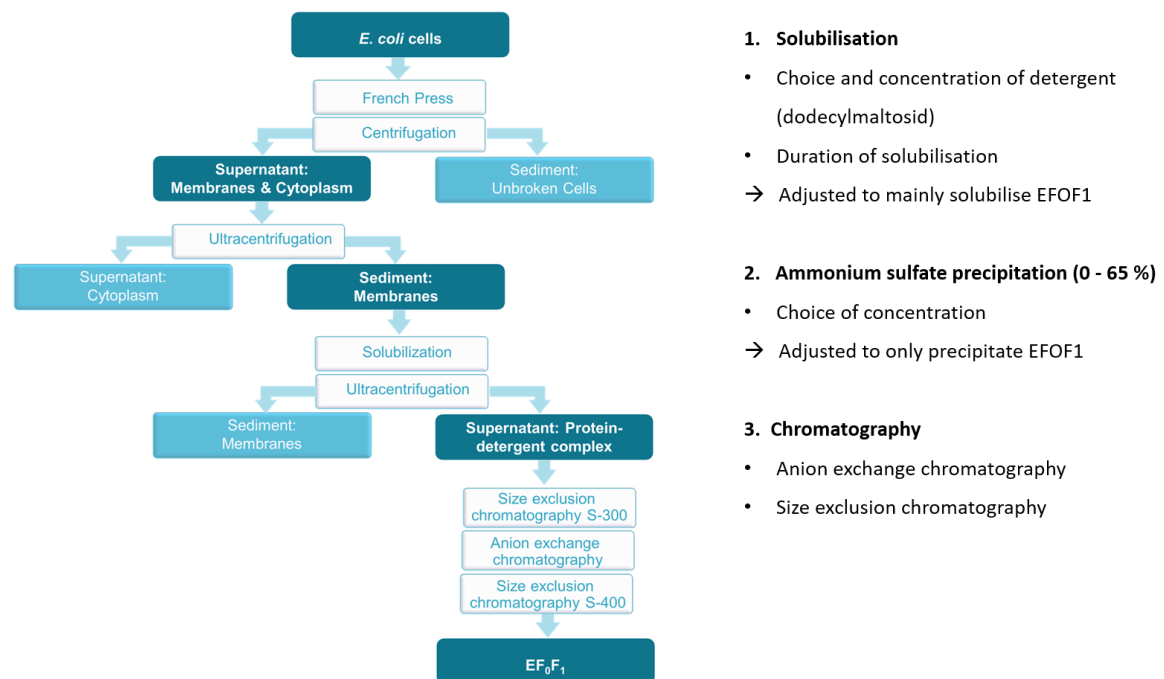


Figure 3.1 Schematic diagram of non-his tagged EF₀F₁ isolation in *E. coli* (45; 48).

Own representation based on Starke et al. (48).

Cell lysis

50 g of cells were defrosted overnight in 300 ml washing buffer (50 mM Tris-HCl, pH 8.0) at 4°C. The cell suspension was centrifuged for 10 min at 9.000 rpm and 4°C and the pellet was resuspended another time in 300 ml washing buffer, stirred for 45 min and centrifuged for 10 min at 9.000 rpm. After washing, the cells were resuspended in 200 ml French Press buffer (Table A.6) supplemented with a spade point tip of DNase and stirred for 30 min. The cell lysis was executed in a cooled French press at 1.300 psi and a drop speed of 1-2 drops/s. The drops were collected in liquid nitrogen and stored at -80°C.

3 Material and Methods

Membrane isolation

The broken cells were thawed and centrifuged for 15 min at 13.000 rpm and 4°C. After separation the supernatant was centrifuged another time (14.000 rpm, 15 min, 4°C). The sediment containing unbroken cells was discarded and another ultracentrifugation (50.000 rpm, 90 min, 4°C) was performed in order to separate the membranes from the cytoplasm.

3.2.1.3 Purification of EF_oF₁

Solubilization of membrane proteins

The sediment containing the membranes was resuspended in membrane buffer (Table A.7) and centrifuged at 54.000 rpm for 90 min at 4°C. After weighting the pellet, the membranes were resuspended in solubilization buffer (Table A.8) supplemented with 1.75% Dodecylmaltoside (DDM). The solution was stirred for 30 min and centrifuged (54.000 rpm, 90 min, 4°C). The supernatant was supplemented with 0.001% Phenylmethanesulfonylfluoride (PMSF) and the pellet was discarded.

Size exclusion chromatography S-300

The solubilized membrane proteins were precipitated slowly in two steps with saturated ammonium sulfate solution till a final concentration of 65%. After adding 0.001% PMSF the solution was stirred overnight and centrifuged for 15 min at 4°C and 17.000 rpm. The sediment was solubilized in 5 ml buffer A (Table A.9) and filtrated (Whatman, 0.45 µm) before the solution was applied to the size exclusion column S-300.

Anion exchange chromatography

Fractions with an absorbance over 0.3 were combined and added to the anion exchange column Poros HQ20.

Size exclusion chromatography S-400

Fractions with an absorbance over 0.1 were combined and supplemented slowly with saturated ammonium sulfate solution till a final concentration of 65%. 0.001% PMSF was added and the solution was stirred overnight and centrifuged (17.000 rpm, 15 min, 4°C). The pellet was resuspended in 500 µl of buffer A (Table A.9) and centrifuged another time (10.000 rpm, 5 min, 4°C). The supernatant was added to the size exclusion column S-400. The fractions containing the protein were frozen in liquid nitrogen and stored at -80°C.

3.2.2 His-tagged ATP synthase

His-tagged *E. coli* F₀F₁-ATP synthase (EF₀F₁) was expressed from the plasmid pBWU13-βHis in the *E. coli* strain DK8 (ΔuncBEFHAGDC) and purified by Ni-NTA affinity chromatography as previously described by Ishmukhametov (49) with slight modifications. The plasmid pBWU13-βHis introduced a hexa-histidine tag at the amino-terminus of the β subunit of the ATP synthase and could be used for efficient purification using the Ni-NTA affinity chromatography.

3.2.2.1 *E. coli* cell growth

As the protocol for expression of his-tagged ATP synthase was adapted from Ishmukhametov (49) and not from the labs of Prof. Börsch, slight difference in the cell growth procedure exist. In general, different media can be used successfully for bacteria cell growth and the growth time depends on the concentration of cells in the preculture. Cells were grown in 0.5 l of LB medium (Table A.10) supplemented with 100 μg/ml ampicillin and 20 μg/ml tetracycline for 4.5 hours under shaking at 37°C. The cells were collected at an optical density of 2 by centrifugation at 7.700g for 15 min at 4°C. Approximately 4-5 g of wet bacteria cells were harvested from 1 l LB medium. The cell pellets were frozen in liquid nitrogen and stored at -80°C.

3.2.2.2 Isolation of EF₀F₁

The cell pellets were defrosted at ambient temperature and resuspended in French press buffer (Table A.11) supplemented with a spade point tip of PMSF and DNase. The cell lysis was executed in a cooled French press at 16.000 psi. The drops were collected in liquid nitrogen and stored at -80°C.

3.2.2.3 Purification of EF₀F₁

Cells were thawed and supplemented with 500 μl PMSF. Unbroken cells were collected by centrifugation (25.000g, 15 min, 4°C) and were discarded. All following steps were performed strictly at 4°C or under cooling using an ice bath. The supernatant fraction containing the membranes was ultracentrifuged for 1 h at 184.000g. The membrane pellet was resuspended in extraction buffer (Table A.12). Approximately 4 ml of buffer was added to 1 g of membrane protein. The extraction was carried out for 90 min on a shaking platform in an ice bath. The extract was afterwards ultracentrifuged for 1 h at 200.000g. The supernatant was applied to a Ni-NTA column that was previously equilibrated with extraction buffer. The flow rate through the column was

3 Material and Methods

adjusted to 0.25 ml/min. To remove other contaminating proteins, the resin was washed with 20 ml of extraction buffer at a flow rate of 0.5 ml/min.

Elution of EF₀F₁ was carried out with 5 ml of extraction buffer supplemented with 150 mM imidazole at a flow rate of 0.25 ml/min. 250 µl fractions were frozen in liquid nitrogen and stored at -80°C.

3.2.3 SDS-PAGE Analysis

The purity of isolated ATP synthase (his-tagged and non his-tagged) was confirmed by SDS-PAGE gelelectrophoresis according to Laemmli et al. (50). A 4% stacking and a 13% running gel was prepared in a Bio-Rad gel apparatus. The samples were loaded with 5 µl of sample buffer (Table A.14) and incubated for 20 min at 90°C. The electrophoresis was carried out with a current of 20 mA in the area of the stacking gel and with 40 mA in the area of running gel for approximately 1 h at room temperature. As reference 5 µl of low range molecular weight standard (PageRuler™ 10-180 kDa, *Thermo Scientific*) was loaded on the gel.

Gels were stained with Coomassie blue R-250. Therefore, the gel was placed in a staining solution (Table A.15) and shortly heated in the microwave (20s, 600 W). Afterwards the gel was incubated for 15 min on a shaker and decolorized with decolorizing solution (Table A.16) till the bands had the desired intensity.

3.2.4 Determination of ATP synthase concentration

ATP synthase concentration was determined by recording the absorption at 280 nm (A_{280}) with the Specord 50 plus spectrophotometer. The concentration c was calculated using the Lambert-Beer equation [3.1]. The extinction coefficient of ATP synthase at 280 nm is $\epsilon_{280}=340.000 \text{ M}^{-1}\text{cm}^{-1}$ (51) and the path length of the cell is $d=1 \text{ cm}$. Extraction buffer (Table A.12) was used as blank.

$$c_{EF_{0}F_{1}} = \frac{A_{280}}{\epsilon_{280} \cdot d} \quad [3.1]$$

3.2.5 Preparation of dialysis liposomes

Dialysis liposomes were prepared according to Fischer et al. (45). 6.8 ml of PC in chloroform (25 g/l) and 3.6 ml phosphatic acid (2.5 g/l) -previously diluted in chloroform and stored at -20°C- were combined. The solvent was removed in a rotary evaporator (water bath temperature 40°C,

final pressure 20 mbar) under nitrogen. The dry lipids were resuspended in 10 ml sonification buffer (Table A.17) and sonicated in an ice bath with a precooled Sonicator three times for 30 s to transfer multilamellar vesicles in unilamellar vesicles. After each pulse a 30 s break was made in order to not overheat the lipids. The maximal intensity used was 30%. Afterwards the suspension looked clearer, almost transparent. The vessel was closed with parafilm and stored overnight at -20°C. The freezing step supports the formation of homogenous vesicles and shouldn't be skipped. After defrosting the suspension, the vesicles were dialyzed against 15 l dialysis buffer (Table A.18) for 5 h at 30°C. The resulting liposomes had a lipid concentration of 16 g/l, were frozen in liquid nitrogen and stored at -80°C.

3.2.6 *ATP synthase reconstitution*

EF₀F₁-ATP synthase was reconstituted into preformed dialysis liposomes according to the method described by Fischer (52) with slight modifications. 100 µl liposomes were mixed with 0.5 µl 1 M MgCl₂, 78 µl reconstitution buffer (Table A.19) and ATP synthase with a final concentration of 0.1 µM, aiming to a theoretical ratio of 1 ATP synthase per liposome. 16 µl of 10% Triton X-100 (Triton) with a final concentration of 0.8% was added under vortexing to slightly destabilize the liposomes. The mixture was incubated under gentle shaking for 15 minutes. For removal of detergent, 80 mg of wet SM-2 Bio-Beads were added and the solution was incubated for further 60 minutes under constant shaking.

3.2.7 *Measurement of ATP synthesis*

Measurement of ATP synthesis was carried out by energizing the proteoliposomes in an acid-base transition experiment as previously described by Schmidt and Gräber (53). 1 ml of basic buffer LII (Table A.20) was mixed with 6 µl of 10 times concentrated luciferin/luciferase reagent and 1 µl of 9.5 mM ultrapure ADP. A baseline was recorded using the Glomax 20/20 Luminometer. In the meantime, 20 µl proteoliposomes were incubated for 3 minutes in a solution containing 90 µl acidic buffer LI (Table A.21) supplemented with the same amount of 0.1 µM ADP and 2 µl of 10 mM valinomycin. The reaction was started by addition of 100 µl of the acidic proteoliposome solution to the basic media and ATP synthesis was recorded over 2 minutes.

3 Material and Methods

3.2.7.1 Calculation of ATP concentration and determination of k_{cat}

The detected luminescence signal was used to calculate the ATP concentration change c_{ATP} and the catalytic constant k_{cat} of ATP synthesis as shown in Figure 3.2. After each measurement 10 μ l ATP (7.8 μ M) was added threefold to normalize the luminescence signal against a defined amount of ATP (Figure 3.2 A). The middle value ΔRLU of these three changes in luminescence intensity ($\Delta RLU_1, \Delta RLU_2, \Delta RLU_3$) was calculated. Dividing the data by ΔRLU gave the ATP concentration change c_{ATP} in nM (Figure 3.2 B). c_{ATP} was corrected to the start of the reaction $t_0=0$. The baseline recorded previous to the reaction was used to correct c_{ATP} to the initial substrate concentration $c_{ATP,0}=0$. Each concentration change was recorded in three separate measurements. The corrected concentration $c_{ATP,cor}$ of each measurement was used to calculate the mean ATP concentration change $c_{ATP,mean}$ (Figure 3.2 C). Afterwards a linear regression through the first two seconds of the reaction was performed (Figure 3.2 D). The slope of the linear fit gave the initial reaction velocity v_0 (nMs^{-1}). The catalytic constant k_{cat} could be determined dividing v_0 by the enzyme concentration $[E]$.

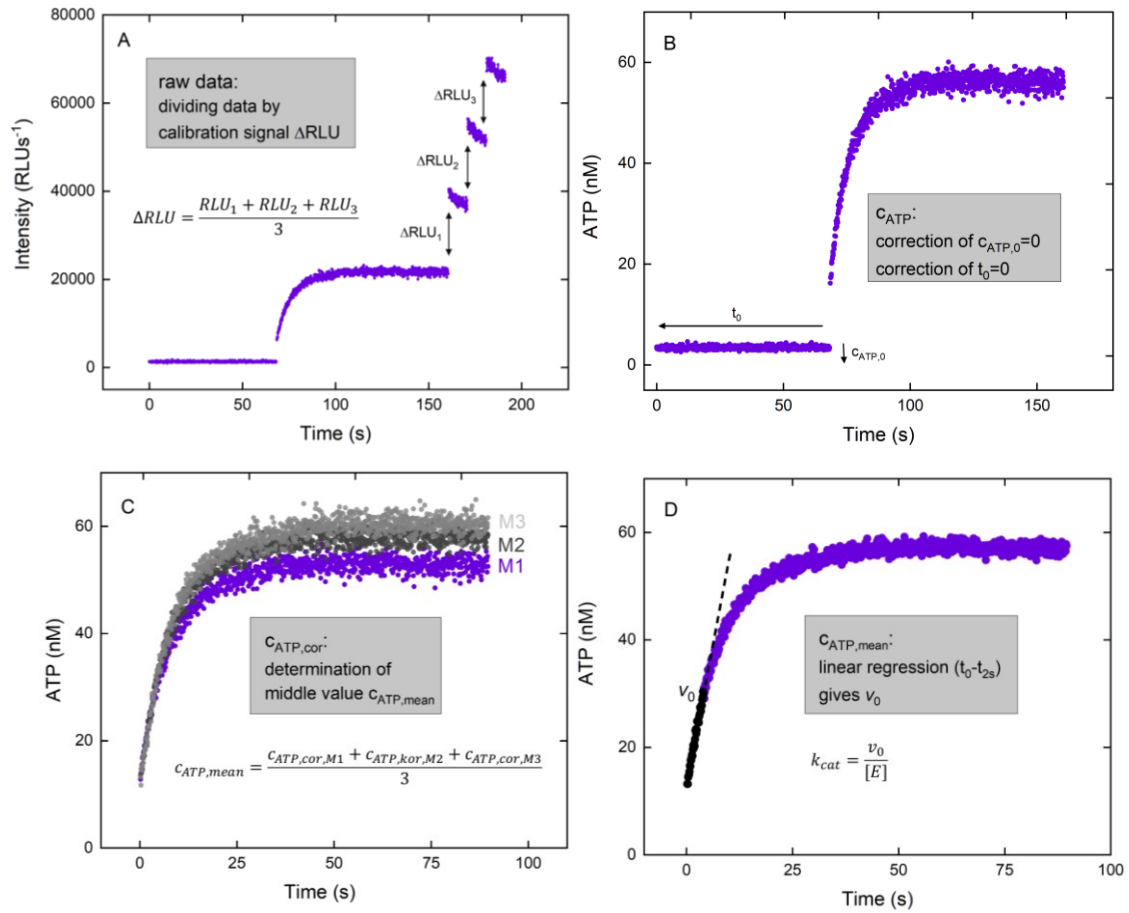


Figure 3.2 Evaluation of the detected luminescence signal to generate the ATP concentration change c_{ATP} .

(A) Raw data (B) ATP concentration change c_{ATP} (C) Corrected ATP concentration change $c_{ATP,cor}$ (D) Middle value of three ATP concentration changes $c_{ATP,mean}$ and determination of v_0 and k_{cat} .

3.2.7.2 Vesicle preparation for determination of ATP synthase ΔpH and $\Delta \Psi$ dependency

The activity of ATP synthase depends on the pH gradient ΔpH and the potential gradient $\Delta \Psi$ over the membrane. For investigation of ΔpH dependency experiments were performed where (A) the pH inside (pH_{in}) was varied and (B) the pH outside (pH_{out}) was varied. For measurement of ATP synthase ΔpH dependency with varies pH_{in} (A), acidic buffer LI (Table A.21) was prepared with different pH (pH 5.6, 6.2, 6.6, 7.0, 7.6). ATP synthase was directly incorporated in these buffers instead of using reconstitution buffer (Table A.19). The precise pH of the solution after reconstitution was determined with a pH electrode and 180 μM valinomycin and 10 μM ADP were added. Measurements were started directly by addition of proteoliposomes to basic buffer LII (Table A.20) supplemented with 0.1 μM ADP without any preincubation in acidic buffer.

3 Material and Methods

In contrast, ATP synthase reconstitution for determination of ΔpH dependency with varies pH_{out} (B) were conducted as described in chapter 3.2.6. For synthesis measurements outer buffer LII (Table A.20) with different pH (pH 8.2, 8.6, 9.2, 9.6) was used.

$\Delta\psi$ dependency of ATP synthase was studied by recording ATP synthesis rates for different ΔK^+ concentrations. Therefore, outer buffer LII (Table A.20) was prepared with varying KCl concentrations ($c(\text{K}^+_{\text{out}}) = 480 \text{ mM}, 160 \text{ mM}, 80 \text{ mM}, 40 \text{ mM}$ and 0.6 mM) while inner buffer LI (Table A.21) had a constant K^+ concentration of $c(\text{K}^+_{\text{in}}) = 0.6 \text{ mM}$. ATP synthase reconstitution and synthesis measurement were conducted as described in chapter 3.2.6 and 3.2.7. The diffusion potential was calculated using the Nernst equation [3.2].

$$\Delta\Psi = 59\text{mV} \cdot \lg \frac{c(\text{K}^+_{\text{out}})}{c(\text{K}^+_{\text{in}})} \quad [3.2]$$

3.2.8 Measurement of ATP hydrolysis

Measurement of ATP hydrolysis was performed using a well-established coupled enzyme reaction as described by Fischer (45). The reaction is schematically shown in Figure 3.3 and is based on detection of NADH consumption by absorption depletion at 340 nm. The measurement buffer (Table A.22) containing the enzyme mix was temperedated at 37°C and the absorbance change after addition of proteoliposomes was recorded using a Microplate Reader. Proteoliposomes were added with a final protein concentration of 3 nM .

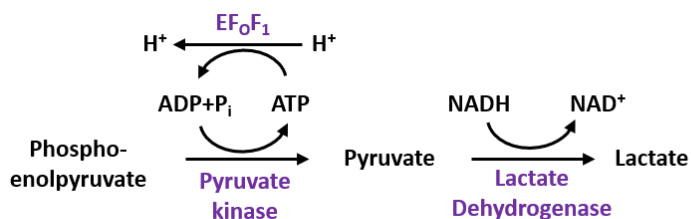


Figure 3.3 Reaction scheme of the coupled enzymatic test for measurement of ATP hydrolysis.

3.2.8.1 Determination of $k_{\text{cat},\text{H}}$

As the reaction from pyruvate to lactate is very fast and NADH and Lactate Dehydrogenase are added in excess, the reaction velocity is only influenced by ATP hydrolysis. The catalytic constant of ATP hydrolysis ($k_{\text{cat},\text{H}}$) could be calculated by the slope of NADH depletion as shown schematically in Figure 3.4.

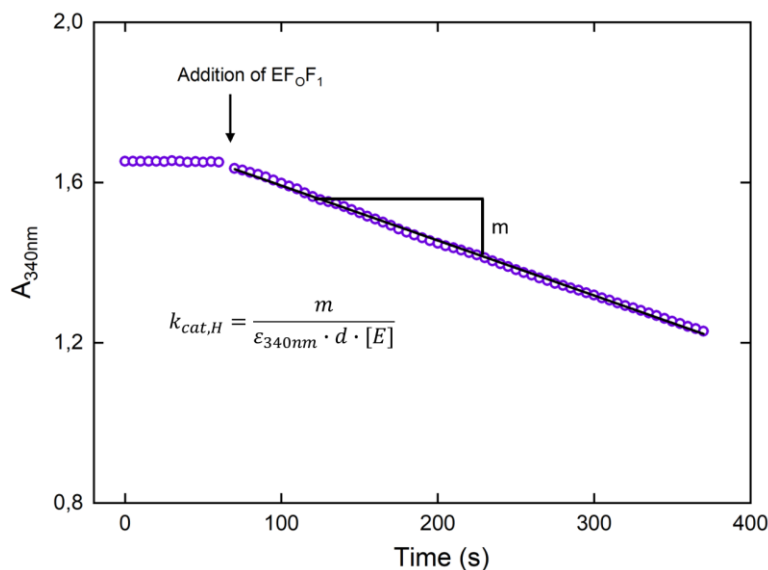


Figure 3.4 Evaluation of NADH absorption depletion for determination of the kinetic constant $k_{cat,H}$ (s^{-1}).

m : absorption depletion at 340 nm, ϵ_{340nm} : extinction coefficient of NADH at 340 nm ($6220 \text{ M}^{-1}\text{cm}^{-1}$) (48), d : path length (0.5 cm for 150 μl volume), $[E]$: concentration of EF_oF_1 .

3.2.9 Characterization of ATP synthase with AFM and cryo-TEM

3.2.9.1 Atomic Force Microscopy (AFM)

ATP synthase investigation with Atomic Force Microscopy (AFM) was conducted with an Agilent Microscope in Tapping Mode, equipped with a liquid cell. A silicon cantilever PPP-NCH-W (*Nanosensors*) with a spring constant of 42 N/m, a resonance frequency of 330 kHz (204-497 kHz) and a tip radius less than 10 nm was used for imaging. Vesicle spreading of reconstituted non his-tagged ATP synthase was performed on Mica (Plano, Wetzlar, Deutschland) substrate. Mica is a non-conducting layered silicate that forms Si_2O_5 phyllosilicates with a strong two-dimensional bonding, but only very weak three-dimensional interactions. Therefore, Mica cleavage results in an atomic planar surface and can be used for imaging of plain samples. Fresh cleavage was conducted using commonly Sellotape. 200 μl of proteoliposomes were added to the liquid cell. As a control liposome on Mica without ATP synthase were prepared in the same way. After 1 h of incubation at room temperature the sample was washed with 10 ml MilliQ water to remove not bonded protein and lipid. Measurements were performed in sterile filtered (0.45 μm) reconstitution buffer (Table A.19). Raw data were evaluated using the software Gwyddion.

3 Material and Methods

3.2.9.2 Sample preparation for cryo-Transmission Electron Microscopy (cryo-TEM)

Cryo-TEM measurements of reconstituted ATP synthase were performed by Ingo Lieberwirth from MPI Mainz (Institute for Polymer Research). Reconstitution of ATP synthase in dialysis liposomes was performed as described in 3.2.6 using non his-tagged ATP synthase.

3.3 Bacteriorhodopsin expression, isolation and characterization

Purple membrane was isolated from *Halobacterium salinarium* (strain S9) as described by Oesterhelt and Stoeckenius (54). This work was mainly performed by Claudia Bednarz and is therefore only explained briefly.

3.3.1 *Halobacterium salinarium* cell growth

Cells were grown in culture medium (Table A.13) under illumination and shaking (200 rpm) at 39°C for approximately 90 h.

3.3.2 Isolation of purple membrane

Cells from a 10-liter culture were harvested by centrifugation (15 min, 13.000g) and were resuspended in 250 ml basal salt medium (culture medium without peptone) supplemented with 5 mg DNase. For lysis, cells were dialyzed overnight against 2 l of 0.1 M NaCl. The lysate was centrifuged for 40 min at 40.000g. The red supernatant containing the red fragment was discarded. The purple pellet was resuspended in 300 ml 0.1 M NaCl and centrifuged under the same conditions. This washing step was repeated till the supernatant was almost colourless. The sediment was resuspended in deionized water and washed again several times. The final pellet was taken up in 6-10 ml water and layered over a linear 30 to 50% sucrose density gradient with a 2 ml of 60% sucrose bottom cushion. After 17 h centrifugation at 100.000g the purple membrane equilibrated at a density of 1.18 g/cm³. The purple bands were collected and sucrose was removed by repeated washing and centrifugation steps (30 min, 50.000g).

3.3.3 Determination of bR concentration

The bR concentration could be calculated by bR absorption at 560 nm (A_{560}) using the following equation:

$$c_{bR} = \frac{A_{560}}{\epsilon_{560} \cdot d} \quad [3.3]$$

c_{bR} : concentration of bR
 ϵ_{560} : extinction coefficient of bR at 560 nm (54000 M⁻¹cm⁻¹) (54)
 d: path length (1 cm)

An absorption spectrum (280 nm – 800 nm) of a 1:20 diluted bR solution in MilliQ water was recorded using the UV/Vis Spectrometer Specord 50 plus. MilliQ water was used as blank. The absorption ratio at 560 nm (A_{560}) and 280 nm (A_{280}) indicated the purity of the isolated bR (55) using equation [3.4].

$$Purity(\%) = \frac{A_{560}/A_{280}}{0.5} \quad [3.4]$$

3.3.4 Solubilization of bR patches

bR patches were solubilized according to the method described by Meyer et al. (56). Therefore, bR patches were supplemented with Triton in a Triton to bR molar ratio of 68. The volume of Triton (V_{Triton}) was calculated using equation [3.5]-[3.8]. After adding the detergent, the suspension was sonicated for ~10 minutes in an ultrasonic bath and stirred for at least 4 days in the dark at 4°C. Membrane pellets were removed by ultracentrifugation for 30 minutes at 400.000g.

$$n_{bR} = c_{bR} \cdot V_{bR} \quad [3.5]$$

$$n_{Triton} = n_{bR} \cdot 68 \quad [3.6]$$

$$V_{Triton} = \frac{n_{Triton}}{c_{Triton}} \quad [3.7]$$

$$\Rightarrow V_{Triton} = \frac{A_{560} \cdot V_{bR} \cdot 68}{\epsilon_{560} \cdot d \cdot c_{Triton}} \quad [3.8]$$

n_{bR} : Molar amount of bR
 V_{bR} : Volume of bR
 n_{Triton} : Molar amount of Triton
 c_{Triton} : Concentration of Triton (10% = 0.16 mol/l)

3.3.5 Preparation of vesicles for bR proton pumping

Vesicles were formed by film rehydration method followed by extrusion as schematically shown in Figure 3.5.

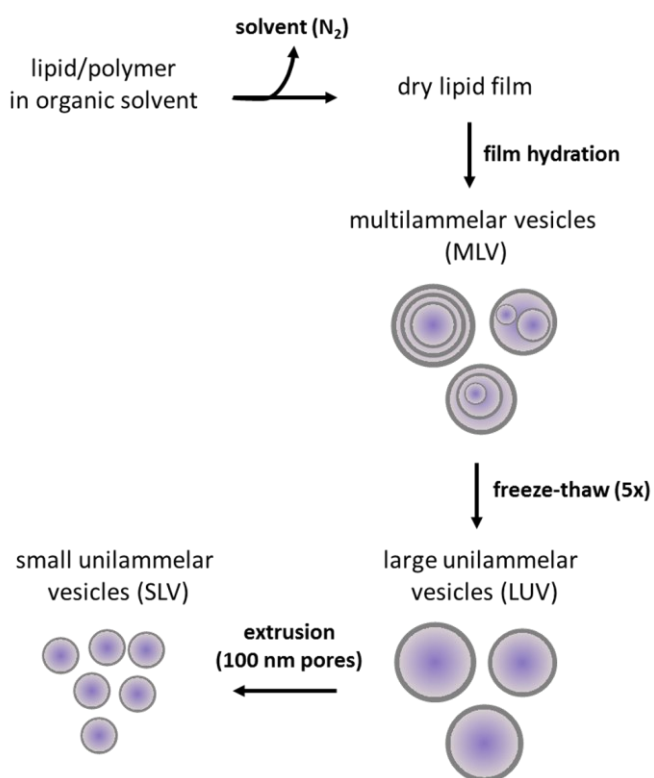


Figure 3.5 Schematic illustration of vesicle preparation using the extrusion method.

10 mg of dissolved lipid/polymer was deposited in a glass vial and solvent was removed using a gentle stream of nitrogen. The prepared hybrid vesicle compositions are listed in Table 3.1 and Table 3.2. Thin lipid/polymer films were rehydrated in HEPES buffer (Table A.23) in the presence of 10 mM 8-hydroxyprone-1,3,6-trisulfonic acid (pyranine) to a final concentration of 10 mg/ml by vortexing. To transform multilamellar vesicles into unilamellar vesicles, the suspension was subjected to 5 freeze-thaw cycles. Each cycle consisted of freezing in liquid nitrogen, thawing in a 35°C water bath and vortexing for 30 s. For PBd-PEO hybrid and polymer vesicles the thawing temperature was 60°C according to Seneviratne et al. (57). Suspensions were extruded 11 times through a 100 nm pore size polycarbonate membrane (Whatman) to form uniform vesicles.

Table 3.1 Lipid and hybrid vesicle compositions used for proton pumping experiments with solubilized bR.

Denomination		Phosphatidylcholine (PC) 10 mg/ml	PDMS-g-PEO (PDMS) 10 mg/ml	PBd-PEO (PBd) 10 mg/ml
0/100	PDMS/PC	1000 μ l	-	-
70/30	PDMS/PC	110 μ l	890 μ l	-
50/50	PBd/PC	423 μ l	-	577 μ l
50/50	PDMS/PBd	-	600 μ l	400 μ l

Table 3.2 Lipid, hybrid and polymer vesicle compositions used for proton pumping experiments with bR patches.

Denomination		Phosphatidylcholine (PC) 10 mg/ml	PDMS-g-PEO (PDMS) 10 mg/ml	PBd-PEO (PBd) 10 mg/ml
0/100	PDMS/PC	1000 μ l	-	-
25/75	PDMS/PC	500 μ l	500 μ l	-
43/57	PDMS/PC	250 μ l	750 μ l	-
100/0	PDMS/PC	-	1000 μ l	-
56/44	PBd/PC	500 μ l	-	500 μ l
71/29	PBd/PC	250 μ l	-	750 μ l
100/0	PBd/PC	-	-	1000 μ l

3.3.6 bR reconstitution and determination of reconstitution efficiency

100 μ l of preformed lipid, hybrid and polymer vesicles were mixed with 80 μ l of 60 μ g/ml bR as monomeric protein in detergent or with 80 μ l of 6 mg/ml bR in form of membrane patches. For proton pumping experiments depending on the number of pumping units, bR patches were added with a final concentration of 0.92 mg/ml, 0.43 mg/ml, 0.22 mg/ml and 0.11 mg/ml. To solubilize the vesicles partially, different amounts of Triton (Table 3.3) were added under vortexing.

After 15 minutes of incubation in the dark under gentle shaking, wet SM-2 Bio-Beads (Table 3.3) were added and the solution was incubated for further 60 minutes under constant shaking in the dark. For removal of non-encapsulated pyranine, vesicles were loaded on a pre-packed G25 size exclusion column (PD Mini Trap™ G-25, GE Healthcare).

3 Material and Methods

Table 3.3 Amount of 10% Triton and SM-2 Bio-Beads used for reconstitution in different lipid, hybrid and polymer vesicles.

Denomination	Triton concentration (%)	SM-2 Bio Beads (mg)
0/100 PDMS/PC	0.3	30
70/30 PDMS/PC	0.06	6
50/50 PBd/PC	0.06	6
50/50 PDMS/PBd	0.06	6
0/100 PDMS/PC	0.8	80
25/75 PDMS/PC	0.8	80
43/57 PDMS/PC	0.8	80
100/0 PDMS/PC	0.8	80
56/44 PBd/PC	0.8	80
71/29 PBd/PC	0.8	80
100/0 PBd/PC	0.8	80

3.3.6.1 Calculation of reconstitution efficiency

The reconstitution efficiency of bR (R_{eff}) was calculated from the absorbance ratio at 560 nm before ($A_{560,before}$) and after gel filtration ($A_{560,after}$) using equations [3.9]-[3.12]. The dilution by gelfiltration is accounted for by precise determination of the volume applied to the column (V_{before}) and the volume eluated from the column (V_{after}).

$$R_{eff} = \frac{c_{bR,after}}{c_{bR,before}} \quad [3.9]$$

$$c_{bR,after} = \frac{A_{560,after}}{\epsilon_{560} \cdot d} \quad [3.10]$$

$$c_{bR,before} = \frac{A_{560,before}}{\epsilon_{560} \cdot d} \cdot \frac{V_{before}}{V_{after}} \quad [3.11]$$

$$\Rightarrow R_{eff} = \frac{A_{560,after}}{A_{560,before}} \cdot \frac{V_{after}}{V_{before}} \quad [3.12]$$

$c_{bR,after}$: concentration of bR after gel filtration
 $c_{bR,before}$: concentration of bR before gelfiltration

3.3.6.2 Proton pumping experiments

The proton pumping activity of bR was monitored using the pH sensitive dye pyranine. Before each measurement, 0.1 μM valinomycin was added to the solution to avoid the formation of a potential gradient that counteracts the generated pH gradient. After 1 hour of equilibration in the dark, the reaction was started by illumination with a 50 W green LED lamp (SMD RGB Floodlight, V-TAC). The absorption changes of pyranine at 405 nm (A_{405}) and 450 nm (A_{450}) were monitored over 10 minutes using a diode array spectrometer (QEPRO, Ocean Optics).

3.3.6.3 pH calculation from absorption changes of encapsulated pyranine

The pH was calculated by the absorbance ratio of A_{405} and A_{450} using a calibration curve (chapter 4.2.2.1) as schematically shown in Figure 3.6. The resulting starting pH (pH_0) was corrected to the pH of the buffer solution ($\text{pH}_{\text{buffer}}$). Each proton pumping curve was recorded in three separate measurements. The corrected pH curves were used to calculate the middle value pH_{mean} .

3 Material and Methods

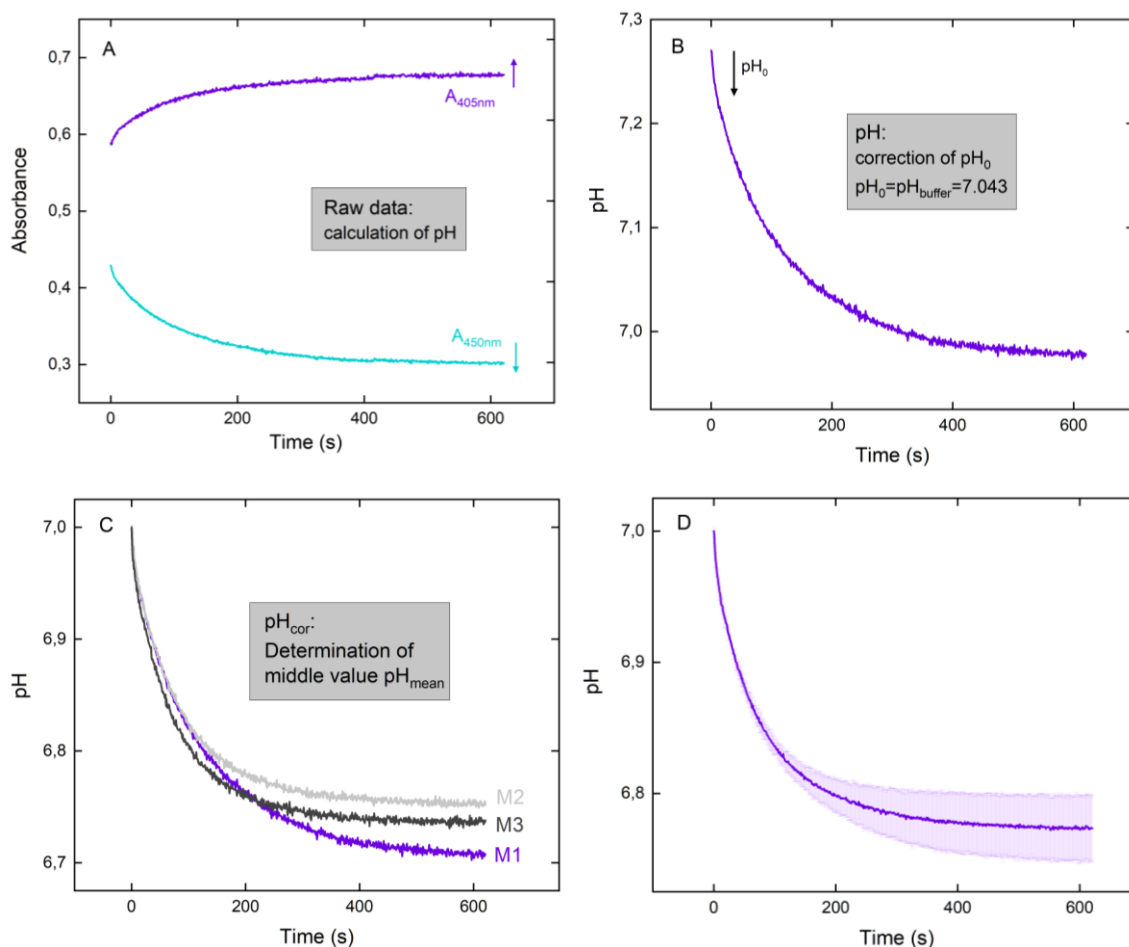


Figure 3.6 Evaluation of pyranine absorption A_{405} and A_{450} to generate vesicles internal pH change.

(A) raw data (B) calculated pH (C) pH corrected to the pH of the buffer (pH_{cor}) (D) Middle value of three independent measurements.

3.3.7 Determination of bR orientation by proteolytic cleavage

Determination of bR orientation by proteolytic cleavage was performed according to Gerber et al. (58). To assay the orientation of bR in lipid and hybrid vesicles, proteinase K (Roche) was added to a final concentration of 2.5 mg/ml. After incubation for 2 hours at 37 °C, the reaction was stopped by addition of protease inhibitor phenylmethanesulfonylfluoride (10 mM). The reaction was cooled down for 30 minutes on ice. The reaction products were loaded onto a 4-20% Tris-HCl Criterion Precast Gels (Bio-Rad). To each sample (20 μ l) 5 μ l of sample buffer (Table A.14) was added and the mixture was incubated for 5 minutes at 90°C. 10 μ l of each sample was loaded on the gel. The electrophoresis was carried out with a current of 100-150 mA for around 40 minutes in

Laemmli buffer (Table A.24). As reference 5 μl of low range molecular weight standard (PageRulerTM 4.6-42 kDa, Thermo Scientific) was loaded on the gel.

Gels were stained with Coomassie blue R-250. Therefore, the gel was placed in a staining solution (Table A.15) and heated shortly in the microwave (20s, 600W). Afterwards it was incubated for 60 min on a shaker and decolorized with decolorizing solution (Table A.16) till the bands had the desired intensity.

3.4 Characterization of the ATP module

3.4.1 *Preparation of vesicles for light-driven ATP production*

Vesicles were formed by film rehydration method followed by extrusion as described in chapter 3.3.5 with slight differences. Lipid/polymer films were rehydrated in vesicle buffer (Table A.25) without any addition of pyranine. Hybrid vesicle compositions were the same and are listed in Table 3.1 and Table 3.2.

3.4.1.1 Determination of destabilization points

100 μl of undiluted 100 nm vesicles were titrated by stepwise addition of 4 μl of 1% Triton X-100. The solubilization of vesicles was followed by measuring the absorption change at 540 nm using the ocean optics spectrometer. Vesicle buffer was used as blank. The solubilization was double checked by Dynamic Light Scattering (DLS) measurements at different points of destabilization.

3.4.1.2 Vesicle size and dispersity by Dynamic Light Scattering (DLS)

The average vesicle size and dispersity was determined by DLS using a Zetasizer Nano ZS (Malvern, Worcestershire, UK) with a 633 nm helium-neon laser and back-scattering detection. 2-5 μl of vesicles were diluted in 1 ml vesicle buffer and samples were measured at a fixed 173° scattering angle at 25°C. All reported values are based on the average of three measurements. Each measurement consisted of 3x5 runs with 70 s duration.

3.4.1.3 Estimation of liposome concentration and number of reconstituted enzymes

The number of lipids per vesicle (N_{tot}) could be calculated using the following equation:

3 Material and Methods

$$N_{tot} = \frac{4\pi \left[\left(\frac{d}{2}\right)^2 + \left(\frac{d}{2} - l\right)^2 \right]}{A_{PC}} \quad [3.13]$$

d is the diameter of the vesicle; l is the thickness of the bilayer (~5 nm) and A_{PC} is the lipid surface area (0.71 nm²) (59). Using equation [3.13] the number of lipids in a 100 nm vesicle is around $5 \cdot 10^4$ lipids. With this information the number of vesicles/ml ($N_{Vesicles}$) could be calculated with equation [3.14] and [3.15].

$$N_{Vesicle} = \frac{c_{Lipid} \cdot N_A}{N_{tot} \cdot 1000} \quad [3.14]$$

$$c_{Lipid} = \frac{c_m}{M_{PC}} \quad [3.15]$$

c_{Lipid} : lipid concentration (6.5 mM for 10 mg/ml lipids)

N_A : Avogadro constant

c_m : mass concentration of lipids (mg/ml)

M_{PC} : molar mass of PC (775 g/mol)

For a 10 mg/ml lipid concentration we can estimate $N_{Vesicle} = 4.9 \cdot 10^{13}$ vesicles/ml using equation [3.14]. The number of proteins/ml (N_{bR} and $N_{EF_{OF1}}$) was determined using equation [3.16] and [3.17].

$$N_{bR} = c_{bR} \cdot N_A \quad [3.16]$$

$$N_{EF_{OF1}} = c_{EF_{OF1}} \cdot N_A \quad [3.17]$$

The number of proteins/vesicle can be obtained by dividing $N_{bR}/N_{Vesicle}$ or $N_{EF_{OF1}}/N_{Vesicle}$.

3.4.2 Co-reconstitution of ATP synthase and bR

100 μ l of preformed lipid and hybrid vesicles were mixed with 0.1 μ M EF_0F_1 -ATP synthase and 2.9 μ M bR as monomeric protein in detergent aiming to a theoretical number of 1 ATP synthase and 29 bR molecules per vesicle. Vesicles were solubilized to the previous determined destabilization point with different amounts of Triton X-100 (Table 3.3) under vortexing. Detergent was removed after 15 minutes of incubation in the dark using wet SM-2 Bio-Beads (Table 3.3).

3.4.3 Light-driven ATP production

For measurement of light-induced ATP production, 25 μl of co-reconstituted vesicles were diluted in 250 μl measurement buffer (Table A.26) containing 10 μl ADP (7.9 mM). In earlier experiments 0.5 μl of 10 mM valinomycin was also added to the solution. The reaction was started by illumination with a 50 W green LED lamp (SMD RGB Floodlight, V-TAC). Aliquots of 25 μl were taken every 5 minutes from the reaction mixtures and the reaction was stopped by addition of the same volume of trichloroacetic acid (40 g/l). The ATP concentration was measured with the luciferin/luciferase assay in three separate measurements. Each luminescence signal was calibrated separately by the addition of 10 μl ATP (7.8 μM).

3.4.3.1 Calculation of ATP concentration

The produced amount of ATP at each reaction time was calculated from the luminescence signal I with equation [3.18].

$$C_{syn} = \frac{I_S - (I_B \cdot \frac{V_0}{V_1})}{I_C - (I_S \cdot \frac{V_1}{V_2})} \cdot \frac{C_C \cdot V_C}{V_2} \cdot \frac{V_1}{V_S} \cdot \frac{V_{TCA}}{V_{syn}} \quad [3.18]$$

C_{syn} :	concentration of ATP during synthesis
I_B :	background luminescence intensity
I_S :	sample luminescence intensity
I_C :	calibration luminescence intensity
V_0 :	volume of luciferase [200 μl]
V_1 :	volume of luciferase + sample [220 μl]
V_2 :	volume of luciferase + sample + calibration [230 μl]
C_C :	concentration of ATP in calibration [7800 nM]
V_C :	volume of Calibration [10 μl]
V_S :	volume of Sample [20 μl]
V_{syn} :	volume of sample when stopping the reaction [25 μl]
V_{TCA} :	volume of sample when stopping the reaction + volume of TCA [50 μl]

3.4.4 Proton Permeability Measurements

3.4.4.1 Preparation of vesicles

Vesicles with different lipid/polymer content (Table 3.1 and Table 3.2) were prepared as described in chapter 3.3.5 with slight modifications. After evaporation, lipid/polymer were rehydrated in PIPES buffer (Table A.27) or in HEPES buffer (Table A.28) in the presence of 10 mM pyranine.

3 Material and Methods

Vesicles were subjected to 5 freeze-thaw cycles, extruded through 100 nm pores and loaded on a pre-packed G25 size exclusion column (PD Mini Trap™ G-25, GE Healthcare) to remove not encapsulated pyranine.

3.4.4.2 Permeability measurements in PIPES buffer

Permeability measurements in PIPES buffer (Table A.27) were performed for membrane compositions listed in Table 3.1. 34 μl vesicles were diluted in 800 μl PIPES buffer supplemented with 180 nM valinomycin or in the absence of valinomycin. The reaction was started by addition of 20 μl 100 mM HCl or 13 μl 100 mM NaOH. The absorption changes of pyranine at 405 nm and 450 nm were monitored over 1 h using a diode array spectrometer (QEPRO, Ocean Optics) as described in chapter 3.3.6.3.

3.4.4.3 Permeability measurements in HEPES buffer

Permeability measurements in HEPES buffer (Table A.28) were conducted for membrane compositions listed in Table 3.2. For PDMS hybrid vesicles and pure PC vesicles different factors that influence proton permeability were analysed in more detail. Different amounts of NaOH (102 mM and 77 mM) were added in the presence or absence of ionophores and the absorbance change of pyranine was detected over 1 h. Absorption measurements were either conducted using the diode array spectrometer (QEPRO, Ocean Optics) or the microplate reader (Biotech, Synergy HT). As ionophores valinomycin in various concentrations (0, 0.015, 0.15, 1.5 mM) and/or nigericin (2.7 μM) were used. The influence of the K^+ concentration in the presence of valinomycin (1.5 mM) was investigated by preparation of vesicles in buffer supplemented with various K^+ concentrations (50 mM or 100 mM).

3.4.4.4 Determination of pyranine calibration curves for different membrane compositions

Pyranine calibration curves were recorded in buffer solution in the absence of any vesicles and specifically for each membrane composition in the presence of vesicles to account for absorption changes induced by the vesicles itself.

Two different methods were conducted. First, different vesicles in buffer solution were supplemented with nigericin (2.5 mM). Nigericin makes the membrane permeable for protons and allows a fast equilibration of pH inside and outside the vesicles. The pH of the vesicle solution was changed by addition of small amounts of KOH and the pH was monitored with a pH electrode. For

each membrane composition at least 10 different pH values between pH 5 and 9 were generated and A_{405} and A_{450} were monitored.

Second, vesicles were prepared directly in buffer solution with various pH. For generation of these standard curves only 6 different pH values between pH 6 and 8 were recorded due to the comparably high preparation effort.

All monitored standard curves were fitted using the Hender-Hasselbach equation [3.19]:

$$pH = \frac{A3 - \log\left(\frac{A2-x}{x-A1}\right)}{A4} \quad [3.19]$$

3.5 IMV isolation and measurement

3.5.1 Purification of Inverted Membrane Vesicles (IMVs)

E. coli (MG1655) cells were grown in LB medium in the presence of 20 mM glucose. The cells were harvested in three centrifugation steps, starting with 20 minutes centrifugation at 10.000g. After adding washing buffer (Table A.29) cells were centrifuged another time (10.000g, 20 min, 4°C). The pellet was resuspended again in washing buffer and centrifuged for 30 minutes at 5.000g. The sediment was frozen in liquid nitrogen and stored at -80°C.

The pellet was defrosted at 30°C and resuspended in washing buffer, centrifuged (15.000g, 10 min) and then resuspended in 300 ml washing buffer. Another centrifugation step (15.000g, 10 min) followed before the pellet was suspended in lysis buffer (Table A.30). After homogenization the cells were stirred for 1 hour on ice. DNase was added and cells were passed through a cooled French press three times at 1000 bar. The broken cells were frozen in liquid nitrogen and stored overnight at -80°C.

The suspension was thawed in a water bath and centrifuged for 20 minutes at 25.000g to remove the cell walls. Further treatment of supernatant and isolation of the membrane were conducted according to Miura and Mizushima (60). In brief, the suspension was ultracentrifuged (120 min, 433.000g, 4°C). and the pellet containing inner and outer membrane was resuspended in membrane buffer (Table A.31) and centrifuged again (90 min, 433.000g, 4°C). Another washing step followed. The pellet was frozen in liquid nitrogen and stored overnight at -80°C.

A density gradient centrifugation was performed according to Jewett (61) and Osborn (62). The ultracentrifugation tubes were filled with 6 ml 50 % sucrose, 8 ml 40 % sucrose, 10 ml 30 % sucrose, 10 ml 20 % sucrose and 1-2 ml of the sample. The tubes were centrifuged for 24 hours at 240.000g.

3 Material and Methods

The membrane was located between 35 % and 45 % sucrose, visible by the darker colour. After collecting the membrane fractions, the protein content was determined using the nanodrop. The membrane was diluted in membrane buffer (1:4) and ultracentrifuged for another two hours at 433.000g. The dry pellet was weighted (63) and resuspended in membrane buffer to a final concentration of 2 g/ml. The solution containing the IMVs was passed through a sterile filter (0.22 μm), frozen in liquid nitrogen (500 μl aliquots) and stored at -80°C .

3.5.2 Measurement of ATP production

Measurement of NADH-driven ATP production in IMVs was performed in a microplate reader (Biotech, Synergy HT) using the luciferin-luciferase assay. A standard curve was generated according to the manufacturer protocol (Figure A.6). To a solution containing 50 μl measurement buffer (Table A.32) and 50 μl luciferin-luciferase assay (prepared double concentrated according to the manufacturer protocol), 2.5 μl IMVs (2.2×10^{11} vesicles/ml) were added and the baseline was recorded. The reaction was initiated by the addition of 10 μl NADH (2 mM, 1.5 mM, 1 mM, 0.5 mM, 0.2 mM and 0.1 mM stock solutions) as soon as a constant background was detected.

3.5.2.1 Calculation of ATP and determination of the initial reaction velocity

ATP concentration was calculated from the luminescence signal using a standard curve (Figure A.6). Therefore, the raw data were divided by 294409 yielding the concentration of ATP in μM . The baseline was normalized to zero and the initial reaction velocity was generated by linear regression of the first 2 seconds of the reaction.

3.5.3 Measurement of NADH consumption

Measurement of NADH consumption was performed in the same experimental setup as described in chapter 3.5.2 using the microplate reader. Instead of detecting the luminescence signal, the absorption of NADH at 340 nm (A_{340}) was observed. To a solution containing 100 μl measurement buffer (Table A.32), 2.5 μl IMVs (2.2×10^{11} vesicles/ml) were added. As soon as a constant background was reached, the reaction was started by addition of 10 μl NADH (2 mM, 1.5 mM, 1 mM, 0.5 mM, 0.2 mM and 0.1 mM stock solutions).

3.5.3.1 Calculation of NADH and determination of the initial reaction velocity

The concentration of NADH was calculated from the absorbance A_{340} using the Lambert-Beer equation [3.1] and the extinction coefficient of NADH ($\epsilon_{340}=6200 \text{ M}^{-1}\text{cm}^{-1}$ (48)). The substrate consumption curves were then corrected to the initial amount of NADH added. The initial reaction velocity was determined by linear regression of the first 30 seconds of the reaction.

3.6 Coupling of the ATP module

3.6.1 *Multistimuli sensing adhesion unit for self-positioning of minimal synthetic cells*

3.6.1.1 Preparation of Ni^{2+} -NTA liposomes

For preparation of liposomes from DGS-NTA- Ni^{2+} and PC, 300 μL 10 mg/mL PC (dissolved in chloroform) was mixed with 20 μL 10 mg/mL DGS-NTA- Ni^{2+} (dissolved in chloroform) and deposited into a round bottom glass vial for solvent evaporation under a gentle stream of nitrogen. The lipid film was rehydrated in vesicle buffer (Table A.25) and resuspended to a final lipid concentration of 10 mg/mL by gentle vortexing. The vesicle suspension was subjected to 5 freeze-thaw cycles and was unified by extrusion through 100 nm pores as explained in chapter 3.3.5.

3.6.1.2 Co-reconstitution of EF_0F_1 -ATP synthase and bR into Ni^{2+} -NTA liposomes

100 μL of preformed Ni^{2+} -NTA liposomes were mixed with 0.5 μM bR and 0.1 μM EF_0F_1 -ATP synthase in the presence of 0.8% Triton. To stabilize ATP synthase, 0.5 μL 1 M MgCl_2 was added to the solution. After 15 minutes of incubation in the dark under gentle shaking, 80 mg of wet SM-2 Bio-Beads were added for removal of detergent. The solution was incubated for further 60 minutes under constant shaking in the dark before the Bio-Beads were removed.

3.6.1.3 ATP production and determination in reconstituted liposomes

ATP production measurements under different conditions were performed by Dongdong Xu at the labs of Prof. Dr. Wegner following the procedures explained in chapter 3.4.3. Briefly, for ATP production, 25 μL of co-reconstituted Ni^{2+} -NTA-ATP vesicles were diluted in 250 μL measurement buffer (Table A.26) containing 400 μM ultra-pure ADP. For measuring the ATP production under

3 Material and Methods

different conditions, the pH was adjusted to 7.4 or 3.5 by adding HCl and/or supplemented with 10 mM H₂O₂ and/or 50 mM EDTA. Afterwards the samples were illuminated with a 15 W blue LED lamp or kept in the dark. Every 5 minutes, 25 µL of reaction solution was taken out and mixed with 25 µL trichloroacetic acid (TCA, 40 g/L) to stop the reaction. The ATP concentration was determined as described above (3.4.3) using a plate reader (TECAN, infinite M1000).

3.6.1.4 QCM-D measurement

QCM-D measurements were performed by Dongdong Xu at the labs of Prof. Dr. Wegner (MPI Mainz) and are therefore only described briefly. Investigations were conducted using a Q-Sense Analyzer at room temperature equipped either with a flow module (dark sample) or a window module illuminated with a 15 W blue LED lamp (blue light sample). The flow rate was kept at 1000 µL/min and SiO₂ crystals (Q-sense) were used in all experiments.

To investigate the adhesion of Nano functionalized ATP liposomes and their ATP production, the Ni²⁺-NTA proteoliposomes were functionalized with Nano by diluting 60 µL of liposomes into 540 µL buffer A (Table A.34) supplemented with 100 nM Nano. The solution was incubated for 2 h at 4°C to form Nano-ATP-liposomes. QCM-D measurements in the dark and under blue were performed in parallel. First, 600 µL of the Nano-ATP-liposomes were passed over the crystal and incubated for 30 min to allow immobilization. Then, buffer A was used to remove all unbound material (15 min). Buffer A was exchanged by measurement buffer (Table A.26) and the crystal was incubated for 30 min under blue light. The chambers were opened and 25 µL of the solution were taken for ATP quantification.

3.6.2 *Reactivation of isolated flagella via light-driven ATP regeneration*

3.6.2.1 Co-reconstitution and measurement of ATP production

Vesicles were prepared by film hydration method followed by extrusion as described in 3.4.1. Instead of vesicle buffer, HMDEKP buffer (Table A.33) was used for rehydration of lipids. HMDEKP buffer is the optimal buffer for isolated flagella and was therefore used in all following steps. 100 µL of fresh prepared vesicles were mixed with 0.1 µM ATP synthase and 9.9 µM bR in form of membrane patches aiming to a theoretical number of 1 ATP synthase and 96 bR molecules per liposome. 0.8 % Triton was added under vortexing and the mixture was incubated for 15 min in the dark under gentle shaking. 80 mg of wet SM-2 Bio-Beads were added and the solution was incubated for further 60 min under constant shaking in the dark.

For measurement of light-induced ATP production, 25 μl of co-reconstituted vesicles were diluted in 250 μl HMDEK buffer supplemented with 1.6 mM ADP. The reaction was started by illumination with a 50 W green LED lamp or a 5 W microscope light. Aliquots of 25 μl were taken at the beginning every 1 minute and later on every 5 minutes from the reaction mixture and the reaction was stopped by addition of the same volume of trichloroacetic acid (40 g/l). The ATP concentration was measured and calculated as described above (chapter 3.4.3).

3.6.2.2 Isolation and reactivation of flagella via light-driven ATP production

Axoneme isolation and reactivation were performed by Raheel Ahmad under the guidance of Dr. Azam Gholami (MPI Göttingen). Axonemes were isolated from wild-type *Chlamydomonas reinhardtii* cells, strain SAG 11-32b and were grown axenically in tris-acetate-phosphate medium on a 12h/12h day-night cycle. Flagella were isolated using dibucaine (64), purified on a 25% sucrose cushion and demembrated using detergent NP-40 in HMDEK solution supplemented with 0.2 mM Pefabloc. The membrane-free axonemes were resuspended in HMDEK buffer plus 1% (w/v) polyethylene glycol, 0.2 mM Pefabloc, 20% sucrose and stored at -80°C . To perform reactivation experiments, axonemes were thawed at room temperature, kept on ice and were used for up to 2 hours. Axonemes were diluted in HMDEK buffer containing the light-driven energy module and were infused into 100 μm deep flow chambers, built from cleaned glass and double-sided tape.

3.6.2.3 Axoneme counter tracking

Axoneme contour tracking of reactivated axonemes was performed by Raheel Ahmad (MPI Göttingen) using a phase-contrast microscope (100X objective, imaging frequency of 1000 fps). The signal to noise ratio was increased (by a factor of three) by inverting phase-contrast images and by subtracting the mean-intensity of the time series. A Gaussian filter was applied to smooth the images. The tracking of axonemes was done using the gradient vector flow technique (65; 66). For the first frame, a region of interest was selected that contained only one actively beating axoneme. The snake was initialized by drawing a line polygon along the contour of the axonemes in the first frame. This polygon was interpolated at N equally spaced points and used a starting parameter for the snake. The gradient vector flow (GVF) was calculated using the GVF regularization coefficient $\mu=0.1$ with 20 iterations. The snake was then deformed according to the GVF where the original algorithm by Xu and Price (65) for open boundary conditions was adapted. Positions of N points

3 Material and Methods

along the contour length s of the filament were obtained so that $s=0$ was the basal end and $s=L$ was the distal side. L was the total contour length of the filament.

3.6.3 Measurement of light-triggered glucose consumption

For measurement of light-triggered glucose consumption ATP synthase and bR were co-reconstituted as described earlier (chapter 3.4.2). To 50 μl of proteoliposomes diluted in 500 μl of basic buffer LII (Table A.20), 10 μl ADP (9.5 mM), 1 μl 6 mM glucose and 15 μl hexokinase (2400 U/ml) were added. The reaction was started by illumination with a 50 W green LED lamp (SMD RGB Floodlight, V-TAC). Aliquots of 50 μl were taken every 5 minutes from the reaction mixture and the reaction was stopped by addition of the same volume of trichloroacetic acid (40 g/l). Afterwards a high sense glucose assay (Sigma) was used to determine the glucose concentration by measuring the fluorescence intensity ($\lambda_{\text{ex}}=533$, $\lambda_{\text{em}}=587$). A standard curve for calibration and the assay reaction mixtures was prepared according to the manufacturers protocol. 10 μl of the sample was added to a mixture of 50 μl assay reagent and 40 μl assay buffer. Each glucose concentration was recorded in three separate measurements. In parallel the ATP concentration of each sample in the presence and in the absence of glucose and hexokinase was determined using the luciferin/ luciferase assay.

3.6.4 Light-triggered actin-myosin contraction

3.6.4.1 Actin preparation and labeling (Actin mix)

Actin preparation and labeling was performed according to Vogel et al. with slight modifications (67). Rabbit skeletal muscle actin monomers (Molecular probes) and biotinylated rabbit actin monomers (tebu-bio) were mixed in a 4:1 (actin:biotin-actin) ratio. 30 μl of this mixture was labelled with Alexa-Fluor 488 Phalloidin (Molecular Probes) according to the manufacturer protocol and diluted in 100 μl of measurement buffer (Table A.26). 130 μl of 16 μM of Alexa-488-Phalloidin labelled biotinylated actin monomers were obtained.

3.6.4.2 Myosin preparation and labeling (Myosin mix)

Myosins were labelled with thiol-reactive dyes AlexaFluor 488 C₅-maleimide as well as AlexaFluor 647 C₂-maleimide (both Molecular Probes) (67) according to the manufacturer protocol. 12 μl of

21 μM of labelled Myosins were mixed with 4 μl of Neutravidin (1 $\mu\text{g}/1 \mu\text{l}$) and were diluted to 400 μl in measurement buffer (Table A.26) to reach a final Myosin concentration of 0.6 μM .

3.6.4.3 Preparation of ATP synthase-Actin/Myosin Droplets

The ATP module was prepared as described in chapter 3.4.1 and the activity was confirmed by determination of the ATP production rate. All following steps were conducted in the dark. 12 μl of ATP synthase liposomes supplemented with 4 μl ADP (7.5 mM) were mixed with 12 μl of previous prepared Actin mix. 20 μl of this solution was added to 20 μl of the Myosin mix and was incubated for 10 minutes. 10 μl of ATP synthase-Actin/Myosin mixtures was taken and added to 50 μl of an oil/lipid mixture. Vortexing and centrifugation yielded droplets with encapsulated Actin/Myosin system together with the ATP module.

3.6.4.4 Detection of Actin/Myosin contraction

The detection of Actin/Myosin contraction was performed using a two colour TIRF microscope with a custom-made setup built around an Axiovert 200 microscope (Zeiss). A α Plan-Apochromat 100x/NA 1.46 oil immersion objective and 488 nm and 647 nm laser lines were used for excitation. The exposure times were 50 ms or 100 ms and the time intervals between each recorded frame ranged from 200-400 ms.

The first measurement was performed after incubating the sample for 40 minutes in the dark. The sample was taken and ATP production and Actin/Myosin contraction was induced by illumination with a self-made 15 W white light LED lamp. Pictures were taken after 10 min, 30 min and 40 min of illumination.

4 Results and Discussion

*The important thing is
to never stop questioning.*

Albert Einstein

Aim of this thesis was to establish a light-driven ATP regeneration module that can be combined with other functional modules to form functional systems. The first step was overexpression, isolation and characterization of proteins, namely ATP synthase and bacteriorhodopsin.

4.1 ATP synthase

4.1.1 Isolation of ATP synthase

ATP synthase was isolated as non his-tagged ATP synthase according to a protocol described by Fischer et al. (45) in the labs of Prof. Michael Börsch resulting in high active ATP synthase. The adaption of the procedure to our labs was difficult probably due to differences in our equipment and chromatography columns. Therefore, we implemented the isolation of his-tagged ATP synthase (chapter 4.1.1.1), which resulted in more active enzyme in our labs and was also more time saving. The results of both isolation methods are compared and described in the following chapters.

The first step of isolation and purification is the extraction of proteins from the *E. coli* cells. This was done by mechanical homogenization of cells using high pressure (French press). As proteases are released during cell lysis, protease inhibitors were added to prevent degradation of ATP synthase. Cell debris were removed by centrifugation. The following ultracentrifugation step separated the cell membranes from the cytoplasm.

4 Results and Discussion

Solubilization of membranes were performed by addition of detergent, namely dodecylmaltoside, in a well-defined concentration. Dodecyl-maltoside is a mild non-ionic detergent, which stabilizes membrane proteins. Earlier isolation protocols for ATP synthase commonly used octyl glucoside as detergent. Reuter et al. (68) showed that the usage of this detergent in the presence of high salt concentrations leads to denaturation of EF_0F_1 proteins.

Dodecylmaltoside (1.75% (w/v), 34 mM) was added as 190-fold of the critical micelle concentration (CMC) in order to solubilize all EF_0F_1 proteins efficiently. Higher concentrations in contrast, would lead to undesired solubilization of other membrane proteins. This solubilization step is therefore the first step of very unspecific purification.

A common step in bulk purification, is the precipitation with increasing amounts of ammonium sulfate ($(NH_4)_2SO_4$). The precipitation is based on the fact that hydrophobic groups that are present on the protein and are exposed to the media will attract other hydrophobic groups, thereby forming hydrophobic aggregates. This process is also known as “salting out”. Ammonium sulfate moreover stabilize the protein structure. Each protein has a specific solubility or starts precipitating at a specific ion concentration (69). ATP synthase precipitates at 65% ammonium sulfate and could be collected by centrifugation after addition of $(NH_4)_2SO_4$. The following size exclusion chromatography (S-300) was mainly done to remove ammonium sulfate and lipids from the protein sample.

Two further steps of purification were following using anion exchange and size exclusion chromatography (S-400). Anion exchange chromatography separates proteins due to their degree of ionic charge. The stationary phase (the column) is positively charged and negatively charged molecules are attracted to it. The pH of the buffer solution were chosen in a way that it is greater than the isoelectric point (pI) (70) of ATP synthase, which is 5.75 (71). Anion exchange chromatography was therefore performed at neutral pH (pH 7).

In size exclusion chromatography molecules or proteins are separated based on their hydrodynamic volume. Separation occurs by using a column of porous packed beads. Smaller molecules can enter the pores more easily, therefore spending more time in the pores and are eluting last (72). In protein purification the time of elution is usually determined by measuring the absorption change at 280 nm. The elution profile of the S-400 size exclusion chromatography of ATP synthase is shown in Figure 4.1 A.

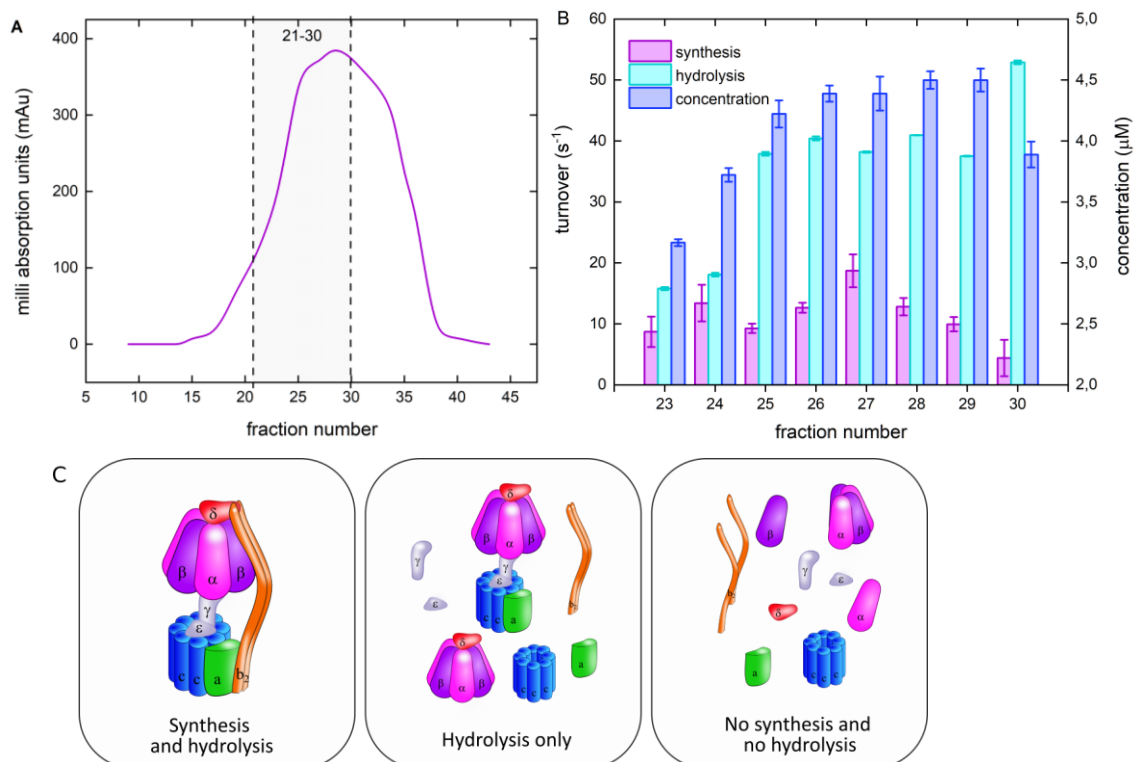


Figure 4.1 Isolation of non his-tagged ATP synthase in *E. coli* (EF_oF₁ ATP synthase).

(A) Elution profile of size exclusion chromatography S-400. Shown are the milli absorption units at 280 nm for different fractions. Fractions 21-30 contained functional ATP synthase and were used for further characterization. Fractions 10-21 contained only very small amounts of protein. Fractions 31-40 contained mainly dissociated subunits of EF_oF₁. (B) Comparison of the catalytic activity of ATP synthase in different fractions towards ATP synthesis and ATP hydrolysis with the corresponding concentrations. Error bars represent standard error of the mean ($n=3$). (C) Schematic presentation of intact ATP synthase and dissembled ATP synthase. ATP synthesis is only possible if all ATP synthase subunits are assembled. ATP hydrolysis in contrast, is also possible if only subunits of the head F₁ (α - ϵ) are assembled.

Active ATP synthase usually eluates at the beginning of the protein peak (fraction 21-30). Therefore, these fractions are further analysed to protein concentration, hydrolysis and synthesis activity (Figure 4.1 B).

ATP synthase concentration was determined by UV/Vis spectroscopy as described in chapter 3.2.4. ATP synthesis was measured using the luciferin/luciferase assay (chapter 3.2.7) and ATP hydrolysis activity was determined by a coupled enzyme test (chapter 3.2.8). The results show that concentration, synthesis and hydrolysis activity are not necessarily correlating. Synthesis activity is only observed when all subunits of the protein are present and correctly assembled (Figure 4.1 C). Synthesis activity is higher in the earlier fractions (23-28) and is decreasing in later fractions

4 Results and Discussion

(29, 30). In contrast, hydrolysis activity displays the opposite effect. This finding can be explained by the fact that also partially disassembled ATP synthase (for example EF_1 only) is able to hydrolyse ATP. In this case hydrolysis is not coupled to any active proton transport. Also, not reconstituted ATP synthase can hydrolyse ATP, but does not show any synthesis activity. Therefore, it is likely that the later eluting fractions contain mainly ATP synthase that got inactive to synthesis due to the loss of subunits. This result is in good agreement with earlier reported results for ATP synthase isolation (45; 48; 68).

SDS-PAGE analysis was used to check purity and completeness of the enzyme (Figure 4.2). The combined use of sodium dodecyl sulfate (SDS) and polyacrylamide gel allows to eliminate influences of protein structure and charge. It is therefore possible to separate proteins only by the molecular weight. SDS acts as surfactant, masking the proteins intrinsic charge and giving them similar charge-to-mass ratios. SDS has also a strong denaturing character which leads to the dissociation of protein complexes. Therefore, subunits are in general separated on the gel and quaternary protein structures cannot be determined with SDS-PAGE.

The overall protein concentration correlates with the intensity of bands specific for ATP synthase. No other bands besides those who can be matched to the ATP synthase subunits are visible, which indicates high purity of isolated protein. Subunit c is known to be very weak on Coomassie-stained SDS-PAGE gels and is therefore barely visible. Figure 4.2 B shows stoichiometry and molar masses of the different subunits of ATP synthase.

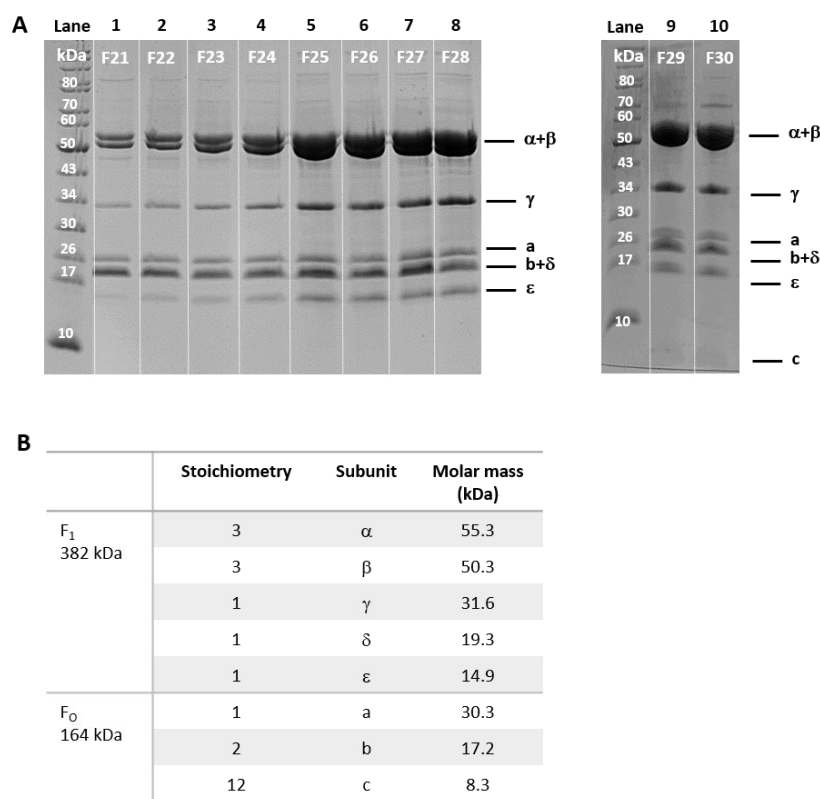


Figure 4.2 SDS-PAGE analysis of non his-tagged ATP synthase.

(A) Coomassie-stained SDS-PAGE of different ATP synthase fractions. Lane 1-10 shows the content of different subunits in the fractions 21-30 (2 μ l protein per lane). (B) Stoichiometry and molar masses of different subunits of EF₀F₁ ATP synthase.

4.1.1.1 Isolation of his-tagged ATP synthase

Isolation of his-tagged ATP synthase was performed according to Ishmukhametov (49) as described in chapter 3.2.2. ATP synthase was expressed from a plasmid (pBWU13- β His) that encodes a hexahistidine tag at the amino-terminus of the β subunit of ATP synthase (49). The histidine tag enables a specific purification of the enzyme using a Ni-NTA column. This has the advantage of time saving on the one hand, and higher purity on the other.

The cell growth and isolation of ATP synthase was conducted similar to the procedure described for non his-tagged ATP synthase. The harvested cells were broken using a French Press and membranes were collected by ultracentrifugation. To extract the protein from the membrane a mixture of octyl glucoside, cholate and deoxycholate was used. The composition of extraction buffer was found to have impact on the purity of the final protein (49). Sucrose and high ionic strength (100 mM KCl) decreased binding of unspecific contaminants at the Ni²⁺ column and

4 Results and Discussion

therefore increased purity of his-tagged ATP synthase. The Mg^{2+} concentration in the buffer solution is in general another important factor. Mg^{2+} keeps F_0 and F_1 bonded to each other and prevents disassemble of head and tail in the case of non his-tagged and his-tagged ATP synthase. The solubilized protein was then added to a Ni-NTA Affinity column. These columns are made of agarose beads that are functionalized with a chelator, namely Nitrilotriacetic acid (NTA). Ni^{2+} ions are forming a complex with the NTA chelator. The his-tag binding motive located at the protein interacts strongly with the Ni^{2+} ions. Using this method, a specific binding of ATP synthase to the column was achieved. Not specific binding contaminants could be easily washed off from the column.

The elution of ATP synthase is initiated by increasing the imidazole concentration of the buffer. The elution profile of his-tagged ATP synthase is shown in Figure 4.3. In contrast to the elution profile of non his-tagged ATP synthase, the peak is very condensed and ATP synthase is concentrated in 5 fractions only. The concentration of the enzyme in each fraction correlates with the hydrolysis activity. It is therefore likely that the F_0 part is intact and that there is no impurity caused by other proteins.

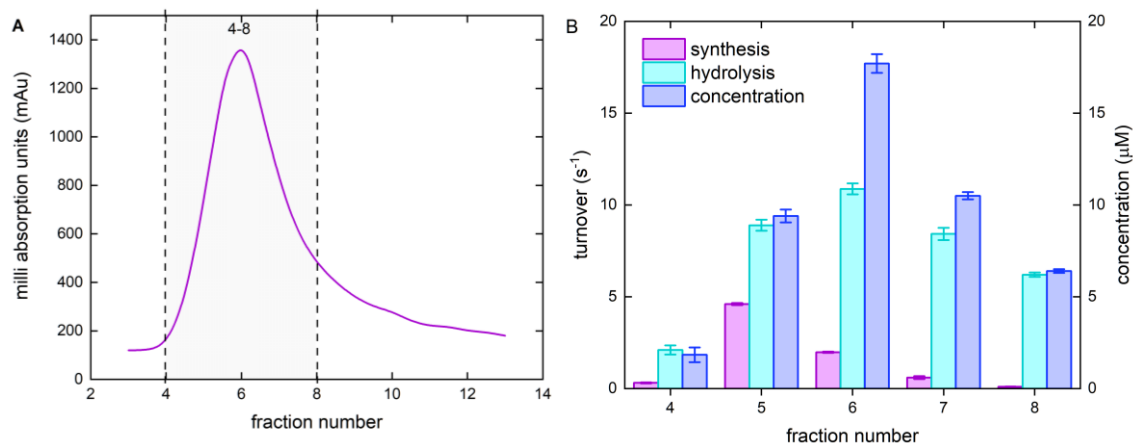


Figure 4.3 Isolation of his-tagged ATP synthase in *E.coli* (EF₀F₁ ATP synthase).

(A) Elution profile of Nickel affinity chromatography. Shown are the milli absorption units at 280 nm for different fractions. Fractions 4-8 are used for further characterization. (B) Comparison of the catalytic activity of ATP synthase in different fractions towards ATP synthesis and ATP hydrolysis. Error bars represent standard error of the mean (n=3).

The ATP synthesis activity in comparison, doesn't correlate neither with the concentration, nor with the hydrolysis activity. Fraction 5 and 6 have the highest activity while synthesis rates are very low in fraction 4, 7 and 8. It is likely that the amount of disassembled ATP synthase in these fractions is higher. The synthesis rates of his-tagged ATP synthase are in general lower compared to that of non his-tagged ATP synthase prepared in the labs of Prof. Börsch. A possible explanation for the comparably low activity is that the F_0 and F_1 are disrupted due to too high flow rates when washing the column. The flow rate through the column is an important parameter that influence the activity and concentration of purified protein. A slow flow rate was found to be essential for both, proper binding and elution of EF_0F_1 . According to the literature a flow rate of 0.25 ml/min should be used throughout the whole procedure (49). In our protocol the flow rate when washing the column was adjusted to 0.5 ml/min for time saving reasons.

SDS-PAGE analysis (Figure 4.4) has been performed in order to check the purity of isolated ATP synthase. All subunits besides the c subunit can be matched to the respective bands in the gel. Interestingly, the intensity of the bands does not completely correlate with the protein concentration of each fraction. Fraction 5 with the most intensive bands also showed the highest synthesis activity, but the protein concentration is much lower compared to fraction 6. It is possible that some subunits of ATP synthase are missing in those fractions with low synthesis activity and that the bands in the gel are therefore less intense.

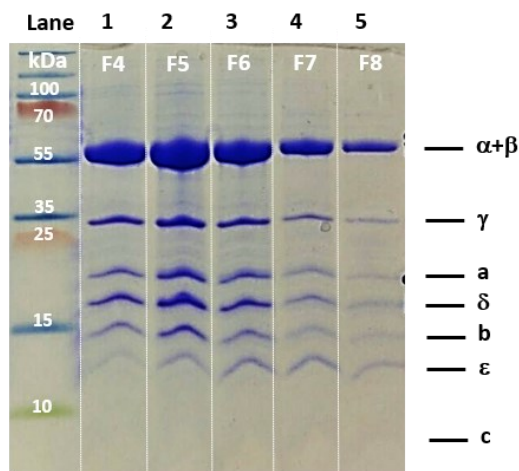


Figure 4.4 SDS-PAGE analysis of his-tagged ATP synthase.

Coomassie-stained SDS-PAGE analysis of purified his-tagged ATP synthase. Lane 1-5 shows the content of different subunits in the fractions 4-8 (10 μ l protein per lane).

4.1.2 ATP synthase characterization in liposomes

According to Mitchell's chemiosmotic theory (73), the electrochemical potential difference $\Delta\mu_H$ that drives the synthesis of ATP consists of two distinct parameters, an electrical potential $\Delta\Psi$ and a transmembrane concentration gradient of protons (ΔpH). Both parameters are related by the following equation:

$$\Delta\mu_H = \Delta\Psi - \frac{2.3RT}{F} \cdot \Delta\text{pH} \quad [4.1]$$

Recent experiments demonstrated that in chloroplast ATP synthase, as well as in mitochondrial and bacterial ATP synthase both forces $\Delta\Psi$ and ΔpH are mandatory for ATP synthesis (74).

To analyse the influence of both driving forces on the synthesis activity of the isolated EF_0F_1 ATP synthase, the synthesis activity as a function of ΔpH and $\Delta\Psi$ was investigated.

4.1.2.1 ATP synthesis as a function of ΔpH

ATP synthesis as a function of ΔpH was determined by energizing EF_0F_1 proteoliposomes with an acid-base transition in combination with a constant K^+ /valinomycin diffusion potential $\Delta\Psi$ as described in chapter 3.2.7.2. All measurements were performed with the same fraction of non his-tagged ATP synthase. The reconstitution and the activity assay were highly reproducible and each value was generated by at least three independent measurements. In all experiments the lipid concentration (0.24 mg/ml) and EF_0F_1 concentration (2.22 nM) was kept constant aiming to a theoretical number of 1 EF_0F_1 per liposome (~110 nm).

To measure the dependency on the internal proton concentration (pH_{in}), proteoliposomes were reconstituted in buffer with various pH. The pH was modified between $\text{pH}_{\text{in}}=5.6$ and 7.6 (Figure 4.5 A). The internal K^+ concentration was kept constant at 0.6 mM and the outer K^+ concentration at 160 mM, which gives a diffusion potential of 143 mV using equation [3.2]. Lower pH_{in} values were not used in order to prevent the denaturation of protein by too acidic surroundings. In the regular ATP synthesis measurements (3.2.7) the protein was only exposed 3 minutes to the acidic solution, while in these measurements ATP synthase was reconstituted directly in low pH buffer solution.

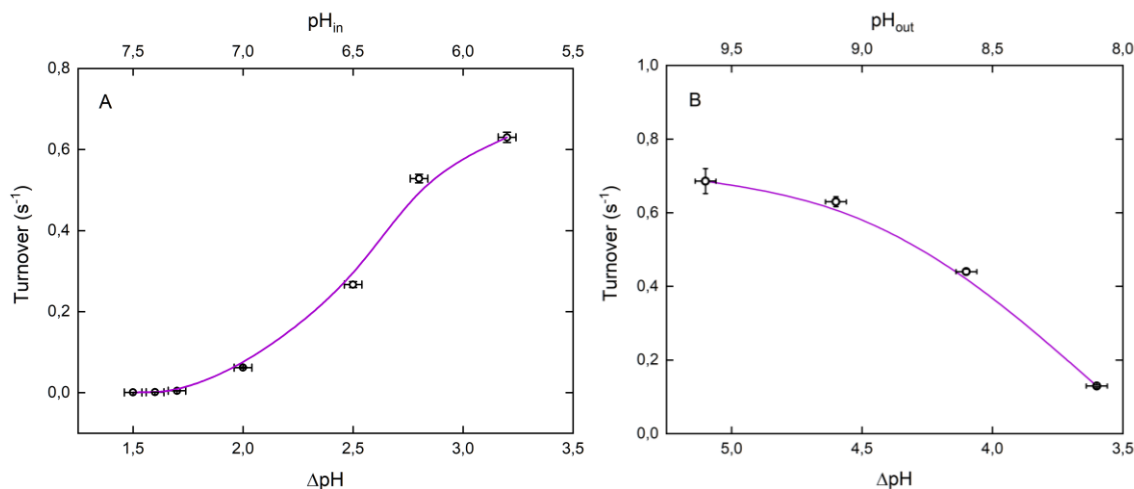


Figure 4.5 Turnover rates of ATP synthesis as a function of pH_{in} and pH_{out} .

(A) Different ΔpH were achieved keeping pH_{out} constant, while pH_{in} varies (see upper axis). (B) Different ΔpH were achieved keeping pH_{in} constant, while pH_{out} varies (see upper axis). Measurements were performed in 20 mM succinate-NaOH, 5 mM NaH_2PO_4 , 0.6 mM KOH (inner solution) and 200 mM tricine-NaOH, 5 mM NaH_2PO_4 , 160 mM KOH (outer solution) adjusted with 18 μM valinomycin at room temperature. $[\text{ADP}] = 10 \mu\text{M}$, $[\text{P}_i] = 5 \text{ mM}$, $[\text{lipid}] = 0.24 \text{ mg/ml}$, $[\text{EF}_0\text{F}_1] = 2.22 \text{ nM}$, $\Delta\psi = 143 \text{ mV}$. ATP synthase was reconstituted with 0.8 % Triton. Error bars represent standard error of the mean ($n=3$).

To drive ATP synthesis, acidic proteoliposomes were injected into basic medium with a pH of 8.8. The resulting ΔpH was calculated as $\text{pH}_{\text{out}} - \text{pH}_{\text{in}}$ where pH_{in} is assumed to be the same as the pH of the proteoliposome suspension. The concentration of P_i was 5 mM and therefore at saturating conditions (48). The ADP concentration was 10 μM and therefore far away from saturation. Higher concentrations were not possible due to the stock concentration of ultra-pure ADP ($\sim 10 \text{ mM}$). Even though ADP concentration is far away from saturation, the reaction can be described by Michaelis-Menten kinetic. Michaelis-Menten kinetic is strictly spoken only valid for irreversible first order reactions. Under the consumption that one substrate (here P_i) is added in large excess, the reaction becomes a reaction pseudo-first order and Michaelis-Menten kinetic is valid.

The amount of synthesized ATP was monitored using the luciferin-luciferase assay as described in chapter 3.2.7. CLSII ATP Assay Kit was used to prevent a decrease of luminescence signal over time. To express the activity as turnover, all enzymes in the reaction mixture were taken into account: no corrections for reconstitution efficiency, enzyme wholeness, orientation, thus, the rate values were underestimated.

A sigmoidal relationship is obtained for the rate of ATP synthesis as a function of ΔpH with various pH_{in} . This result is in good agreement with results reported earlier and a sigmoidal dependency for pH_{in} and ΔpH is predicted by a model described by Jain and Nath (75). The highest rates were

4 Results and Discussion

observed for maximal ΔpH ($\text{pH}_{\text{in}} = 5.6$). The rates are decreasing with decreasing ΔpH . At a ΔpH lower as two, the synthesis rates are almost zero.

To measure the dependency on the external pH (pH_{out}) ATP synthase was incorporated in liposomes in the presence of reconstitution buffer (Table A.19) as described in chapter 3.2.6. Proteoliposomes were then incubated in acidic buffer (pH 4.7, 3 minutes) and subjected in basic buffer with various pH_{out} . The internal and external K^+ concentrations were constant and the same as above with a resulting K^+ diffusion potential of 143 mV. P_i and ADP concentration were 5 mM and 10 μM , respectively. The dependency of pH_{out} shows a different course as the dependency of pH_{in} (Figure 4.5 B). This result is in agreement with earlier reported pH_{out} dependencies and has the same course as the theoretical model described by Jain and Nath (75).

4.1.2.2 ATP synthesis depending on $\Delta\Psi$

ATP synthesis as a function of $\Delta\psi$ was determined in acid-base transition experiments at constant ΔpH ($\Delta\text{pH}=4.1$). In order to produce different K^+ diffusion potentials, different outer buffer solutions with various KCl concentrations were prepared, while the inner K^+ concentration was kept constant at 0.6 mM. All measurements were performed with the same fraction and concentration of non his-tagged ATP synthase (2.22 nM). All other parameters (P_i , ADP, lipid concentration), besides the outer K^+ concentration, were kept constant.

To measure the $\Delta\psi$ dependency of ATP synthesis, EF_0F_1 was reconstituted as described in chapter 3.2.6. Proteoliposomes were incubated for three minutes in acidic medium supplemented with 180 μM valinomycin. The concentration of valinomycin during the measurements was 18 μM due to dilution. Valinomycin is a neutral ionophore that allows the specific transport of K^+ ions over the membrane. The transmembrane electrical potential was calculated using the Nernst equation [3.2]. Figure 4.6 B shows the influence of valinomycin on the ATP synthesis rate. In the absence of valinomycin protons will diffuse through the membrane till an equilibrium between inside and outside protons is reached. The charge inside and outside of the membrane will change by the influx of protons and no further ATP synthesis will occur (Figure 4.6 C). The production of ATP is only determined by the proton concentration gradient (ΔpH).

In the presence of valinomycin K^+ ions will counteract to the change of membrane potential. If the K^+ concentration is outside higher, the concentration gradient will lead to the influx of K^+ ions, thereby keeping the inside of the membrane positively charged and the outside negatively. The flux called K^+ diffusion potential stops further diffusion of ions and keeps the difference in the concentration inside and outside.

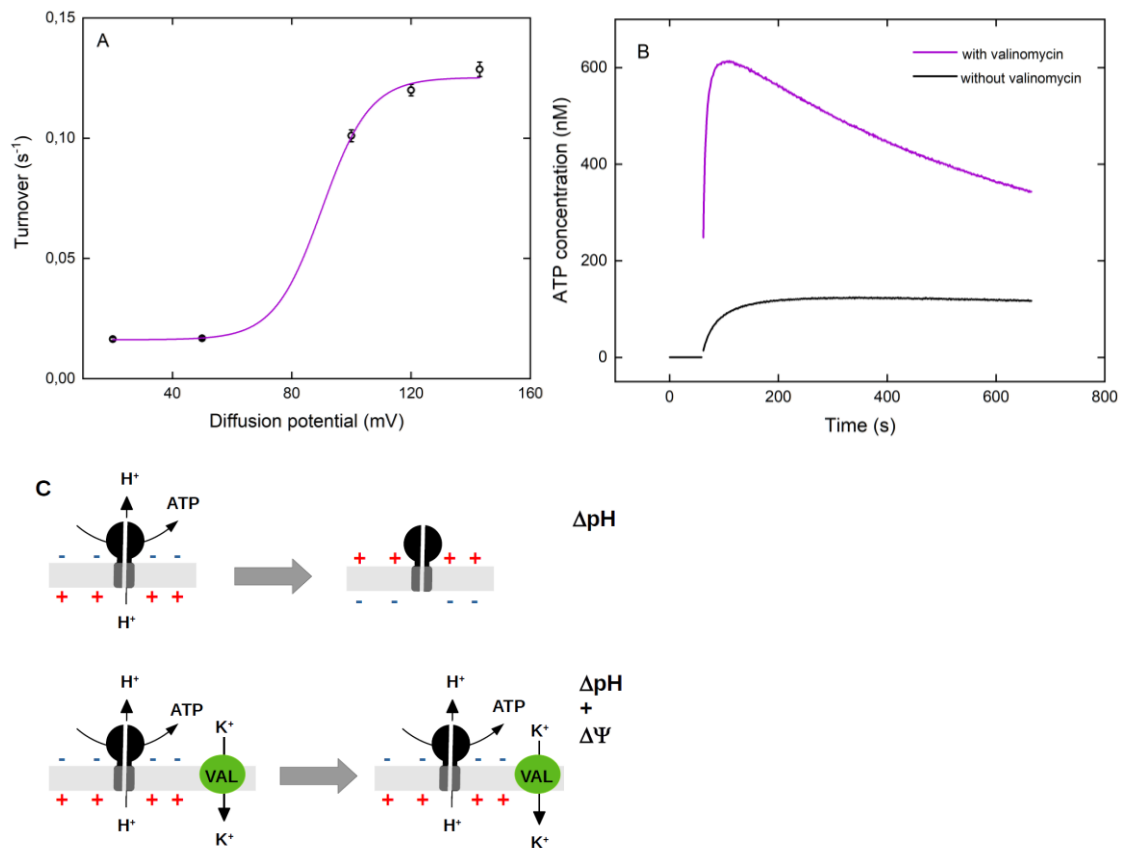


Figure 4.6 Turnover rates of ATP synthesis as a function of the diffusion potential $\Delta\psi$.

(A) The diffusion potential was adjusted by various concentrations of K⁺ inside and outside of the vesicle in the presence of 18 μ M valinomycin. Measurements were performed in 20 mM succinate-NaOH, 5 mM NaH₂PO₄, 0.6 mM KOH, pH 4.7 (inner solution) and 200 mM tricine-NaOH, 5 mM NaH₂PO₄, 160 mM KOH, pH 8.8 (outer solution) at room temperature. [ADP]= 10 μ M, [P_i]= 5 mM, [lipid]= 0.24 mg/ml, [EF_oF₁]= 2.22 nM, $\Delta\psi$ = 143 mV. ATP synthase was reconstituted with 0.8 % Triton. Error bars represent standard error of the mean (n=3). (B) Direct comparison of the influence of valinomycin on the ATP production curve. (C) Schematically presentation of the influence of valinomycin on the membrane potential.

The K⁺ diffusion potential can therefore be seen as the electrical potential $\Delta\psi$. With increasing valinomycin-induced ΔK^+ , electrical potential $\Delta\psi$ and ATP synthesis will increase. A sigmoidal dependency between the ATP synthesis rates and the diffusion potential can be observed (Figure 4.6 A). A diffusion potential of at least 100 mV is necessary to efficiently drive ATP synthesis. For diffusion potentials lower than 50 mV the synthesis activity is almost zero. These results are in good agreement with the results from Kaim and Dimroth (74), who found that the ATP synthesis rates of the *E.coli* ATP synthase were very low for diffusion potentials of $\Delta\psi$ =40 mV or below. An exponentially increase of ATP synthesis with increasing electrical

4 Results and Discussion

potential was observed with an inflection point at around 70 mV. In the here presented results the inflection point is somewhat higher (~90 mV).

Overall, these results suggest that both, the electrical gradient $\Delta\psi$ and the concentration gradient ΔpH are indispensable driving forces for ATP synthesis. These findings are in contrast to the general view that both gradients are kinetically equivalent driving forces and that one parameter of sufficient magnitude can compensate for the other (76). A very high ΔpH was chosen in the here presented study. Anyway, at low electrical gradient $\Delta\psi$ the synthesis rates were almost zero. The same effect was observed for ΔpH at high electrical potential (143 mV). For ΔpH values lower than two, the rates of ATP synthesis were almost zero.

4.1.2.3 Long-term measurements of ATP synthesis

To check the stability of ATP synthase over time, synthesis measurements with the same proteoliposomes and buffer solutions were performed at day 1, 6 and 27 (Figure 4.7). The rates were determined in an acid-base transition experiment as described above. Vesicles were stored at 4°C during this time. The synthesis rates were decreasing over time in an exponential manner. Fitting the data with a first order kinetic model yielded a half-life of 9 ± 1 days.

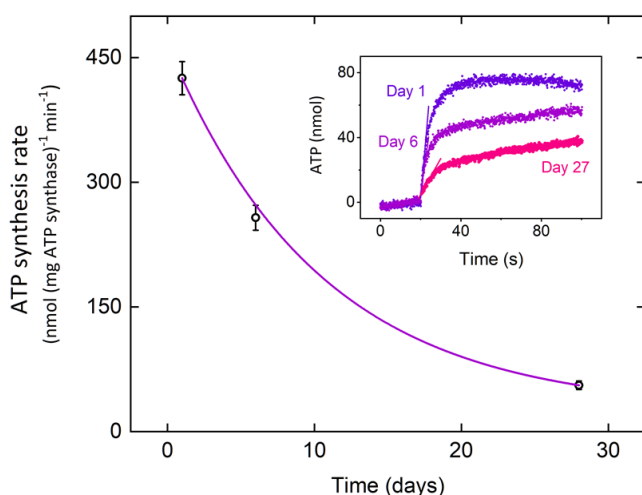


Figure 4.7 Measurement of ATP synthesis over 27 Days.

ATP synthesis rates are decreasing in an exponential manner. Measurements were performed in 20 mM succinate-NaOH, 5 mM NaH_2PO_4 , 0.6 mM KOH, pH 4.7 (inner solution) and 200 mM tricine-NaOH, 5 mM NaH_2PO_4 , 160 mM KOH, pH 8.8 (outer solution) at room temperature. $[\text{ADP}] = 10 \mu\text{M}$, $[\text{P}_i] = 5 \text{ mM}$, $[\text{lipid}] = 0.24 \text{ mg/ml}$, $[\text{EF}_0\text{F}_1] = 2.22 \text{ nM}$, $\Delta\psi = 143 \text{ mV}$. ATP synthase was reconstituted with 0.8 % Triton. Error bars represent standard error of the mean ($n=3$).

4.1.2.4 Characterization of ATP synthase with AFM and Cryo-TEM

Atomic Force Microscopy (AFM)

To image the surface of ATP synthase in liquid, the tip-sample interaction in lateral and normal directions must be minimized. Lateral forces usually arise due to scanning motion. Operating the AFM in tapping mode minimizes these forces (77). To get a faster feedback response and to decrease the thermal noise, small cantilevers were used that were recently reported for high-resolution imaging (78). The use of relatively small tapping amplitudes supports the reduction of thermal noise by giving low forces while maintaining the signal-to-noise ratio. Using a low scan speed for imaging, reduces forces that are caused by feedback error.

To image the ATP synthase in a planar lipid bilayer spread on Mica, ATP synthase was first reconstituted in dialysis liposomes as described in chapter 3.2.6. Supported Lipid Bilayers (SLBs) with (Figure 4.8 A) and without ATP synthase (Figure 4.8 B) were assembled on hydrophilic Mica using the vesicle fusion technique (79). Lipid diffusion to a certain extent is possible in a thin water layer between the lipid leaflet closer to the substrate and the substrate itself. This layer also enables the hosting of transmembrane proteins (80).

An image of a SLB in a homogenous phase without any protein is shown in Figure 4.8 B. Small defects of around 1 nm in depth could be determined (Figure 4.8 B, bottom). This presence of small defects is well known, even though defect free bilayers are usually preferred.

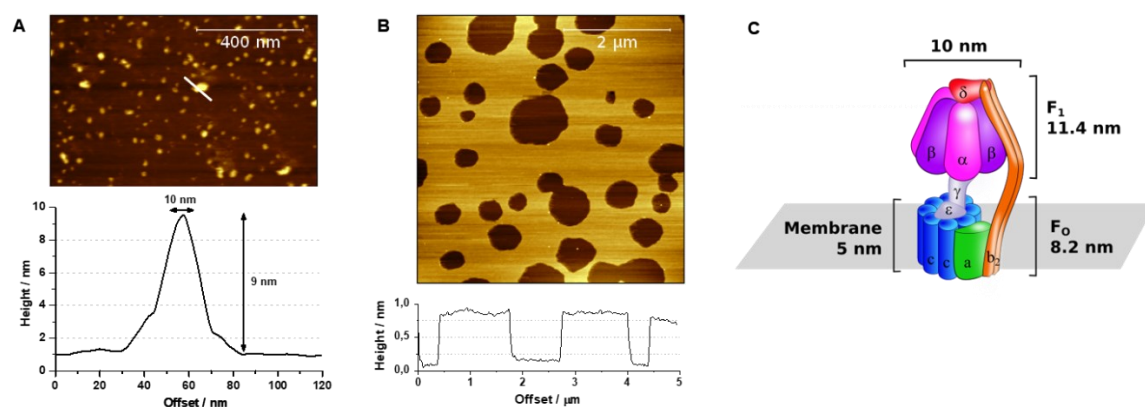


Figure 4.8 Characterization of ATP synthase with Atomic Force Microscopy (AFM).

(A) Atomic Force Microscopy (AFM) image of reconstituted ATP synthase after vesicle spreading on mica. The height profile of a statistically representative spot shows sizes characteristic for ATP synthase (B) AFM image after empty vesicle spreading on mica (no ATP synthase). (C) Schematic presentation of ATP synthase with the corresponding dimensions.

4 Results and Discussion

Anyway, these defects can be used to prove the presence of a bilayer on the substrate, which is a big advantage. Typical defects using a single lipid component for spreading can be up to 2 nm in depth (79). The mechanism of SLB formation from unilamellar vesicles in solution is based on the adsorption and rupture of the vesicles on the substrate. Thereby forming a continuous planar lipid bilayer on the support.

Figure 4.8 A shows an AFM image of ATP synthase in a SLB with a statistically representing height profile. Due to the comparably large height of ATP synthase, small defects in the SLB are not visible anymore. An intact ATP synthase protrudes approximately 11 nm from the lipid surface (Figure 4.8 C) with a width of around 10 nm (81). The extracted profile indicates a height of 9 nm which is slightly lower than expected. This difference in height might be explained by defects in lipid bilayer which can lead to divergences of ± 2 nm. The width of 10 nm in contrast, fits very well to the values reported in the literature (81). Another explanation for underestimating the height of ATP synthase is, that the protein was not completely intact and it lost some subunits. Due to the large topography and the fragile nature of ATP synthase it is possible, that subunits were disassembled even while imaging.

Cryo-Transmission Electron Microscopy (Cryo-TEM)

Reconstituted ATP synthase was visualized using Cryo-TEM. Cryo-TEM measurements were performed by Ingo Lieberwirth from MPI Mainz (Institute for Polymer Research). The proteoliposomes were prepared using dialysis vesicles as described in chapter 3.2.6. The size of vesicles before and after reconstitution was checked by Dynamic Light Scattering (Figure 4.9 A).

Vesicles before reconstitution had a mean diameter of around 600 nm. The addition of detergent during reconstitution broke the vesicles slightly and leads to rearrangement. As a result, vesicles after reconstitution only had a diameter of around 110 nm, leading to a theoretical ATP synthase number of approximately 1 ATP synthase per vesicle.

Cryo-TEM images confirmed the size of the vesicles to be around 110 nm (Figure 4.9 B) and to be unilamellar. A small protrusion with a diameter of around 10 nm was found to stick out of the membrane (F_1 , indicated by an arrow). The diameter of the protrusion agrees well with the size of the ATP synthase head group (F_1) which was reported to be 10 nm (81) and was also found to be 10 nm in AFM investigations.

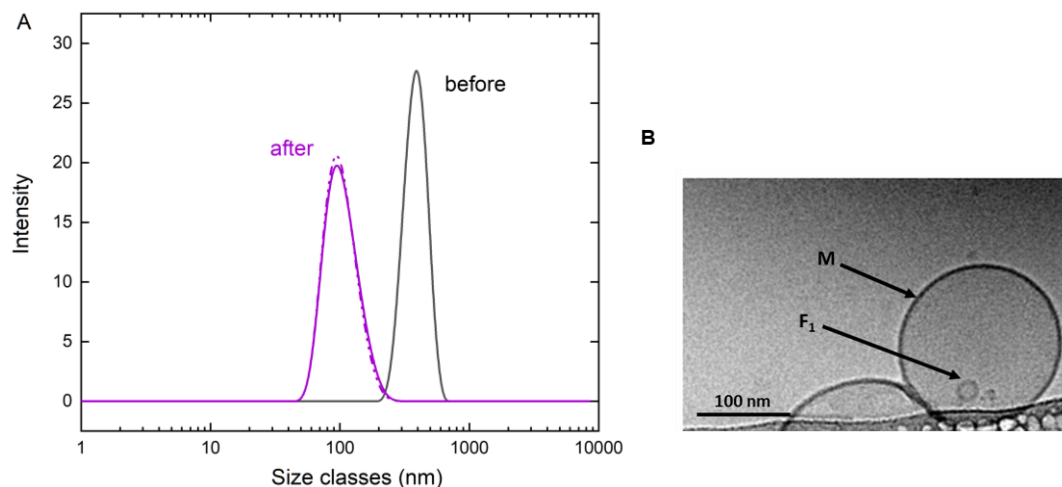


Figure 4.9 Characterization of ATP synthase vesicles with Dynamic Light Scattering (DLS) and Cryo-TEM.

(A) Size distribution after ATP synthase reconstitution into small unilamellar vesicles (SUVs). The proteoliposomes have an average diameter of 110 nm as shown by dynamic light scattering. (B) Cryo-TEM image after reconstitution of ATP synthase into SUVs. M: Vesicle Membrane, F₁: hydrophilic head F₁ of ATP synthase.

The theoretical number of 1 ATP synthase per vesicle is also in good agreement with the results of Electron Microscopy measurements. It is unlikely, that this protrusion is a smaller vesicle. Vesicles of 10 nm size should have been visible in DLS measurements and DLS results confirmed that there are no smaller particles. Similar Cryo-TEM images of ATP synthase reconstituted in 50 nm vesicles have been reported by Tutus et al. (61). In other literature ATP synthase is imaged free in solution and looks slightly different depending on the angle of imaging.

4.2 Bacteriorhodopsin

Bacteriorhodopsin (bR) was first used as a lyophilized powder bought from Sigma. The main problem with this enzyme was the solubility. According to the manufacturer protocol the powder should be soluble in regular MilliQ water. However, solubilization in water wasn't possible. Further solubilization approaches using Triton X-100 or octyl glucoside in various concentrations under shaking up to 10 days, didn't lead to monomeric bR either. The bought protein was moreover quite expensive. Therefore, we implemented bR isolation using a standard procedure (54).

4 Results and Discussion

4.2.1 Isolation of bacteriorhodopsin

Bacteriorhodopsin isolation was performed by Claudia Bednarz. Further characterization (determination of activity, concentration,...) was part of this thesis. The concentration of the protein was determined by absorption spectroscopy as described in chapter 3.3.3, leading to concentrations in between 2.5 mg/ml and 7.7 mg/ml depending on the batch of isolation.

An exemplary spectrum of a 1:20 dilution of the isolated enzyme is shown in Figure 4.10 B. The band at 560 nm is characteristic for bR and gives the protein the characteristic purple colour. The band at 280 nm is a band typical for all proteins and arises by amino acids with aromatic rings. Therefore, the ratio between both peaks can define the purity (protein to bR ratio) of the isolated enzyme (55) (Figure 4.10 C), which is 99% in the shown example.

Almost all batches led to bR with a comparable purity. Only one batch was impure due to a failed separation from the red purple fragment. This contamination was easily visible by additional peaks in the absorption spectrum at approximately 480 nm and 510 nm. This bR batch didn't show any proton pumping activity and wasn't used for further experiments.

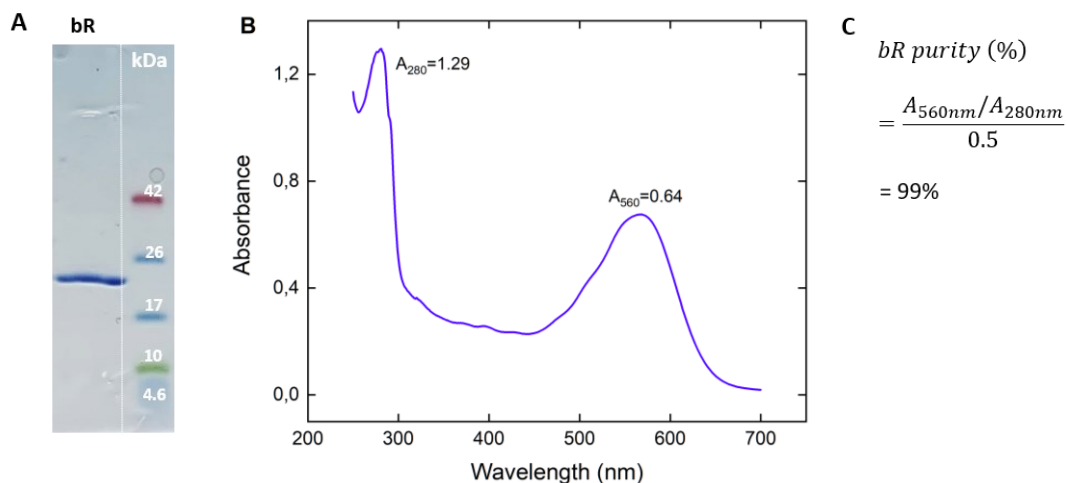


Figure 4.10 Characterization of isolated bacteriorhodopsin (bR).

(A) Coomassie-stained SDS-PAGE of purified bR shows a single band at the expected molecular mass of monomeric bR. (B) Absorbance spectra (dilution 1:20) of bR after expression has two characteristic peaks at 280 nm and 560 nm which correspond to the protein and the pigment, respectively. The ratio of the two amplitudes indicates a purity of around 99% (C) (55).

The purity of the protein was additionally checked using SDS-PAGE analysis (Figure 4.10 A). As expected, a single intensive band at 22 kDa arises, which can be correlated to monomeric bR. The discrepancy between the theoretical mass of bR (26.8 kDa) (82) and the molecular size determined in the gel (22 kDa) can be explained by a phenomenon known as gel shifting. Membrane proteins are often not completely denaturated in SDS-PAGE gels and are therefore migrating with smaller molecular size (83; 84).

4.2.2 Characterization of bacteriorhodopsin in liposomes

Bacteriorhodopsin was characterized by measuring the proton pumping activity after reconstitution in liposomes as described in chapter 3.3.6. In contrast to ATP synthase reconstitution, which was usually conducted in thawed dialysis liposomes, liposomes for bR reconstitution were always prepared freshly by film hydration method. This enabled the encapsulation of pyranine, which was used as internal probe for quantification of the proton concentration.

4.2.2.1 Pyranine as internal probe

Pyranine or 8-hydroxyprene-1,3,6-trisulfonic acid (HPTS) is a hydrophilic, pH-sensitive dye from the group of chemicals known as arylsulfonates (85). The chemical structure is shown in Figure 4.11 C. The polyanionic character of pyranine avoids significant binding to phospholipids that have a net anionic surface charge. This allows vesicle preparation in the presence of pyranine. These vesicles have pyranine entrapped in the internal compartment after external dye is removed by gel filtration. Therefore, pyranine can be used as reliable reporter of pH changes inside of anionic vesicles (86).

Using pyranine, the pH change can be either detected by a change of fluorescence intensity at 510 nm or by monitoring the change in absorbance at 450 nm and 405 nm. In this work, the absorbance change was detected, due to the lack of suitable excitation sources for fluorescence measurements. The pyranine spectrum at various pH is shown in Figure 4.11 A. The maxima at 405 nm is increasing with decreasing pH, while the peak at 450 nm decreases with decreasing pH. This contrary effect facilitates a very precise identification of pH.

4 Results and Discussion

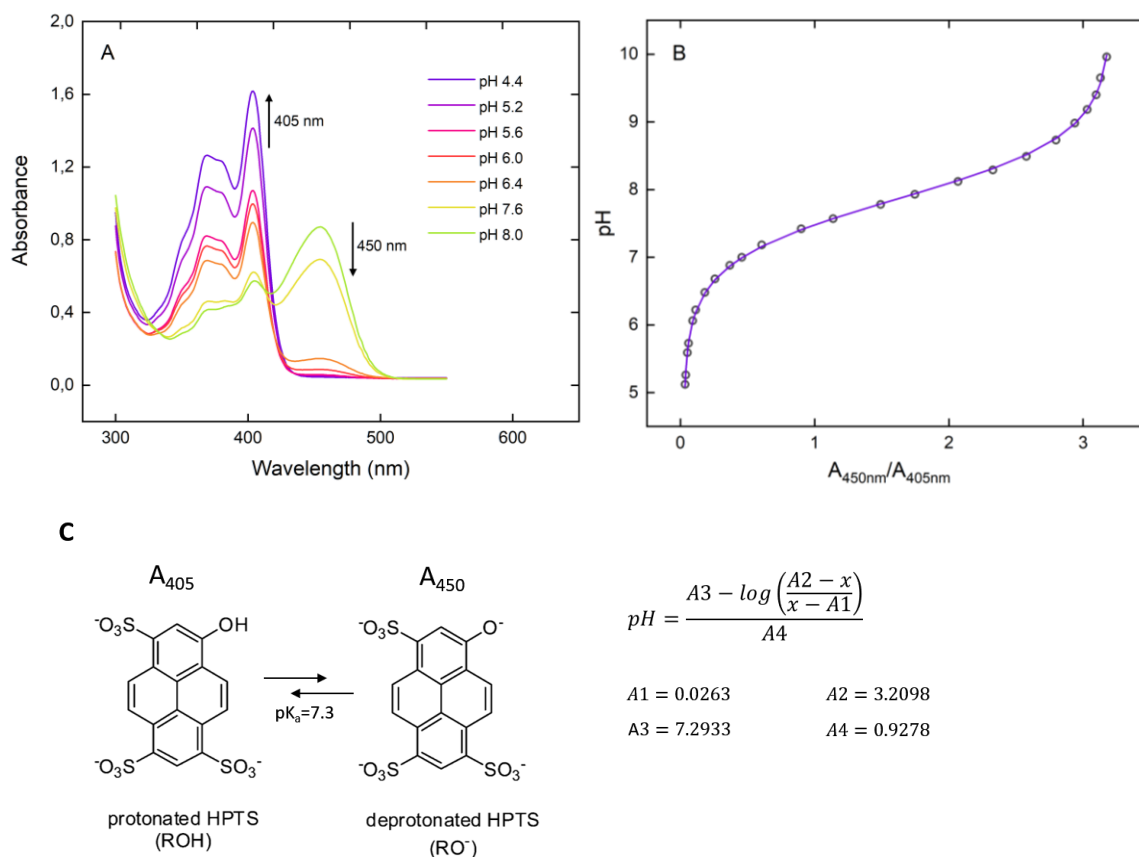


Figure 4.11 Calibration curve for pH determination using the absorption of pyranine at 450 nm ($A_{450\text{nm}}$) and 405 nm ($A_{405\text{nm}}$).

(A) Pyranine spectrum at various pH. (B) Calibration curve of pyranine in 40 mM HEPES buffer. (C) Henderson-Hasselbalch equation with the determined values $A1$, $A2$, $A3$, $A4$ and structural formula of pyranine.

To determine the internal pH using pyranine as probe, a calibration curve has to be recorded (Figure 4.11 B). The pH of a continuously stirred 1 mM pyranine solution in 40 mM HEPES buffer was monitored with a pH electrode and adjusted by addition of small amounts of 1 M KOH. At regular pH intervals (~ 0.2), 500 μl of the solution was taken and analysed by absorption measurements at 405 nm and 450 nm. The detected results for various pH values were plotted and fitted with a formulation of the Henderson-Hasselbalch relation using Matlab (Figure 4.11 C).

4.2.2.2 Proton pumping using bR patches

- Dependence on the number of pumping units

To determine the dependence of proton pumping rates on the bR concentration, vesicles were prepared as described in chapter 3.3.5 and different amounts of bR were reconstituted using Triton as detergent. In general, each of the following measurement series was always strictly conducted using bR from a single batch.

The amount of Triton was identical with the amount used for ATP synthase reconstitution in order to check the possibility to co-reconstitute both proteins with this amount of Triton later on. bR was used in form of membrane patches to avoid material loss during solubilization. Hereby, higher concentrations up to 0.92 mg/ml could be obtained.

After removal of Bio-Beads, gel filtration was conducted in order to remove not encapsulated pyranine. Additionally, gel filtration separated bR proteoliposomes from not incorporated bR. Therefore, the reconstitution efficiency of bR (R_{eff}) could be calculated by the absorbance ratio at 560 nm before ($A_{560,\text{before}}$) and after gel filtration ($A_{560,\text{after}}$) using equation [3.12]. All reconstitution efficiencies are in the range of around 65-85%. Interestingly, the highest R_{eff} could be achieved for a bR concentration of 34 μM , which was the highest used (Figure 4.12). According to the literature (45) ATP synthase reconstitution efficiencies are decreasing with increasing protein concentration. To the best of my knowledge there are no detailed studies in this regard about bR. To clarify the reason for this outcome further measurements would have been necessary.

Before each proton pumping measurement, valinomycin was added to the vesicles in order to prevent the formation of a potential gradient that counteracts proton pumping. As in the absence of valinomycin, all present ions of the medium are impermeable, proton translocation develops a large transmembrane electrical potential ($\Delta\psi$) (87). As a consequence, no further protons are pumped. In contrast, when adding valinomycin, K^+ diffusion equilibrates the built up of transmembrane charge. K^+ is passively diffusing from the inside to the outside and proton pumping is not inhibited by $\Delta\psi$. A schematical presentation of the influence of valinomycin on the membrane potential is shown in Figure 4.12 C. Indeed, lower steady-state ΔpH values were obtained in the absence of valinomycin (data not shown).

4 Results and Discussion

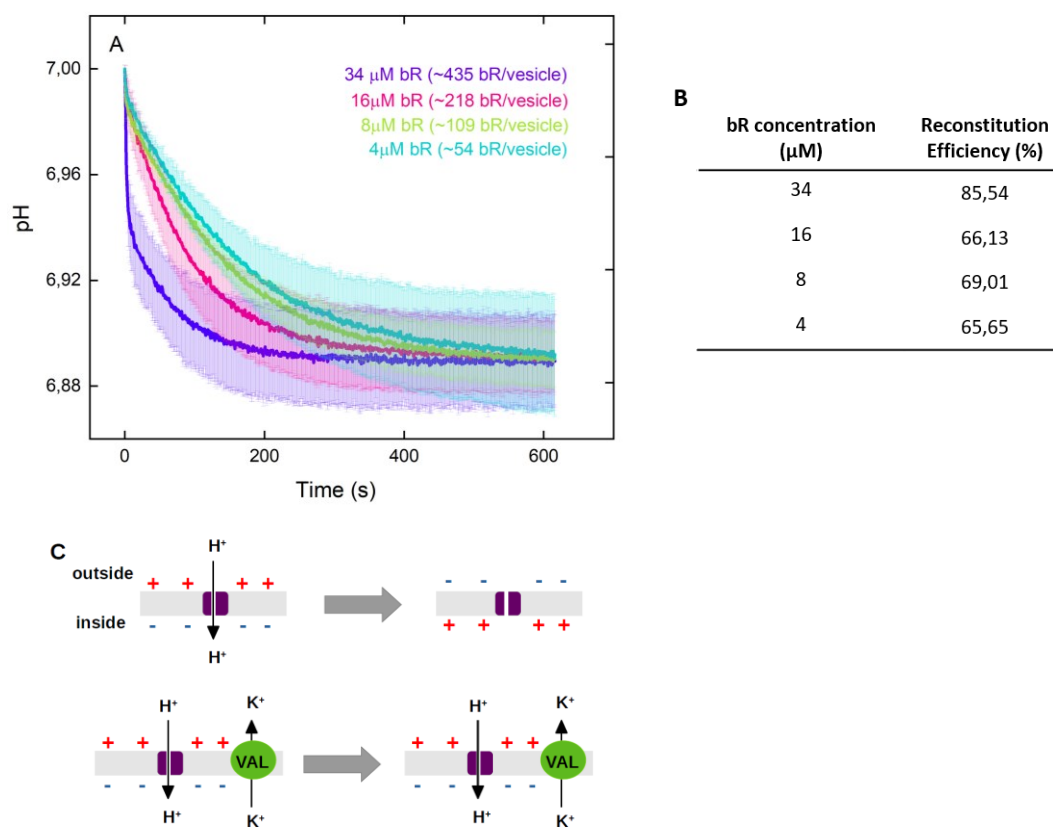


Figure 4.12 Effect of the lipid to protein ratio on bR proton pumping rates.

(A) Initial rates of proton pumping are increasing with the protein content, while the steady state ΔpH remains unchanged. Measurements were performed in 10 mM HEPES (pH 7.0), 100 mM K_2SO_4 , 15 mM MgCl_2 in the presence of 0.1 μM valinomycin at room temperature. Proteins were reconstituted with 0.8 % Triton. Concentration of bR is given as concentration after removal of not incorporated bR. Error bars represent the standard error of the mean ($n=3$). (B) Reconstitution efficiency for different bR concentrations. (C) Schematically presentation of the influence of valinomycin on the membrane potential.

Samples were equilibrated in the dark before the reaction was started by illumination with a green light LED lamp. At the same time absorbance measurements were started. The calibration curve shown in Figure 4.11 B was used to generate the pH change by the absorption time courses ($A_{450\text{nm}}$, $A_{405\text{nm}}$). A detailed description can be found in the material and methods (3.3.6.3). The pH values at $t=0$ (pH_0) was corrected to the pH of the buffer solution ($\text{pH}=7$). Some membrane systems show deviations between the actual and apparent pH due to interactions between pyranine and the vesicle material. As the pH for these experiments was in the linear range of the calibration curve, all data points could be offset by the same value for each series.

Each proton pumping curve was recorded in three separate measurements. The middle values of these measurements are shown in Figure 4.12 A. As expected, initial rates of proton pumping are increasing with the amount of bR while the steady-state ΔpH remains unchanged. These results were also found by Seigneuret et al. (87) who further proved this outcome by potentiometric measurements. It is likely, that back-pressure effects of ΔpH decreasing the proton pump activity of bR progressively as ΔpH is established. Therefore, the steady-state ΔpH becomes independent of the number of pumping units.

4.2.2.3 Bacteriorhodopsin solubilization

bR isolation yielded bR in form of two-dimensional crystalline patches known as “purple membrane”. The repeating element of the hexagonal lattice is composed of three identical protein chains, each rotated by 120 degree relative to the others (88). To gain the protein as monomeric protein in detergent, bR patches were solubilized. Different detergents, which has been proposed by the literature (89) for bR solubilization, were investigated (Figure 4.13). The procedure after addition of the detergent was always the same: 10 minutes of sonification followed by at least 4 days under stirring in the dark. Not solubilized membranes were removed by centrifugation.

All solubilization experiments led to high losses of bR, or in other words solubilization never reached 100%. The best results were observed using the solubilization procedure with Triton X-100 described by Meyer et al. (56). The concentration of Triton was calculated according to the concentration of the bR solution with equation [3.8]. Using this method, solubilization efficiencies of around 30% could be observed (Figure 4.13 B).

In contrast, the solubilization efficiency using octyl glucoside as detergent was very low as shown in Figure 4.13 C. Only 6% of membrane patches could be dissolved using this detergent. Moreover, the spectrum indicates that mainly the red fragment was released, resulting in absorption peaks at 480 nm and 510 nm. All further bR solubilizations were therefore conducted using Triton as detergent.

4 Results and Discussion

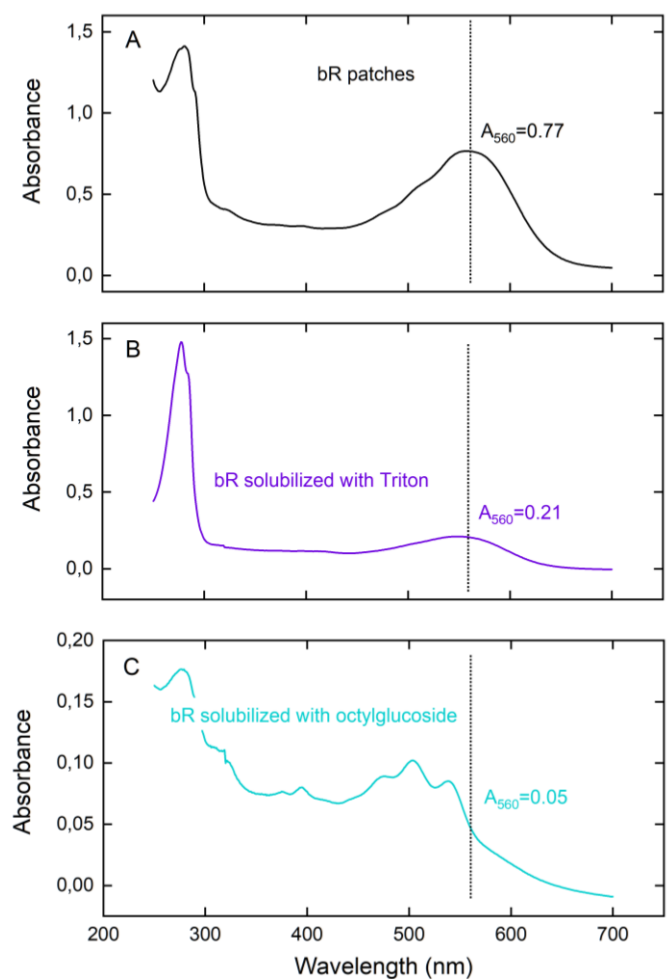


Figure 4.13 Absorbance spectrum of bR before (A) and after solubilization with Triton X-100 (B) and octyl glucoside (C).

Around 30% bR could be solubilized using 0.36% Triton X-100 as detergent. Octyl glucoside solubilized predominantly the red membrane fragment as can be seen from the absorbance spectra.

4.3 Light-driven ATP regeneration

His-tagged EF_0F_1 ATP synthase and bR were combined to form a light-driven ATP regeneration module. Both enzymes were co-reconstituted in lipid, polymer and hybrid vesicles. The functionality of enzymes and the ATP production rates in different compartments were investigated. The ATP production rate in liposomes is later used as a benchmark to evaluate the biocompatibility of enzymes in polymer and hybrid vesicles.

4.3.1 The ATP module in liposomes

The light-driven ATP regeneration module consists of a compartment and two transmembrane proteins, ATP synthase and bacteriorhodopsin, as schematically shown in Figure 4.14 A. Bacteriorhodopsin acts as a proton pump and establishes a proton gradient that drives ATP synthase.

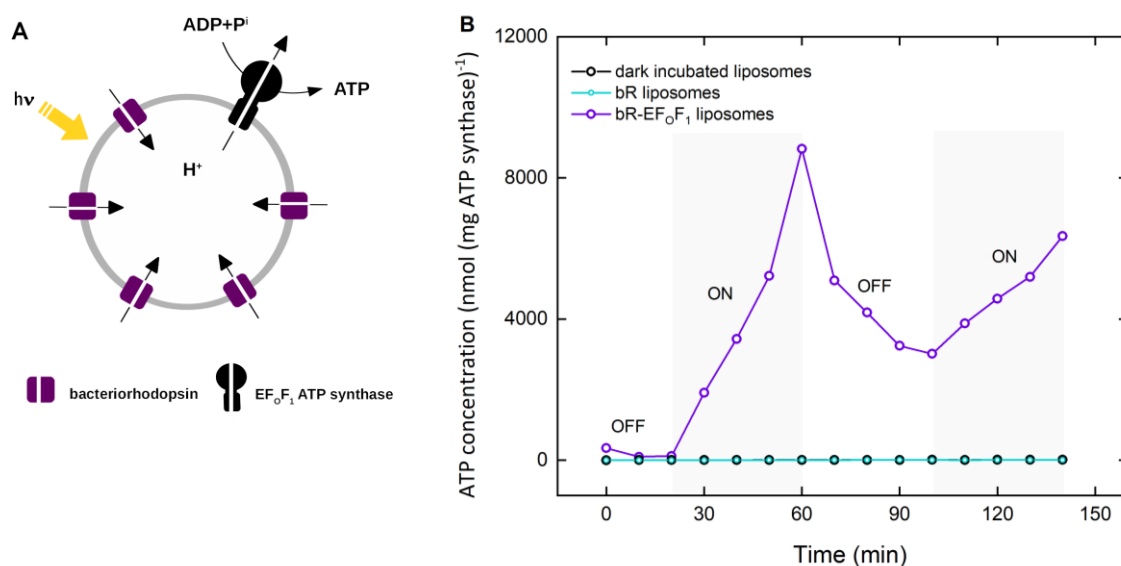


Figure 4.14 Light-driven ATP synthesis in lipid vesicles (100-150 nm).

(A) Schematic representation of the ATP generating system reconstituted with bacteriorhodopsin (bR) and EF_oF_1 -ATP synthase. F_oF_1 -ATP synthase uses the electrochemical gradient generated by bR to synthesize ATP. (B) Photoinduced ATP synthesis in bR- EF_oF_1 liposomes through on-off cycles of light, in the absence of light (dark incubated liposomes), and in liposomes containing only bR (bR liposomes). Measurements were performed in 20 mM tricine-NaOH, 20 mM succinate, 0.6 mM KCl, 80 mM NaCl (inner solution) and 200 mM tricine-NaOH, 5 mM NaH_2PO_4 , 160 mM KOH, pH 8.8 (outer solution) in the presence of 18 μ M valinomycin at room temperature. [ADP]= 57 μ M, [P_i]= 5 mM, [lipid]= 0.022 mg/ml, [EF_oF_1]= 1.3 nM, [bR]= 88 nM, $\Delta\Psi$ = 143 mV. Proteins were reconstituted with 0.8 % Triton.

Vesicles from phosphatidylcholine (PC) were prepared using the film hydration method as described in chapter 3.4.1 and were slightly destabilized using Triton, similar to the method described by Fischer (52).

The activity of both enzymes was quantified by recording the produced ATP under illumination using the luciferin/luciferase assay (3.4.3). The ATP concentration at each time point was recorded in three independent measurements. Each luminescence signal was calibrated separately by the addition of ATP. Calculation of ATP is illustrated in chapter 3.4.3.1 and was implemented using equation [3.18]. Figure 4.14 B shows the course of ATP production in liposomes through on-off

4 Results and Discussion

cycles of light. The concentration of ATP increased under illumination and decreased again in the dark due to the absence of a proton motive force (presumably due to ATP hydrolysis), which demonstrated successful ATP production triggered by light. As control, ATP was measured in complete absence of light, as well as in liposomes containing only bR. In both experiments no measurable increase of ATP was detected.

The performance of ATP production depends on different factors, which makes a straightforward comparison with literature reports difficult. Besides the choice of reconstitution method and detergent, the origin and activity of the F_0F_1 ATP synthase as well as the bR/ATP synthase ratio per liposome, have to be considered. The commonly used incorporation method is a co-reconstitution of both enzymes using different detergents, mainly octyl glucoside and Triton-X-100, to mediate the insertion of proteins into preformed liposomes (24; 23; 25; 26; 90). As already mentioned above, in this work Triton was used as detergent because octyl glucoside has been reported to inactivate MF_0F_1 and CF_0F_1 ATP synthase (25) and also led to much lower ATP production rates in my experiments (data not shown).

To check the ATP production over longer timescales, light-driven ATP synthesis was monitored over 5 hours (Figure 4.15). The results indicate that even after 5 hours, ATP is further increasing and no saturation point is reached. ATP concentrations up to 20 μM could be achieved in this experiment. Higher rates would be possible by increasing the time of illumination, the protein or ADP to ATP concentration. This result might be of importance when coupling the ATP module with other functional modules.

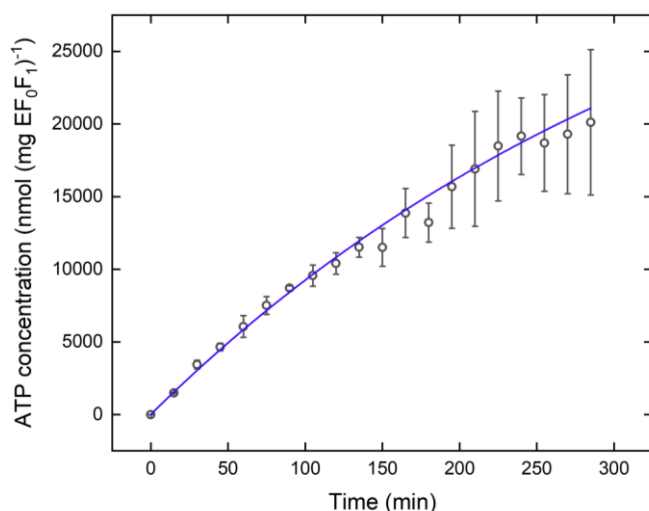


Figure 4.15 Light-driven ATP synthesis in lipid vesicles over 5 hours.

Measurements were performed in 20 mM tricine-NaOH, 20 mM succinate, 0.6 mM KCl, 80 mM NaCl (inner solution) and 10 mM Tris-HCl, 5 mM NaH_2PO_4 , 50 mM KCl, 2 MgCl_2 , 1 mM DTT, pH 7.5 (outer solution) at room temperature. $[\text{ADP}] = 300 \mu\text{M}$, $[\text{P}_i] = 5 \text{ mM}$, $[\text{lipid}] = 0.022 \text{ mg/ml}$, $[\text{EF}_0\text{F}_1] = 1.3 \text{ nM}$, $[\text{bR}] = 88 \text{ nM}$. Proteins were reconstituted with 0.8 % Triton.

4.3.1.1 ATP synthesis rates as a function of bR concentration

As mentioned above, the ATP production of the light-driven module might be further improved by varying the protein concentrations while keeping the phospholipid concentration constant. For coupling bR with ATP synthase in lipid vesicles, different bR/ F_0F_1 ATP synthase ratios, ranging from 1/1 (29; 24) to 170/1 (90), have been covered in the literature.

Figure 4.16 shows typical results of Triton X-100 mediated reconstitutions at different lipid/bR ratios. In this experiment the ATP synthase concentration and the lipid concentration during reconstitution were kept constant at 100 nM and 5 mg/ml, respectively. This corresponds to a theoretical number of approximately 1 ATP synthase per vesicle (100-150 nm). The bR concentration was varied between 0.8 and 6.2 μM corresponding to a theoretical number of ~8-60 bR per vesicle. Higher amounts of bR couldn't be reached due the stock concentration of isolated protein. The results (Figure 4.16 A) clearly show that ATP synthesis rates are increasing with the number of bR molecules per vesicle. This increase of ATP synthesis cannot be related to an increase of steady state ΔpH . bR proton pumping measurements (4.2.2.2) showed that the steady-state ΔpH is independent of the number of pumping units. All observations reported suggest that the bulk-to-bulk ΔpH , as sensed by trapped pyranine, is not the sole driving force for ATP synthesis which appears to rely also on the number of bR molecules per liposome.

4 Results and Discussion

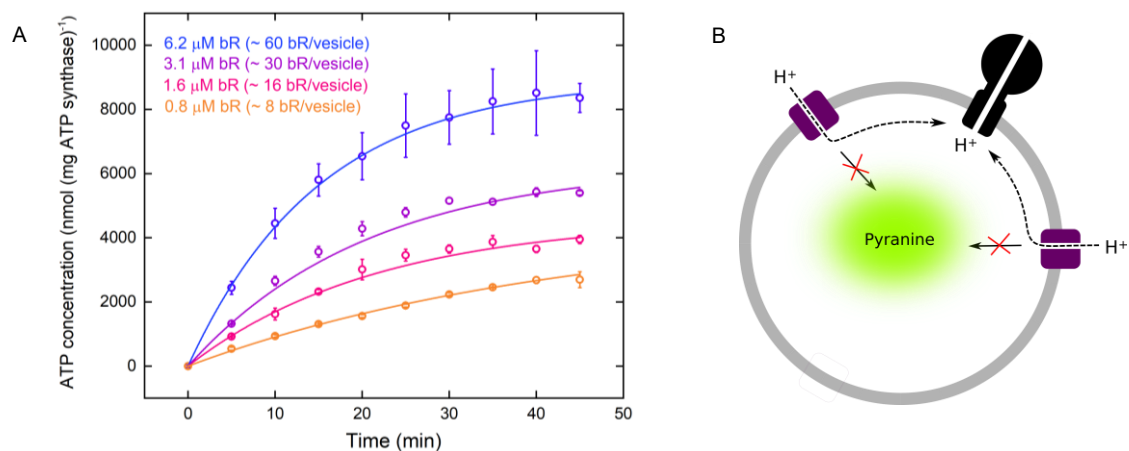


Figure 4.16 ATP production after co-reconstitution with 1 EF_oF₁/liposomes and various amounts of bR.

(A) Increasing ATP production rates with increasing number of bR molecules per liposome. bR was reconstituted in form of patches. The concentration is given as concentration during reconstitution. Measurements were performed in 20 mM tricine-NaOH, 20 mM succinate, 0.6 mM KCl, 80 mM NaCl (inner solution) and 200 mM tricine-NaOH, 5 mM NaH₂PO₄, 160 mM KOH, pH 8.8 (outer solution) in the presence of 18 μM valinomycin at room temperature. [ADP]= 57 μM, [P_i]= 5 mM, [lipid]= 0.022 mg/ml, [EF_oF₁]= 1.3 nM, [bR]= 79 nM, 39 nM, 20 nM, 10 nM, ΔΨ= 143 mV. Proteins were reconstituted with 0.8 % Triton. All error bars represent the standard error of the mean (n=3). (B) Schematically presentation of direct proton diffusion along the membrane without dissipation losses into the bulk.

Similar results were obtained by Pitard et al. (26). His results moreover indicated that protein-protein interactions are not likely being the cause of higher ATP synthesis with increasing bR concentration. He strongly suggested the existence of direct H⁺ transfer from bR to ATP synthase (schematically shown in Figure 4.16 B) and demonstrated that raising the number of bR molecules results in an increase of the local electrochemical potential difference Δμ_H in the vicinity of ATP synthase which is not detected by pyranine. In accordance to this, Heberle et al. (91) recently evidenced that protons pumped by bR can efficiently diffuse along the membrane surface between a source (bR) and a sink (ATP synthase) without dissipation losses into the aqueous bulk.

4.3.1.2 ATP synthesis rates – bR patches vs. solubilized bR

The efficiency of proton pumping of monomeric bR compared to bR patches was detected by monitoring light-driven ATP production (Figure 4.17). Linear regression yielded a rate of 3.3 nmol (mg bR)⁻¹ min⁻¹ for bR patches and 6.8 nmol (mg bR)⁻¹ min⁻¹ for bR solubilized with Triton as described in chapter 3.3.4. Besides the step of solubilization all other steps of reconstitution were the same and ATP synthase from the same batch and fraction was used. As a consequence of concentration losses during solubilization, the final monomeric bR concentration was lower than

that of membrane patches. The results were therefore normalized to the amount of bR used (per mg bR) and indicate that the ATP production per mg bR is around double as high using monomeric bR compared to bR patches. This outcome is in good agreement with the results reported by Wagner et al. (29). Wagner and colleagues found around 6 times higher ATP production rates when using monomeric bR instead of bR patches and explained it by the fact that monomeric bR is distributed more homogeneously among the liposomes.

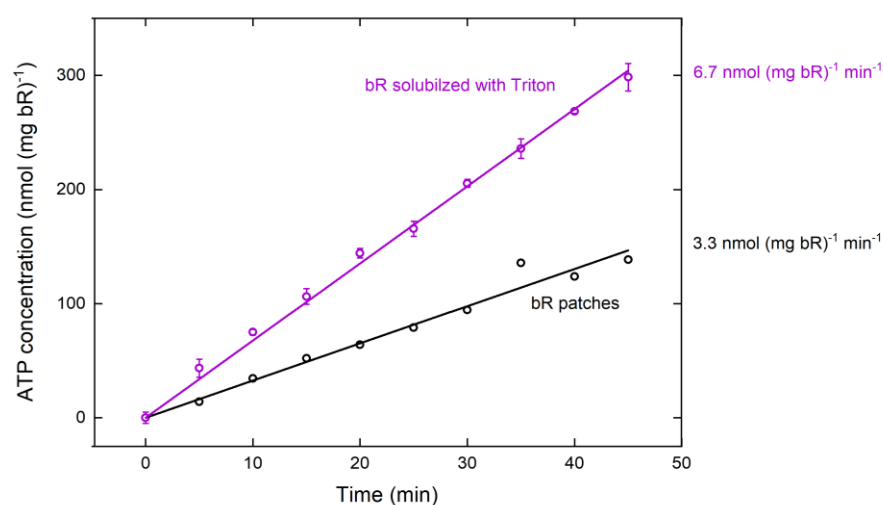


Figure 4.17 ATP production in lipid vesicles co-reconstituted with Triton X-100 (0.36 %) solubilized bR compared to bR patches.

The ATP production per mg bR is higher for solubilized bR compared to bR patches. The activity was determined by linear regression. Measurements were performed in 20 mM tricine-NaOH, 20 mM succinate, 0.6 mM KCl, 80 mM NaCl (inner solution) and 200 mM tricine-NaOH, 5 mM NaH₂PO₄, 160 mM KOH, pH 8.8 (outer solution) in the presence of 18 μ M valinomycin at room temperature. [ADP]= 300 μ M, [Pi]= 5 mM, [lipid]= 0.022 mg/mL, [EF_oF₁]= 1.3 nM, $\Delta\Psi$ = 143 mV. Proteins were reconstituted with 0.8 % Triton.

4.3.1.3 ATP synthesis rates as a function of EF_oF₁ concentration

Increasing the bR concentration clearly led to an increase of ATP synthesis rates. In the following, the dependency of ATP synthesis on the number of EF_oF₁ molecules per liposome is investigated.

In the here presented set of experiments various ATP synthase concentrations between 49 nM and 590 nM were used for co-reconstitution. These concentrations correspond to a theoretical number of 0.5 to 4 ATP synthase molecules per vesicle.

4 Results and Discussion

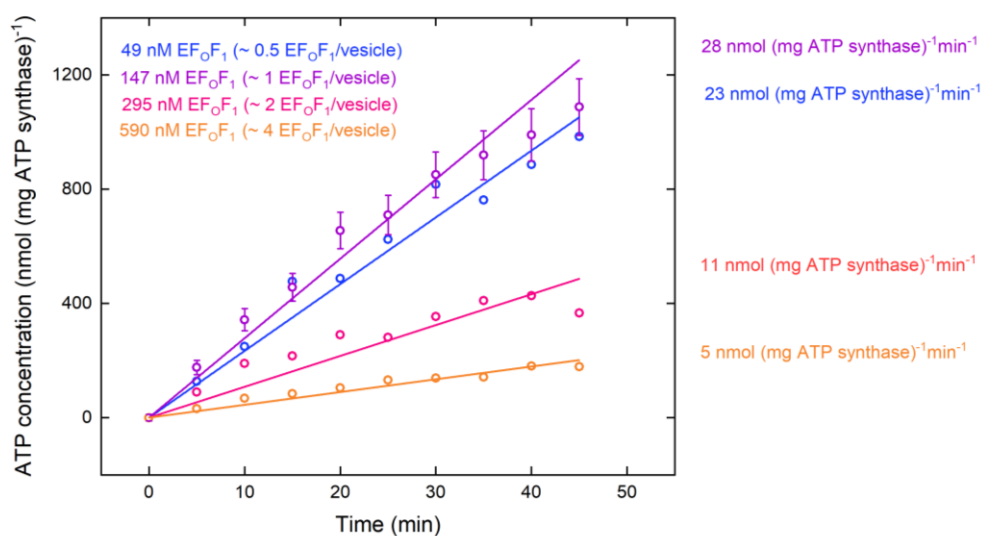


Figure 4.18 ATP production in lipid vesicles co-reconstituted with different amounts of ATP synthase at constant bR concentration.

The concentration is given as concentration during reconstitution. Maximal ATP production rates per mg of ATP synthase were reached when reconstituting approximately 1 ATP synthase per vesicle. The activity is determined by linear regression. Measurements were performed in 20 mM tricine-NaOH, 20 mM succinate, 0.6 mM KCl, 80 mM NaCl (inner solution) and 200 mM tricine-NaOH, 5 mM NaH₂PO₄, 160 mM KOH, pH 8.8 (outer solution) in the presence of 18 μM valinomycin at room temperature. [ADP]= 300 μM, [P_i]= 5 mM, [lipid]= 0.022 mg/ml, [EF₀F₁]= 0.6 nM, 1.9 nM, 3.8 nM, 7.5 nM [bR]= 88 nM, ΔΨ= 143 mV. Proteins were reconstituted with 0.8 % Triton.

Besides changing the concentration, the co-reconstitution was performed as described in chapter 3.4.2 and lipid as well as bR concentration were kept constant. Highest activity could be observed for 147 nM EF₀F₁ (Figure 4.18), which corresponds to a theoretical number of 1-2 ATP synthase molecules per liposome.

Similar results were earlier observed by Fischer et al. (45) for the sole reconstitution of EF₀F₁ ATP synthase. Fischer tested EF₀F₁ concentrations from 10 nM to 640 nM with the result that the activity was decreasing continuously with concentrations lower or higher than 100 nM. The explanation was that with higher concentrations of EF₀F₁ the reconstitution efficiency was drastically decreasing. This finding was underlined by cryo-electron microscopy measurements with the CF₀F₁ ATP synthase from chloroplasts by Böttcher et al. (92). Pitard and colleagues (25) made the observation that no ATP synthesis could be detected for TF₀F₁ concentrations higher than 200 μg/ml and that below this concentration ATP synthesis increased with decreasing protein content. Highest activity was observed for 1-2 ATP synthase complexes/liposome of 150 nm diameter which is in good agreement with the results made in this study.

Pitard explained this outcome by an increase of permeability with increasing TF_0F_1 concentrations, which was settled by the observation that the extent of light-induced pH gradient generated by bR was also decreasing with increasing ATP synthase content.

4.3.1.4 Influence of the light source on the ATP synthesis rate

Regarding the coupling of the energy module to the multistimuli responsive unit for self-positioning described later on (chapter 4.5.1), the range of applicable wavelength for excitation of bR was determined. In this context, three different light sources were studied in respect to ATP synthesis (Figure 4.19). A 15 W white light source (15 W LED), a 50 W red light source (50 W LED) and a 50 W green light source (50 W LED) were used to activate bR proton pumping in the same batch of proteoliposomes (Figure 4.19).

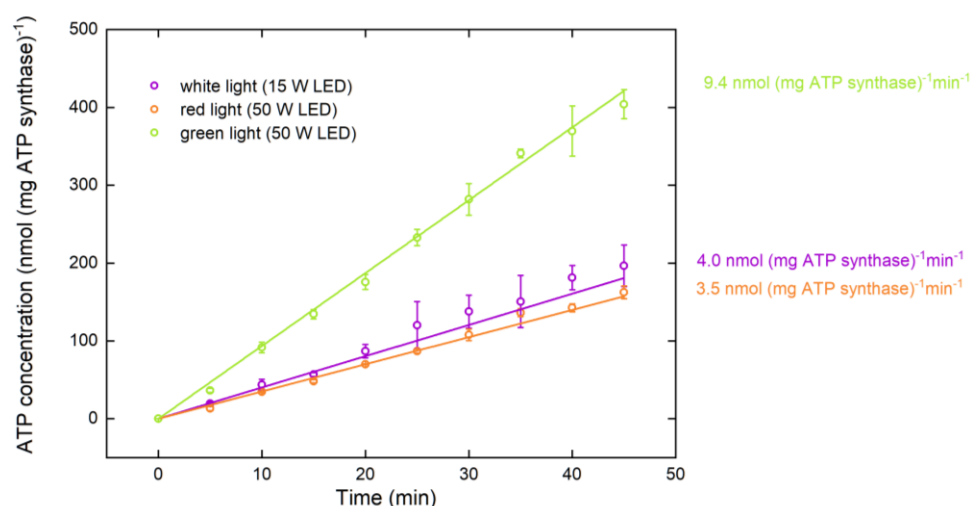


Figure 4.19 Influence of different light sources on the ATP production rate.

Light in the area of 500-650 nm (green light) was optimal to activate proton pumping in bR and leads to higher ATP production rates. The activity was determined by linear regression. Measurements were performed in 20 mM tricine-NaOH, 20 mM succinate, 0.6 mM KCl, 80 mM NaCl (inner solution) and 200 mM tricine-NaOH, 5 mM NaH_2PO_4 , 160 mM KOH, pH 8.8 (outer solution) in the presence of 18 μM valinomycin at room temperature. $[\text{ADP}] = 300 \mu\text{M}$, $[\text{P}_i] = 5 \text{ mM}$, $[\text{lipid}] = 0.022 \text{ mg/ml}$, $[\text{EF}_0\text{F}_1] = 1.3 \text{ nM}$, $[\text{bR}] = 88 \text{ nM}$, $\Delta\psi = 143 \text{ mV}$. Proteins were reconstituted with 0.8 % Triton. All error bars represent the standard error of the mean ($n=3$).

As expected, the results show highest ATP synthesis rates for illumination with a 50 W green LED lamp. Bacteriorhodopsin is purple and therefore most efficient absorbing green light (500-650 nm) with an absorption maximum of 568 nm. As bR has a broad excitation spectrum (94), proton pumping and ATP synthesis are also possible using white light or red light for excitation. In the case of white light, a loss of 57 % of performance can be observed, which is probably related to the

4 Results and Discussion

lower power of the light source (15 W vs. 50 W). The red LED lamp in contrast, has the same power as the green LED lamp (50 W). Anyway, even lower synthesis rates compared to the white light were detected. In this case the loss in activity of 63% compared to green light, can be explained by the suboptimal wavelength of the light (~800 nm).

4.3.1.5 Influence of valinomycin on the ATP production rate

The influence of the ionophore valinomycin on the ATP production rate is shown in Figure 4.20 A. Results indicate that valinomycin has a negative impact on the ATP production rate with activity losses of around 72%. In the first view this outcome might be surprising as valinomycin increased the rates of ATP synthase reconstituted alone (4.1.2.2) as well as the bR proton pumping rates (4.2.2.2). Anyway, in contrast to these experiments, valinomycin leads to uncoupling of the electrochemical potential $\Delta\mu_{\text{H}}$ in the co-reconstituted system. The presence of valinomycin eliminates the contribution of the electrical potential $\Delta\psi$ to the synthesis of ATP. This influence is schematically shown in Figure 4.20 D. In the absence of valinomycin bR pumps protons to the inside, resulting in an electrical potential $\Delta\psi$ caused by the unequal distribution of protons on either side of the membrane. This electrical potential contributes to the synthesis of ATP. As the protons are used by ATP synthase to produce ATP, no inhibitory effect of $\Delta\psi$ on proton pumping can be observed. Therefore, ATP production is higher in the absence of valinomycin. This result is in good agreement with the results earlier made by Pitard et al. (26). Pitard reported that in the absence of valinomycin a transmembrane electrical potential is present that contributes to the yield of ATP synthesis.

Valinomycin enables the selective transport of K^+ ions over the membrane and has therefore a critical effect on the membrane potential. To understand this effect in more detail, measurements with different concentrations of K^+ in the absence and presence of valinomycin were performed (Figure 4.20 B, C). The results indicate a negative effect of high K^+ concentrations on the ATP production rate. This effect is more relevant in the presence of valinomycin than in the absence. Higher K^+ concentrations in the presence of valinomycin causing faster equilibration of $\Delta\psi$ compared to lower K^+ concentrations. In the absence of valinomycin, higher ATP production rates can also be observed using low K^+ concentrations. This might be explained by the fact that $\Delta\psi$ breaks down slower in the presence of high concentrations of K^+ .

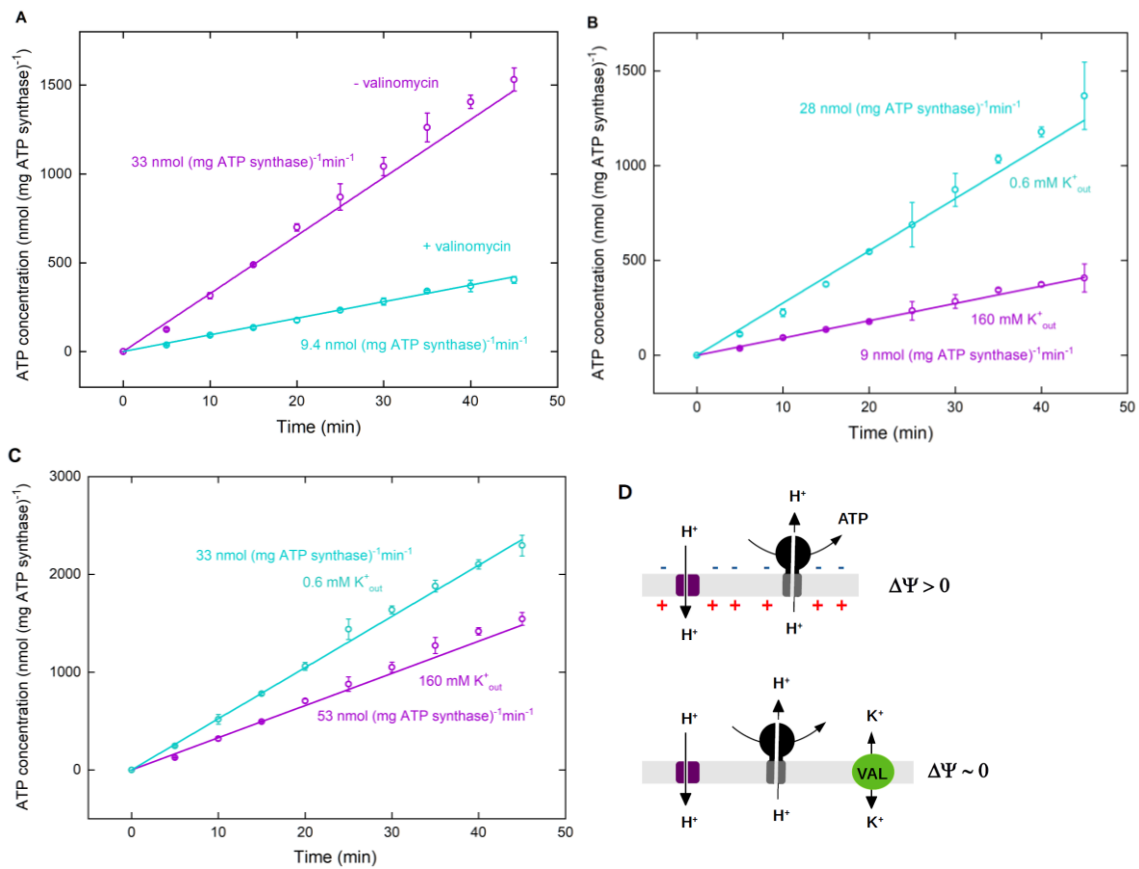


Figure 4.20 Influence of valinomycin and different K⁺ concentrations on the ATP production rate.

(A) ATP production with and without valinomycin. (B) ATP production with different K⁺ concentrations outside the vesicle in the presence of valinomycin (B) and in the absence of valinomycin (C). The activity was determined by linear regression. Measurements were performed in 20 mM tricine-NaOH, 20 mM succinate, 0.6 mM KCl, 80 mM NaCl (inner solution) and 200 mM Tricine-NaOH, 5 mM NaH₂PO₄, 160 mM KOH or 0.6 mM KOH, pH 8.8 (outer solution) at room temperature. [ADP]= 300 μM, [P_i]= 5 mM, [lipid]= 0.022 mg/ml, [EF_oF₁]= 1.3 nM, [bR]= 88 nM, ΔΨ= 0 mV or 143 mV. Proteins were reconstituted with 0.8 % Triton. All error bars represent the standard error of the mean (n=3). (D) Schematically presentation of the influence of valinomycin on the membrane potential in the co-reconstituted system.

4.3.1.6 Influence of the ADP concentration on the ATP production rate

The influence of the substrate concentration on the activity of an enzyme is well known and can be described by the Michaelis-Menten kinetic. The reaction velocity is increasing with increasing substrate concentration till all enzymes are occupied with the substrate and a constant velocity (v_{max}) is reached (94).

4 Results and Discussion

The production of ATP by the ATP module depends on two substrates (and $\Delta\mu_H$): phosphate (P_i) and ADP. As P_i was present in excess (5 mM), the kinetic of ATP production was mainly dependant on the ADP concentration when keeping $\Delta\mu_H$ constant. This dependency is exemplary shown for ADP concentrations of 73 μM and 512 μM (Figure 4.21).

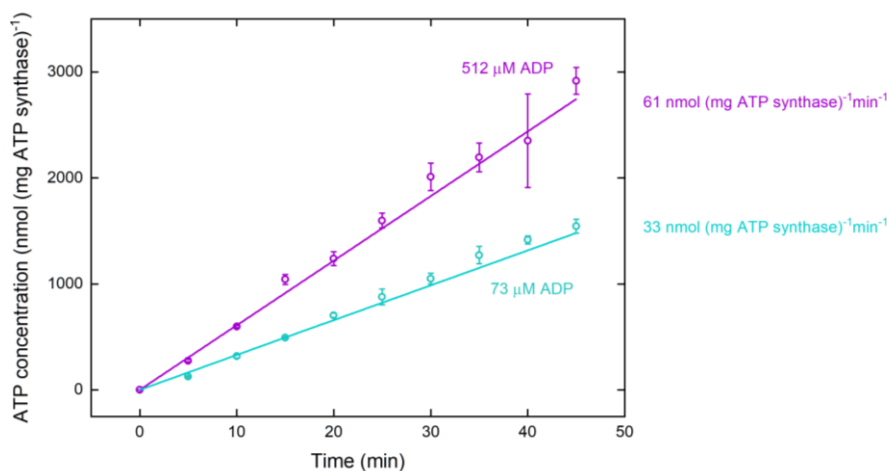


Figure 4.21 Influence of the ADP concentration on the ATP production rate.

The rates are increasing with increasing ADP concentration. The saturation point couldn't be reached due to the limited concentration of ultra pure ADP stock solution. The activity was determined by linear regression. Measurements were performed in 20 mM tricine-NaOH, 20 mM succinate, 0.6 mM KCl, 80 mM NaCl (inner solution) and 200 mM tricine-NaOH, 5 mM NaH_2PO_4 , 160 mM KOH, pH 8.8 (outer solution) at room temperature. $[P_i]=5\text{ mM}$, $[\text{lipid}]=0.022\text{ mg/ml}$, $[\text{EF}_0\text{F}_1]=1.3\text{ nM}$, $[\text{bR}]=88\text{ nM}$, $\Delta\psi=143\text{ mV}$. Proteins were reconstituted with 0.8 % Triton. All error bars represent the standard error of the mean ($n=3$)

As expected, higher ADP concentration led to higher ATP production. The rate for 512 μM ADP is approximately double as high as the rate for 73 μM ADP, but the ADP concentration is indeed seven times higher. This reflects the well-known theory of nonlinear dependency between production rate and substrate concentration expected for enzyme kinetics. Probably, the ADP concentration chosen here is close to saturating conditions, so that the reaction velocity is only changing slightly when increasing substrate concentration.

Additional measurements with various ADP concentrations have been conducted using ADP salt. Unfortunately, the high contamination of the salt with ATP led to falsified results, as high ATP concentrations inhibit the enzyme. Therefore, all further measurements were strictly conducted using an ultra-pure ADP solution. Due to the limited concentration of the stock solution (10 mM) and due to cost reason, only two different ADP concentrations were tested. As the kinetic

parameters of ATP synthase depending on the ADP concentration were studied several times in the past (45; 48; 25), no further attention was set on the investigation of ADP dependency.

4.3.1.7 Influence of the liposome preparation method on the ATP synthesis rate

The ATP production rate of the energy module also depends on the liposome preparation method as proven by the results illustrated in Figure 4.22. Dialysis liposomes have been reported by Fischer et al. (45) to be the optimal choice for maximal ATP synthesis in acid/base transition experiments when ATP synthase is reconstituted alone. For bR proton pumping experiments vesicles had to be prepared freshly by film hydration in the presence of pyranine. Therefore, ATP synthesis rates in liposomes prepared by dialysis and by extrusion method were compared.

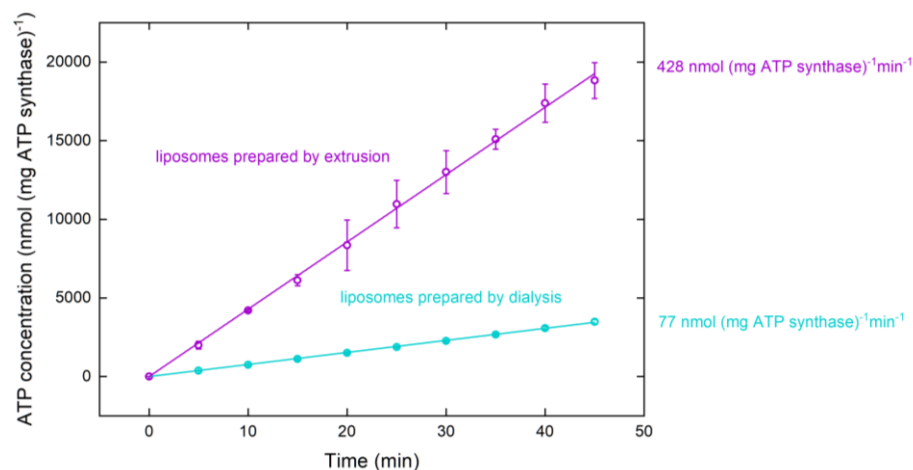


Figure 4.22 Influence of the liposome preparation method on the ATP production rate.

Fresh prepared PC liposomes yield by extrusion show much higher ATP synthesis rates compared to liposomes (PC/PA mixture) yield by dialysis. The activity was determined by linear regression. Measurements in dialysis liposomes were performed in 20 mM Tricine-NaOH, 20 mM succinate, 0.6 mM KCl, 80 mM NaCl (inner solution) and 10 mM Tris-HCl, 5 mM NaH₂PO₄, 50 mM KCl, 2 MgCl₂, 1 mM DTT, pH 7.5 (outer solution) at room temperature. Measurements in extrusion vesicles were performed in 20 mM HEPES, 25 mM MgCl₂, 50 mg/ml sucrose, pH 7.5 (inner solution) and 10 mM Tris-HCl, 5 mM NaH₂PO₄, 50 mM KCl, 2 MgCl₂, 1 mM DTT, pH 7.5 (outer solution) at room temperature. [ADP]= 360 μM, [P_i]= 5 mM, [lipid]= 0.022 mg/ml, [EF₀F₁]= 1.3 nM, [bR]= 88 nM. Proteins were reconstituted with 0.8 % Triton. All error bars represent the standard error of the mean (n=3).

Dialysis liposomes were prepared as described in chapter 3.2.5 with a mixture of phosphatidylcholine (PC) and phosphatic acid (PA). Extrusion vesicles in contrast, were exclusively prepared by PC lipids (95%) (3.3.5).

The recorded ATP production curves clearly indicate higher rates in fresh prepared extrusion vesicles (Figure 4.22). Only ~20% of activity is measurable in dialysis liposomes. The most probable

4 Results and Discussion

explanation for this outcome is, that dialysis liposomes were frozen and stored before usage while extrusion vesicles were prepared freshly. Freezing and unfreezing might lead to degradation of lipids. Another possible explanation would be a negative influence on the ATP rates caused by the phosphatic acid present in dialysis liposomes. Anyway, this is unlikely as phosphatic acid is natural component of the membrane and promote amongst others membrane curvature (95).

Another probable reason for higher activities in film hydration vesicles, might be the usage of different buffer systems. While dialysis vesicles were prepared in Tricine buffer (Table A.18), extrusion vesicles were prepared in HEPES buffer (Table A.25).

To sum up, many factors are changing in both vesicle preparation method. Anyway, extrusion vesicles are working better and were therefore used for all following experiments in order to maximize ATP production rates.

4.3.1.8 Influence of different buffers on the ATP synthesis rates

According to the literature (48) the optimal buffer for ATP synthase reconstituted alone, is Tricine buffer (pH 8.8) However, in order to combine the ATP module with other functional modules, it had to be proven that ATP synthase activity was preserved under different buffer conditions.

To combine the ATP module with the actin-myosin system at the MPI Martinsried, Tris-HCl buffer (actin-myosin buffer) at pH 7.5 and pH 8 was tested for ATP synthesis (Figure 4.23). Surprisingly, even higher rates were detected using this buffer. The assumption that higher rates could be traced back to fact that this buffer was supplemented with Dithiothreitol (DTT) could be proven by ATP synthesis measurement in Tris-HCl buffer without DTT. DTT conserves proteins in their functional form as it prevents the oxidation of sulfhydryl groups (SH-) to disulfide-bonds in the presence of air oxygen. All measurements were performed using the same fraction of ATP synthase and bacteriorhodopsin in exactly the same concentration. Due to this result all following measurements were performed in Tris-HCl buffer (pH 7.5) supplemented with 1 mM DTT.

The module was also tested in the following other buffer systems:

- LI buffer (Table A.21)
- HMDEK buffer (Table A.33)
- Measurement buffer (Table A.26) supplemented with 10 mg/ml polyvinyl alcohol
- MOPS buffer (Table A.35)
- HEPES buffer (Table A.25)

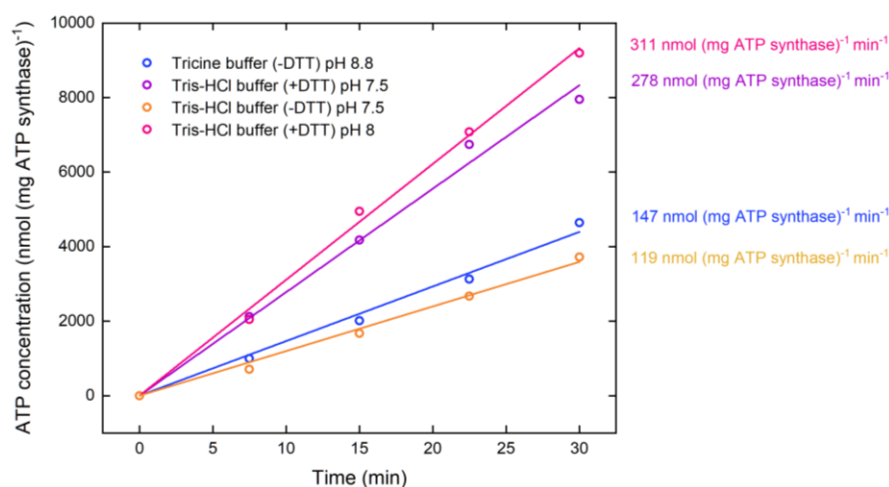


Figure 4.23 Influence of different buffers on the ATP production rates.

Highest rates were obtained in Tris-HCl buffer (pH 7.5) supplemented with Dithiothreitol (DTT). DTT conserves proteins in their functional form as it prevents oxidation of sulfhydryl groups (SH-) to disulfide-bonds in the presence of air oxygen. The activity was determined by linear regression. Measurements were performed with [ADP]= 300 μ M, [P_i]= 5 mM, [lipid]= 0.022 mg/ml, [EF_oF₁]= 1.3 nM, [bR]= 88 nM and $\Delta\Psi$ = 143 mV at room temperature. Proteins were reconstituted with 0.8 % Triton.

The general observation could be made that the ATP module was working in each tested buffer with fairly high activity (data not shown). This outcome is especially important in respect to bottom-up assembly of different modules to functional systems. The robustness in respect to the buffer solution makes the light-driven ATP module an attractive choice as energy supply unit.

4.3.1.9 Freezing and storing of the ATP module

Freezing and storing of the ATP module is a very important point to consider when planning to couple it to other functional parts or modules. In particular, the transport of the module to other MPI institutions and the fact that our cooperation partners couldn't always use the samples instantly, initiated the investigation about activity loss during freezing and storing.

Figure 4.24 shows the activity of the ATP module before freezing as well as after freezing and 1 day, 1 week and 2 weeks of storing at -80 °C. As expected, highest rates were obtained before freezing, but freezing only led to activity losses less than 10%. After two weeks of storing around 70% activity remains. Overall, the loss in activity is fairly small.

This finding allowed the preparation and characterization of bigger amounts of EF_oF₁-bR liposomes in our labs and the subsequently shipping to our cooperation partners in Mainz and Göttingen.

4 Results and Discussion

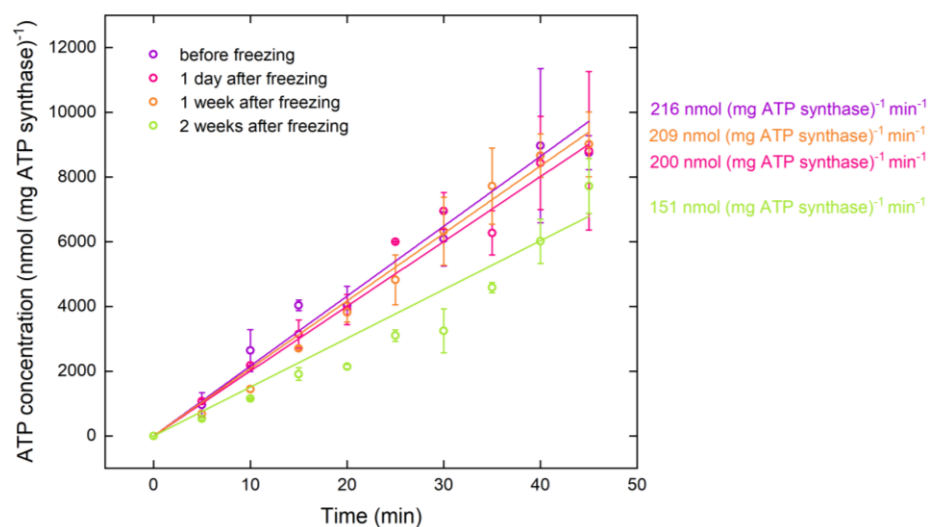


Figure 4.24 Freezing and storing of the ATP module leads to little losses in activity.

The duration of storing at -80°C has impact on the functionality of the enzymes and therefore the ATP production rate. The activity was determined by linear regression. Measurements were performed in 20 mM HEPES, 25 mM MgCl_2 , 50 mg/ml sucrose, pH 7.5 (inner solution) and 10 mM Tris-HCl, 5 mM NaH_2PO_4 , 50 mM KCl, 2 MgCl_2 , 1 mM DTT, pH 7.5 (outer solution) at room temperature. $[\text{ADP}] = 360 \mu\text{M}$, $[\text{P}_i] = 5 \text{ mM}$, $[\text{lipid}] = 0.022 \text{ mg/ml}$, $[\text{EF}_0\text{F}_1] = 1.3 \text{ nM}$, $[\text{bR}] = 88 \text{ nM}$. Proteins were reconstituted with 0.8 % Triton. All error bars represent the standard error of the mean ($n=3$).

4.3.2 The ATP module in lipid, polymer and hybrid vesicles with solubilized bR

In the framework of bottom-up synthetic biology, new exciting possibilities for the combination of natural and synthetic based materials arise. In this regard, Choi and Montemagno (30) reported the first successful incorporation of bacteriorhodopsin (bR) and ATP synthase from *thermophilic Bacillus* PS3 (TF_0F_1) into polymersomes consisting of ABA triblock copolymers. Since then the interest in protein reconstitution into polymer-based membranes increased.

According to the literature, one major benefit of polymersomes, compared to natural liposomes, is their enhanced functional durability (96). Here, the high mechanical stability and low proton permeability of polymersomes can be viewed as a positive factor, but also as a limiting feature in some applications where controlled permeation of species is required. A very promising method has recently emerged to overcome intrinsic limitations of both, polymersomes and liposomes. The proposed approach employs mixed hybrid vesicles from copolymers and lipids, enabling fine-tuning of the membrane physical properties (97; 98). A recent example demonstrated the

functional incorporation of cytochrome bo_3 quinol oxidase (bo_3 oxidase) in such hybrid vesicles, consisting of diblock copolymer polybutadiene-*b*-poly(ethylene oxide) (PBd-PEO) and 1-palmitoyl-2-oleoyl-*sn*-glycero-3-phosphocholine (POPC) (96). This combination resulted in a better biocompatibility of the hybrid membranes, compared to pure polymer membranes, alongside a remarkable enhancement in functional lifetime of the enzyme (96). In other work, Jacobs et al. (99) showed an increased folding of a mechanosensitive channel protein during cell-free expression in PBd-PEO hybrid vesicles compared to pure liposomes.

It is known that a key parameter for the functionality of transmembrane proteins is the lateral mobility within the membrane, which largely depends on its flexibility and fluidity (100). Therefore, another graft copolymer poly(dimethylsiloxane)-graft-poly(ethylene oxide) (PDMS-*g*-PEO) with higher fluidity (101) and lower core thickness (102) has been recently suggested for co-assembly of F_0F_1 -ATP synthase and bo_3 oxidase in hybrid vesicles (103). The functional incorporation of both enzymes in these hybrid vesicles has been demonstrated, but the functional durability has not been tested yet.

In the present work, light-driven ATP regeneration has been studied in hybrid vesicles based on two different kinds of polymers, diblock copolymer PBd-PEO and grafted polymer PDMS-*g*-PEO as schematically shown in Figure 4.25. The influence of membrane composition on the performance, proton permeability, reconstitution efficiency, long-term stability and orientation of proteins in the membrane was investigated (104).

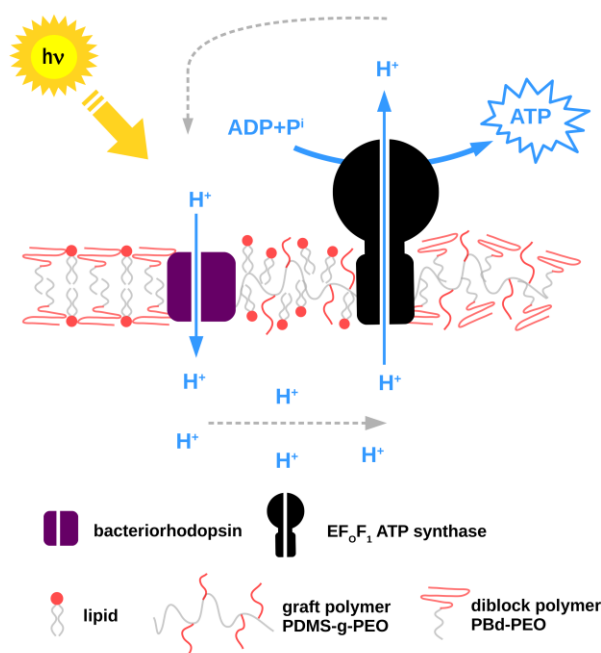


Figure 4.25 Schematic presentation of light-driven ATP production in lipid, polymer and hybrid vesicles.

4.3.2.1 Membrane composition

To study the influence of hybrid membranes on the performance of the ATP regeneration system, four different kinds of vesicles were analysed (schematically shown in Figure 4.26). Pure soy PC vesicles (100/0 PC) were used as a benchmark for enzyme activity in other compartments. The other three types of vesicles are hybrid vesicles made of PC lipids (Figure 4.26 B) and two types of polymers with different fluidities and structure: comb-type siloxane surfactant, poly(dimethyl siloxane)-g-poly(ethylene oxide) (PDMS-g-PEO) (103), and diblock copolymer, polybutadiene-b-poly(ethylene oxide) (PBd-PEO) (96; 97; 98; 105) (Figure 4.26 C, D). Both polymers have the same hydrophilic block (PEO), while the hydrophobic block as well as the polymer architecture differs. PDMS-g-PEO (denoted as PDMS afterwards) is known to form vesicular structures with a membrane thickness of around 5 nm, close to that of natural lipid membranes. This grafted copolymer self-assembles into monolayers, flexible enough to incorporate complex membrane proteins (31) and forms well-mixed membranes above 70 mol % polymer. Therefore, hybrids made of 70 mol % polymer (70/30 PDMS/PC) were investigated in this study.

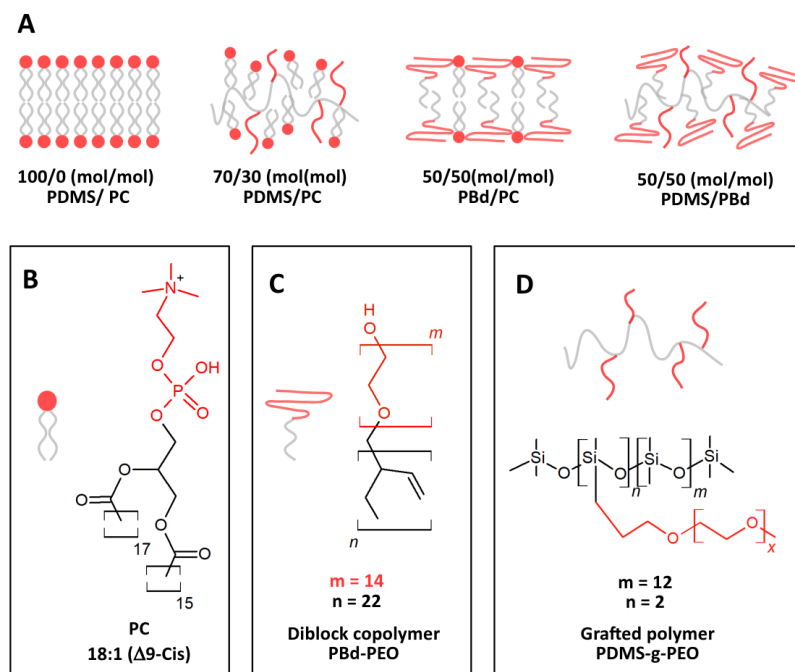


Figure 4.26 Schematic presentation of different membrane compositions used for co-reconstitution with solubilized bR.

(A) Membrane compositions of pure PC vesicles (0/100 PDMS/PC), hybrid vesicles made of 70 mol % PDMS-g-PEO (70/30 PDMS/PC), 50 mol % PBd-PEO (50/50 PBd/PC) as well as a mixture of 50 mol % PDMS-g-PEO and 50 mol % PBd-PEO (50/50 PDMS/PBd). Scheme of the nanoscale structure of phosphatidylcholine (B), diblock polymer PBd-PEO (C) and grafted polymer PDMS-g-PEO (D).

PBd-PEO (denoted as PBd afterwards) in contrast, is a diblock copolymer that self-assembles into bilayers. The 1.8 kDa polymer PBd₂₂-b-PEO₁₄ was chosen in this work as these polymer chains are expected to have similar membrane thickness as lipid vesicles, estimated ~4 -5 nm, thereby minimizing the hydrophobic mismatch between polymer and lipid (99). PBd polymer with higher molecular size, as for example PBd₃₇-PEO₂₂, forms membranes with increased thickness and the mismatch between lipid and polymer thickness presumably results in lower biocompatibility of hybrid vesicles. PBd is known to form homogeneous, well-mixed hybrid vesicles with POPC within the whole range of compositions (106). Hybrid vesicles made of 50 mol % polymer (50/50 PBd/PC) were investigated in this study as this composition has been shown to be the best with inserted bo₃ oxidase (96; 105).

Hybrid vesicles made of PDMS-g-PEO and PBd-PEO form well-mixed vesicles, bearing the strength and toughness characteristics of pure PBd-PEO vesicles as recently shown by Gaspard et al. (107). As both polymers have different membrane permeabilities and fluidities, a combination of both

4 Results and Discussion

may allow for systematic, application-specific tuning of membrane fluidity and permeability. The functional reconstitution of proteins in hybrid membranes made of these two polymers could offer new possibilities for the design of nanoreactors, biosensors or artificial organelles. In this respect, the fourth vesicle system was based on a mixture of 50 mol % PDMS and 50 mol % PBd (50/50 PDMS/PBd) (104).

4.3.2.2 Reconstitution procedure

For insertion of transmembrane proteins in hybrid compartments, Triton X-100 was used as detergent according to the measurements described above for the reconstitution into liposomes. Hybrids were prepared by film rehydration method, followed by extrusion through 100 nm pores. The size distribution profiles after extrusion as measured by Dynamic Light Scattering (DLS) (Figure 4.27 A) are indicating that all vesicles are uniform in size with an average diameter of 141 nm for 100/0 PC, 116 nm for 70/30 PDMS/PC, 136 nm for PBd/PC and 121 nm for 50/50 PDMS/PBd.

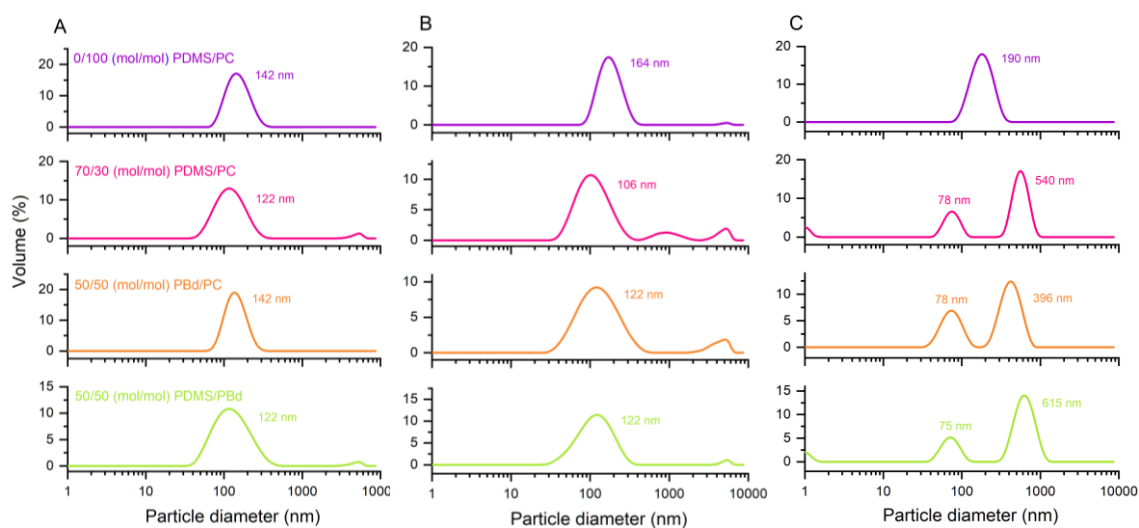


Figure 4.27 Size distribution of vesicles made of 0/100 PDMS/PC, 70/30 PDMS/PC, 50/50 PBd/PC and 50/50 PDMS/PBd.

(A) Sizes of vesicles after extrusion through 100 nm pores. (B) Size distribution of detergent-treated vesicles prior to reconstitution. (C) Sizes of vesicles after reconstitution and removal of detergent using bio beads.

Turbidity profiles for each membrane composition were taken (Figure 4.28) to determine the amount of Triton necessary for partial solubilization of lipid and hybrid vesicles. The destabilization point at the onset of solubilization was chosen, even though optimal protein

performance for Triton mediated reconstitution has been earlier reported for the intermediate step of total solubilization (25; 108). This has been done to account for additional detergent brought in the reconstitution mixture by Triton solubilized bR, which was slightly higher as reported by Pitard et al. (25).

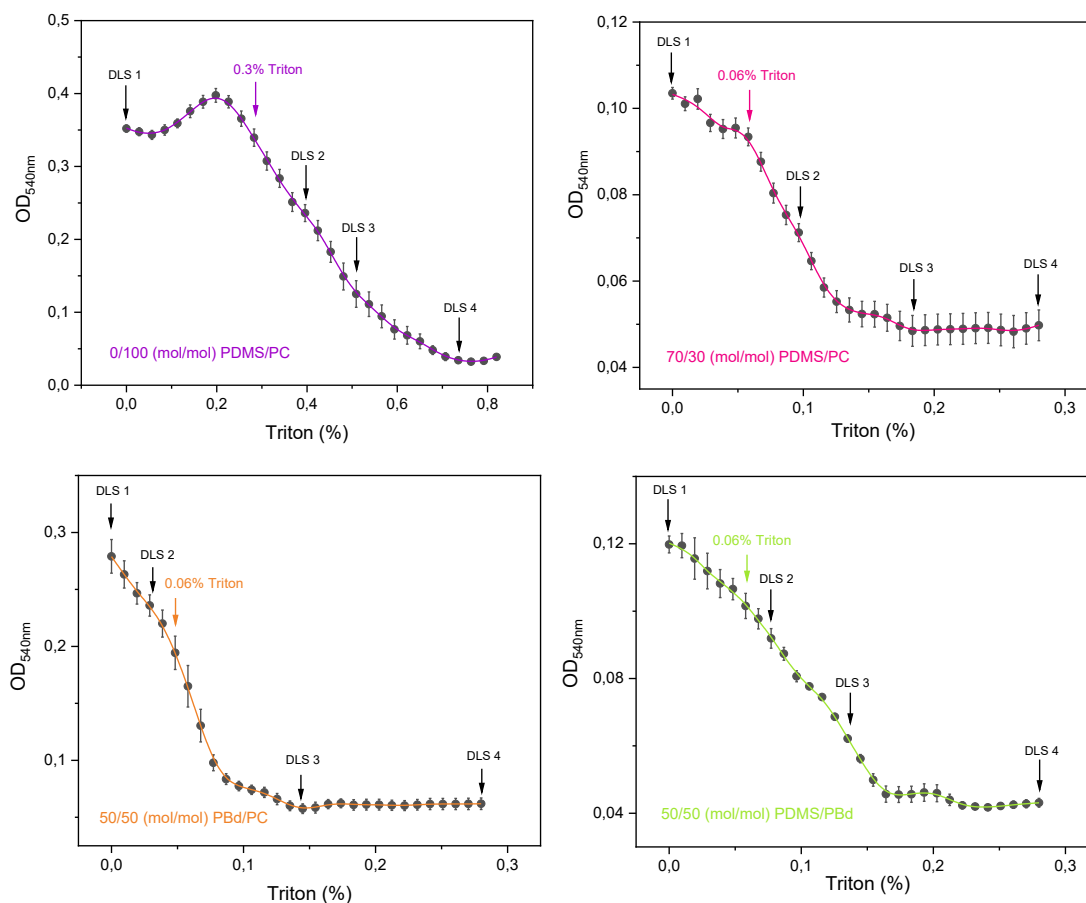


Figure 4.28 Detergent destabilization profiles for vesicles made of 0/100 PDMS/PC, 70/30 PDMS/PC, 50/50 PBd/PC and 50/50 PDMS/PBd.

Plots show the change in absorption at 540 nm upon addition of several amounts of Triton X-100. The destabilization points with the corresponding amount of Triton chosen for reconstitution are indicated with colourful arrows. DLS measurements have been performed at several points of destabilization marked as DLS1-4 and are shown in Figure 4.29.

PC liposomes were solubilized with 0.3% Triton X-100, while all hybrid vesicles were solubilized with remarkably lower Triton X-100 concentration of 0.06%. DLS data after treatment with detergent were taken prior to reconstitution (Figure 4.27 B) and indicated that vesicles remain intact and are existent as detergent-saturated membranes. ATP synthase and bR were added to the vesicles as detergent-solubilized monomeric proteins aiming to a theoretical protein-per-liposome

4 Results and Discussion

ratio of approximately 1 ATP synthase and 28 bR molecules. After 1h incubation in the dark, the detergent was removed by addition of bio beads. The amount of bio beads has been chosen in a way to allow for rapid detergent removal and thus to avoid self-aggregation of ATP synthase.

DLS data after detergent treatment evidenced that all vesicles remained intact and were existent as detergent-saturated membranes (onset of solubilization). In contrast, significant differences between lipid and hybrid vesicles were obtained after removal of detergent using bio beads (Figure 4.27 C). Liposomes remained their original size while all hybrid vesicles seem to split in two distinct fractions of different size (~75 nm and 400–600 nm). Even though all vesicles were treated in the same way with bio beads, hybrid vesicles seem to behave differently. This might be explained by the slow, viscous dynamics of the polymers which might influence vesicles formation during detergent removal (96). Khan et al. (96) showed comparable DLS data after reconstitution of bo₃ oxidase in 50/50 PBd/PC and 75 PBd/PC. DLS data in their study also indicated two distinct fractions, but with comparably smaller molecular size (~10 nm and ~100 nm). Cryo-TEM images of 50/50 PBd/PC in contrast evidenced large worm-like micelles of several microns' length coexisting with the vesicles. In general, DLS data from highly non-spherical particles needs to be interpreted carefully and cryo-TEM images should be taken in the future to investigate hybrid vesicle formation during reconstitution (104).

Interestingly, the splitting in two fractions upon detergent removal has no big impact on the global ATP production rates as shown in the next chapter by the performance of the ATP module in different membranes. In the present study, both populations of bigger and smaller sized vesicles were used for further measurements without separation. It might be possible that even higher rates are attainable if these two fractions would be separated. Unlike lipid-detergent interactions, detergent-polymer interactions are currently not well understood (109) and measurements are necessary to clarify differences between lipid and polymer. The molecular understanding of these interplays will enable adjustment of reconstitution procedures in an appropriate way.

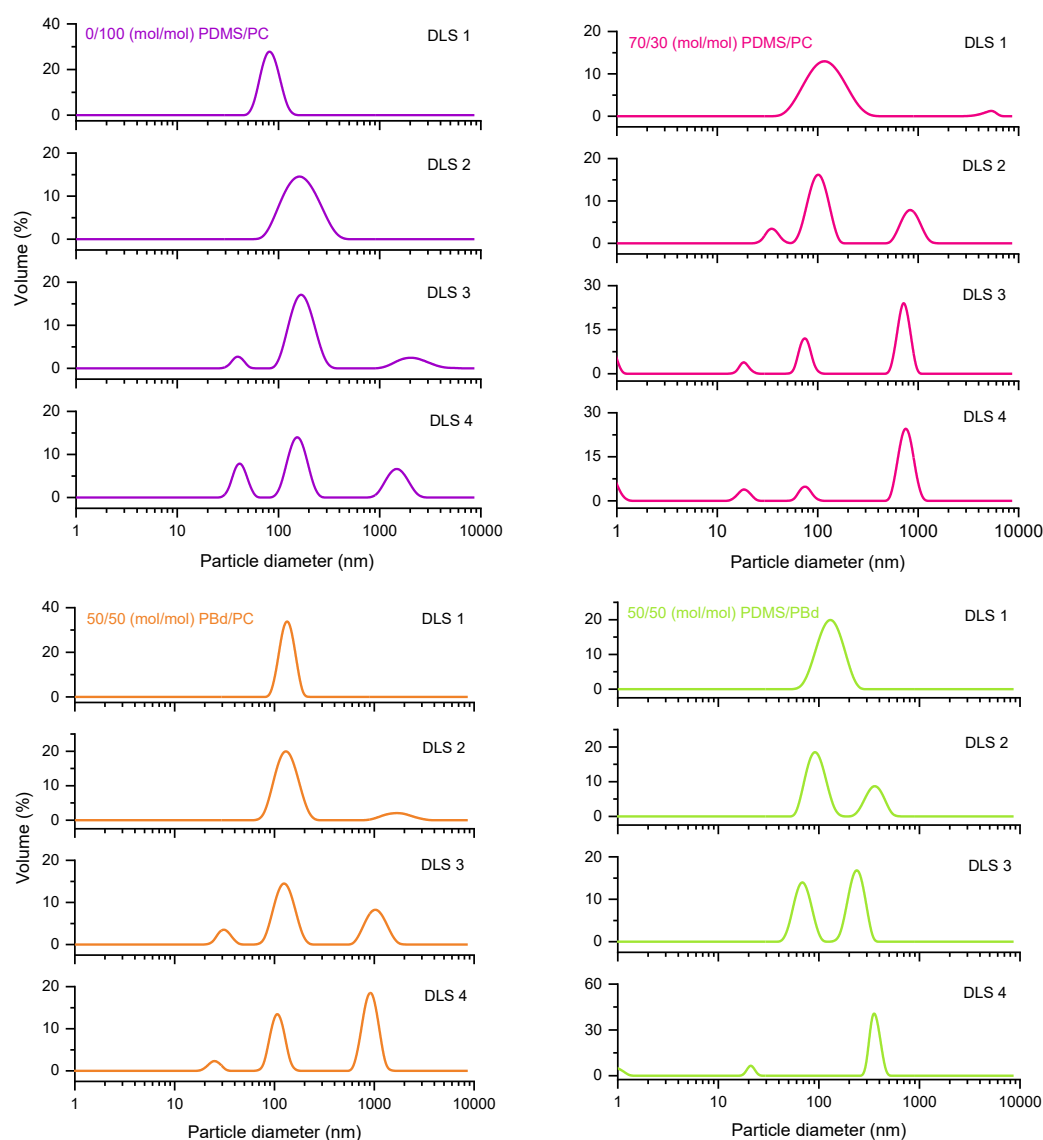


Figure 4.29 Size distribution of hybrid vesicles made of 0/100 PDMS/PC, 70/30 PDMS/PC, 50/50 PBd/PC and 50/50 PDMS/PBd.

Plots show vesicle size distribution at different points of destabilization (DLS 1-4 in Figure 4.28).

4.3.2.3 Performance

Light-driven ATP production in hybrid vesicles was quantified using the luciferin-luciferase assay as described above and the activity was compared with the activity in pure lipid vesicles (Figure 4.30). The results show a fairly small reduction in activity for 70/30 PDMS/PC (98% activity) and 50/50 PBd/PC (92% activity), but more considerable reduction in activity for 50/50 PDMS/PBd hybrids (54% activity). The lower activity of the system in 50/50 PDMS/PBd hybrids can be

4 Results and Discussion

explained by the fact that bio-functional lipids are missing in this composition. In general protein activity has been shown to decrease with decreasing lipid content (103; 96).

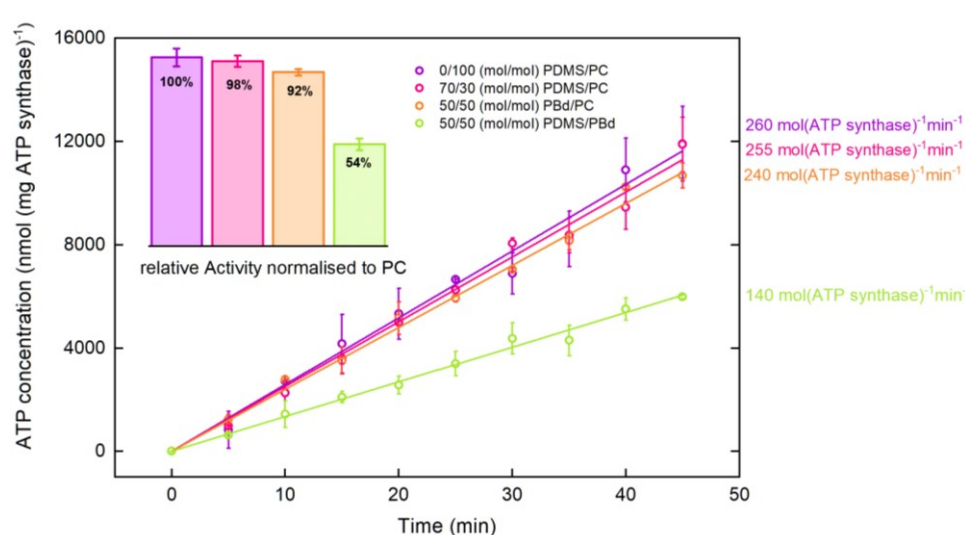


Figure 4.30 Light-driven ATP synthesis in lipid and hybrid vesicles using solubilized bR for co-reconstitution.

The activity was determined by linear regression. The inset bars show the activity normalized to pure PC liposomes. Measurements were performed in 20 mM HEPES, 25 mM MgCl₂, 50 mg/ml sucrose, pH 7.5 (inner solution) and 10 mM Tris-HCl, 5 mM NaH₂PO₄, 50 mM KCl, 2 MgCl₂, 1 mM DTT, pH 7.5 (outer solution) at room temperature. [ADP]= 360 μM, [P_i]= 5 mM, [lipid]= 0.022 mg/ml, [E_{F₀F₁}]= 1.3 nM, [bR]= 37 nM. Proteins are reconstituted with 0.3 % Triton (0/100 PDMS/PC) or 0.06% Triton (70/30 PDMS/PC, 50/50 PBd/PC, 50/50 PDMS/PBd). All error bars represent the standard error of the mean (n=3).

Previous work integrating bo₃ oxidase and ATP synthase in 70/30 PDMS/PC hybrids (103) confirmed bo₃ oxidase activities of 93% compared to liposomes, while the overall ATP production activity was around 56%. One reason for this comparably lower performance might be a deviant reconstitution procedure using octyl glucoside as detergent, since as mentioned above, octyl glucoside has been shown to inactivate ATP synthase (25; 26). Khan et al. (96) reached activities of around 80% when reconstituting bo₃ oxidase in hybrid vesicles made of 50% PBd. Choi et al. (30) reported absolute ATP production rates of 120 nmol (mg ATP synthase)⁻¹(min)⁻¹ when reconstituting TF₀F₁ ATP synthase and bR patches in ABA triblock polymersomes. Absolute ATP production rates governed here are slightly higher (255 ± 8 nmol (mg ATP synthase)⁻¹(min)⁻¹ for 70/30 PDMS/PC, 240 ± 5 for 50/50 PBd/PC and 140 ± 8 for 50/50 PDMS/PBd).

To quantify the effect of the membrane environment on the activity of both proteins in detail, future work should address limiting factors for ATP production as well as stoichiometric and substrate effects that have impact on the kinetic parameters of the enzyme (K_m and v_{max}).

As mentioned above a theoretical protein-per-vesicle ratio of approximately 1 ATP synthase (0.1 μM) and 28 bR molecules (2.9 μM) was chosen. Earlier studies (23; 25; 26) have shown that a 1:1 ATP synthase to bR ratio is not enough to drive ATP synthase efficiently. Figure 4.16 in chapter 4.3.1.1 represents the dependence of the ATP production rate on the concentration of bR. The results indicate that the ATP production is still limited by the amount of bR when using a protein-per-vesicle ratio of 1:28 (ATP synthase/bR). The functionality of bR is therefore relevant for the overall efficiency of the ATP production module. In this regard, the influence of different membrane compositions on the activity of bR reconstituted alone, in the absence of ATP synthase, was investigated.

4.3.2.4 bR reconstitution efficiency and proton pumping activity

For measurement of bR proton pumping activity in different compartments, PC liposomes and hybrid vesicles were prepared in the presence of 8-hydroxyprone-1,3,6-trisulfonic acid (pyranine), a pH-sensitive dye. bR was then reconstituted following the co-reconstitution method described above. After removal of detergent using bio beads, the vesicles were passed over a gel filtration column as explained in 4.2.2. The reconstitution efficiencies for each membrane composition were calculated using equation [3.12]. Results indicate highest reconstitution efficiency in liposomes (82%) and slightly lower reconstitution efficiency (71-78%) in hybrid vesicles (Figure 4.31 B). A significant difference (*) in reconstitution efficiency compared to liposomes is only indicated for 70/30 PDMS/PC and 50/50 PDMS/PBd hybrids.

Proton pumping rates of bR upon green light irradiation are shown in Figure 4.31 A. Calculation of the internal pH was performed using the calibration curve shown in chapter 4.2.2.1.

A rapid acidification during the initial seconds of illumination was followed by a negligibly small change in pH. This progressive decrease as the gradient is established can be attributed to the back-pressure effect of ΔpH (87). The maximal steady-state ΔpH (0.22) was found in pure PC lipid vesicles and remarkably lower values were detected in lipid/polymer-mix hybrid vesicles. One possible reason could be the presence of two populations of lipid/polymer-mix vesicles (Figure 4.27) compared to a single lipid vesicle population. It might be possible that these differences in proton pump activity are caused by vesicle size effects.

4 Results and Discussion

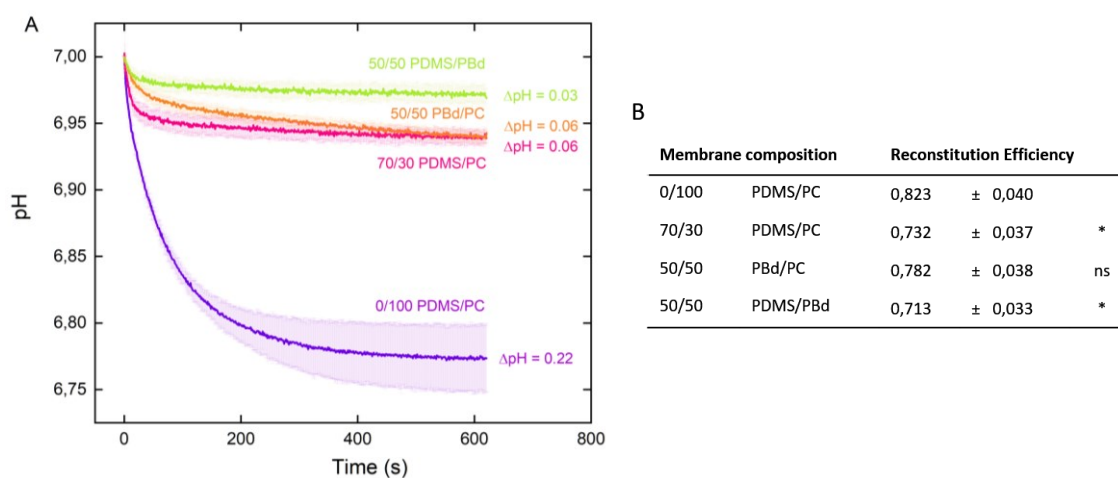


Figure 4.31 Proton pump activity of solubilized bR in liposomes and hybrid vesicles as measured by pH change upon green light irradiation.

pH change is detected by encapsulated pyranine. Measurements were performed in 10 mM HEPES, 100 mM K_2SO_4 , 15 mM $MgCl_2$ in the presence of 3 μM valinomycin at room temperature. Proteins were reconstituted with 0.3 % Triton (0/100 PDMS/PC) or 0.06% Triton (70/30 PDMS/PC, 50/50 PBd/PC, 50/50 PDMS/PBd). Error bars represent the standard error of the mean ($n=3$). The table shows the reconstitution efficiency of bR in different compartments. * $P \leq 0.05$, nonsignificant (ns) $P > 0.05$ (P values were generated by unequal variance t-test (Welch's test) for comparison of each hybrid membrane composition to the lipid vesicle sample).

The lowest steady-state ΔpH (0.03) was observed in 50/50 PDMS/PBd. The initial pumping rate in 70/30 PDMS/PC vesicles was higher compared to that in 50/50 PBd/PC vesicles, while the steady state ΔpH (0.06) remained unchanged. The investigation of pumping rates depending on the amount of pumping units (Figure 4.10) indicated a similar effect. Initial rates of proton pumping were increasing with the protein content, while the steady-state ΔpH stayed constant. The reason why the total proton uptake, in this case, remained unchanged, might be either explained by back-pressure effect of ΔpH or by passive proton permeability of the membrane (87). In the case of hybrid vesicles, results might indicate that more active pumping units were present in 70/30 PDMS/PC hybrids compared to 50/50 PBd/PC hybrids, but that back-pressure effects and passive proton permeability led to a similar steady state ΔpH . Another interpretation would be a slower turnover rate of bR in 50/50 PBd/PC hybrids due to the higher viscous environment. It has to be mentioned that the slope of the curve of 50/50 PBd/PC vesicles indicate that the actual steady-state ΔpH is not achieved after 600 s. Higher ΔpH might be reached if the experiment have been run for longer.

In contrast to the relative high performance of the co-reconstituted system in hybrid vesicles, the performance of bR in hybrid vesicles is comparably low. The steady-state ΔpH reached in 70/30

PDMS/PC and 50/50 PBd/PC remained only ~30% compared to liposomes. The steady-state ΔpH of 50/50 PDMS/PBd was with ~14% even lower.

According to Seigneuret et al. (87) light-induced proton uptake in bR liposomes is determined by three factors: the number of active pumps, the passive permeability of the membrane, and the back-pressure effects (potential gradient $\Delta\psi$ and pH gradient ΔpH) that inhibits proton pumping. Back-pressure effects caused by the build-up of charge (potential gradients $\Delta\psi$) are only relevant when the non-proton permeability of the membrane is low. These effects are overcome in the present case by the addition of valinomycin. Back-pressure effects caused by the proton gradient itself (concentration gradient ΔpH) are mainly influenced by the buffering capacity and should be constant for all membrane compositions. Therefore, discrepancies of ΔpH in different vesicles should be either explained by the number of active pumping units or by the passive proton permeability of the membrane (104).

In order to estimate the number of active pumping units, the orientation of bR in different membranes has been investigated and is presented in the next chapter.

4.3.2.5 bR orientation in different membranes

The orientation of bR in the membrane is one of the major factors that determines the protein pumping activity. While ATP synthase is mainly orientated with the hydrophilic head outwards (110), the orientation of bR is more random. bR orientation in different compartments was determined using a proteolytic digestion assay with a nonspecific serine protease (proteinase K, ProtK) similar to the approaches of Gerber (58) and Kalmbach (111) (Figure 4.32). When a membrane protein is reconstituted in a vesicle, the core of the protein is shielded by the membrane. Therefore, only hydrophilic parts of the protein that form loop regions are exposed to the solution.

In the case of properly folded and incorporated bR, only small parts are accessible to proteolysis. These cleavage sites are located asymmetrically on both sides of the membrane (82). Consequently, ProtK-induced cleavage on different sides of the membrane produced a distinct set of protein fragments (Figure 4.32 A). These fragments could be distinguished by SDS-PAGE analysis of digestion products (Figure 4.32 B). bR-containing samples that have not been exposed to ProtK show an intensive band at around 22 kDa (Figure 4.32 B, lane 7) due to gel shifting as explained in 4.2.2.

4 Results and Discussion

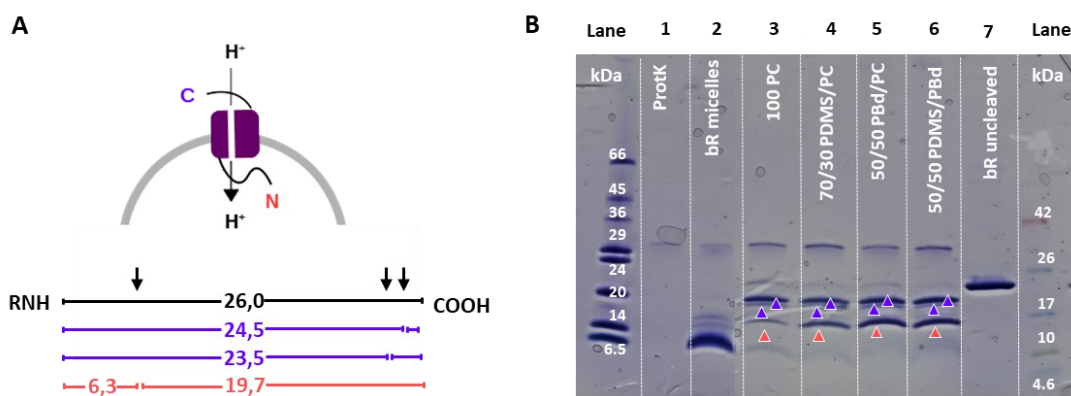


Figure 4.32 Proteolytic cleavage of reconstituted bR with proteinase K (ProtK) shows mixed orientation in all lipid and hybrid vesicles.

(A) Expected sizes of proteolytic fragments for ProtK digestion of bR when the N-terminal (orange values) or C-terminal (violet values) is exposed to the bulk solution (B) SDS PAGE gel analysis of the digestion products. Lane 1: band specific for ProtK enzyme only; lane 2: digestion product of not reconstituted bR; lanes 3-6: digest patterns for different lipid/hybrid vesicles containing solubilized bR; lane 7: undigested bR in lipid vesicles.

ProtK itself (Figure 4.32 B, lane 1) showed a single band at around 34 kDa. Not reconstituted bR in micelles (Figure 4.32 B, lane 2) after cleavage with ProtK revealed a set of digestion products between 5 and 16 kDa. In this case, a majority of small digestion products was expected as ProtK could access bR unrestricted when there is no membrane shielding. Digestion products of proteovesicles (Figure 4.32 B, lane 3-6) were found to be different to the digestion products of bR in micelles.

SDS PAGE showed 3 distinct bands for all membrane compositions at approximately 16, 19 and 21 kDa. The 16 kDa band (Figure 4.32 B, orange arrow) can, under the assumption of gel shifting, be related to the N-terminal protein fragments. The 19 and 21 kDa bands (Figure 4.32 B, violet arrows) in contrast, can be related to the C-terminal fragments with a theoretically supposed size of 23.5 and 24.5 kDa (58). These results prove that there is no uniform bR orientation in all vesicles. Anyway, a better orientation was indicated in 100/0 PC, as the band at 16 kDa (orange arrow) is lighter compared to that of hybrid vesicles.

The overall number of pumping units can be determined by taking the reconstitution efficiency and the orientation of bR in the membrane into account. Slightly lower reconstitution efficiencies were detected in hybrid vesicles (71–78%) compared to lipid vesicles (82%) and the bR digestion assay shown above strongly indicate that there is more bR correctly orientated in liposomes compared to hybrid vesicles. Anyway, the number of active bR molecules should only influence

initial pumping rates. Steady-state ΔpH values should be constant due to back-pressure effects of ΔpH .

When the conditions are met in a way that the non-proton permeability of the membrane is large (e.g. by addition of valinomycin), the establishment of steady-state ΔpH is to a certain extent determined by the passive proton-back leakage (87). Proton permeability of different membranes was determined and is described in the next chapter. The results show higher permeability for hybrid vesicles compared to liposomes and might explain comparably small steady-state ΔpH in bR-hybrid vesicles. In general, steady-state ΔpH is reached when pumping and leakage rates are identical.

Even though steady-state ΔpH values in hybrid vesicles are low, the ATP production rates in bR- EF_0F_1 ATP synthase vesicles are barely influenced by this. One explanation already mentioned in chapter 4.2.2 is that protons pumped by bR can efficiently diffuse along the membrane surface without dissipation losses into the aqueous bulk as recently evidenced by Heberle et al. (91). Besides, no back-pressure effects are relevant in the co-reconstituted system because protons are transported back outside by ATP synthase. Moreover, the non-proton permeability is low due to the absence of valinomycin. Under these conditions passive proton leakage has only little influence (104).

In future studies higher uniform orientation of bR molecules should be envisaged to increase ATP production rates. To do so, different methods have been reported. For example, the protein RC from *Rhodobacter sphaeroides* could be almost unidirectional orientated by reconstitution at very low ionic strength. (112) Another just as important factor for directed insertion was shown to be the charge of the utilized lipids. In case of polymersomes it has been demonstrated that the chemical composition of the amphiphilic polymers forming the vesicles is able to affect the orientation of membrane proteins as well. (112) In general, a directed insertion of membrane proteins might be achieved by using asymmetric membranes, which could be realized by the usage of ABC triblock copolymers. A very elegant solution for directed insertion was reported for proteorhodopsin (pR) by genetically engineering of the N-terminus with a water-soluble red fluorescent protein (112).

4.3.2.6 Passive proton permeability

bR proton pumping experiments alone indicated much higher activity in PC lipids compared to hybrid membranes, which could be not completely explained by the reconstitution efficiency or the orientation of bR in the membrane. Another factor influencing the magnitude of ΔpH is the

4 Results and Discussion

passive proton permeability of the membrane. The kinetics of pH change inside different lipid/hybrid vesicles were recorded upon addition of HCl/NaOH to the outer solution in order to determine the permeability coefficient (P) for different membrane compositions (Figure 4.33). All measurements were conducted in PIPES buffer adjusted to pH 7.5 with KOH (50 mM KOH) according to Paxton et al. (113) Valinomycin was added to prevent the build-up of electrostatic potential differences, which are counteracting to the passive proton flux.

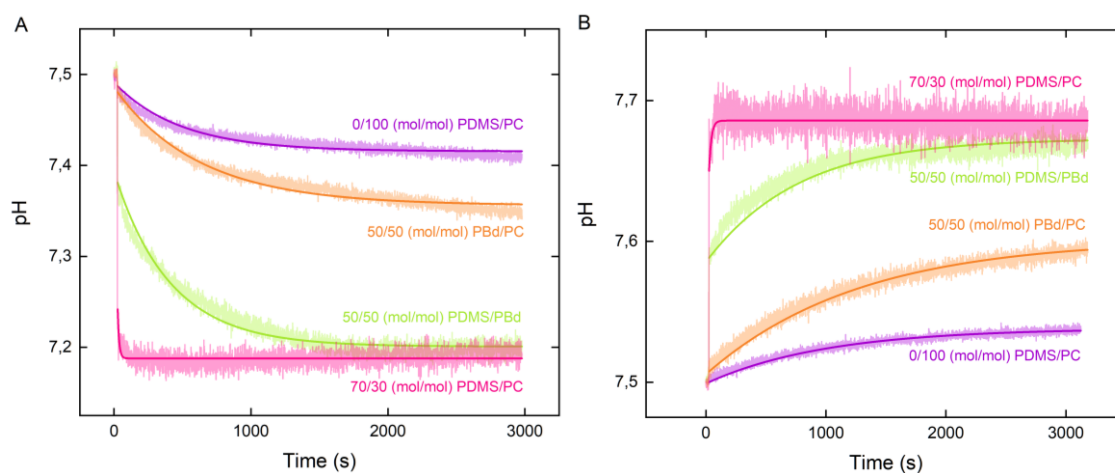


Figure 4.33 Proton permeability of vesicles as measured by pH change after addition of 2.4 mM HCl (A) and 1.6 mM NaOH (B) in the presence of 1.5 nM valinomycin.

pH change is detected by encapsulated HPTS. Measurements were performed in 25 mM PIPES, 200 mM sucrose, 50 mM KOH, 0.02 % sodium azide, 0.5 mM HPTS. The solid lines represent the simulations as predicted by the model described below.

The interaction between pyranine and the polymers used in this study was not yet investigated. It is known that due to its polyanionic character, pyranine does not interact with phospholipids having a net anionic surface charge (114). As the net surface charge of the different hybrid vesicles is not known, an interaction between polymer and pyranine could not be excluded. In order to prevent artefacts caused by this issue, pyranine calibration curves were recorded specifically for each membrane composition (Figure A.5). Two different methods were used to generate the calibration curves. First, hybrid vesicles were prepared in buffer of different pH (Figure A.5 A). This procedure was quiet time consuming. Therefore, only 5 different pH values in the physiological area between pH 6 and 8 were used for calibration. Second, hybrid vesicles were added to buffer of different pH and complete proton permeability was enabled by addition of nigericin (Figure A.5. B) Nigericin acts as an H^+ , K^+ and Pb^{2+} ionophore (115) and makes the membrane completely permeable to protons. Nine different pH values were measured between

pH 5 and 9. All monitored measurement points were fitted using the Henderson-Hasselbach equation (Figure 4.11). Afterwards, the pH of different permeability data was calculated using the corresponding calibration curves. The resulting pH curves were compared with the curves yielded by calculation using the calibration curve described in 4.2.2.1. The finding was that this calibration curve (Figure 4.11) produced the most reliable results. For example, by using this curve the starting pH of the calculated pH curve matched the actual starting pH of the buffer solution most. Therefore, all permeability data were evaluated using the calibration curve described in 4.2.2.1. Figure 4.33 shows the pH time course after addition of acid or base. The pH inside the vesicles changed rapidly with the addition of NaOH/HCl, and then increased/decreased much more gradually. All time courses show a fast-initial jump directly after adding acid/base. This jump was more significant in PDMS hybrids (70/30 PDMS/PC, 50/50 PDMS/PBd) compared to a more gradual increase in the case of PBd hybrids (50/50 PBd/PC) or liposomes (100/0 PC). The final pH (after 3000 s) also varied depending on the vesicle composition. In the case of 50/50 PDMS/PBd and 70/30 PDMS/PC, final pH values were lower (HCl) or higher (NaOH) and addition of nigericin (data not shown) induced no further equilibration of outer and inner pH. In contrast, the addition of nigericin to 50/50 PBd/PC and 100/0 PC vesicles caused a rapid pH jump.

The two-stage pH change described above is well known (113; 116; 117; 114). The initial pH jump inside the vesicles upon addition of acid/base has been attributed by some literature to a rapid H⁺/OH⁻ permeability, which results in an uncompensated build-up of charge. The H⁺/OH⁻ diffusion then slows down to a rate limited by the permeability of charge-compensating co-ions or counter-ions (113; 86; 118). Other reports in contrast (87), supposed leakage of small amounts of pyranine in the outer solution.

Paxton et al. (113) evidenced that this initial fast jump is critically influenced by the choice of buffer. In accordance to this, we also observed stronger initial jump with decreasing buffer capacity (data not shown), which is predicted by a mathematical model described below (104).

To check the influence of valinomycin on the proton flux, measurements under the same conditions without adding valinomycin were performed (Figure 4.34). As expected, the proton flux slows down due to the build-up of electrostatic potential differences. It can be seen that also the initial jump is decreasing in the absence of valinomycin. Interestingly, this effect is more relevant when adding HCl instead of NaOH. In general, it has to be mentioned that the activity of ionophores is not yet investigated in detail for all hybrid vesicles used here. The activity of valinomycin in these polymer-based membranes is just an assumption.

4 Results and Discussion

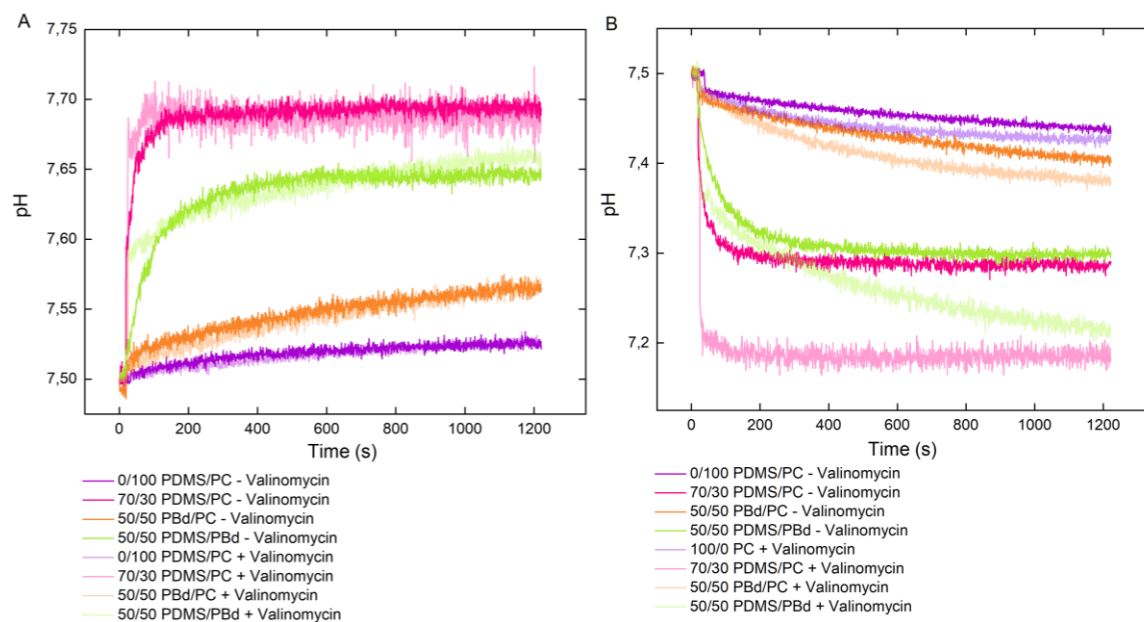


Figure 4.34 Proton permeability of vesicles as measured by pH change after addition of 2.4 mM HCl (left) and 1.6 mM NaOH (right) to the outer solution in the absence of valinomycin.

Measurements were performed in 25 mM PIPES, 200 mM sucrose, 50 mM KOH, 0.02 % sodium azide, 0.5 mM HPTS in the presence of 1.5 nM valinomycin (+Valinomycin) or in the absence of valinomycin (-Valinomycin).

To quantify the passive permeability of different vesicles, membrane permeability for protons and hydroxide ions was estimated. Different methods for determination and calculation of permeability coefficients (P) have been reported (87; 113; 116; 119). Kuyper et al. (116) for example derived the proton permeability coefficient by double exponential fitting under consideration of the vesicle size. As all models reported so far have its drawbacks, we used a model developed by Christian Wölfer (Method 1) and compared the results with two other models reported in the literature (Method 2 (113), Method 3 (116)). A detailed description of these models can be found in the appendix (A.3 Models for calculation of permeability coefficients).

The proton permeability coefficients yielded by all three methods are summarized in Table 4.1. Permeability coefficients using Method 2 recently described by Paxton et al. (113) were calculated using the data during the first 200 s of the reaction (Figure A.3). Thereby, the assumption of linear pH change during this period is made, which is not supported by experimental evidences for 50/50 PDMS/PBd and 70/30 PDMS/PC systems due the two-stage pH change described above. Therefore, no permeability coefficients were calculated for these two cases (104).

Using Method 2 proton permeability coefficient P_{H^+} was additionally calculated in the absence of valinomycin (-VAL) to investigate the influence of valinomycin. For P_{OH^-} barely any influence of

valinomycin was visible (Figure 4.34). All other permeability coefficients are related to the measurements in the presence of valinomycin.

Table 4.1 Permeability coefficients for different membrane compositions as yield by model simulation (Method 1), coefficients calculated according to Paxton et al. (Method 2) and coefficients derived by double exponential fitting (Method 3).

Membrane composition		$P \times 10^9 \text{ (cm}^2\text{s}^{-1}\text{)}$	$P_{\text{OH}^-} \times 10^{10} \text{ (cm}^2\text{s}^{-1}\text{)}$	$P_{\text{H}^+} \times 10^{10} \text{ (cm}^2\text{s}^{-1}\text{)}$	$P_{\text{OH}^-} \times 10^8 \text{ (cm}^2\text{s}^{-1}\text{)}$	$P_{\text{H}^+} \times 10^8 \text{ (cm}^2\text{s}^{-1}\text{)}$
		<u>Method 1</u> +VAL	<u>Method 2</u> +VAL	<u>Method 2</u> +VAL/-VAL	<u>Method 3</u> +VAL	<u>Method 3</u> +VAL
0/100	PDMS/PC	1.88	3.4	9.4/6.2	1.2	1.0
70/30	PDMS/PC	1100	-	-	7.1	5.9
50/50	PBd/PC	2.41	6.2	19.8/9.7	3.7	85.5
50/50	PDMS/PBd	2.96	-	-	8.4	7.0

Permeability coefficients for 100/0 PC and 50/50 PBd/PC vesicles determined by all methods show the same trend. Pure liposomes have the lowest proton permeability and slightly higher permeabilities are calculated for PBd/PC hybrids. The observation that vesicles with intermediate lipid/PBd-PEO ratios tend to be surprisingly more permeable to ion transport than pure lipid or pure polymer vesicles, has been made earlier by Paxton and colleagues (113). They used the larger PBd₃₇-PEO₂₂ polymer and suggested that the higher permeability likely arises from the size mismatch between lipid and polymer. In the present case, lipid and PBd₂₂-PEO₁₄ polymer have a similar size. P values determined here for lipid and 50/50 PBd/PC hybrids are in between the values earlier reported by Paxton et al. using the PBd₃₇-PEO₂₂ polymer (113) and the permeability coefficients identified by Seneviratne and colleagues (105) for the smaller PBd₂₂-PEO₁₄ polymer. Their results showed higher permeability for 25% PBd-PEO hybrids compared to liposomes, but in contrast lower permeability for 50% PBd-PEO hybrids. This difference might arise by the usage of slightly different lipid (POPC) compared to the egg PC used here or by minor variances in vesicle preparation. In general, their permeability coefficients are one order of magnitude lower than those reported here. This could be explained by the fact that they didn't use valinomycin in their experiments. The calculation of permeability coefficients in the absence of valinomycin (Table 4.1, -VAL) show clearly that the addition of valinomycin results in higher permeability coefficient. The high proton permeability of PDMS/PC hybrids determined by Method 1 compared to liposomes is in good agreement with recently reported results (120). In contrast, Method 3

4 Results and Discussion

indicates only slightly higher coefficients for PDMS/PC hybrids compared to liposomes. In general, permeability coefficients determined with Method 3 fit not very well to the recorded pH curves. For example, P_{H^+} of PBd/PC hybrids is much higher compared to P_{H^+} of PDMS/PC and PDMS/PBd hybrids, even though the pH curve of PBd/PC hybrids proceeds more gradual. It is possible that errors occur using this method by neglecting important parameters as buffer capacity and amount of acid/base added. Method 3 only considers the size of the vesicles and the pH change over time. Carlson and colleagues (126) investigated the water permeability of PDMS GUVs under osmotic stress. Their calculated permeability coefficients indicate that PDMS/PC hybrids have high apparent permeability, which may be ascribed to proton transport through transient pores. A literature study of PDMS GUVs has shown that these vesicles under stress conditions might form transient pores, without losing its integrity.

To my best knowledge, permeability coefficients for PDMS/PBd hybrids have not been reported yet. The permeability coefficient of mixed PDMS/PBd vesicle without consideration of an initial pH jump (Method 1) is similar to the permeability coefficient of the other membrane compositions.

4.3.2.7 Long-term stability

According to the literature, one of the major benefits of hybrid and polymer vesicles over natural proteoliposomes is their enhanced functional durability (96). To prove this hypothesis, the activity of the system was monitored over 42 days (Figure 4.35).

Samples were stored at 4 °C during this period. To prove significant differences ($*P \leq 0.05$) between lipid and hybrid vesicles, an unequal variance t-test (Welch's test) was performed. Relative protein activities indicated the highest improvement of long-term stability for 50/50 PDMS/PBd. Significant differences were evidenced from day 5 on with remaining activities of around 80% after 42 days. For hybrid vesicles made of lipid and polymer (70/30 PDMS/PC and 50/50 PBd/PC) significant enhancement of activity compared to liposomes was demonstrated from day 19 on. In addition to this, the results show that not only the relative activity (activity normalized to day 1), but also the absolute protein activity in hybrid vesicles overreached that of liposomes after day 19.

Both lipid/polymer hybrid vesicles seem to improve stability in a similar way, while the stability in polymer/polymer hybrid vesicles was remarkably higher. This outcome is in good agreement with recently reported extended functional lifetime of cytochrome bo_3 oxidase in PBd-PEO hybrid vesicles (96; 105).

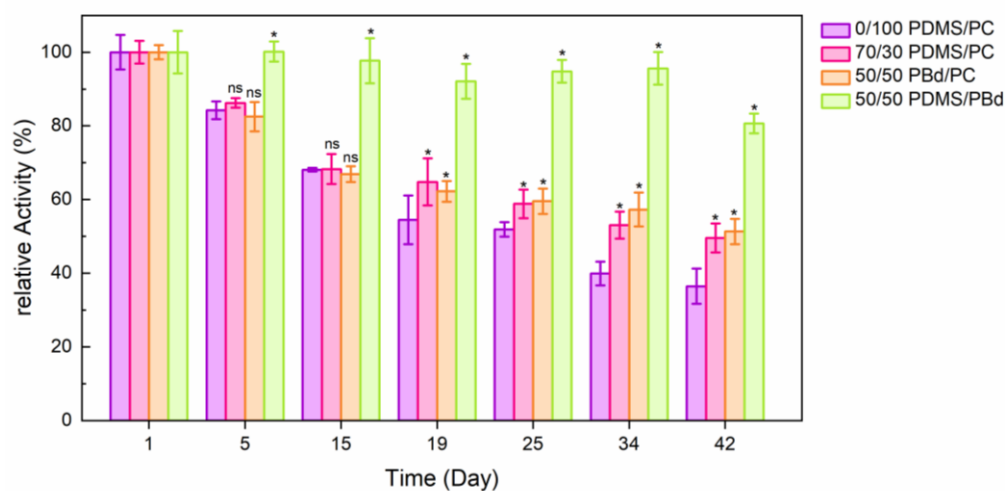


Figure 4.35 Hybrid vesicles improve long-term stability of the ATP regeneration module.

The activity was normalized to the activity at day 1. * $P \leq 0.05$, nonsignificant (ns) $P > 0.05$ (P values are generated by unequal variance t-test (Welch's test) for comparison of each hybrid membrane composition to the lipid vesicle sample). $n \geq 4$; error bars represent standard error of the mean (SEM). Measurements were performed in 20 mM HEPES, 25 mM MgCl₂, 50 mg/ml sucrose, pH 7.5 (inner solution) and 10 mM Tris-HCl, 5 mM NaH₂PO₄, 50 mM KCl, 2 MgCl₂, 1 mM DTT, pH 7.5 (outer solution) at room temperature. [ADP]= 360 μ M, [Pi]= 5 mM, [lipid]= 0.022 mg/ml, [EFOF1]= 1.3 nM, [bR]= 37 nM. Proteins were reconstituted with 0.3 % Triton (0/100 PDMS/PC) or 0.06% Triton (70/30 PDMS/PC, 50/50 PBd/PC, 50/50 PDMS/PBd).

To check whether the increased long-term stability of the ATP module was related to an increased stability of vesicles, the vesicles average diameter (Z_{ave}) and polydispersity index (PDI) were monitored over 42 days (Figure 4.36). Linear regression of all data points was performed in order to visualize the trend over time. The results indicate that for all vesicles the average size (Z_{ave}) as well as the PDI are not significantly changing over time and that there is no clear trend for an increase or decrease of Z_{ave} and PDI.

4 Results and Discussion

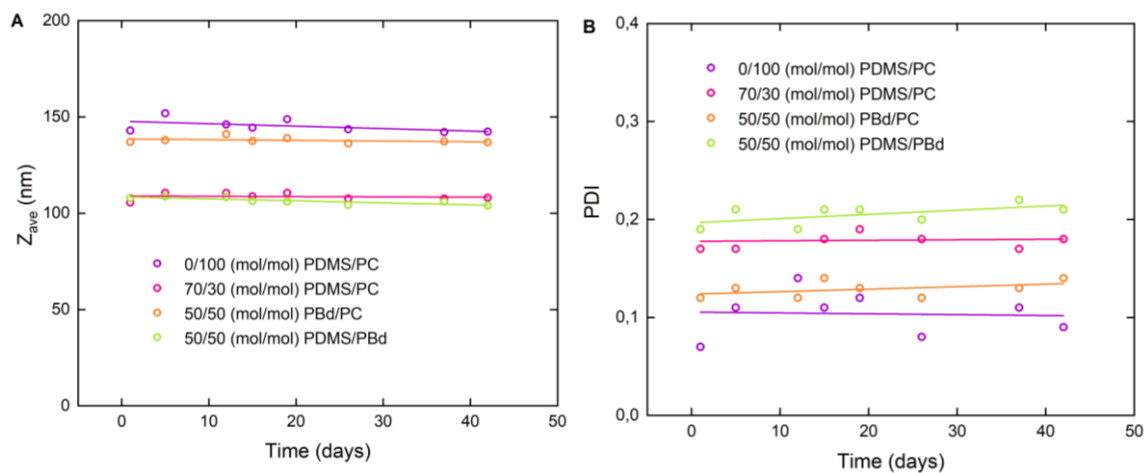


Figure 4.36 Vesicles average diameter (A) and Polydispersity Index (B) stay almost constant over 42 days as determined by Dynamic Light Scattering (DLS).

Measurements were performed in 20 mM HEPES, 25 mM MgCl_2 , 50 mg/ml sucrose, pH 7.5. Measurement points for each membrane composition were fitted by linear regression to visualize the trend over time.

To visualize that the size distribution profile of vesicles is not significantly changing either, size distribution profiles at day 1 and at day 42 are plotted in one diagram for each membrane composition (Figure 4.37).

As a consequence, it can be summarized that the stability of vesicles itself did not cause the increased long-term stability of the ATP module. It can be rather assumed that the interaction between polymer and protein increased the long-term stability of enzymes.

The here presented long-term stability measurements clearly evidenced the advantageous in using hybrid vesicles instead of liposomes. This enhanced stability may not only be critical to synthetic biology but could also become an important tool in handling membrane proteins in fundamental biochemical studies (109). Both lipid-polymer hybrid vesicles seem to increase the long-term stability in a similar way, while the activity at day 1 is slightly better in 70/30 PDMS/PC vesicles. Presumably, this can be mainly attributed to the higher fluidity of the PDMS polymer compared to PBd. PBd in contrast, is packed more tightly in the membrane which might cause higher steric interactions between the hydrophilic PEO chains of the polymer and the head of ATP synthase. However, this increased viscosity compared to lipid membranes is also supposed to be a critical factor in stabilizing proteins over time (57). In general, the flexibility of the polymer chains and the hydrophobic thickness of the membrane are important parameters for successful integration of membrane proteins: flexible, linear hydrophobic polymers allow conformational adaption to the preferred hydrophobic thickness of the protein (109).

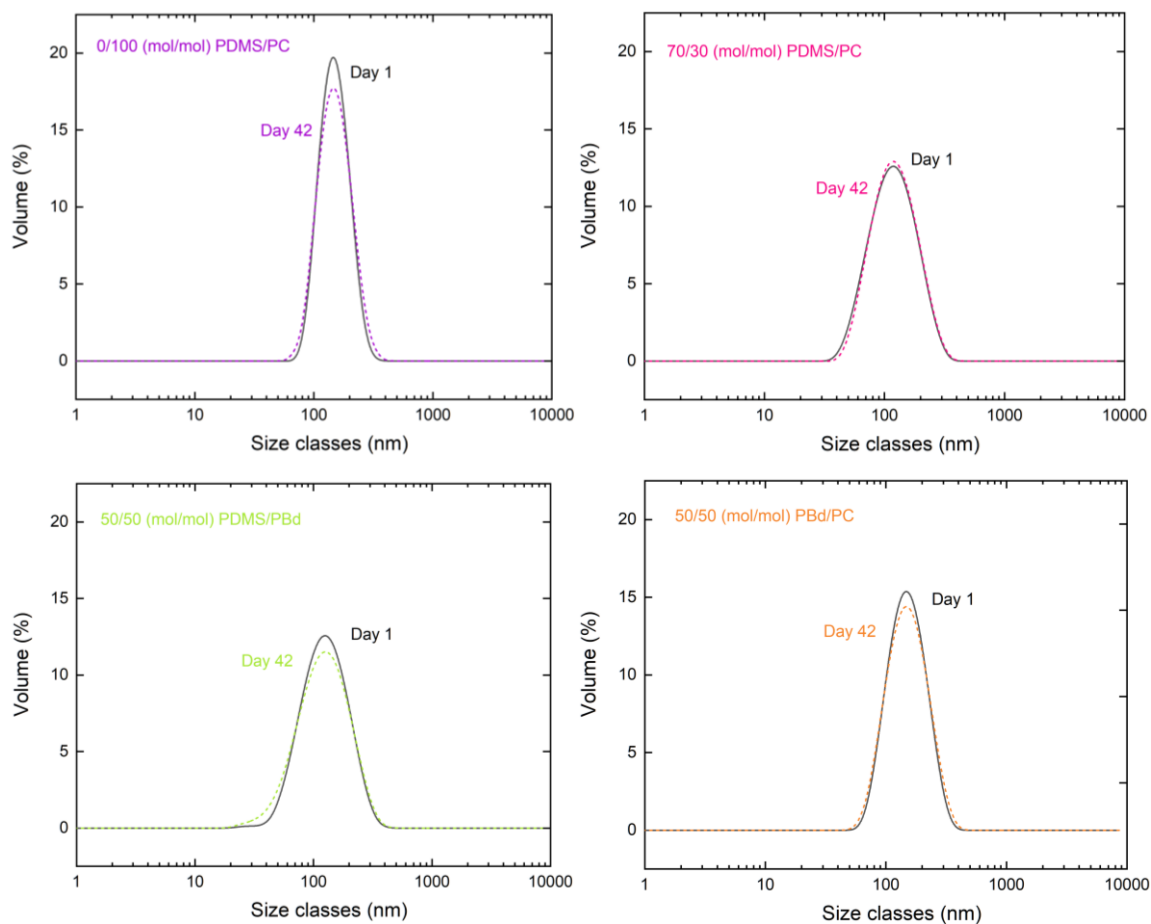


Figure 4.37 Comparison of the size distribution profile of vesicles at day 1 and day 42.

Jacobs and colleagues (99) recently showed increased folding of a membrane protein during cell-free expression when using PBd hybrid membranes instead of pure lipid membranes. In their work, they evidenced that the mechanical properties of the membrane (e.g. the area expansion module) highly influenced the interactions between protein and membrane. Changes in membrane elastic properties can lower or increase the energy of membrane deformation and can therefore increase or decrease the conformational freedom of a protein. The decrease of conformational freedom might slow down the process of protein unfolding and therefore increase long-term stability. Enhanced functional durability of membrane proteins could especially play an important role when designing biosensors, drug delivery systems, nanoreactors, energy capture, storage devices or artificial cells.

4 Results and Discussion

Further optimization of membrane composition (e.g. different polymers and/or lipids) and reconstitution procedure, might further increase biocompatibility and long-term stability. The lipid-polymer or polymer-polymer ratio seems to be another important parameter influencing the chemical and mechanical properties of the membrane and therefore the interaction with proteins embedded in them. Phase-separated membranes with lipid- and polymer-rich domains might be also attractive for transmembrane reconstitution by combining native-like lipid solvation with the high structural stability of polymersomes.

4.3.3 *The ATP module in lipid, polymer and hybrid vesicles with bR patches*

Another study integrating the ATP module in lipid, polymer and hybrid vesicles have been made. In this study bR was used in form of membrane patches instead of detergent solubilized monomeric bR. In purple membrane patches bR is arranged in a 2D hexagonal crystalline lattice and contains 75% bR embedded in 25% lipid. Additionally, slightly different membrane compositions (with the same polymers) were applied in this study using a deviant reconstitution procedure.

4.3.3.1 Membrane composition

Overall, 7 different membrane compositions have been chosen in order to analyze the ATP module co-reconstituted with bR patches as schematically shown in Figure 4.38. Pure soy PC vesicles (100/0 PC) were used as a benchmark for enzyme activity in other compartments. Three types of vesicles containing PDMS as well as PBd were prepared aiming to a mass/mass (m/m) ratio of 50% polymer, 75% polymer and 100% polymer. For clearance, the m/m ratios were recalculated to mol/mol ratios.

PDMS forms well mixed membranes above 70 mol % polymer. Therefore, the here analyzed PDMS hybrid vesicles are present as phase-separated membranes. As mentioned above phase-separated membranes might be also interesting for membrane protein insertion, combining native-like lipid solvation with enhanced structural stability of polymers.

PBd in contrast is known to form homogenous, well-mixed membranes with POPC within the whole range of compositions (97).

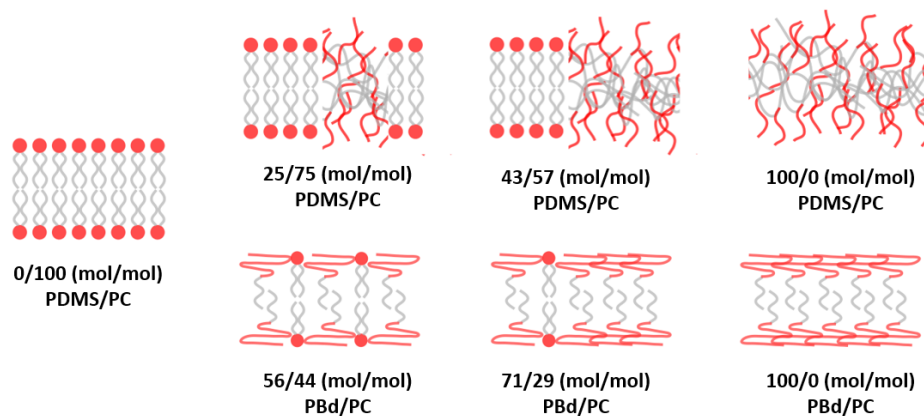


Figure 4.38 Schematic presentation of different membrane compositions used for co-reconstitution with bR patches.

4.3.3.2 Reconstitution procedure

For insertion of transmembrane proteins in hybrid and polymer compartments 0.8% Triton was used for reconstitution according to the method described above for the reconstitution into liposomes. Hybrids and polymers were prepared by film rehydration method, followed by extrusion through 100 nm pores. The size distribution profiles after extrusion as measured by Dynamic Light Scattering (DLS) are shown in Figure 4.39 A for PDMS vesicles and in Figure 4.40 A for PBd hybrids. All measurements indicate uniform size of vesicles with an average diameter between approximately 80 to 150 nm.

4 Results and Discussion

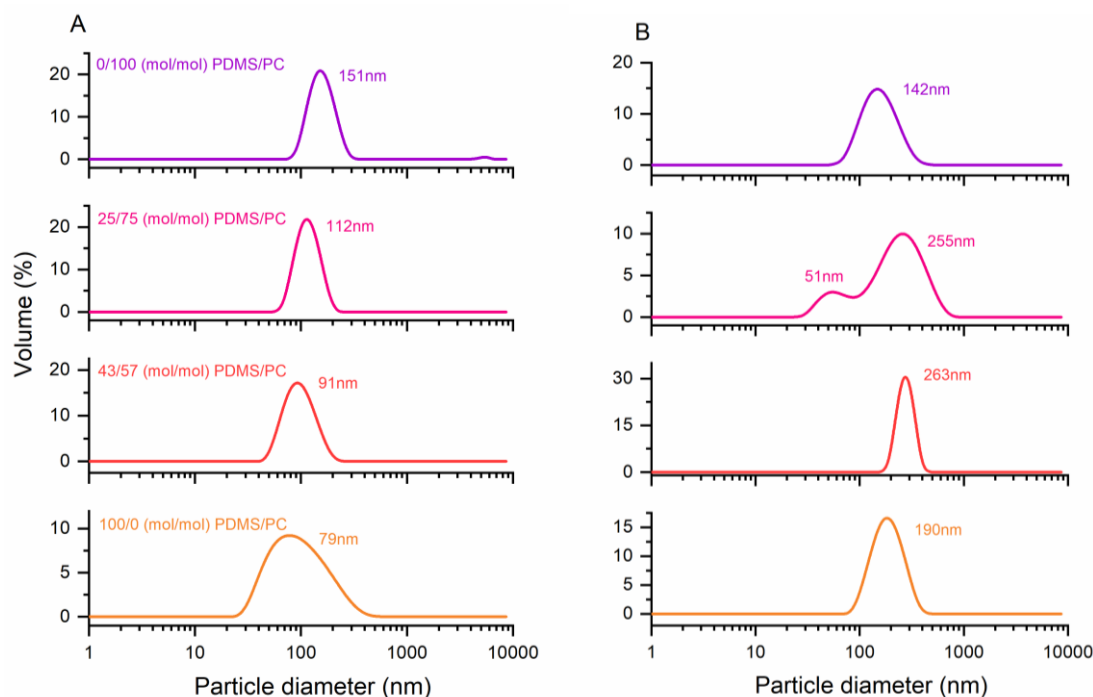


Figure 4.39 Size distribution of vesicles made of different mixtures of PDMS and PC before (A) and after (B) reconstitution and removal of detergent using bio beads.

DLS measurements after removal of detergent using Bio Beads (Figure 4.39 B, Figure 4.40 B) show a different behaviour of hybrid and polymer vesicles compared to liposomes, which is in accordance to the results reported in chapter 4.3.2.2. Liposomes remain their original size with a slightly increased PDI, while hybrid and polymer vesicles either change their size or split in two distinct fractions. In the case of PDMS hybrids only 25/75 PDMS/PC shows two populations of vesicles with sizes of 51 and 255 nm, respectively. The other two compositions (43/57 PDMS/PC and 100/0 PDMS/PC) form larger vesicles (263 nm and 190 nm) after detergent removal.

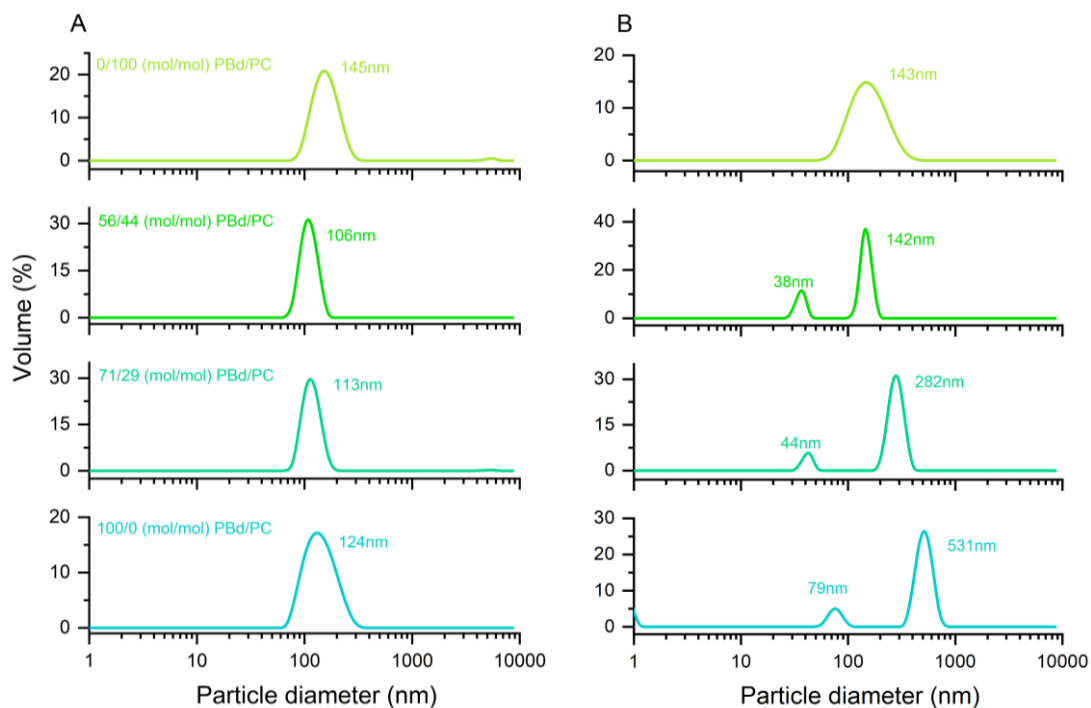


Figure 4.40 Size distribution of vesicles made of different mixtures of PBd and PC before (A) and after (B) reconstitution and removal of detergent using bio beads.

In contrast, all PBd hybrid and polymer vesicles split in two distinct fractions after detergent removal. It is possible that this is due to the more viscous character of PBd compared to PDMS. The slower dynamics might influence vesicle formation during detergent removal (96). The results are in good agreement with the results from Khan et al. (96) who detected small particles of 10 nm size after detergent removal with Bio Beads. In the present study, both populations of bigger and smaller sized vesicles were used for further measurements without separation.

Turbidity profiles for each membrane composition were taken (Figure 4.41) to determine the point of solubilization reached by the addition of 0.8% Triton. Results show that the point of solubilization was at the intermediate or at the offset of solubilization depending on the membrane composition.

4 Results and Discussion

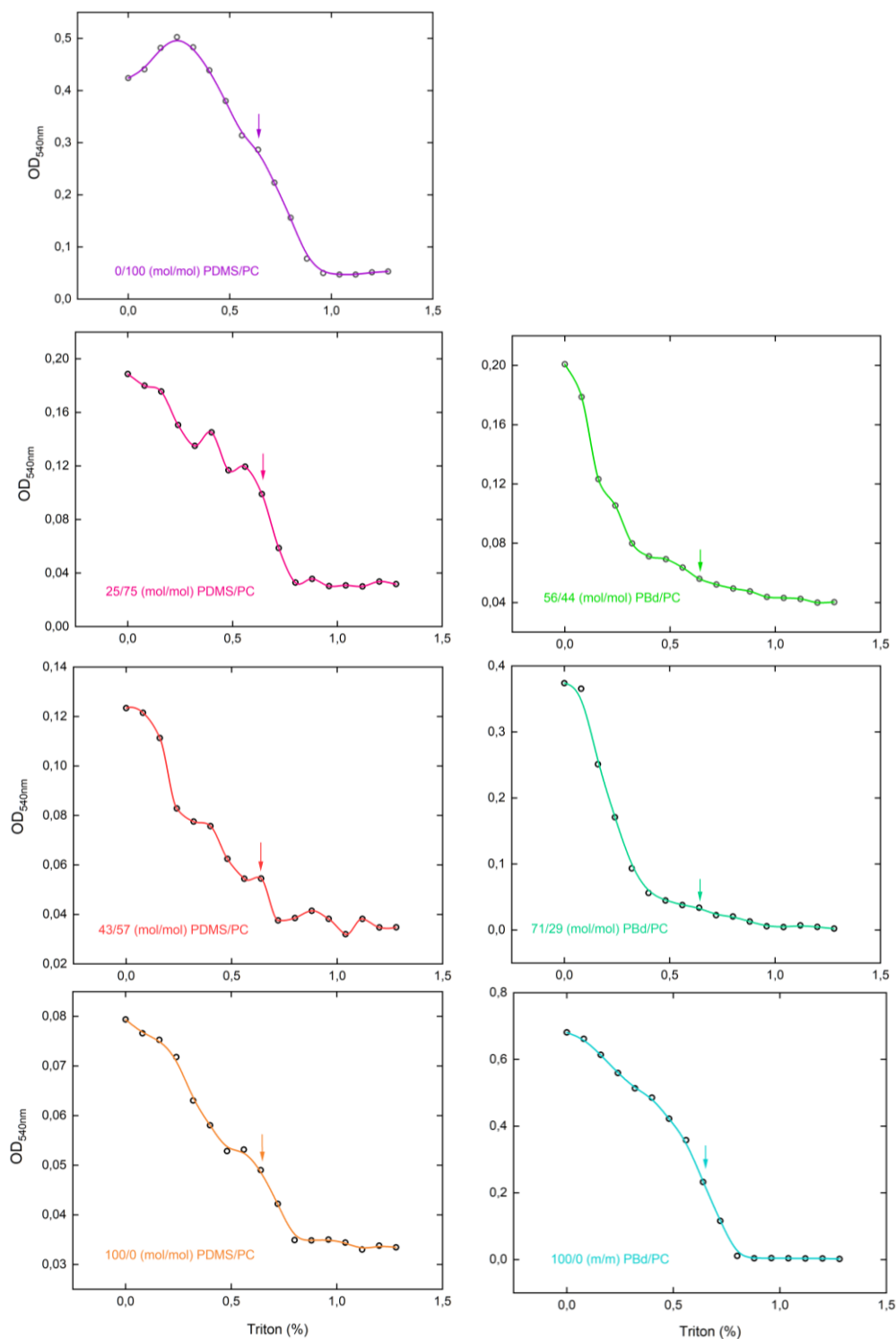


Figure 4.41 Detergent destabilization profiles for hybrid vesicles made of different mixtures of PC, PDMS and PBd. Plots show the change in absorption at 540 nm upon addition of several amounts of Triton X-100. The destabilization points with the corresponding amounts of Triton X-100 chosen for reconstitution are indicated with colourful arrows.

Due to the literature (25) the optimal point of solubilization for Triton X-100 mediated reconstitution is the intermediate step of solubilization. Anyway, it has to be mentioned that this point was determined when using monomeric detergent solubilized bR for reconstitution (25). Therefore, detergent was additionally brought to the reconstitution mixture by solubilized bR itself. In the present study bR was used as membrane patch without any supplementation of detergent. Therefore, the usage of higher amounts of detergent for reconstitution is justified.

In addition, other reconstitution methods were tested reported to be suitable for each of the polymers respectively. For example, recently reported method for optimized co-reconstitution of ATP synthase and bo_3 oxidase in PDMS-g-PEO hybrid vesicles was applied (103). This method was based on adding octyl glucoside to preformed hybrid vesicles or introducing it during vesicle formation (103). In the present case this procedure resulted in significant lower ATP production rates (Figure 4.42 A). For the incorporation of bR and EF_0F_1 into PBd-PEO hybrids lower Triton concentration (0.1%) as proposed by Khan et al. (96) was used. This co-reconstitution led to slightly lower ATP production rates (Figure 4.42 B). Even though significant progress in understanding the mechanism of protein reconstitution in lipid membranes have been made (108), optimal reconstitution procedures for polymer or hybrid membranes have to be still established empirically for each membrane protein and polymer membrane (100).

4 Results and Discussion

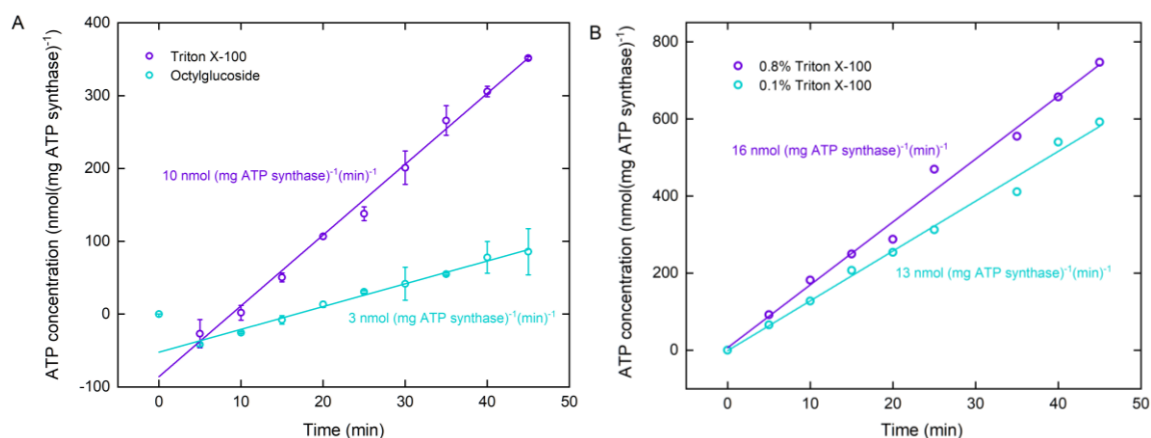


Figure 4.42 ATP production performance in hybrid vesicles using different reconstitution procedure.

(A) Triton X-100 and octyl glucoside mediated reconstitution in 43/57 (mol/mol) PDMS/PC hybrids. (B) Triton X-100 mediated reconstitution in 71/29 (mol/mol) PBd/PC hybrids. The activity was determined by linear regression. Measurements were performed in 20 mM HEPES, 25 mM MgCl₂, 50 mg/ml sucrose, pH 7.5 (inner solution) and 10 mM Tris-HCl, 5 mM NaH₂PO₄, 50 mM KCl, 2 MgCl₂, 1 mM DTT, pH 7.5 (outer solution) at room temperature. [ADP]= 360 μM, [P_i]= 5 mM, [lipid]=0.022 mg/ml, [EF_oF₁]= 1.3 nM, [bR]= 88 nM.

4.3.3.3 Performance

Measurement of ATP production after co-reconstitution into polymer and hybrid vesicles produced from different ratios of PDMS/PC (Figure 4.43 A) and PBd/PC (Figure 4.43 B) indicated functional integration of bR and EF_oF₁ ATP synthase.

As expected, the highest rate is reached for the system in pure lipid vesicles. For PDMS polymer, the protein activity is decreasing with increasing polymer content with a fairly small reduction in activity from liposomes to 50% PDMS and 75% PDMS, but a more considerable reduction in activity for pure polymersomes. The performance in PBd hybrid vesicles is smaller compared to that in PDMS hybrids. The lower activity of the system in pure polymersomes can be explained by the fact that bio-functional lipids are missing. In general protein activity has been shown to decrease with decreasing lipid content (105).

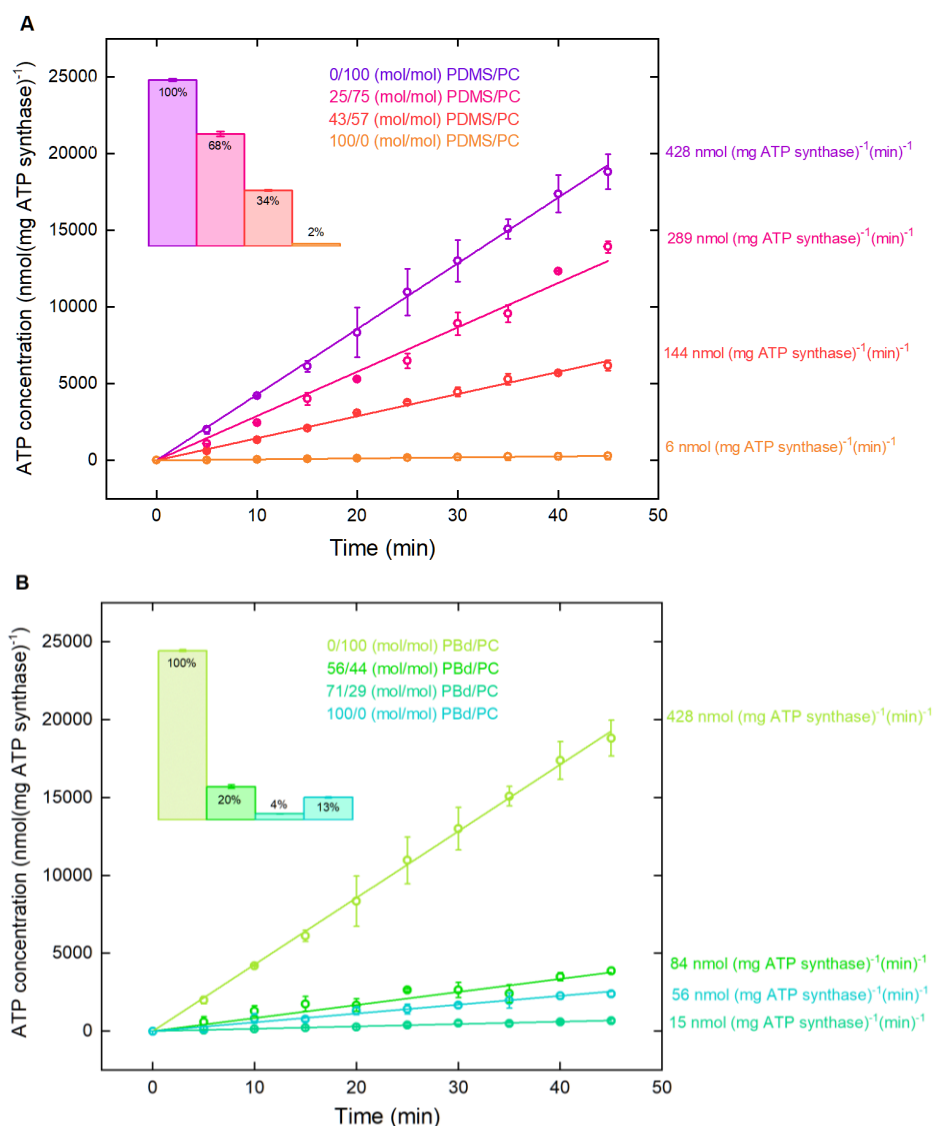


Figure 4.43 Light-driven ATP synthesis in hybrid vesicles made of PC and PDMS (A) and PC and PBd (B) co-reconstituted with bR patches.

The activity was determined by linear regression. The inset bars show the activity normalized to pure PC liposomes. Measurements were performed in 20 mM HEPES, 25 mM MgCl₂, 50 mg/ml sucrose, pH 7.5 (inner solution) and 10 mM Tris-HCl, 5 mM NaH₂PO₄, 50 mM KCl, 2 MgCl₂, 1 mM DTT, pH 7.5 (outer solution) at room temperature. [ADP]= 360 μM, [P_i]= 5 mM, [lipid]= 0.022 mg/ml, [EF_oF₁]= 1.3 nM, [bR]= 88 nM. Proteins were reconstituted with 0.8 % Triton. All error bars represent the standard error of the mean (n=3).

Interestingly, the functionality of the model system in pure PBd polymersomes is higher (13%) compared to that of pure PDMS polymersomes (2%) and even higher than that in 75% PBd hybrids (4%). It is likely that the performance of the system is not only influenced by the functionality of

4 Results and Discussion

ATP synthase itself, but also critically relies on the established proton motive force in different compartments, which depends among others on the proton permeability of the membrane.

In general, relative ATP production rates of hybrid and polymer membranes are low compared to the results presented in chapter 4.3.2.3 for co-reconstitution with solubilized bR. This can be either explained by the usage of bR patches, by differences in membrane compositions or by differences in the reconstitution procedure. The batch of ATP synthase used was the same as in the measurements presented with solubilized bR: Therefore, activity of ATP synthase should be constant.

Differences in reconstitution procedure are mainly based on the usage of higher concentrations of detergent (0.8% Triton instead of 0.3% for liposomes or 0.06% for hybrids). It has to be mentioned that the absolute ATP production rate reached for 0/100 PDMS/PC is higher (428 nmol (mg ATP synthase)⁻¹min⁻¹) compared to the rate achieved with solubilized bR (255 nmol (mg ATP synthase)⁻¹(min)⁻¹) which can be explained by bR material loss during solubilization. As a consequence, absolute ATP production rates for 25/75 PDMS/PC (298 nmol (mg ATP synthase)⁻¹(min)⁻¹) are still higher compared to that of 0/100 PDMS/PC with solubilized bR.

4.3.3.4 bR reconstitution efficiency and proton pumping activity

bR patches were reconstituted in the absence of ATP synthase following the method described for co-reconstitution (chapter 4.3.3.2) with slight modifications. In contrast to co-reconstitution procedure, vesicles were prepared in the presence of pyranine. After removal of bio beads, the vesicles were passed over a gel filtration column to remove not encapsulated pyranine and not reconstituted bR. The reconstitution efficiencies for each membrane composition were calculated using equation [3.12] and are summarized in the table in Figure 4.44.

The maximal reconstitution efficiency (86%) of bR is obtained in PC lipids, which is slightly higher than the reconstitution efficiency in 0/100 PDMS/PC using solubilized bR (82%). In the case of PDMS polymer, the reconstitution efficiency is decreasing with increasing polymer content from ~81% to 66%. In contrast, for PBd-PEO polymer the reconstitution efficiency is increasing with increasing polymer content from 68% to 81%. A significant difference (*) in reconstitution efficiency compared to liposomes is indicated for 43/57 PDMS/PC, 100/0 PDMS/PC, 56/44 PBd/PC and 71/29 PBd/PC.

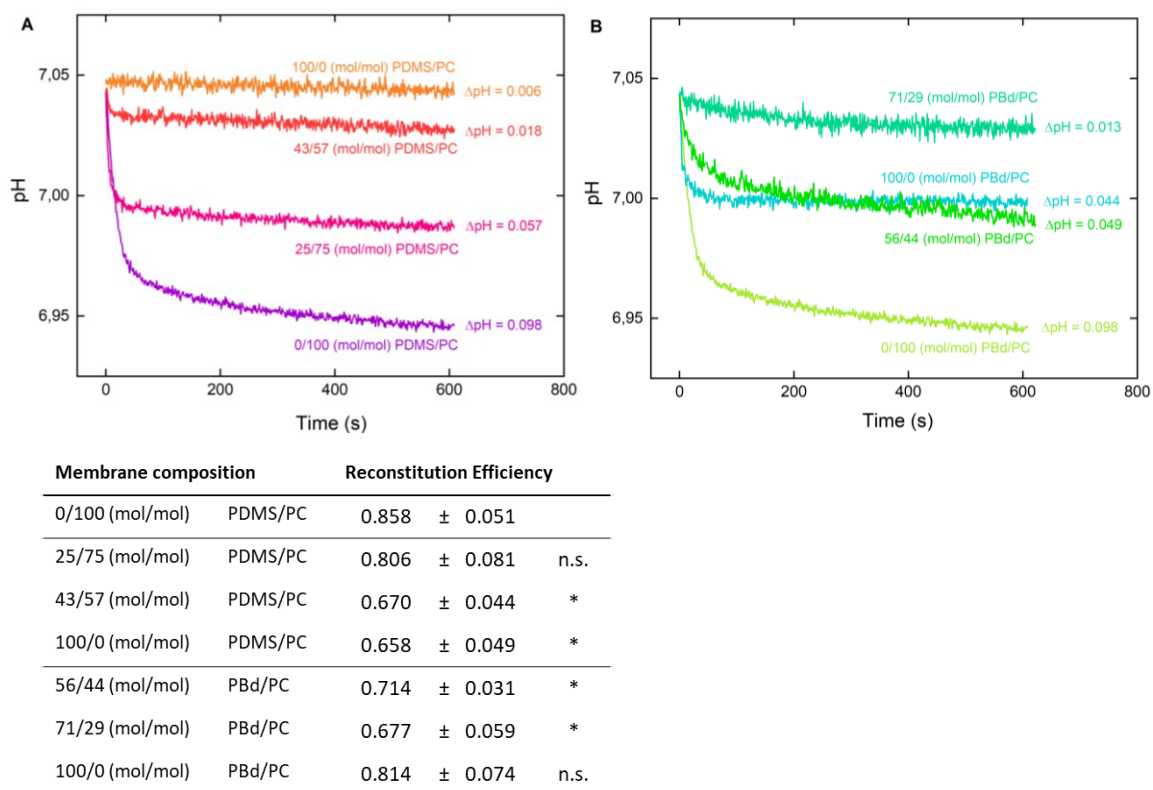


Figure 4.44 Proton pump activity of bR patches in lipid and hybrid vesicles made of PC/PDMS (A) and PC/PBd (B) as measured by pH change upon green light irradiation.

pH change was detected by encapsulated pyranine. Measurements were performed in 10 mM HEPES, 100 mM K_2SO_4 , 15 mM $MgCl_2$ in the presence of 3 μM valinomycin at room temperature. Proteins were reconstituted with 0.8 % Triton. Error bars represent the standard error of the mean ($n=3$). The table shows the reconstitution efficiency of bR in different compartments. * $P \leq 0.05$, nonsignificant (ns) $P > 0.05$ (P values are generated by unequal variance t-test (Welch's test) for comparison of each hybrid membrane composition to the lipid vesicle sample). $n = 3$; error bars represent standard error of the mean (SEM).

Proton pumping rates of bR upon green light irradiation are shown in Figure 4.44 A and B. Calculation of the internal pH was performed using the calibration curve shown in chapter 4.2.2.1. The maximal rates were found for pure PC lipid vesicles and in case of PDMS polymer, the rates were decreasing with increasing polymer content, comparable to the performance of the co-reconstituted system. For PBd vesicles, the results indicate a different trend, but also a comparable outcome when matching it to the co-reconstituted system in PBd vesicles. While the activity in 56/44 PBd/PC and 71/29 PBd/PC vesicles is slightly lower (50 and 13%) than that in corresponding PDMS hybrid vesicles (58 and 18%), the performance in pure PBd polymersomes (45%) is significantly higher compared to that in pure PDMS polymersomes (6%).

4 Results and Discussion

The initial pumping rate in 100/0 PBd/PC vesicles is higher compared to that of 56/44 PBd/PC, while the steady state ΔpH is almost the same. This can be likely explained by higher reconstitution efficiency and therefore higher number of pumping units in 100/0 PBd/PC vesicles. It is known that pure PBd polymersomes have a very low passive proton permeability (98). Moreover, the reconstitution efficiency in these polymersomes is not significantly different compared to liposomes. The reason why lower steady state ΔpH values are reached anyway, might be explained by slower turnover rates in PBd polymersomes due to the high viscous environment.

As already mentioned above discrepancies of ΔpH in different vesicles should be either explained by the number of active pumping units or by the passive proton permeability of the membrane (121). In order to estimate the number of active pumping units, the orientation of bR in different membranes was investigated and is presented in the next chapter.

4.3.3.5 bR orientation in different membranes

bR orientation in different compartments was determined using a proteolytic digestion assay according to the method described in chapter 4.3.2.5.

Digestion of 0/100 PDMS/PC and 25/75 PDMS/PC vesicles (Figure 4.45, lane 3 and 4) produced a mixture of digestion products with two characteristic bands at approximately 19 and 21 kDa. These bands can be related to C-terminal protein fragments with a theoretically supposed size of 23.5 and 24.5 kDa⁵⁰. As a consequence, the results suggest that the bR orientation in these vesicles was almost one-sided with the right side out. Such results couldn't be observed for co-reconstitutions with solubilized bR. The purple membrane arranges bR in a 2D hexagonal crystalline lattice and contains 75% bR embedded in 25% lipid. In these patches all bR is orientated uniformly. Moreover, no additional detergent is added to the reconstitution by solubilized bR itself. As the patches stay partially intact a more uniform orientation might be favoured.

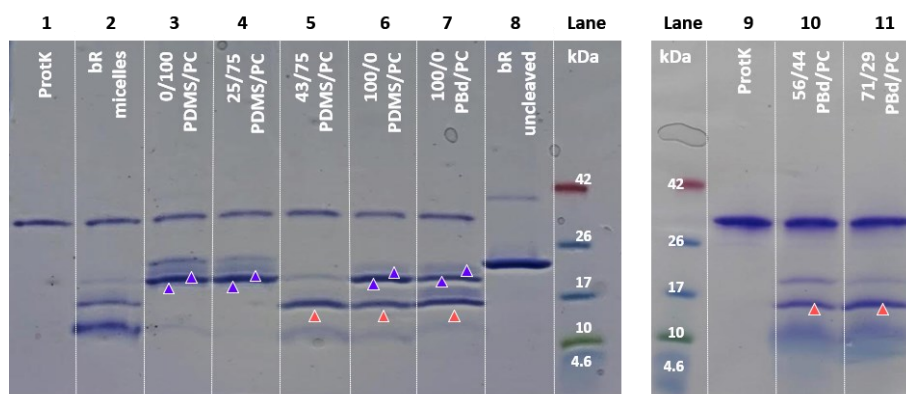


Figure 4.45 SDS-PAGE analysis after proteolytic cleavage of reconstituted bR patches with proteinase K (ProtK) shows different orientation in lipid, hybrid and polymer vesicles.

Lane 1 shows bands specific for ProtK enzyme only; lane 2 shows near complete digestion of not reconstituted bR; lanes 3-6 show digest patterns for vesicles containing different PDMS/PC ratios; lane 7 shows digest pattern for bR reconstituted in pure PBd-PEO vesicles lane 8 shows undigested bR, lane 10 and 11 show digest patterns for vesicles made of different mixtures of PBd/PC.

This result is in good agreement with the results obtained by proton pumping measurements. The activity in 25/75 PDMS/PC vesicles is relatively high compared to that in vesicles with higher PDMS content and the proteolytic digestion assay confirms a more unidirectional orientation in this kind of vesicles.

Digest fragments of 43/57 PDMS/PC, 56/44 PBd/PC and 71/29 PBd/PC (Figure 4.45, lane 5, 10, 11) show a rather different picture with two additional bands corresponding to those detected for bR in micelles. The band at 16 kDa can be related to the 19.7 kDa fragment produced when the N-terminal of bR is exposed to ProtK. Interestingly, SDS pattern of pure PDMS and PBd vesicles (Figure 4.45, lane 6, 7) show both, C-terminal and N-terminal digestion products, indicating that compared to hybrid vesicles more bR molecules are orientated inside out. These results could explain comparable small activities in PBd/PC hybrids compared to pure PBd polymersomes.

Besides protein orientation, passive proton leakage through the membrane is an important parameter that influences attainable ΔpH values established by bR (87).

4.3.3.6 Passive proton permeability

The kinetic of pH change inside different lipid/hybrid vesicles upon addition of NaOH to the outer solution was recorded and is shown in Figure 4.46.

4 Results and Discussion

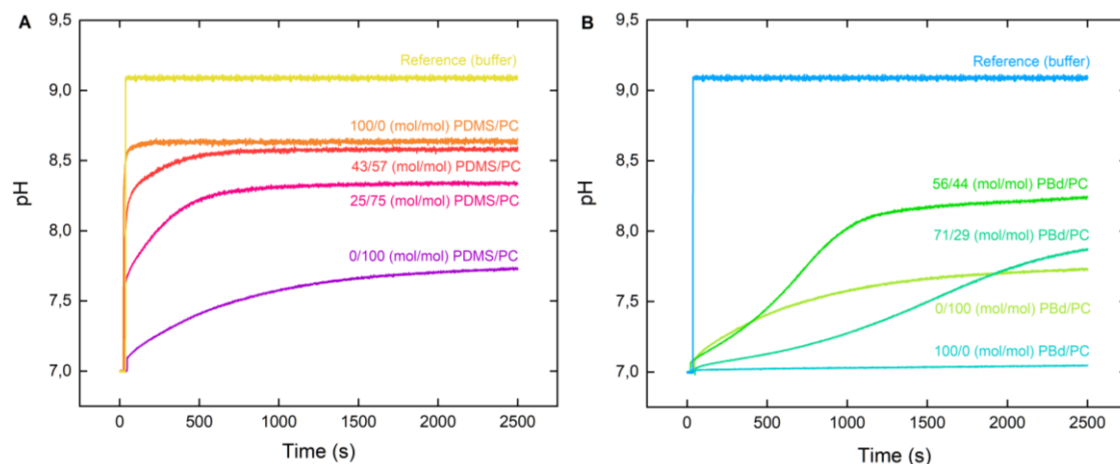


Figure 4.46 Proton permeability of vesicles as measured by pH change after addition of 102 mM NaOH to the outer solution.

pH change was detected by encapsulated HPTS. Measurements were performed in 40 mM HEPES, 20 mM K_2SO_4 , pH 7.0 in the presence of 1.5 μM valinomycin.

All measurements were conducted in HEPES buffer containing 20 mM K_2SO_4 . Valinomycin was added to prevent the build-up of electrostatic potential differences, which are counteracting to the passive proton flux. All pH courses show a fast-initial jump according to the results presented in chapter 4.3.2.6. This jump is more significant in PDMS hybrids compared to a more gradual increase in the case of PBd hybrids or liposomes.

For PDMS hybrids, the results indicate increasing proton permeability with increasing polymer content which is in agreement with the results observed in PIPES buffer (chapter 4.3.2.6). The highly disordered and fluid PDMS membranes are likely very permeable to protons, making it hard to establish and maintain significant pH differences across the membrane. This might explain the poor performance of PDMS hybrids in proton pumping experiments.

For PBd polymersomes very low permeability can be observed. According to the literature (105) PBd polymersomes have exceptionally low passive proton permeability, which is a significant advantage for this system in respect to the establishment of pH differences across the membrane. Battaglia and colleagues (122) recently reported that pH differences of 10 units can maintain in these vesicles for up to 8 days. The low permeability of these vesicles could explain the comparably high bR pumping rates detected in these vesicles. PBd hybrid vesicles in contrast, show remarkably higher proton permeability compared to PBd polymersomes and liposomes. These results are in good agreement with the results reported in chapter 4.3.2.6 and in the literature (113). In order to modulate the permeability of vesicles, further measurements using PDMS hybrid and polymer

vesicles have been conducted, inserting the potassium ionophore valinomycin or nigericin (Figure 4.47).

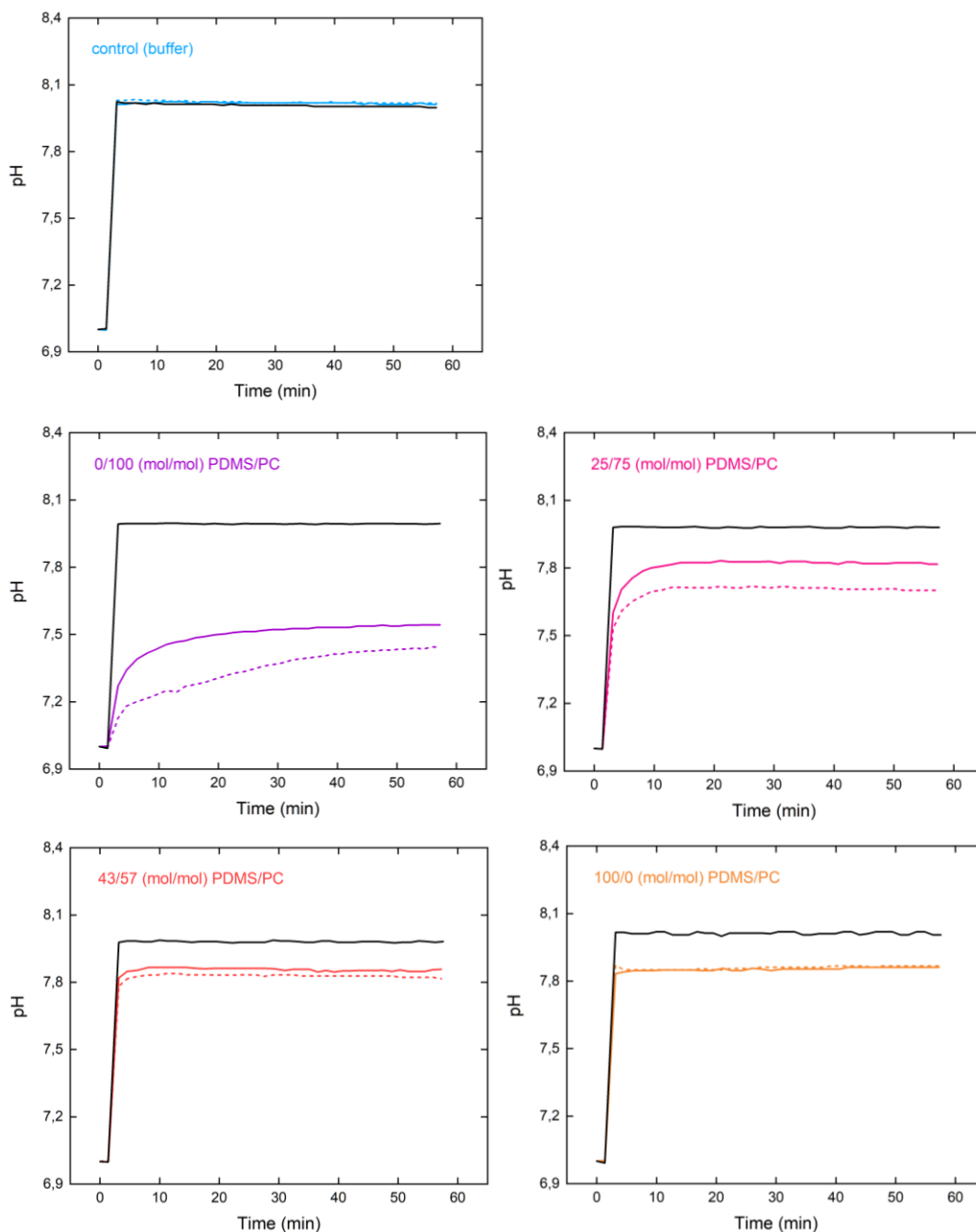


Figure 4.47 Internal vesicle pH with valinomycin and nigericin after addition of 77 mM NaOH.

Control: without vesicles (buffer only), Black line: vesicles after incubation with nigericin, Solid colourful line: vesicles after incubation with valinomycin, Dashed colourful line: vesicles without any addition of ionophore. Measurements were performed in 40 mM HEPES, 20 mM K_2SO_4 , pH 7.0.

4 Results and Discussion

Although both ionophores are well-known potassium carriers (123), it was observed that both facilitated the dissipation of a large imposed pH gradient ($\Delta\text{pH}>2$). This observation is consistent with the rapid initial flux of H^+/OH^- described above that slows to a rate limited by the co/counter-diffusion of other ions (117). With the introduction of the potassium ionophores, the co-diffusion of K^+ - necessary to compensate for the net H^+/OH^- flux across the membrane - is greatly facilitated, allowing the corresponding, and much faster, flux of H^+/OH^- to increase as well. It has to be mentioned that this effect is higher in pure liposomes compared to PDMS hybrids and barely visible in pure PDMS polymersomes. It is possible that pure PDMS polymersomes are highly permeable to H^+ and K^+ ions even in the absence of valinomycin. Therefore, no further increase of pH response could be detected.

In the case of liposomes and PDMS hybrids the pH response can be controlled by the amount of ionophore added as shown in Figure 4.48. While valinomycin is primarily a K^+ ionophore, nigericin is a well-known antiporter capable of facilitating the transport of both, K^+ and H^+ ions. As such, there is a marked increase in observed permeability for nigericin, relative to valinomycin. Indeed, the samples with valinomycin all demonstrated enhanced permeability. On the other hand, nigericin was effective at dissipating the pH gradient completely. The introduction of both ionophores had a substantial impact on membrane permeability and therefore these ionophores offer a relatively straightforward way of modulating ion flux across lipid and hybrid vesicles (113). All measurements so far have been conducted in HEPES buffer supplemented with 20 mM K_2SO_4 . Comparing the pH response of vesicles in buffer supplemented with different amounts of K^+ (Figure 4.49), provide a strategy to infer co-/counter-ion limited response of vesicle suspensions to pH gradients. For lower K^+ concentrations in the presence of valinomycin, a reduced pH response was expected. Indeed, it was found that the vesicle suspensions containing less K^+ had a significantly lower pH response compared to vesicle suspensions with higher K^+ concentration. Again, this effect was only observed in vesicles containing low amounts of PDMS polymer (0/100 PDMS/PC and 25/75 PDMS/PC). For 43/57 PDMS hybrids and PDMS polymersomes permeability didn't change significantly.

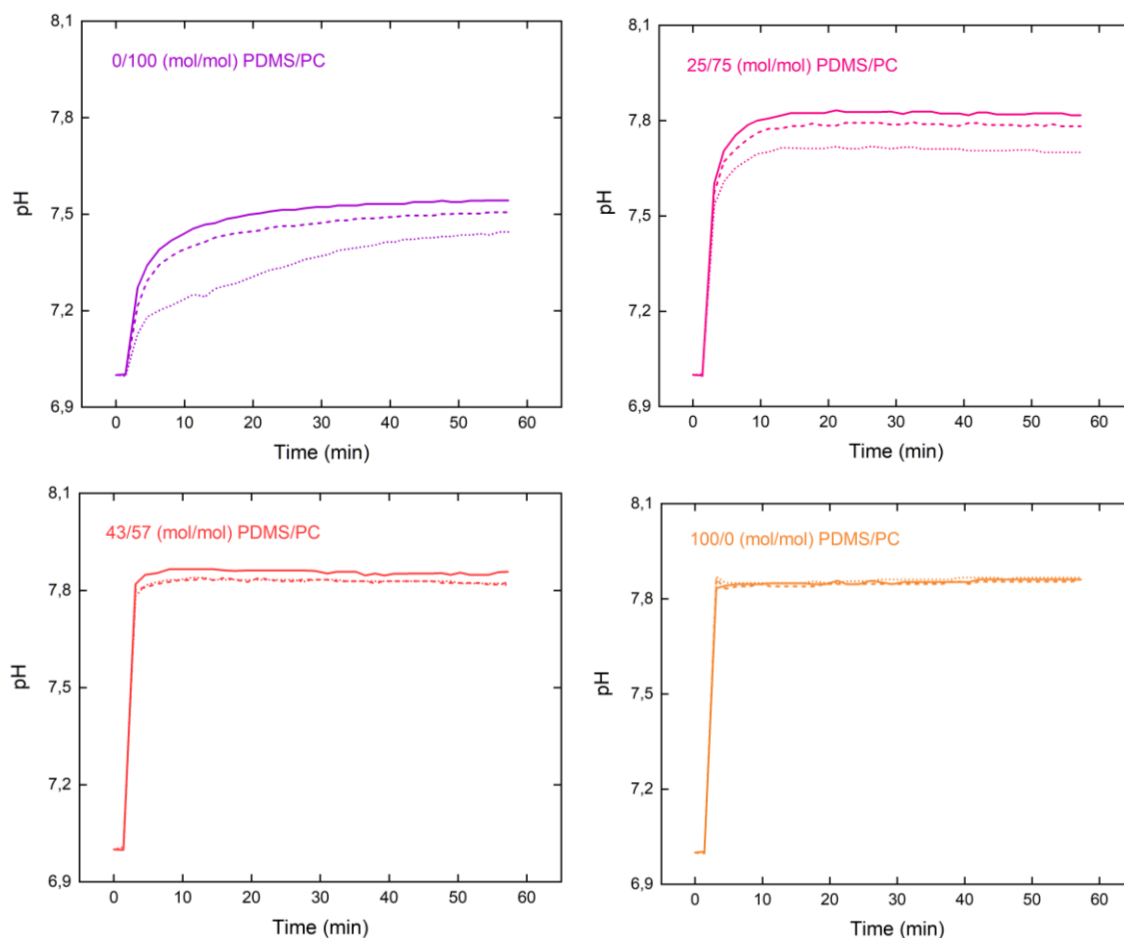


Figure 4.48 pH response of vesicles after addition of 77 mM NaOH in the presence of different amounts of valinomycin.

Solid line: 1.5 mM valinomycin, dashed line: 0.15 mM valinomycin, dotted line: 0 mM valinomycin. Measurements are performed in 40 mM HEPES, 20 mM K_2SO_4 , pH 7.0.

The data shown in Figure 4.49 reveal a different behaviour depending on the available co-ions that is inconsistent with a non-selective detergent effect, and more consistent with a selective transport of K^+ across the membrane. This outcome can be underlined by previous literature work (113).

4 Results and Discussion

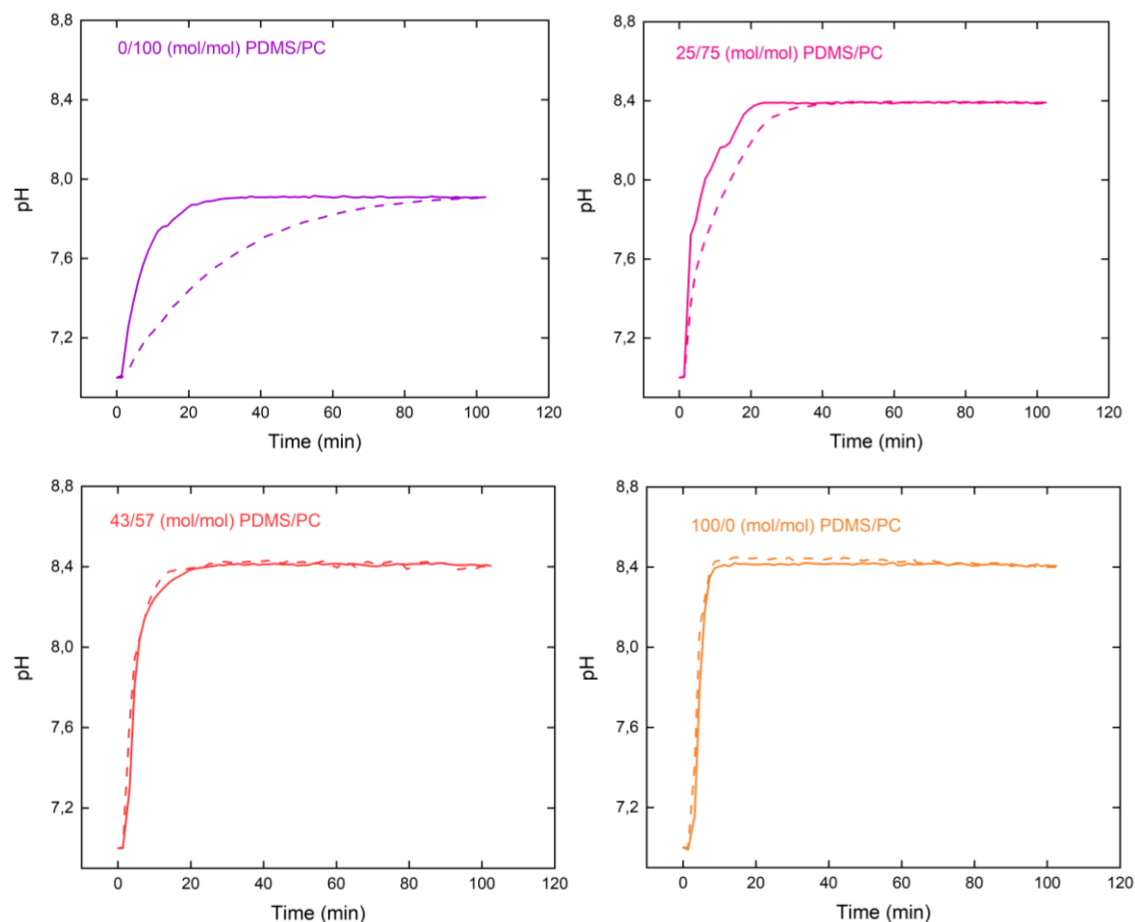


Figure 4.49 pH response of vesicles after addition of 77 mM NaOH and 1.5 mM valinomycin in the presence of various concentrations of K^+ .

Solid line: 100 mM K^+ ($K^+_{in} = K^+_{out} = 100$ mM), dashed line: 50 mM K^+ ($K^+_{in} = K^+_{out} = 50$ mM). Vesicles were prepared in 40 mM HEPES, 100 mM K_2SO_4 , pH 7.0 or 40 mM HEPES, 50 mM K_2SO_4 , pH 7.0. Measurements were performed in the same buffer, respectively.

4.3.3.7 Long-term stability

To prove the hypothesis of improved long-term stability of proteins in hybrid and polymer compartments over pure liposomes, the ATP module co-reconstituted with bR patches into different compartments, was monitored over 28 days (Figure 4.50). Samples were stored at 4°C during this period. To prove significant differences ($*P \leq 0.005$) between lipid and hybrid vesicles, an unequal variance t-test (Welch's test) was performed.

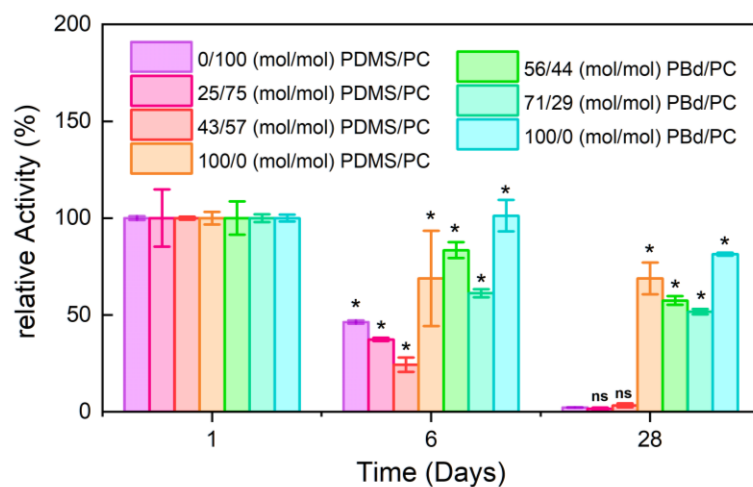


Figure 4.50 Hybrid vesicles co-reconstituted with bR patches improve long-term stability of the ATP module.

The activity is normalized to the activity at day 1. * $P \leq 0.005$, nonsignificant (ns) $P > 0.005$ (P values are generated by unequal variance t-test (Welch's test) for comparison of each hybrid membrane composition to the lipid vesicle sample). $n \geq 3$; error bars represent standard error of the mean (SEM). Measurements were performed in 20 mM HEPES, 25 mM $MgCl_2$, 50 mg/ml sucrose, pH 7.5 (inner solution) and 10 mM Tris-HCl, 5 mM NaH_2PO_4 , 50 mM KCl, 2 $MgCl_2$, 1 mM DTT, pH 7.5 (outer solution) at room temperature. $[ADP] = 360 \mu M$, $[P_i] = 5 \text{ mM}$, $[\text{lipid}] = 0.022 \text{ mg/ml}$, $[EF_oF_1] = 1.3 \text{ nM}$, $[bR] = 88 \text{ nM}$. Proteins were reconstituted with 0.8 % Triton.

Figure 4.50 shows the functionality normalized to the activity at day 1. All values were derived by the middle value of three independent measurements. The error bars show the standard deviation, respectively. The results indicate that compared to PC lipids all hybrid and polymer vesicles show a significant difference regarding the protein activity at day 6. At day 28 significant differences compared to liposomes could be only proven for PDMS polymersomes and PBd hybrid and polymer vesicles. PDMS hybrids in contrast didn't show any significant difference.

4.4 ATP production in IMVs

Another option to supply a synthetic cell with energy, can be realized by directly using the metabolic pathway including oxidative phosphorylation from already existing endogenous energy regeneration in *E. coli* lysates (124). Optimizing lysate production conditions to keep this pathway active, enables the use of inexpensive substrates including pyruvate and glutamate or even maltodextrose for energy production. These compounds are metabolized by the enzymes of glycolysis and the TCA-cycle to provide reduction equivalents ($NADH/FADH_2$). These reduction equivalents are, as in living cells, converted to ATP within the lysate using oxidative phosphorylation on Inverted inner Membrane Vesicles (IMVs) (124). IMVs can be isolated

4 Results and Discussion

relatively easy from *E. coli* cells with a special cell homogenization procedure, whereby the catalytic domain of ATP synthase can be accessed from the outer environment. ATP is produced by simple consumption of NADH (125).

The reduction equivalents drive the respiratory chain. Oxygen acts a final electron acceptor. A proton gradient over the membrane is established which enables ATP regeneration. A schematic presentation of IMVs is shown in Figure 4.51.

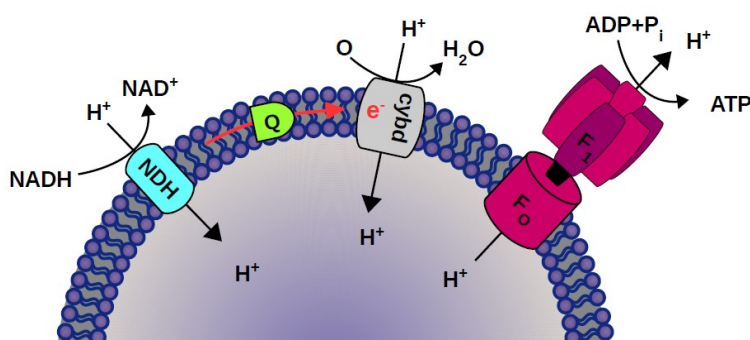


Figure 4.51 Scheme of inverted membrane vesicles (IMVs).

NADH is oxidized by NADH dehydrogenase (NDH). Ubiquinone (Q) is reduced and re-oxidized by terminal oxidases (cybd) whereby electrons are transferred to oxygen. The established proton gradient is used by ATP synthase to form ATP via oxidative phosphorylation.

One NADH is converted in 2 protons that are passing the membrane. The *E. coli* ATP synthase uses 4 protons to synthesize one ATP (126). Therefore, the theoretical stoichiometry is 2 NADHs are converted in 1 ATP.

4.4.1 ATP production in Wildtype IMVs

The ATP production of IMVs was monitored using the luciferin-luciferase assay as described in chapter 3.5.2. The IMV concentration was kept constant at a final concentration of 5.3×10^9 vesicles/ml and the amount of NADH added was varied between 9 and 178 μ M. The addition of NADH initiated the production of ATP and the reaction was recorded by an increase in luminescence intensity. The ATP production curves (Figure 4.52 A) were generated from the luminescence signal using a standard curve (Figure A.6).

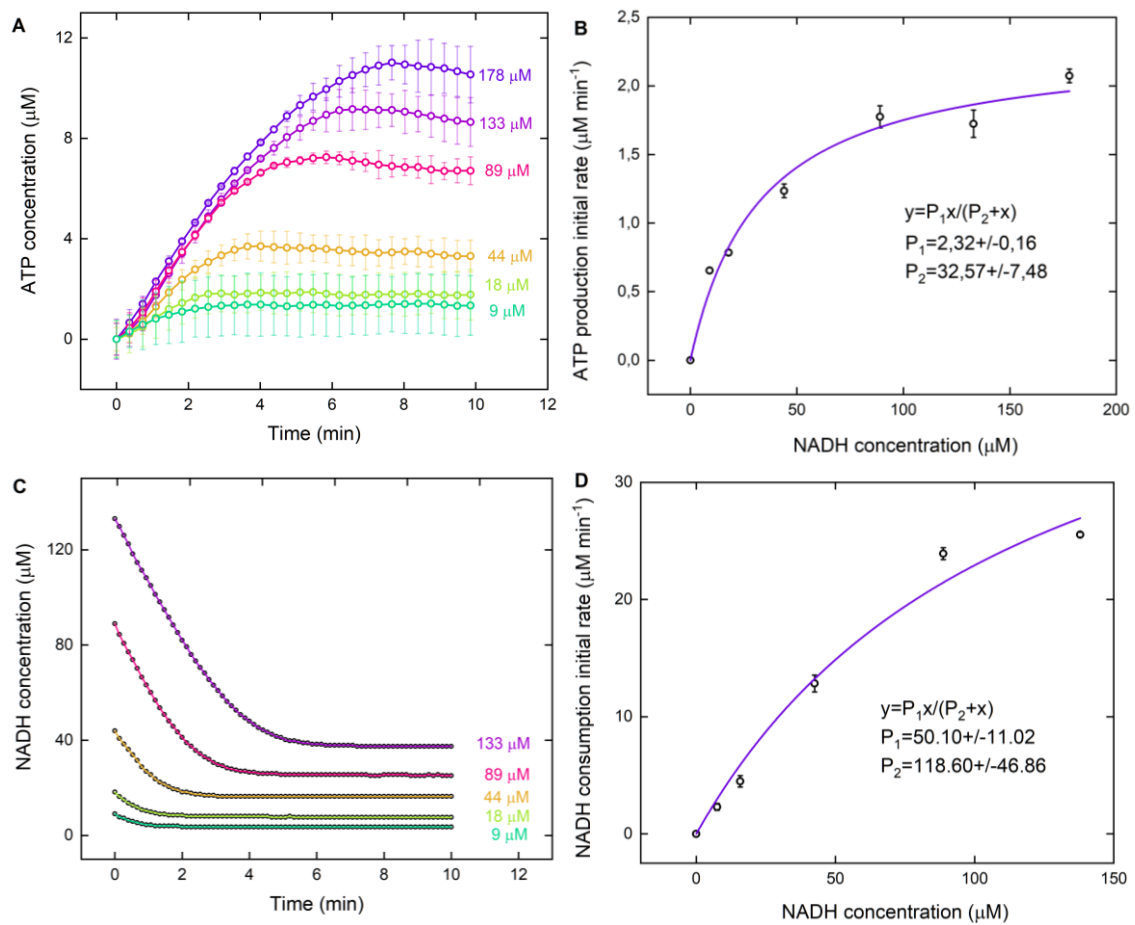


Figure 4.52 ATP production and NADH consumption in wildtyp IMVs.

(A) NADH-driven ATP production at different NADH concentrations. ATP concentration over time was determined using the luciferin/luciferase assay. (B) Initial rates of ATP production as a function of NADH concentration. (C) NADH consumption over time as measured by absorption change at 340nm. (D) Initial rates of NADH consumption as a function of NADH concentration. All measurements were performed in 20 mM Tris acetate (pH 7.8), 5 mM $\text{Mg}(\text{CH}_3\text{COO})_2$, 1 mM DTT, 0.5 mM KH_2PO_4 , 0.5 mM MgCl_2 , 0.25 mM ADP, 0.1 mM EDTA.

All curves were corrected to $[\text{ATP}] = 0$ at $t = 0$. Afterwards the initial reaction velocity v_0 (ATP production initial rate) was determined by linear regression from $t = 0$ to $t = 2$ s. The reaction velocities v_0 were plotted against the NADH substrate concentration (Figure 4.52 B). Fitting the data using the Michaelis Menten equation yielded the kinetic parameter for ATP production $v_{\text{max,ATP}} = P_1 = 2.32 \text{ min}^{-1}$ and $K_{\text{m,ATP}} = P_2 = 32.57 \text{ } \mu\text{M}$. It has to be mentioned that Michaelis Menten kinetic is actually only valid for simple first order reactions. In this case there are three substrates: ADP, P_i and NADH (H^+ ions). Under the assumption that both substrates (ADP, P_i) are present in excess and that the conversion from NADH to H^+ is not the limiting step of the reaction, one can assume a reaction pseudo-first order. Anyway, describing this reaction with Michaelis Menten kinetic is a

4 Results and Discussion

vast simplification and should be replaced by a suitable model description in the future. Therefore, also ATP production kinetics depending on ADP and P_i concentration, while NADH is present in excess and is kept constant, should be analysed. Determination of the exact ATP synthase concentration in IMVs is difficult due to the presence of other enzymes and proteins in the *E. coli* lysate. This is another issue to be addressed in the future for the correct kinetic description of this system. Due to various differences in this reaction compared to the ATP production using the ATP module (chapter 4.3), a direct comparison of these kinetics is difficult.

In the next experiment the NADH substrate consumption was detected instead of the ATP production. Besides that, all other parameters of the experiment were kept constant (buffer, IMV concentration). The NADH consumption curves could be calculated directly by the absorption depletion at 340 nm as described in chapter 3.5.3.1. The results are shown in Figure 4.52 C. The consumption curves were corrected to the initial NADH substrate concentration and the initial reaction velocity v_0 was determined by linear regression from $t=0$ to $t=30$ s. Plotting v_0 against the NADH concentration yielded the results shown in Figure 4.52 D. A hyperbole fitting using the Michaelis-Menten equation produced the kinetic parameter for NADH consumption $v_{\max, \text{NADH}}=P_1=50.10 \text{ min}^{-1}$ and $K_{m, \text{NADH}}=118.60 \text{ }\mu\text{M}$.

4.4.2 ATP production in overexpressed IMVs

IMVs with overexpressed ATP synthase were isolated by Claudia Bednarz and were tested for ATP production as described in chapter 4.4.1 for wildtype IMVs. The ATP production curves with constant IMV concentration of 5.3×10^9 vesicles/ml and various NADH substrate concentrations are shown in Figure 4.53 A.

Initial reaction velocities v_0 were determined and plotted against the NADH substrate concentration (Figure 4.53 B). The kinetic parameters for ATP production $v_{\max}=P_1=0.88 \text{ min}^{-1}$ and $K_m=P_2=61.51 \text{ }\mu\text{M}$ were determined using the Michaelis-Menten equation. Comparing the data with the data for wildtype IMVs, the ATP production in overexpressed IMVs is only around half as much as in wildtype IMVs. This result shows that the amount of ATP synthase in IMVs is not the limiting factor for ATP production. It is therefore likely, that rather the established proton gradient is the limiting factor. In this regard, it has to be mentioned that a high number of proteins (especially ATP synthase) can increase the passive proton permeability of the membrane, resulting in a decrease of ATP production rates (25).

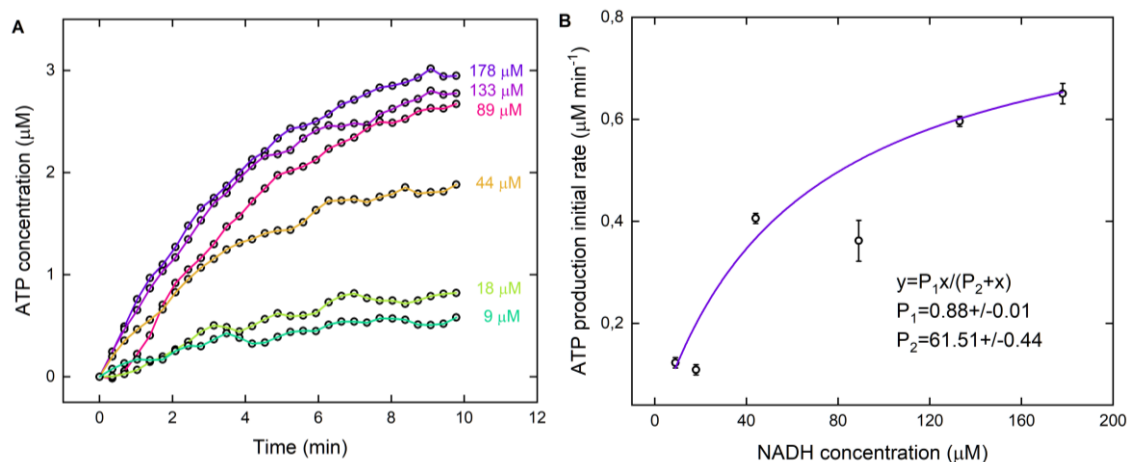


Figure 4.53 ATP production in overexpressed IMVs.

(A) NADH-driven ATP production. ATP concentration over time was determined using the luciferin/luciferase assay. (B) Initial rates of ATP production as a function of NADH concentration. All measurements were performed in 20 mM Tris acetate (pH 7.8), 5 mM Mg(CH₃COO)₂, 1 mM DTT, 0.5 mM KH₂PO₄, 0.5 mM MgCl₂, 0.25 mM ADP, 0.1 mM EDTA.

4.4.3 Comparison of kinetic data in bulk and droplets

Thomas Beneyton and his group from Bordeaux encapsulated the NAD regenerating IMVs into water-in-oil droplets (Figure 4.54).

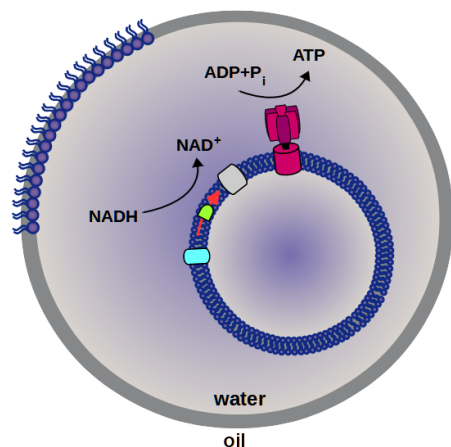


Figure 4.54 Scheme of IMVs encapsulated in water-in-oil droplets.

They determined the NADH consumption kinetic in bulk and inside the droplets using the NADH fluorescence depletion (Figure 4.55 B) (127). In contrast to the measurements performed in this work, they kept the NADH concentration constant at 250 μM and varied the IMV concentration between 1×10^9 and 1×10^8 vesicles/ml.

4 Results and Discussion

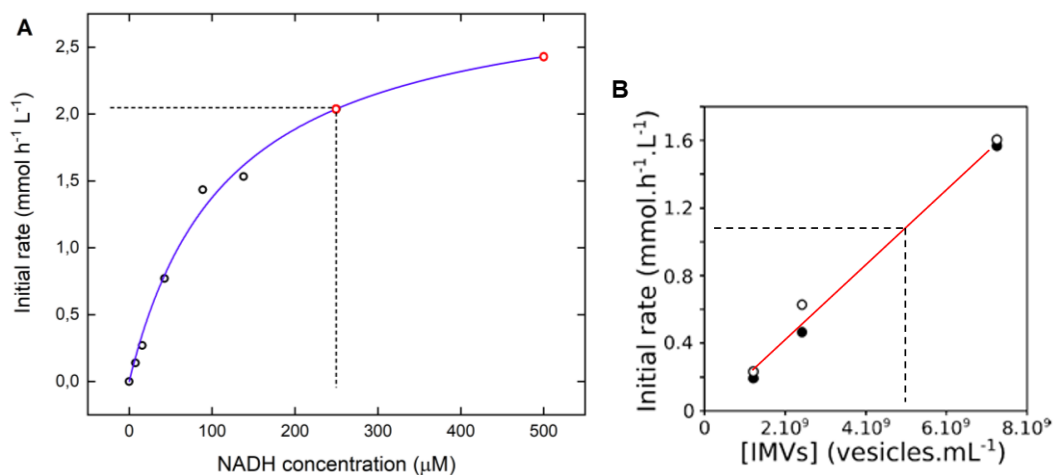


Figure 4.55 Comparison of IMVs kinetic in bulk and in droplets.

(A) Initial rates of NADH oxidation for different NADH concentrations for a solution containing 5.3×10^9 vesicles per ml. The red points were calculated using the fit from Figure 4.52 D. The dotted line indicates the initial rate for 250 μM NADH. Measurements were performed in 20 mM Tris acetate (pH 7.8), 5 mM Mg (CH₃COO)₂, 1 mM DTT, 0.5 mM KH₂PO₄, 0.5 mM MgCl₂, 0.25 mM ADP, 0.1 mM EDTA. (B) Initial rates of NADH oxidation for different IMV concentrations in 30 μl droplets (black circles) and in bulk (open circles) as measured by Thomas Beneyton (University Bordeaux) after addition of 250 μM NADH. The dotted line indicates the initial rate for approximately 5.3×10^9 vesicles/ml. Reactions were performed in NaOH-Tricine buffer (100 mM, pH 8.0) with 5 mM MgCl₂.

To compare their kinetic data with the data of this work, the Michaelis-Menten fit from Figure 4.52 D was used to calculate the initial rate of NADH consumption for a NADH substrate concentration of 250 μM (Figure 4.55 A). The initial rates at the same NADH and IMV concentrations are visualized by the dotted lines in Figure 4.55. Comparing both data, it gets clear that the rates determined in this work are somewhat higher compared to the rates determined by Thomas Beneyton. This might be explained by differences in the measurement methods or by the usage of different buffer systems. For example, in this work DTT was added to the buffer in order to stabilize proteins, which might result in higher enzyme activity. According to the measurement method, in this work NADH depletion is detected by absorption changes at 340 nm. Thomas Beneyton determined the rates by fluorescence measurements.

4.5 Combining the ATP module with other functional modules

The ATP regeneration module was coupled with different other functional modules in order to serve as an energy supply unit. Overall, 4 different combinations could be realized due to the close collaborations inside of the MaxSynBio consortium. With this respect the energy module was combined with a multistimuli sensing adhesion unit for self-positioning (Prof. Dr. Seraphine Wegner, formerly MPI Mainz and currently Institute of Physiological Chemistry & Pathobiochemistry), with flagella movement (Dr. Azam Gholami, MPI Göttingen) and with actin-myosin contraction (Dr. Sven Vogel, MPI Martinsried). For these integrations the energy modules were prepared in our lab and optimized with respect of the operating conditions. The coupling experiments were done in the partner lab by Ph. D students working on the development of the coupling modules (e.g. Mainz, Göttingen), by myself in our labs (simple metabolism) or by Dr. Sven Vogel and me during my research visit at the MPI Martinsried.

4.5.1 *Multistimuli sensing adhesion unit for the self-positioning of minimal synthetic cells*

The work described in the following is the ongoing research in the labs of Prof. Wegner. The experiments were conducted in cooperation with Dongdong Xu.

In order to support their survival, cells have the ability to sense different environmental signals, which allow them to react and position themselves. Introducing such features to bottom-up assembled minimal cells is an important step forward to their autonomy.

In this study, a multistimuli sensitive adhesion unit was coupled to the ATP module to form a minimal system that adheres to places that have the right environmental parameters for its ATP production. The multistimuli sensitive adhesion unit can sense environmental stimuli including light, pH, oxidative stress and the presence of metal ions and can regulate the adhesion of the synthetic cell to a substrate in response to these stimuli following a chemically coded logic (Figure 4.56). The adhesion is based on an interaction between the improved Light Induced Dimer (iLID) and Nano. Interaction between these proteins is only possible in presence of light and under non-oxidizing conditions (Figure 4.56, right). On the other hand, the adhesion unit is composed on a His-tag binding motive that binds to NTA complexes in the presence of Ni^{2+} ions at neutral pH (Figure 4.56, middle).

4 Results and Discussion

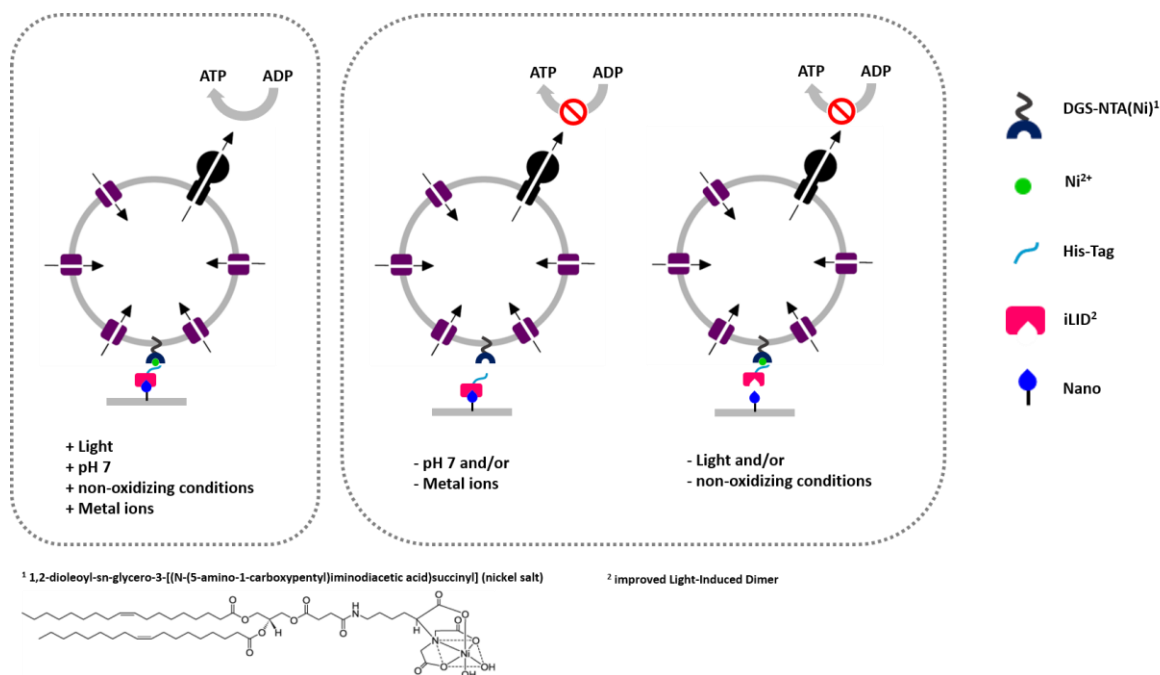


Figure 4.56 Schematic presentation of a multistimuli responsive adhesion unit, which responds to light, pH, oxidative stress and the presence of metal ions.

The adhesion unit is composed of the proteins iLID and Nano, which bind to each other under blue light and non-oxidizing conditions. iLID consists of a His-Tag. A functionalized lipid (DGS-NTA) is integrated in the vesicle membrane of the ATP module. In the presence of Ni^{2+} and neutral pH (pH 7) DGS-NTA can bind to iLID/Nano over a Ni^{2+} mediated interaction. Only if all four conditions are met, the ATP module will anchor on the surface and ATP is produced. This project has been conducted in cooperation with Prof. Dr. Wegner (formerly MPI for Polymer Research and currently Institute of Physiological Chemistry & Pathobiochemistry).

By combining the adhesion unit with the light-driven ATP regeneration module in one synthetic cell, this cell could adhere to places optimal for ATP production showing the capability of this adhesion unit to allow synthetic cells to self-position and carry out their functions (128).

The adhesion unit was designed in a way that leads to the adhesion under conditions that the ATP module requires to function. Therefore, following molecular components were defined as adhesion receptors for the minimal cell. First, a sensitivity unit for light was defined using the protein interaction between iLID (Improved Light-induced Dimer) and Nano. Both proteins are specifically binding to each other under blue light (129; 130). The iLID protein is an engineered version of the LOV2 domain (light oxygen voltage sensing domain) and is therefore also sensitive to oxidative stress. A second unit for sensitivity to pH and the presence of metal ions was defined by the interaction between a His-tag and a NTA group, which relies on the presence of a metal ion

such as Ni^{2+} at neutral pH. (131) The integration of the adhesion unit was realized by including a Ni^{2+} linker modified lipid (DGS-NTA) in the membrane of the ATP module.

Therefore, liposomes were prepared from a mixture of PC lipids and DGS-NTA- Ni^{2+} with the film hydration method. Co-reconstitution of bR and ATP synthase was performed with the standard procedure described in chapter 3.6.1.2. As a control, proteins were co-reconstituted in otherwise identical conditions in liposomes made of PC only. The results of ATP synthesis measurements show that the integration of DGS-NTA- Ni^{2+} had only little influence on the functionality of the ATP module, remaining around 87% activity (Figure 4.57).

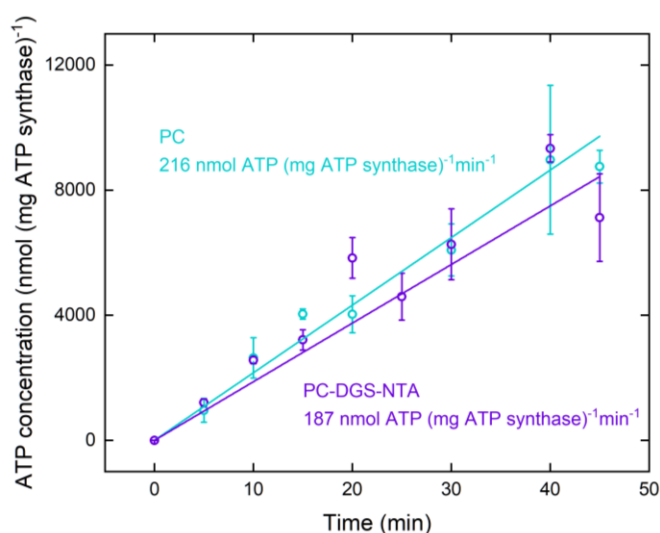


Figure 4.57 Light-driven ATP synthesis of vesicles in the absence (PC) and presence (PC-DGS-NTA) of the functionalized DGS-NTA lipids.

Results show that the integration of DGS-NTA in the membrane has only little influence on the ATP production rate. The activity was determined by linear regression. Measurements were performed in 20 mM HEPES, 2.5 mM MgCl_2 , 50 mg/ml sucrose, pH 7.5 (inner solution) at room temperature. The same outer solution is adjusted with 5 mM NaH_2PO_4 , 2 mM MgCl_2 , 1 mM DTT and 360 μM ADP. $[\text{ADP}] = 360 \mu\text{M}$, $[\text{P}_i] = 5 \text{ mM}$, $[\text{lipid}] = 0.022 \text{ mg/ml}$, $[\text{EF}_0\text{F}_1] = 1.3 \text{ nM}$, $[\text{bR}] = 81 \text{ nM}$. Proteins were reconstituted with 0.8 % Triton. All error bars represent the standard error of the mean ($n=3$).

Figure 4.58 A shows the ADP to ATP conversion of the modified ATP module coupled to the multistimuli sensing adhesion unit when changing the environmental parameters as measured in the labs of Prof. Wegner. Considering all possible combinations of these four parameters (Light, pH, non-oxidizing conditions, presence of metal ions), the synthesis of ATP was tested under 16 different conditions. The results prove that ATP is only produced when all four conditions are met (blue or white light irradiation, neutral pH, non-oxidizing conditions and the presence of Mg^{2+}

4 Results and Discussion

ions). Changes of any of these parameters result in malfunction of different components in the ATP synthesis machinery and no conversion of ADP to ATP occurs. For instance, bR will not pump any protons in the absence of light. EDTA removes Mg^{2+} ions, which are a cofactor of ATP synthase and are required for its activity. Likewise, oxidative stress (induced by H_2O_2) can lead to the oxidation of sulphur containing amino acids (cysteine and methionine) and alter protein structure and activity, which can damage highly sensitive membrane proteins like ATP synthase and bR. Both of these proteins are pH sensitive and inactive at low ($pH < 4$) or high ($pH > 9$) pH.

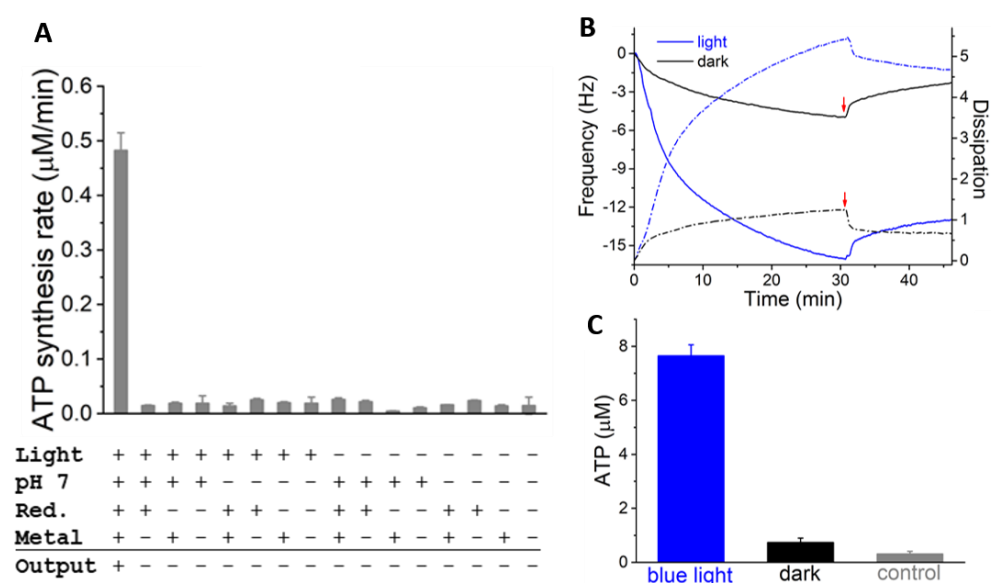


Figure 4.58 Integration of the multistimuli responsive adhesion module with the ATP module. (128)

(A) ATP synthesis rates under different conditions. ATP is only produced under illumination (+ Light), at neutral pH (+ pH 7), non-oxidizing conditions (Red. +) and/or in the presence of metal ions (Metal +). (B) Quartz Crystal Microbalance (QCM) curves of Nano functionalized light to ATP module on iLID functionalized lipid bilayers in the dark (black) and under blue light (blue). Changes in frequency are shown with solid and changes in dissipation with dashed lines. Red arrows indicate the washing step. (C) ATP synthesis of the energy module that adhered to the QCM-D crystal under blue light and in the dark, after 30 min subsequent exposure to blue light. As a control, one sample was kept in the dark throughout the whole experiment. Measurements were performed by Dongdong Xu (MPI Mainz).

To monitor the adhesion of the proteoliposomes and subsequently their ATP production, Quartz Crystal Microbalance measurements with Dissipation monitoring (QCM-D) have been performed by Dongdong Xu at the MPI Mainz (Figure 4.58 B). The setup had a window module that allowed non-interfering and label free illumination during the measurements. The Nano functionalized liposomes capable of ATP production were either added onto the iLID decorated QCM-D crystal in

the dark or under blue light illumination at pH 7.4 and in the absence of H₂O₂ and EDTA. Subsequently, nonbinding vesicles were washed off after 30 min of incubation. The results of the QCM-D measurements showed that the frequency decreased more under blue light illumination than in the dark ($\Delta f_{\text{blue}} = -12.8$ Hz, $\Delta f_{\text{dark}} = -2.3$ Hz). As a decrease in frequency correlates with the absorption of mass to the crystal, the results evidenced that more vesicles bound under blue light than in the dark. In parallel, the dissipation increased more under blue light than in the dark ($\Delta D_{\text{blue}} = 4.8$, $\Delta D_{\text{dark}} = 0.6$), which demonstrated the formation of a soft and highly hydrated layer. In particular, a large increase under blue light reveals that entire liposomes filled with buffer adhere to the surface. In comparison, if not entire vesicles but just pure protein bound to the surface, the change in dissipation would be much smaller ($\Delta D_{\text{blue}} = 1.2$ for pure Nano protein) due to the formation of a more rigid protein layer.

To evaluate the functionality of the energy conversion module in regard to adhesion on these QCM-D surfaces, buffer with ADP was flushed into the chambers. Both chambers (previously kept in the dark and under blue light during the adhesion step) were illuminated with blue light for 30 minutes to allow light-driven ATP conversion. At the end, the QCM-D chambers were opened and ATP was measured (Figure 4.58 C). This analysis indicated that the liposomes that adhere to the surface under blue light are also capable to produce ATP. In contrast, for the crystal kept in the dark, only few liposomes adhered, resulting in low ATP production upon illumination. As a negative control, one sample was kept in the dark during both the adhesion and the ATP production step. No ATP production was observed in the negative control.

This study shows the coupling between a multiple stimuli response and the conversion of light to ATP. The adhesion unit is able to bring different functional modules of a synthetic cell into places, which are favourable for many life forms including neutral pH, free metal ions and the absence of oxidative stress. Light illumination is among the most effective ways to power synthetic cells, where also the adhesion upon light illumination is an important asset in this context. The idea of using stimuli responsive adhesion elements to position cells or modules is highly transferable and other interactions than the Ni²⁺-NTA/His-tag and iLID/Nano can be used to colonize different environments with functional modules or synthetic cells (128).

4.5.2 Reactivation of isolated flagella via light-driven ATP regeneration module

Bottom-up assembly of artificial systems capable of self-sustained directed movement is still a challenge in the context of synthetic biology. Artificial systems capable of directed movement are of high interest in the development of applications in the field of medical treatments or technical applications. In this regard, the light-driven ATP module has been combined with a motility functional unit based on demembranated flagella together with the MPI for Dynamics and Self-Organization (Göttingen). Successful coupling enabled the ATP supply for the dynein molecular motors that converted chemical energy into mechanical work (Figure 4.59).

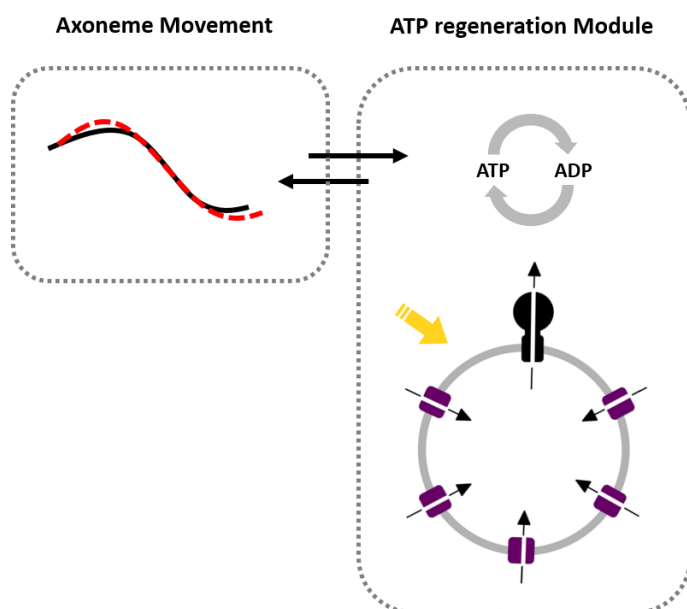


Figure 4.59 Scheme of coupling the ATP regeneration module with flagella movement triggered by light.

The chemical energy in form of ATP produced by the ATP module is converted in active movement of demembranated flagella. This project has been conducted in cooperation with the MPI for Dynamics and Self-Organization (Göttingen).

To drive flagella movement the ATP module has been prepared as described in chapter 3.6.2.1 using bR in form of membrane patches to avoid material loss during solubilization and consequently to maximize ATP production rates. To ensure functional activity of flagella, vesicles were prepared in HMDEK buffer, which is the optimal buffer reported for flagella. Under these conditions ATP production rates of $4.5 \mu\text{M ATP (mg EF}_0\text{F}_1) \text{ min}^{-1}$ could be achieved (Figure 4.60). This ATP production rate is relatively high compared to the rates earlier reported in this work,

which is probably due to a relatively high concentration of bR and quiet active ATP synthase fraction used in this co-reconstitution. Another factor improving ATP production rate was a comparably high ADP concentration used in this experimental setup.

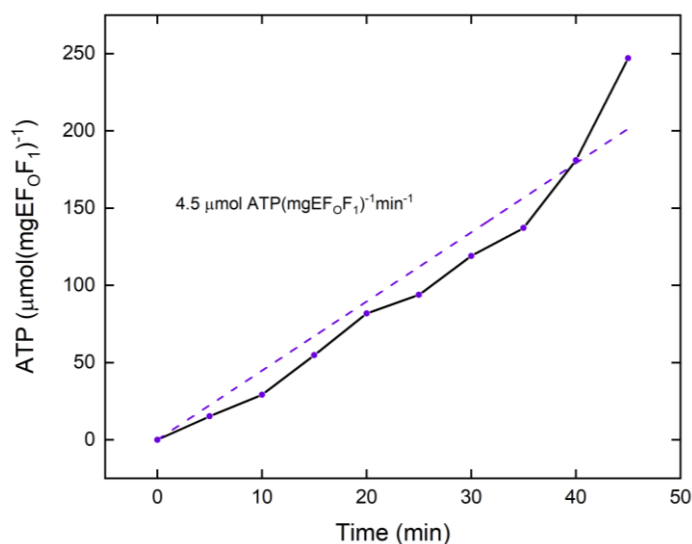


Figure 4.60 Light-driven ATP synthesis in axoneme buffer using a microscope light (5 W) for irradiation.

The activity was determined by linear regression. Measurements were performed in 30 mM HEPES, 5 mM MgSO₄, 1 mM DTT, 1 mM EGTA, 50 mM Kalium acetate, 1% PEG, 0.2 mM Pefabloc, pH 7.35 (inner solution) at room temperature. The same outer solution was adjusted with 5 mM NaH₂PO₄, 2 mM MgCl₂, 1 mM DTT and 810 μM ADP. [ADP] = 810 μM, [P_i] = 5 mM, [lipid] = 0.022 mg/ml, [EF_oF₁] = 2.6 nM, [bR] = 160 nM. Proteins were reconstituted with 0.8 % Triton.

As shown in Figure 4.61 A and B, different light sources can be used for ATP production without significant losses in ATP production. Figure 4.60 A shows the ATP production under a 5 W microscope lamp and confirms that a conventional microscope lamp is enough to drive ATP synthesis.

The ATP module was coupled to flagella (10 μm in length) isolated from green algae *C. reinhardtii* at the MPI Göttingen. Upon illumination, ATP is produced and powers the activity of axonemal dyneins, converting chemical energy to mechanical energy by sliding neighbouring microtubule drouplets relative to each other. Due to mechanical constraints, mircotubuli (MT) doublets are not free to slide, instead sliding will be converted to rhythmic bending deformations that propagate along the contour length of axonemes with a frequency which depends on the ATP concentration. Higher ATP concentrations are achieved by longer illumination times of the ATP module. Interestingly, we observed that even after 1 min of illumination, axonemes could be reactivated with a beating frequency of 20 Hz. Therefore, we analysed the first 5 minutes of ATP production

4 Results and Discussion

in more detail (Figure 4.61 A, inset) and could prove ATP concentrations of around 650 nM after one min of illumination. The quantitative analysis of the beating frequency of reactivated axonemes confirmed that they beat faster at higher ATP concentrations generated by longer illumination periods (Figure 4.61 D). These results are in good agreement with the frequency trend reported by Geyer et al. (132). However, we observed that axonemes beat even at ATP concentrations well below 30 μ M when using the ATP module for ATP regeneration. Therefore, we performed further measurements with fluorescent labelled vesicles to examine the possibility of vesicle accumulation around the axonemes which might cause higher locally ATP concentrations. These experiments didn't confirm any higher concentrations of vesicles.

Figure 4.62 A and B shows exemplary oscillatory motion of an axoneme in response to ATP generated by light. Curvature waves propagating with frequencies up to 72 Hz along the contour length could be observed (Figure 4.62 C). For quantification of the oscillatory motion of axonemes, filaments were tracked using the gradient vector flow technique (GVF) as described in chapter 3.6.2.3. The curvature of the mean shape was measured and configurations of an actively beating axoneme were rotated and translated such as the basal end defined as $s=0$ is at position (0,0). The tangent vector at the basal end is orientated in the x direction (Figure 4.62 D).

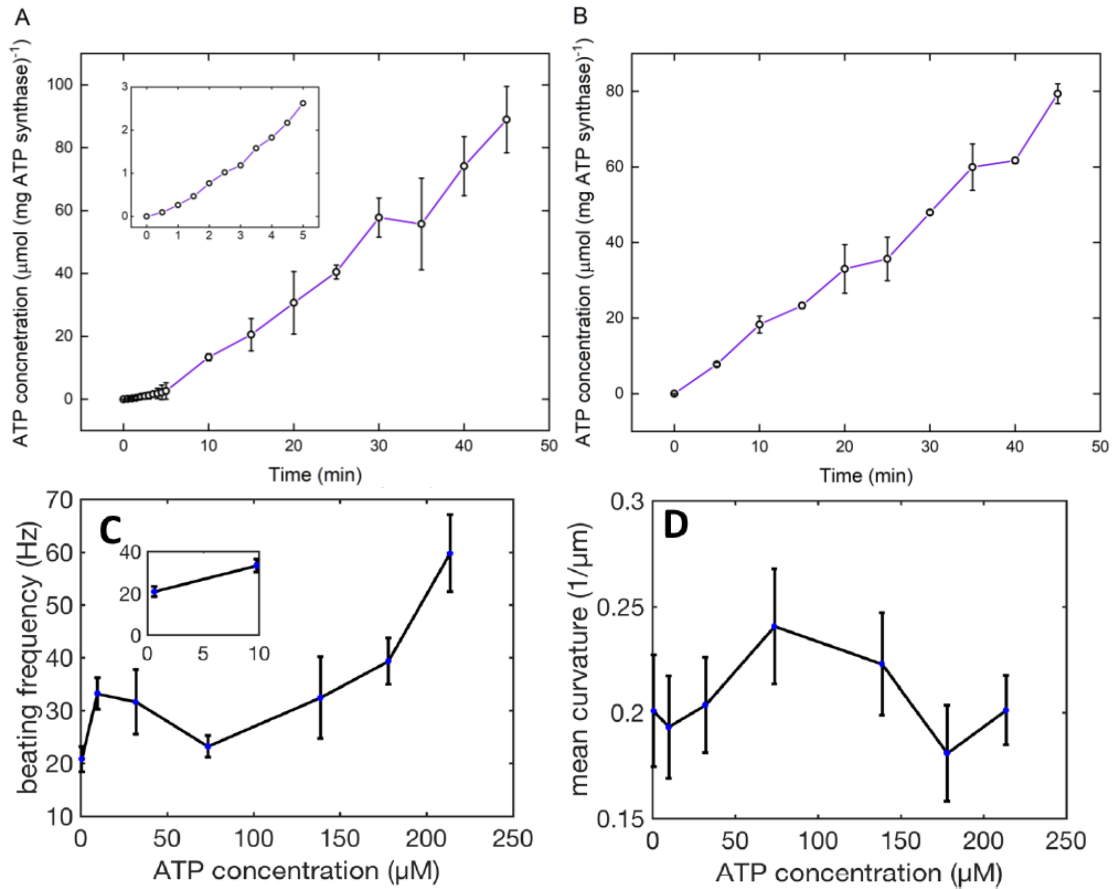


Figure 4.61 Functionalized liposomes were illuminated for different times, generating ATP concentrations up to 330 μM before being mixed with axonemes for reactivation process.

(A) Illumination under microscope light (5W) located 25 cm away from the sample. (B) Illumination with a LED lamp (50 W) located 25 cm away from the sample. All measurements were performed in 30 mM HEPES, 5 mM MgSO_4 , 1 mM DTT, 1 mM EGTA, 50 mM Kalium acetate, 1% PEG, 0.2 mM Pefabloc, pH 7.35 (inner solution) at room temperature. The same outer solution was adjusted with 5 mM NaH_2PO_4 , 2 mM MgCl_2 , 1 mM DTT and 810 μM mM ADP. $[\text{ADP}] = 810 \mu\text{M}$, $[\text{P}_i] = 5 \text{ mM}$, $[\text{lipid}] = 0.022 \text{ mg/mL}$, $[\text{EF}_0\text{F}_1] = 2.6 \text{ nM}$, $[\text{bR}] = 80 \text{ nM}$. Proteins were reconstituted with 0.8 % Triton. All error bars represent the standard error of the mean ($n=3$). (C) Axonemes beat faster at higher ATP concentrations produced by longer illumination times of the ATP module. (D) Mean curvature of axoneme's mean shape does not significantly depend on the ATP concentration. Measurements of (C) and (D) were performed by Raheel Ahmed (MPI Göttingen).

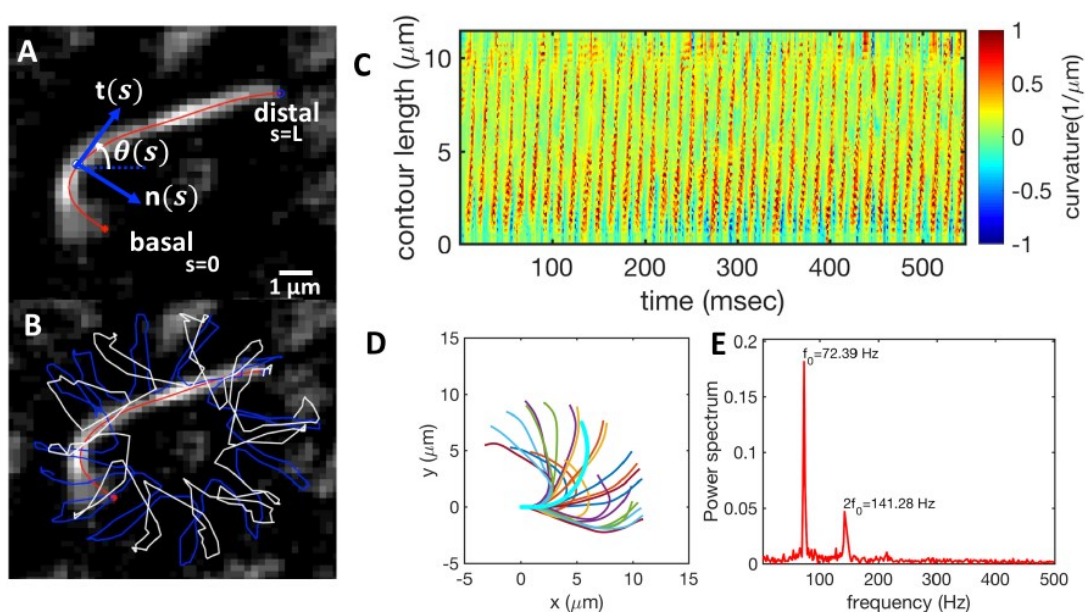


Figure 4.62 Reactivation of axonemes by light-driven ATP module.

(A) Actively beating axoneme in the presence of $213 \mu\text{M}$ ATP produced upon illumination of energy module for 45 min by microscope light. (B) As axoneme beats with frequency of 72 Hz, it rotates with slower frequency of 2 Hz. Blue and white trajectories show the trace of basal and the distal end, respectively. (C) Curvature waves propagating along the contour. (D) Axoneme's shape at different time points were translated and rotated to have the basal end at (0,0) and the orientation of the tangle vector at the basal end in the x direction. (E) Power spectrum showing dominant peak at $f_0 = 72 \text{ Hz}$ and higher frequency of $\sim 2 f_0$. Measurements were performed by Raheel Ahmed (MPI Göttingen).

The measurements presented in this study demonstrate that light-switchable photosynthetic liposomes can drive ATP-dependent activity of axonemal dyneins, thus inducing flagellar beating at constant ATP concentration. The beating frequency of axonemes could be controlled as a function of illumination of the ATP module. The light-driven ATP module can serve as efficient energy module for a variety of in vitro microtubule- and actin-based motility assays where molecular motors are actively engaged in generating and sustaining active stresses in the network. Our developed scheme could serve as a potential platform to encapsulate constituent elements such as actin, microtubules and various regulatory components inside functionalized liposomes, providing ATP in an optical-controllable fashion. ATP-driven motor activity in filamentous biopolymer networks is expected to generate active forces, driving morphological deformations in liposomes, and will further contribute to achieving the challenging goal of designing an artificial cell from the bottom-up.

4.5.3 Light-triggered glucose consumption

The coupling of the light-driven ATP module to a metabolic module has been implemented by combining light-driven ATP production with the consumption of glucose as schematically shown in Figure 4.63. As a proof of concept, a relatively simple metabolic reaction has been chosen: Hexokinase converts glucose (G) to glucose-6-phosphate (G-6-P) under the consumption of one molecule ATP.

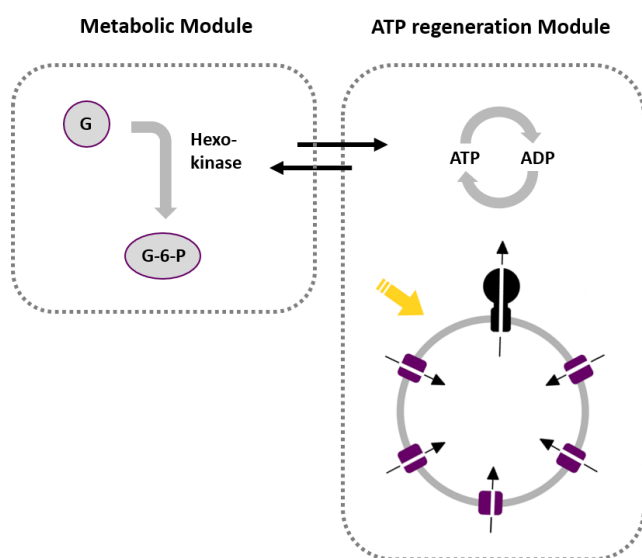


Figure 4.63 Scheme of coupling the ATP regeneration module with a metabolic module for glucose consumption triggered by light.

For measurement of light-triggered glucose consumption a solution containing the ATP module was supplemented with ADP, P_i , glucose and hexokinase as described in chapter 3.6.1. As a control, a solution containing only the ATP module, ADP and P_i was run in parallel. The reaction was started by illumination and samples were taken each 5 minutes from the reaction mixture. The reaction was stopped by the addition of trichloroacetic acid. The ATP concentration of the sample and the control was calculated as described in chapter 3.4.3.1 and the reaction rates were determined by linear regression (Figure 4.64 A). The suspension containing the ATP module, hexokinase and glucose (ATP module +hexokinase +glucose) showed barely any ATP production (0.01 nM/min). All ATP is constantly consumed by hexokinase to convert glucose in glucose-6-phosphate. This result confirmed that the concentration of hexokinase was chosen high enough and consequentially the glucose consumption reaction was not the limiting step. In contrast, the

4 Results and Discussion

control sample (ATP module) verified that the ATP module was working and that it produced 58.6 nM ATP per min.

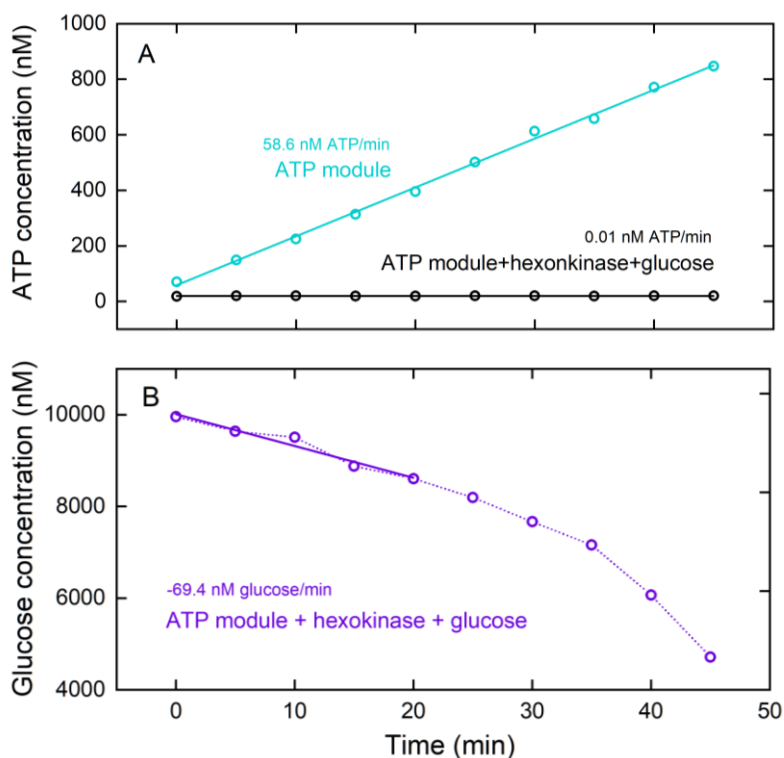


Figure 4.64 ATP and glucose concentration over time under green light illumination.

Measurements were performed in 20 mM tricine-NaOH, 20 mM succinate, 0.6 mM KCl, 80 mM NaCl (inner solution) and 200 mM tricine-NaOH, 5 mM NaH_2PO_4 , 160 mM KOH, pH 8.8 (outer solution) in the presence of 20 μM valinomycin at room temperature. $[\text{ADP}] = 180 \mu\text{M}$, $[\text{P}_i] = 5 \text{ mM}$, $[\text{lipid}] = 0.022 \text{ mg/ml}$, $[\text{EF}_0\text{F}_1] = 1.3 \text{ nM}$, $[\text{bR}] = 88 \text{ nM}$, $\Delta\psi = 143 \text{ mV}$. Proteins were reconstituted with 0.8 % Triton. For measurement of glucose consumption 10 μM glucose and 2.7 $\mu\text{g/ml}$ hexokinase (2400 U/ml) was added to the outer solution. Glucose concentration was determined using a highly sensitive glucose assay (Sigma).

The glucose concentration was determined using a highly sensitive glucose assay, which allows the detection of glucose by measuring the fluorescence intensity. Therefore, a standard curve relating glucose concentration and fluorescence signal was taken according to the manufacturers protocol (Figure A.5). The glucose concentration over time is shown in Figure 4.64 B. The glucose concentration at $t=0$ complies well with the concentration of glucose added to the solution (10 μM), which certifies that the determination of glucose with the highly sensitive assay worked. The concentration of glucose was decreasing over time with a consumption rate of -69.4 nM glucose per min. This rate is slightly higher (18%) compared to the detected ATP production rate. This

result is as expected because ATP synthase is product inhibited by ATP itself (45). Therefore, higher turnover rates are expected when ATP is constantly removed from the system.

4.5.4 Light-triggered actin-myosin contraction

Light-triggered actin-myosin contraction experiment was performed together with Dr. Sven Vogel at the MPI for Biochemistry in Martinsried. Cytoskeletal elements such as actin-myosin form a network of interlinking filaments throughout the cytoplasm and have important function in the cell, such as chromosome segregation and cytokinesis. Filamentous actin polymerizes by growing at the one end and shrinking at the other. This process is ATP-driven and allows rapid changes in the actin-myosin cytoskeletal. These changes are necessary for processes like motility or endocytosis. So far, minimal actin cytoskeleton systems have been mainly reconstituted in bulk (133). In this project, we combined ATP regeneration with the ATP-driven process of actin-myosin contraction inside of droplets (Figure 4.65).

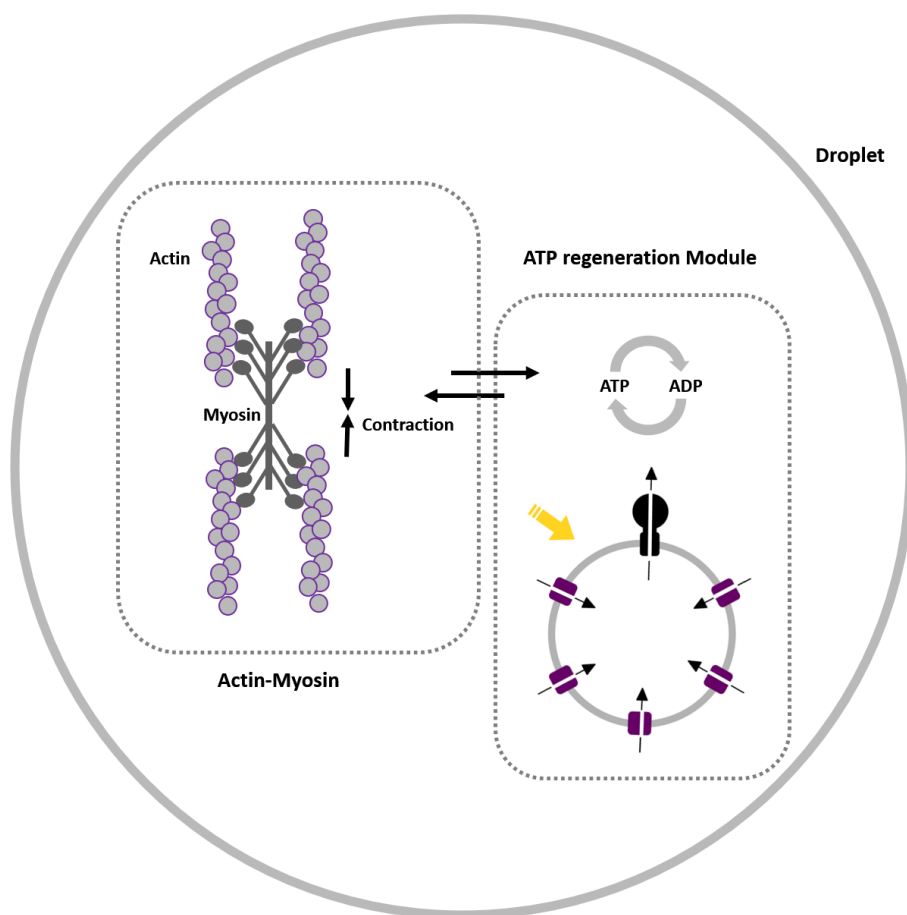


Figure 4.65 Scheme of light-triggered actin-myosin contraction (filamentation) in droplets. This project has been conducted in cooperation with the MPI for Biochemistry (Martinsried).

Actin and myosin were labelled with fluorescence dye and were encapsulated together with the ATP module in water-in-oil droplets. All following steps were performed strictly in the dark to avoid ATP production and consequently the actin-myosin filamentation. Anyway, the results in Figure 4.66 A show that already some smaller filaments have been formed before light exposure. It is possible that the short impulse of light that was necessary to take the picture with the microscope was enough to activate the ATP module. As shown in chapter 4.5.2 illumination with a microscope light is enough for effective ATP production.

After taking the first image (before light), the sample was illuminated with a 15 W white light LED lamp for 10, 30 and 40 minutes and images were taken (Figure 4.66 C-D). The results show clearly that bigger filaments are formed upon illumination, which can be related to the light-driven contraction of actin-myosin filaments.

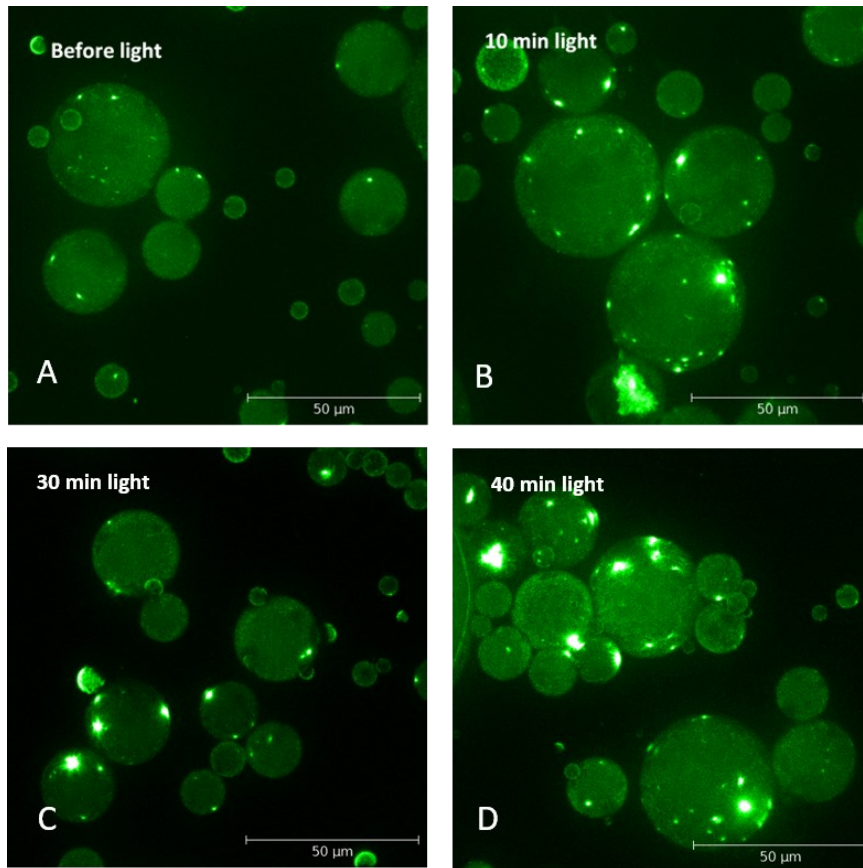


Figure 4.66 Contraction of actin/myosin after incubation with the ATP module under light.

The ATP module is encapsulated in droplets together with fluorescence-marked actin/myosin. Before illumination only very small filaments are visible. Upon green light irradiation actin/myosin is contracting and bigger filaments are visible. Measurements were performed in 10 mM Tris-HCl, 5 mM NaH₂PO₄, 50 mM KCl, 2 MgCl₂, 1 mM DTT, pH 7.5 at room temperature. [ADP]= 300 μM, [P_i]= 5 mM, [lipid]= 0.022 mg/mL, [EF_oF₁]= 1.3 nM, [bR]= 88 nM. Proteins were reconstituted with 0.8 % Triton X-100.

5 Conclusion and Outlook

*We cannot solve problems
with the same thinking we used to create them.*

Albert Einstein

This last chapter concludes the work of this thesis and puts the outcomes into the larger scale of bottom-up synthetic biology.

In the present work the successful integration of two complex transmembrane proteins, bR and F_oF₁ ATP synthase, in lipid, hybrid and polymer vesicles was demonstrated. Both membrane proteins can be defined as functional parts in the scope of bottom-up synthetic biology. For assembly of a well-defined module from bottom-up, it is essential to initially characterize the smallest building blocks, the functional parts, in detail.

ATP synthase was isolated as non his-tagged and his-tagged ATP synthase in *E. coli*. Investigation of ATP synthesis and hydrolysis rates allowed to draw conclusions about the general functionality of the enzyme as well as of the expression and isolation procedure. The driving force for ATP synthesis is the so-called electrochemical potential gradient $\Delta\mu_{\text{H}}$ which comprises the proton gradient ΔpH as well as the potential gradient $\Delta\psi$. Measurements of ATP synthase kinetics with varies $\Delta\psi$ and ΔpH proved that both gradients are indispensable driving forces for ATP synthesis. bR functionality after reconstitution was determined using the pH sensitive probe pyranine, which was encapsulated inside of the vesicles. Proton pumping of bR could be detected spectroscopically, whereby maximal obtainable changes in pH were $\Delta\text{pH}=0.22$.

After proving functionality of both building blocks, bR and ATP synthase were combined in order to create a functional module. Successful combination of both enzymes could be verified by light-triggered ATP production. The performance of the module was optimized by investigation of different influence factors. Highest rates were obtained for 1 ATP synthase molecule per liposome, while increasing bR concentrations led to a continuously increase of ATP production rates.

5 Conclusion and Outlook

Solubilized bR worked better compared to bR patches, probably due to the fact that monomeric bR is distributed more homogeneously over the membrane. Anyway, it has to be mentioned that the solubilization procedure itself leads to high losses of protein and moreover to a less uniform orientation of the enzyme. Therefore, it is questionable if bR should be solubilized prior to co-reconstitution. Valinomycin has shown to decrease the performance of the system due to uncoupling of the electrochemical potential gradient. The ATP module turned out to be very robust, working in each tested buffer system with fairly high activity. Moreover, freezing and storing of the module was possible. This robustness makes the light-driven ATP module an attractive choice as energy supply unit for a minimal synthetic cell. As other modules might be more sensitive, the adaptability of the energy module is a huge advantage. After optimization of different factors influencing synthesis rates, maximal ATP production rates of around $4.5 \mu\text{M ATP (mg ATP synthase)}^{-1}(\text{min}^{-1})$ were achieved. This rate is remarkably higher than rates so far reported for this system (see Table 2.1) probably due to the usage of higher concentrations of bR, a divergent vesicle preparation method and partially differing reconstitution procedure. For further increase of ATP production, it would be necessary to further increase the amount of ATP synthases per compartment or enable a more uniform insertion of bR molecules.

Keeping the bioactivity of the energy converting proteins high for a long time period is of high relevance for biotechnology applications, but also when planning to create a minimal cell from bottom-up (112). Therefore, part of this thesis was to increase the long-term stability of the energy supply unit by usage of hybrid and polymer compartments for co-reconstitution. A detailed study of membrane protein functionality in different hybrid compartments made of graft polymer PDMS-g-PEO and diblock copolymer PBd-PEO was presented. An excellent biocompatibility of the hybrid compartments was demonstrated by protein activities of more than 90% in polymer/lipid vesicles and 56% in polymer/polymer-based vesicles. For further increase of activity in the polymer-based surroundings, further optimization of the reconstitution procedure might be necessary. In this respect, a detailed study about the polymer-detergent interaction should be addressed in future work. Only the molecular understanding of these interplays will enable adjustment of the reconstitution procedure in an appropriate way.

Permeability coefficients of different hybrid vesicles were determined using a new model designed in cooperation with Christian Wölfer. The results suggested that all hybrid vesicles had higher passive permeability to protons compared to liposomes. In contrast, pure PBd-PEO vesicles were shown to be almost impermeable to protons. Anyway, it turned out that in the case of the co-reconstituted system, the passive proton permeability had only little influence on the

performance, which could be explained by direct diffusion of protons along the membrane surface without dissipation losses in the aqueous bulk.

Relative protein activities measured over time, indicated the highest improvement of long-term stability for a mixture of high fluid PDMS polymer and robust block copolymer PBd. Significant differences were evidenced from day 5 on with remaining activities of around 80% after 42 days. In liposomes in contrast, remaining activities of only 40% could be detected. To increase the activity of membrane proteins in artificial polymer membranes, protein engineering to optimize the protein structure may yield some success, for example by matching their hydrophobic thickness. As mentioned above, improvement and understanding of polymer-detergent interactions might also prevail. Anyway, further optimization of the membrane composition (e.g. different polymers and/or lipids) for increased bio functionality is likely a more straight forward approach, with broad applicability to a wide range of membrane proteins. The lipid-polymer or polymer-polymer ratio seems to be another important parameter influencing the chemical and mechanical properties of the membrane and therefore the interaction with proteins embedded in them (104).

A well-defined light-driven energy module in natural and artificial membranes was demonstrated, ready for further integration with other functional modules from bottom-up. The combination with other modules confirmed the capability of the ATP module to serve as energy supply to power for example metabolic pathways in artificial protocell. Moreover, the adhesion of the module upon light illumination was demonstrated using a multistimuli sensing adhesion unit in cooperation with MaxSynBio project partners (Prof. Dr. Wegner). The idea of using stimuli responsive adhesion elements to position cells or modules is highly transferable and could be used to colonize different environments with functional modules or synthetic cells. Another here presented study that was performed in close cooperation with our MaxSynBio cooperation partners in Göttingen, demonstrated that the ATP module can efficiently drive the activity of axonemal dyneins. This is transferable for a variety of other microtubule- or actin-based motility assays, where they are actively engaged in generating and sustaining active stresses in networks. In this regard, the presented work could serve as potential platform to encapsulate constituent elements such as actin, microtubules and various regulatory components inside functionalized liposomes, providing ATP in an optical-controllable way.

The construction and implementation of the artificial energy module and the possibility to mimic nature but also to create new compartments or functions that did not exist before, opens many exciting opportunities for further research. So far current examples of light-driven energy

5 Conclusion and Outlook

regeneration are only of academic interest. However, these studies have to be seen as pioneering examples for reaction systems using light energy for generation of organic compounds. Biotransformation's using purified enzymes to drive ATP- or NADH-consuming reactions, which are not compatible with current cofactor regeneration systems, would be a good starting point. In the long time, one could even think about the production of low-cost compounds such as biofuels. For sure, in this regard further advances in the area of membrane protein production have to be made in order to improve cost-efficiency of the synthesis procedure (112).

On the other hand, the usage of artificial energy conversion modules could open new ways to fabricate novel, artificial systems as well as to understand the interconnection pathways among the chemical species inside the cell. Therefore, artificial cell models, that simulate the complex cellular system with minimal components can provide the ability to solve the origin-of-life puzzle. By appropriately incorporating and engineering a minimum of essential biological components, it might be possible to stimulate the activities of higher organisms, such as protein synthesis or DNA replication. The information provided by this will lead to greater understanding of the evolution of higher complex organisms. Recently cell research was dealing with multiple biochemical cascade reactions that occurs within an artificially engineered cell. To maintain those reactions in artificial cells is still difficult due to the lack of sustainable energy regeneration. To drive any metabolic activities, energy in form of ATP is needed. Thus, the production and consumption of ATP is a critical factor to achieve autotrophic or heterotrophic functions *in vitro*. The energy provided allows cells to grow, reproduce, maintain structures, and respond to their environment (134; 112).

A Appendix

A.1 Chemicals & Devices

A.1.1 Chemicals, Dyes, Enzymes and Kits

Chemicals	Manufacturer
Adenosine Diphosphate (ADP) sodium salt	Sigma-Aldrich
ADP (ultrapure, >99.9%)	Cell technology
Adenosine Triphosphate (ATP) (≥99%)	Roche Life Science
Ammonium sulfate (≥99.5%)	Sigma-Aldrich
Ampicillin sodium salt	Applichem
Chloroform (≥99%)	Sigma-Aldrich
Cholic Acid sodium salt (≥98%)	Serva
Coomassie blue R-250	Sigma-Aldrich
Deoxycholic Acid sodium salt (≥99%)	Serva
Desoxyribonuclease I (DNase) DN-25	Sigma-Aldrich
Dithiothreitol (DTT)	Sigma-Aldrich
Ethylenediaminetetraacetic acid (EDTA) (99.5%)	Sigma-Aldrich
Ethyleneglycoltetraacetic acid (EGTA) (≥99%)	Roth
Glucose	Sigma-Aldrich
Glycerine (99.5%)	Roth
Glycerol (Bio Reagent)	Sigma-Aldrich
Glycine	Merck
Imidazole (Bio Ultra)	Sigma-Aldrich

Appendix

Chemicals	Manufacturer
Low range molecular weight standard (PageRuler™ 10-180 kDa) (PageRuler™ 4.6-42 kDa)	Thermo Scientific
Nicotinamide adenine dinucleotide (NADH) disodium salt	Roth
Magnesium acetate tetrahydrate	Sigma-Aldrich
Magnesium chloride (MgCl ₂) hexahydrate	Sigma-Aldrich
Methanol (99.9%)	Sigma-Aldrich
Milli-Q Water	Milli-Q® Integral Water Purification System (Merck)
3-(N-Morpholino) propane sulfonic acid (MOPS) (99%)	Roth
p-aminobenzamidide dihydrochloride	Sigma-Aldrich
Phenylmethanesulfonylfluoride (PMSF) (99.9%)	Merck
Phosphoenolpyruvate (PEP) (99.5%)	Fluka
Potassium chloride (KCl)	Sigma-Aldrich
Potassium sulfate (K ₂ SO ₄)	Sigma-Aldrich
Sucrose (≥99.5%)	Sigma-Aldrich
Tetracycline	Sigma-Aldrich
Trichloroacetic Acid (TCA) (≥99%)	Sigma-Aldrich
Tricine (≥99%)	Sigma-Aldrich
Tris (Ultrapure)	Applichem
Tris acetate (Bio Ultra)	Sigma-Aldrich
Valinomycin (≥98%)	Sigma-Aldrich
ε-aminocaproic acid	Sigma-Aldrich

Detergents	Manufacturer
Dodecyl maltoside (DDM)	Sigma-Aldrich
Octyl glucoside	Glycon
Sodium cholate	Sigma-Aldrich
Sodium deoxycholate	Sigma-Aldrich
Sodium Dodecyl sulfate (SDS) 20%	Sigma-Aldrich
Triton X-100 (10%) (Triton)	Sigma-Aldrich

Lipids, polymers and dyes	Manufacturer
Alexa-Fluor 488 Phalloidin	Molecular Probes
Alexa-Fluor 488 C5-maleimide	Molecular Probes
Alexa-Fluor 647 C2-maleimide	Molecular Probes
1,2-dioleoyl-sn-glycero-3-[[N-(5-amino-1-carboxypentyl)iminodiacetic acid) succinyl]] Ni ²⁺ -Salt (DGS-NTA-Ni ²⁺)	Avanti Polar Lipids
1,2-dioleoyl-sn-glycero-3-phosphoethanolamine-N-(lissamine rhodamine B sulfonyl) ammonium salt (Liss-Rhod PE)	Avanti Polar Lipids
Phosphatic Acid (PA)	Avanti Polar Lipids
Poly(dimethylsiloxane)-graft-poly (ethylene oxide) (PDMS-g-PEO) (PDMS) ¹	Dow Corning
Poly(butadiene-b-ethylene oxide) (PBd ₂₂ -b-PEO ₁₄) (PBd) ²	Polymer Source (P9089-BdEO)
Soy L- α phosphatidylcholine (PC) (95%)	Avanti Polar Lipids

¹ PDMS-g-PEO has an average viscous-metric molecular size weight of 3000 g/mol with 47% weight fraction of ethylene oxide (in average 2 arms of PEO per PDMS chain) and an average degree of polymerization of 12.

² PBd-PEO has an average molecular weight of 1200 g/mol for PB and 600 g/mol for the PEO block.

Enzymes and Proteins	Manufacturer
Actin monomers	Molecular Probes
Biotinylated Actin monomers	Tebu-bio
L-Lactate Dehydrogenase (L-LDH)	Roche
Proteinase K	Roche
Pyruvate kinase	Roche

Kits	Manufacturer
ATP bioluminescence assay kit CLSII	Roche Life Science
Glucose assay (high sense)	Sigma-Aldrich

Appendix

A.1.2 Materials and Devices

Materials	Manufacturer
Bio-Beads SM-2 ³	Bio-Rad
Cantilever PPP-NCH-W	Nanosensors
G25 size exclusion column (PD Mini Trap™ G-25)	GE Healthcare
Mica	Plano, Wetzlar
Ni-NTA column His Trap™ FF crude	GE Healthcare
Sterile filter (0.22 µm)	Sartorius Stedim
4-20% Tris-HCl Criterion Precast Gels	Bio-Rad
Polycarbonate membrane (100 nm)	Whatman

³ Bio-Beads are extensively washed before usage as described by Holloway. (135)

Devices	Manufacturer
Atomic Force Microscope (AFM) Keysight 5500	Agilent
Fermenter Biostat C-plus	Sartorius Stedim
Fermenter Laborpilot LP351	Bioengineering
French Press	SLM Amino French cell press
Gel apparatus Mini Protean 3 Cell	Bio-Rad
Glomax® 20/20 luminometer	Promega
High Pressure Liquid Chromatography (HPLC)	Amersham Äkta purifier
Incubator, Thermomixer 5436	Eppendorf
Microplate reader	Biotech, Synergy HT
Mini Extruder	Avanti Polar Lipids
Nanodrop 2000 Spectrophotometer	Thermo Scientific
pH electrode	Mettler Toledo
G25 Incubator-Shaker	New Brunswick Scientific
Shaker Multitron Pro	Infors HT
Sonicator	Branson Sonifier 250
UV/Vis Spectrometer Specord 50 plus r	Analytik Jena

Devices	Manufacturer
Ultracentrifuge	Optima XPN 100 (Beckmann Coulter) Beckmann Instruments (Ti-60, Ti-70)
QEPRO diode array spectrometer	Ocean Optics
Zetasizer Nano ZS	Malvern, Worcestershire
50 W green LED lamp	SMD RGB Floodlight, V-TAC

A.2 Buffer and Media

Table A.1 Composition of Luria Media.

Luria Media	
Peptone	10 g/l
Yeast extract	5 g/l
NaCl	5 g/l

Table A.2 Composition of culture medium.

Culture Medium	
NaH ₂ PO ₄	34 mM
K ₂ HPO ₄	64 mM
(NH ₄) ₂ SO ₄	20 mM
FeSO ₄	1 μM
ZnCl ₂	1 μM
MgSO ₄	300 μM
CaCl ₂	10 μM
Glycerine	75 mM
Asparagine	50 mg/l
Isoleucine	50 mg/l
Valin	50 mg/l
Thymine	50 mg/l
Thiamine	3 mg/l

Appendix

Table A.3 Composition of T1 media.

T1	
NaH ₂ PO ₄	340 mM
K ₂ HPO ₄	640 mM
(NH ₄) ₂ SO ₄	200 mM
FeSO ₄	10 μM
ZnCl ₂	10 μM

Table A.4 Composition of T2 media.

T2	
MgSO ₄	30 mM
CaCl ₂	1 mM

Table A.5 Composition of amino acid solution.

Amino acid solution	
Asparagine	100 g/l
Isoleucine	100 g/l
Valin	100 g/l
Thymine	100 g/l
in 1 M NaOH	

Table A.6 Composition of French Press buffer.

French Press buffer	
Tris-HCl, pH 8	20 mM
KCl	140 mM
MgCl ₂	5 mM
DTT	2 mM
PABA	5 mM
PMSF	0.002%

Table A.7 Composition of membrane buffer.

Membrane buffer	
Tris-HCl, pH 8	50 mM
KCl	100 mM
MgCl ₂	5 mM
DTT	2 mM
Saccharose	2% (w/v)
Glycerine	10% (v/v)
PABA	5 mM

Table A.8 Composition of solubilization buffer.

Solubilization buffer	
Mes-KOH, pH 7	20 mM
Tricin-NaOH, PH 7	20 mM
MgCl ₂	2 mM
Thioglycerine	5 mM

Table A.9 Composition of buffer A.

Buffer A	
MOPS-KOH, pH 7.5	40 mM
KCl	80 mM
Saccharose	2 % (w/v)
DTT	2 mM
MgCl ₂	4 mM
Glycerine	10 % (v/v)
DDM	0.1 %

Table A.10 Composition of LB media.

LB Media	
Tryptone	10 g/l
Yeast extract	5 g/l
NaCl	5 g/l
Adjusted with NaOH to pH 7.0	

Appendix

Table A.11 Composition of French press buffer.

French Press buffer	
Tris-HCl, pH 7.77	200 mM
KCl	100 mM
MgCl ₂	5 mM
EDTA	0.1 mM
Glycerol	2.5%

Table A.12 Composition of extraction buffer.

Extraction buffer	
Tris-HCl, pH 7.5	50 mM
KCl	100 mM
Sucrose	250 mM
MgCl ₂	5 mM
ϵ -aminocaproic acid	40 mM
p-aminobenzamidine	15 mM
EDTA	0.1 mM
DTT	0.2 mM
Phosphatidylcholine	0.8%
Octyl glucoside	1.5%
Sodium cholate	0.5%
Glycerol	2.5%
Imidazole	30 mM

Table A.13 Composition of culture medium.

Culture medium	
NaCl	250g/l
MgSO ₄	20g/l
Trisodium citrate	3g/l
KCl	2g/l
Peptone	10g/l

Table A.14 Composition of sample buffer for SDS-PAGE Analysis.

Sample buffer	
Tris-HCl, pH 8	100 mM
SDS	10%
DTT	5 mM
Glycerine	50%
BPB	0.2%

Table A.15 Staining solution Coomassie Blue R250 for SDS-PAGE Analysis.

Staining solution	
Ethanol	25%
Acetic Acid	10%
Coomassie Blue R250	0.1%

Table A.16 Decolorizing solution for SDS-PAGE Analysis.

Decolorizing solution	
Ethanol	30%
Acetic Acid	10%

Table A.17 Composition of sonification buffer for preparation of dialysis liposomes.

Sonification buffer	
Tricine-NaOH, pH 8	100 mM
EDTA	0.1 mM
DTT	0.5 mM
Cholic Acid	7.2 g/l
Desoxycholic Acid	3.6 g/l

Appendix

Table A.18 Composition of dialysis buffer for preparation of dialysis liposomes.

Dialysis buffer	
Tricine-NaOH, pH 8	150 mM
MgCl ₂	37.5 mM
EDTA	3 mM
DTT	3.75 mM

Table A.19 Composition of reconstitution buffer.

Reconstitution buffer	
Tricine-NaOH, pH 8	20 mM
Succinate	20 mM
KCl	0.6 mM
NaCl	80 mM

Table A.20 Composition of basic buffer LII for ATP synthesis measurements.

Basic buffer	
Tricine-NaOH, pH 8.8	100 mM
MgCl ₂	2.5 mM
Natrium phosphate	5 mM
KOH	160 mM

Table A.21 Composition of acidic buffer LI for ATP synthesis measurements.

Acidic buffer	
Succinic acid-HCl, pH 4.7	20 mM
MgCl ₂	2.5 mM
Natrium phosphate	5 mM
KOH	0.6 mM

Table A.22 Composition of measurement buffer for ATP hydrolysis measurements.

Measurement buffer	
Tris-HCl, pH 8	100 mM
KCl	25 mM
MgCl ₂	4 mM
Phosphoenolpyruvate (PEP)	2.5 mM
ATP	2 mM
NADH	0.4 mM
Pyruvate kinase	18 U/ml
Lactate Dehydrogenase	16 U/ml

Table A.23 Composition of HEPES buffer for proton pumping experiments.

HEPES buffer	
HEPES (pH 7)	10 mM
MgCl ₂	15 mM
K ₂ SO ₄	100 mM

Table A.24 Composition of Laemmli buffer for SDS PAGE analysis of bR fragments.

10x Laemmli buffer	
Tris	30 g/l
Glycine	144 g/l
SDS	10 g/l

Table A.25 Composition of vesicle buffer for characterization of the ATP module.

Vesicle buffer	
HEPES (pH 7.5)	20 mM
MgSO ₄	2.5 mM
Sucrose	50 mg/ml

Appendix

Table A.26 Composition of measurement buffer for light-induced ATP synthesis.

Measurement buffer	
Tris-HCl (pH 7.5)	10 mM
KCl	50 mM
MgCl ₂	2 mM
K ₂ HPO ₄	5 mM
DTT (fresh)	1 mM

Table A.27 Composition of PIPES buffer for permeability measurements.

PIPES buffer	
PIPES-KOH (pH 7.5)	25 mM (50 mM KOH)
Sucrose	200 mM

Table A.28 Composition of HEPES buffer for permeability measurements.

Measurement buffer	
HEPES-NaOH (pH 7)	40 mM
K ₂ SO ₄	20 mM

Table A.29 Composition of washing buffer for IMV isolation.

Washing buffer	
Tris-HCl (pH 8)	50 mM
EGTA	1 mM

Table A.30 Composition of lysis buffer for IMV isolation.

Lysis buffer	
MOPS (pH 7.0)	50 mM
KCl	175 mM
MgCl ₂	10 mM
EGTA	0.2 mM
DTT (fresh)	0.2 mM
PMSF	0.1 mM

Table A.31 Composition of membrane buffer for IMV isolation.

Membrane buffer	
Tris-HCl (pH 8.0)	50 mM
PAB	6 mM
MgCl ₂	5 mM
Glycerine	10% (v/v)
EGTA	0.2 mM
DTT (fresh)	2 mM
PMSF	0.1 mM

Table A.32 Composition of measurement buffer for ATP measurement in IMVs.

Measurement buffer	
Tris acetate (pH 7.8)	20 mM
Magnesium acetate	5 mM
K ₂ SO ₄	0.5 mM
MgCl ₂	0.25 mM
EDTA	0.1 mM
DTT (fresh)	1 mM
ADP (fresh)	0.25 mM

Table A.33 Composition of HMDEKP buffer for reactivation of isolated flagella.

HMDEKP buffer	
HEPES-KOH (pH 7.4)	30 mM
MgSO ₄	5 mM
EGTA	1 mM
Potassium acetate	50 mM
Polyethylene glycol (M=20 kg mol ⁻¹)	1% (w/v)
Pefabloc	0.2 mM
DTT (fresh)	1 mM

Appendix

Table A.34 Composition of buffer A for multistimuli sensing adhesion unit.

Buffer A	
Tris-HCl (pH 7.4)	50 mM
NaCl	300 mM

Table A.35 Composition of MOPS buffer.

MOPS buffer	
MOPS	100 mM
NaCl	5 mM
KCl	50 mM

A.3 Models for calculation of permeability coefficients

1) Determination of P by Model fitting (Method 1)

The mathematical model for the description of membrane permeability considers chemical as well as electrochemical driving forces for proton diffusion through the membrane (136) and takes the size of the vesicles and the buffer capacity into account. The model cannot describe the initial fast jump, except by introducing unrealistically large values of permeability coefficients (e.g. the case of 70/30 PDMS/PC) or by accepting higher fitting errors at initial times (e.g. 100/0 PC) (Figure 4.33). Therefore, all data were fitted without taking the initial jump into account.

Since the buffering properties of the system influence the pH change in addition to membrane permeability (Figure A.1), the dynamic buffering capacity β should be taken into account when determining the permeability constant P independent of the buffer system. The buffering capacity is defined as the proton concentration to be added to achieve a pH change:

$$\beta = -\frac{d[H^+]}{dpH} \quad [A.1]$$

$$\frac{dpH}{dt} = \frac{dpH}{d[H^+]} \cdot \frac{d[H^+]}{dt} \quad [A.2]$$

$$\frac{dpH}{dt} = -\beta \cdot \frac{d[H^+]}{dt} \quad [A.3]$$

Assuming that the pH value inside the vesicle changes only due to proton through the membrane (r_L), the following rate for the pH value inside the vesicle results, considering the total volume ratio between inner and exterior phase $V_R = \frac{V_I}{V_E}$:

$$\frac{dpH_I}{dt} = \frac{-\beta}{V_R} \cdot (-r_L) \quad [A.4]$$

Due to the vesicle concentration of $7 \cdot 10^{12}$ liposomes/mL with a mean diameter of 125 nm the ratio of bulk vesicle volume to external volume is very small ($V_R = 0.009$). Since the pH value in the outer and inner medium is also buffered (here PIPES; $pK_B = 6.7$), the external proton change is very small and therefore negligible. In the following, the equation for dynamic buffer capacity β is derived for buffer equilibrium:



Appendix

By considering the law of mass action and the buffer equilibrium constant K_b follows:

$$[BH] = \frac{[H^+][B^-]}{K_b} \quad [A.6]$$

The total buffer concentration c_b is defined as:

$$c_b = B^- + BH \quad [A.7]$$

Combining equation [A.6] and [A.7] it follows:

$$[B^-] = \frac{c_b \cdot K_b}{K_b + [H^+]} \quad [A.8]$$

Taking the charge balance

$$[B^-] + [OH^-] = [H^+] + [n] \quad [A.9]$$

into account, the following applies:

$$[n] = \frac{K_w}{[H^+]} - [H^+] + \frac{c_b \cdot K_b}{K_b + [H^+]} \quad [A.10]$$

By calculating the derivatives, the equation for dynamic buffer capacity follows:

$$\beta = \frac{dn}{dpH} = \frac{dn}{dH^+} \cdot \frac{dH^+}{dpH} \quad [A.11]$$

$$= \left[-\frac{K_w}{[H^+]^2} - 1 - \frac{c_b \cdot K_b}{(K_b + [H^+])^2} \right] \cdot (-\ln(10) \cdot [H^+]) \quad [A.12]$$

$$= \ln(10) \cdot \left[\frac{K_w}{[H^+]^2} + [H^+] + \frac{c_b \cdot K_b \cdot [H^+]}{(K_b + [H^+])^2} \right] \quad [A.13]$$

Equation [A.13] shows that at pK_B (derived from the buffer constant) the buffer system has the largest buffer capacity (Figure A.1). For pH values close to pK_B , protons must be added to the inner medium the most in order to obtain a pH change.

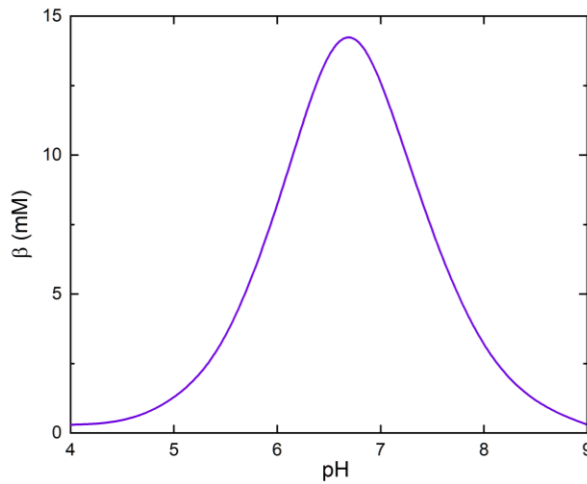


Figure A.1 Buffer capacity for different pH (Pipes buffer: $pK_B = 6.71$, $c_B = 25$ mM) as determined by model simulation (Method 1).

The experimental observations of proton permeability showed that pH change inside the vesicles upon the addition of acid/base never tends towards the external pH in equilibrium. For NaOH the pH inside is always below the external pH and for HCl always above the external pH. This indicates that in the experiment the membrane permeability of protons is not only driven by the chemical gradient but also by the membrane potential built up by different internal and external ion concentrations. For this reason, a permeability proton flux through the interface r_L is derived using the Nernst-Planck equation, which takes both the chemical and electrical potential (E_m) into account:

$$j = -D_c \left(\frac{dc}{dx} - \frac{z \cdot F}{R \cdot T} \cdot \frac{E_m}{L} \cdot c \right) \quad [\text{A.14}]$$

The terms of the Nernst-Planck equation represent the Fick's law of diffusion, which gives the flux due to diffusion and the flux due to the electric potential. Using separation of variables and integrate between interior ($x=0$) and exterior ($x=L$) yields to:

$$j = P_c \cdot \mu \cdot E_m \cdot \left(\frac{c_e - c_i e^{\mu E_m}}{1 - e^{\mu E_m}} \right) \quad [\text{A.15}]$$

with

$$\mu = -\frac{F}{R \cdot T} \quad [\text{A.16}]$$

And the permeability coefficient P_c is defined as:

Appendix

$$P_c = \frac{D_c}{L} \quad [\text{A.17}]$$

Assuming spherical vesicles surface volume ratio is defined as:

$$\frac{A}{V} = \frac{3}{\rho} \quad [\text{A.18}]$$

Combining equations [A.15]- [A.18] the permeability rate r_L can be defined as follows:

$$r_L = P_H \cdot \mu \cdot \frac{3E_m}{\rho} \cdot \left(\frac{[H_e^+] - [H_i^+] e^{\mu E_m}}{1 - e^{\mu E_m}} \right) \quad [\text{A.19}]$$

Equation [A.19] is only valid for constant electrical potential. Since in the present case the membrane potential is mainly determined by the ion imbalance between the inner and outer phase in the individual experiments (Na^+ or Cl^-), which can only balance very slowly through the membrane, it is assumed that the membrane potential is approximately constant over the observed period. With vesicle radius $\rho = 125$ nm as determined by DLS. If no membrane potential is present, the kinetics is simplified by applying the rule of L'Hopital to the purely chemically driven rate:

$$r_L = P_H \cdot \frac{3}{\rho} \cdot ([H_e^+] - [H_i^+]) \quad [\text{A.20}]$$

This correlation is used by Paxton et al. (113) for the determination of permeability coefficients and is described below as Method 2.

Parameter sets were estimated (Table A.36) to fit the experimental datasets, consisting of a permeability constant per membrane type with a membrane potential for acid and base addition to the external medium, respectively. The parameter estimation was performed by minimizing the residual sum of squares RSS between simulation and experimental datasets, using the toolbox Copasi (137). The optimization algorithm evolutionary programming was used to identify an approximation of a parameter set for a suitable global minimum of the RSS (138). Additionally, the gradient orientated simplex algorithm was applied to certainly reduce the RSS into potential global minimum and optimal parameter set, respectively (139).

Table A.36 Fitted parameter set for calculation of permeability coefficients using Method 1.

Membrane composition		$P_H \times 10^9$ (cm s ⁻¹)	E_m (mV) $pH_e = 7.77$	E_m (mV) $pH_e = 7.11$
100/0	PC	1.88	13.7	-18.0
70/30	PDMS/PC	1100	5.0	-4.6
50/50	PBd/PC	2.41	9.9	-14.5
50/50	PDMS/PBd	2.96	5.7	-5.3

The calculated membrane potentials correspond to the expected charge difference after acid or base addition. The addition of acid to the external medium leads to an excess of negative ions and thus to a negative membrane potential. The opposite counts for the addition of base (Table A.36).

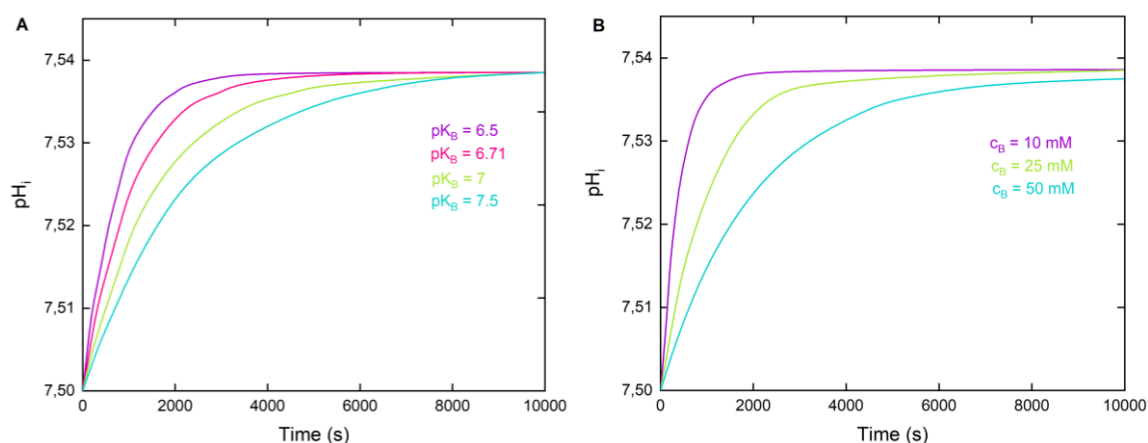


Figure A.2 pH change inside of vesicles depending on different (A) pK_B and (B) buffer concentrations as predicted by model simulation (Method 1).

The initial pH inside the vesicles is 7.5 and the external pH is 7.77.

2) Determination of P according to Paxton et al. (113) (Method 2)

Using the method of Paxton, the pH values at $t=0$ were corrected to the pH of the buffer solution ($pH=7.5$). Some membrane systems show deviations between the actual and apparent pH due to interactions between pyranine and the vesicle material. As the pH for these experiments is in the linear range of the calibration curve (Figure 4.11), all data points could be offset by the same value for each series. The concentration of free hydroxide $[OH^-]$ or free protons $[H^+]$ could be calculated from the pH values using equation [A.21] or [A.22]:

Appendix

$$[OH^-] = 10^{-pOH} = 10^{-(14-pH)} \quad [A.21]$$

$$[H^+] = 10^{-pH} \quad [A.22]$$

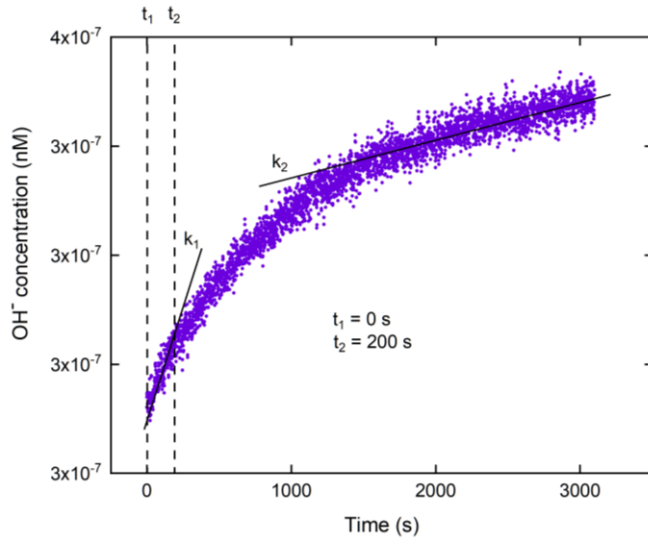


Figure A.3 Determination of permeability coefficients (P) using Method 2.

Exemplary shown for 0/100 PDMS/PC after addition of NaOH. The concentration of free $[OH^-]$ was calculated from the pH response versus time by equation [4.22]. The $[OH^-]$ values at $t_1 = 0$ s and $t_2 = 200$ s were used for calculation of P.

For calculation of permeability coefficients, the initial part of the reaction (0-200 s) has been chosen according to Seneviratne (105). Proton permeation into vesicles occurs via a two-step mechanism (117; 140; 114; 121; 116) (shown as k_1 and k_2 in Figure A.3). k_1 can be attributed to the rapid net H^+/OH^- permeability (118) which results in an uncompensated build-up of charge. The net H^+/OH^- flux then slows to a rate, limited by the permeation of the charge-compensating co-ions (k_2). As k_1 actually reflects H^+/OH^- permeability, this initial linear range of the reaction has been chosen for determination of P.

Calculation of the permeability coefficient P_{OH^-} is demonstrated for addition of NaOH. The permeability coefficient P is defined by the flux r_L and the hydroxide ion concentration gradient Δc as follows:

$$P = \frac{r_L}{\Delta c} \quad [A.23]$$

$$\Delta c = [OH^-]_2 - [OH^-]_1 \quad [A.24]$$

The flux of hydroxide ions r_L can be calculated by subtracting the flux $r_{L,2}$ at t_2 from the flux $r_{L,1}$ at t_1 :

$$r_L = r_{L,2} - r_{L,1} \quad [\text{A.25}]$$

Whereby the flux $r_{L,1}$ and $r_{L,2}$ are:

$$r_{L,1} = \frac{[\text{OH}_i^-]_{t_1} + [\text{PIPES}^-]_{t_2} - [\text{PIPES}^-]_{t_1}}{\Delta t} \cdot \frac{V}{A} \quad [\text{A.26}]$$

$$r_{L,2} = \frac{[\text{OH}_i^-]_{t_2} + [\text{PIPES}^-]_{t_1} - [\text{PIPES}^-]_{t_2}}{\Delta t} \cdot \frac{V}{A} \quad [\text{A.27}]$$

V is the volume and A the surface area of the vesicle and can be calculated using the size distribution of vesicles determined by DLS:

$$V = \frac{4}{3} \cdot \pi \cdot \rho^3 \quad [\text{A.28}]$$

$$A = 4 \cdot \pi \cdot \rho^2 \quad [\text{A.29}]$$

The ionized form of PIPES $[\text{PIPES}^-]_{t_1}$ and $[\text{PIPES}^-]_{t_2}$ can be derived by using the K_b value of PIPES with the following equations:

$$[\text{PIPES}^-]_{t_1} = \frac{[\text{OH}_i^-]_{t_1} \cdot [\text{PIPES}]}{K_b} = \frac{[\text{OH}_i^-]_{t_1} \cdot [\text{PIPES}]}{-0.86M} \quad [\text{A.30}]$$

$$[\text{PIPES}^-]_{t_2} = \frac{[\text{OH}_i^-]_{t_2} \cdot [\text{PIPES}]}{K_b} = \frac{[\text{OH}_i^-]_{t_2} \cdot [\text{PIPES}]}{-0.86M} \quad [\text{A.31}]$$

3) Determination of P according to Kuyper et al. (116)(Method 3)

Another method for determination of permeability coefficients has been proposed by Kuyper et al. (116). He derived proton permeability coefficients by double exponential fitting as shown in Figure A.4 exemplary for 0/100 PDMS/PC after addition of NaOH. Two different rate constants (k_1 , k_2) are defined in accordance to Figure A.3 . Kuyper defined k_1 as the rate constant for proton permeation, while he assumed that k_2 can be attributed to K^+ permeation. Therefore, k_1 is defined from double exponential fitting as follows:

$$k_1 = \frac{1}{t_1} \quad [\text{A.32}]$$

Appendix

Moreover, Kuyper took the vesicle size into account by integrating the vesicle size ρ into the following equation for calculation of permeability coefficient P :

$$P = k_1 \left(\frac{\rho}{3} \right) \quad [\text{A.33}]$$

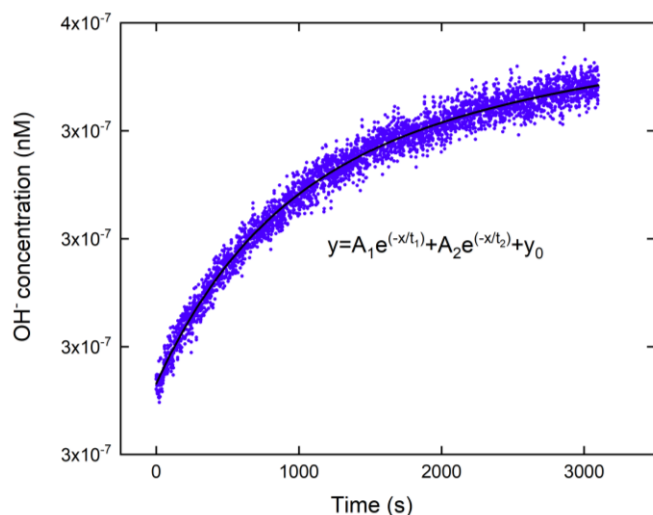


Figure A.4 Determination of permeability coefficients using Method 3 (double exponential fitting). Exemplary shown for 0/100 PDMS/PC after addition of NaOH.

A.4 Supporting Figures

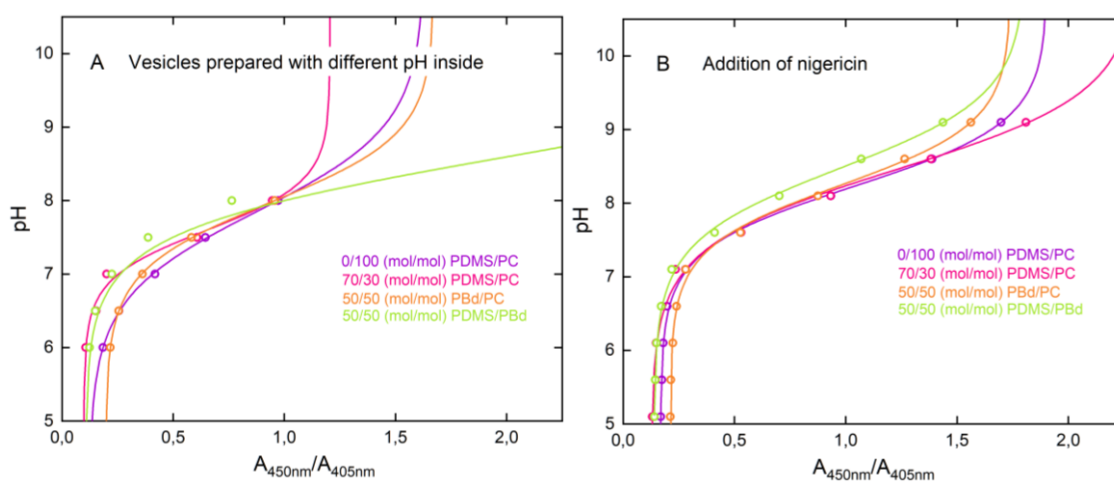


Figure A.5 Calibration curves of pyranine for different membrane compositions.

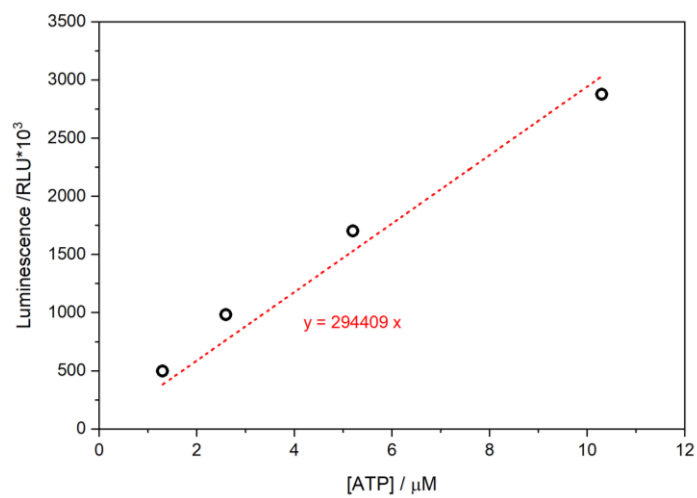


Figure A.6 ATP standard curve for calculation of ATP concentration in IMVs experiments.

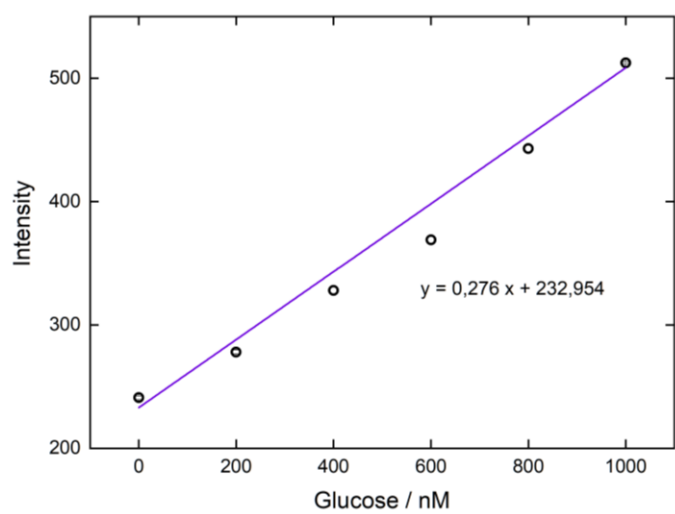


Figure A.7 Glucose standard curve for calculation of glucose concentration by the fluorescence signal using a highly sensitive glucose assay.

References

1. B. Wang (2010) Design and Functional Assembly of Synthetic Biological Parts and Devices . *Dissertation*, Imperial College London.
2. D. Endy (2005) Foundations for engineering biology. *Nature* 438, 449-453.
3. M. A. J. Roberts, R. M. Cranenburgh, M. P. Stevens, P. C. F. Oyston (2013) Synthetic biology: biology by design. *Microbiol.* 159, 1219-1220.
4. M. L. Simpson (2006) Cell-free synthetic biology: a bottom-up approach to discovery by design . *Mol. Syst. Biol.* 12.
5. E. Andrianantoandro, S. Basu, D. K. Karig, R. Weiss (2006) Synthetic biology: new engineering rules for an emerging discipline. *Mol. Syst. Biol.* 2, 28.
6. N. J. Guido, X. Wang, D. Adalsteinsson, D. McMillen, J. Hasty, C. R. Cantor, T. C. Elston, J. J. Collins (2006) A bottom-up approach to gene regulation. *Nature* 439, 856-860.
7. J. Hasty, D. McMillen, J. J. Collins (2002) Engineered gene circuits. *Nature* 420, 224-230.
8. D. Sprinzak, M. B. Elowitz (2005) Reconstitution of genetic circuits. *Nature* 438, 443-448.
9. H. Mutschler, T. Robinson, T.-Y. Dora Tang, S. Wegner (2019) Special Issue on Bottom-Up Synthetic Biology. *ChemBioChem* 20, 2533-2534.
10. D. Krafft, S. Lopez-Castellanos, R. B. Lira, R. Dimova, I. Ivanov, K. Sundmacher (2019) Compartments for Synthetic Cells: Osmotically Assisted Separation of Oil from Double Emulsions in a Microfluidic Chip. *ChemBioChem* 20, 2604-2608.
11. T. Robinson, P. S. Dittrich (2019) Observations of Membrane Domain Reorganization in Mechanically Compressed Artificial Cells. *ChemBioChem* 20
12. M. M. Hanczyc, S. M. Fujikawa, J. W. Szostak (2003) Experimental Models of Primitive Cellular Compartments: Encapsulation, Growth, and Division. *Science* 302 (5645), 618-622.
13. T. Oberholzer, R. Wick, P. L. Luisi, C. K. Biebricher (1995) Enzymatic RNA replication in self-reproducing vesicles: an approach to a minimal cell. *Biochem. Biophys. Res. Commun.*

References

14. I. A. Chen, K. Salehi-Ashtiani, J. W. Szostak (2005) RNA Catalysis in Model protocell vesicles. *J. Am. Chem. Soc.* 127 (38), 13213-13219.
15. P. Schwille, S. Diez (2009) Synthetic biology of minimal systems. *Crit. Rev. Biochem. Mol. Biol.* 44 (4), 223-242.
16. A. R. Bausch, K. Kroy (2006) A bottom-up approach to cell mechanics. *Nat. Phys.* 2, 231-238.
17. B. C. Ma, L. Caire da Silva, S.-M. Jo, F. R. Wurm, M. B. Bannwarth, K. A. I. Zhang, K. Sundmacher, K. Landfester (2019) Polymer-Based Module for NAD⁺ Regeneration with Visible Light. *ChemBioChem* 20.
18. D. Hürtgen, J. Mascarenhas, M. Heymann, S. M. Murray, P. Schwille, V. Sourjik (2019) Reconstitution and Coupling of DNA Replication and Segregation in a Biomimetic System. *ChemBioChem* 20.
19. P. Schwille, J. Spatz, K. Landfester, E. Bodenschatz, S. Herminghaus, V. Sourjik, T. J. Erb, P. Bastiaens, R. Lipowsky, A. Hyman, P. Dabrock, J.-C. Baret, T. Vidakovic-Koch, R. Dimova, H. Mutschler, T. Robinson, T.-Y. Dora Tang, S. Wegner, K. Sundmacher (2018) MaxSynBio: Avenues Towards Creating Cells from the Bottom Up. *Angew. Chem. Int. Ed.* 57, 13382-13392.
20. I. Otero-Muras, J. R. Banga (2017) Automated Design Framework for Synthetic Biology Exploiting Pareto Optimality. *ACS Synth. Biol.* 6, 1180-1193.
21. S. Rupp (2013) Next-generation bioproduction systems: Cell-free conversion concepts for industrial biotechnology. *Engineering in Life Sciences* 13 (1), 19-25.
22. P. Richard, J. L. Rigaud, P. Gräber (1990) Reconstitution of CF₀F₁ into liposomes using a new reconstitution procedure. *Eur. J. Biochem.* 193 (3), 921-926.
23. P. Richard, P. Gräber (1992) Kinetics of ATP synthesis catalyzed by the H⁺-ATPase from chloroplasts (CF₀F₁) reconstituted into liposomes and coreconstituted with bacteriorhodopsin. *Eur. J. Biochem.* 210, 1992, 287-291.
24. S. Matuschka, K. Zwicker, T. Nawroth, G. Zimmer (1995) ATP Synthesis by Purified ATP-Synthase from Beef Heart Mitochondria after Coreconstitution with Bacteriorhodopsin. *Arch. Biochem. Biophys.* 322, 135-142.
25. B. Pitard, P. Richard, M. Dunach, G. Girault, J. L. Rigaud (1996) ATP synthesis by the F₀F₁ ATP synthase from thermophilic *Bacillus PS3* reconstituted into liposomes with bacteriorhodopsin. 1. Factors defining the optimal reconstitution of ATP synthases with bacteriorhodopsin. *Eur. J. Biochem.* 235, 769-778.
26. B. Pitard, P. Richard, M. Dunach, G. Girault, J. L. Rigaud (1996) ATP synthesis by the F₀F₁ ATP synthase from thermophilic *Bacillus PS3* reconstituted into liposomes with bacteriorhodopsin. 2. Relationships between proton motive force and ATP synthesis. *Eur. J. Biochem.* 235, 779-788.

27. L. Otrin, C. Kleineberg, L. Caire da Silva, K. Landfester, I. Ivanov, M. Wang, C. Bednarz, K. Sundmacher, T. Vidakovic-Koch (2019) Artificial Organelles for Energy Regeneration. *Adv. Biosys.* 3 (6).
28. E. Racker, W. Stoeckenius (1974) Reconstitution of purple membrane vesicles catalyzing light-driven proton uptake and adenosine triphosphate formation. *J. Biol. Chem.* 249 (2), 662-665.
29. N. Wagner, M. Gutweiler, R. Pabst, K. Dose (1987) Coreconstitution of bacterial ATP synthase with monomeric bacteriorhodopsin into liposomes. *Eur. J. Biochem.* 165, 177-183.
30. H. J. Choi, C. D. Montemagno (2005) Artificial Organelle: ATP Synthesis from Cellular Mimetic Polymersomes. *Nano Lett.* 5 (12), 2538-2542.
31. X. Feng, Y. Jia, J. Cai, J. Li (2016) Coassembly of Photosystem II and ATPase as Artificial Chloroplast for Light-Driven ATP Synthesis. *ACS Nano* 10, 556-561.
32. K. Y. Lee, S.-Y. P., K. A. Lee, S.-H. Kim, H. Kim, Y. Meroz, L. Mahadevan, K.-H. Jung, T. K. Ahn, K. K. Parker, K. Shin (2018) Photosynthetic artificial organelles sustain and control ATP-dependent reactions in a protocellular system. *Nature Biotechnol.* 36, 530.
33. G. Steinberg-Yfrach, R.-L. R., E.N. Durantini, A. L. Moore, D. Gust, T. A. Moore (1998) Light-driven production of ATP catalysed by FOF1-ATP synthase in an artificial photosynthetic membrane. *Nature* 392, 479.
34. Y. Li, X. F., A. Wang, Y. Yang, J. Fei, B. Sun, Y. Jia, J. Li (2019) Supramolecularly Assembles Nanocomposites as Biomimetic Chloroplasts for Enhancement of Photophosphorylation. *Angew. Chem. Int. Ed.* 58, 796-800.
35. Y. Xu, J. Fei, G. Li, T. Yuan, J. Li (2017) Compartmentalized Assembly of Motor Protein Reconstituted on Protocell Membrane toward Highly Efficient Photophosphorylation. *ACS Nano* 11, 10175-10183.
36. G. Li, J. Fei, Y. Xu, J.-D. Hong, J. Li (2019) Proton-consumed nanoarchitectures toward sustainable and efficient photophosphorylation. *J. Colloid Interface Sci.* 535, 325-330.
37. E. Altamura, F. Milano, R. R. Tangorra, M. Trotta, O. H. Omar, P. Stano, F. Mavelli (2017) Highly oriented photosynthetic reaction centers generate a proton gradient in synthetic protocells. *Proc. Natl. Acad. Sci. USA.* 114, 3837.
38. H. Sielaff, T. M. Duncan, M. Börsch (2018) The regulatory subunit e in Escherichia coli FOF1-ATP synthase. *Biochim. Biophys. Acta Bioenerg.* 1859 (9), 775-788.
39. D. Okuno, R. Iino, H. Noji (2011) Rotation and structure of FoF1-ATP synthase. *J. Biol. Chem.* 149 (6), 655-654.
40. J. P. Abrahams, A. G. Leslie, R. Lutter, J. E. Walker (1994) Structure at 2.8 Å resolution of F1-ATPase from bovine heart mitochondria. *Nature* 370, 621-628.

References

41. M. J. Gresser, J. A. Myers, P. D. Boyer (1982) Catalytic site cooperativity of beef heart mitochondrial F1 adenosine triphosphatase. Correlations of initial velocity, bound intermediate, and oxygen exchange measurements with an alternating three-site model. *J. Biol. Chem.* 257 (20), 12030-12038.
42. S. Havashi, E. Tajkhorshid, K. Schulten (2003) Molecular Dynamics Simulation of Bacteriorhodopsin's Photoisomerization Using Ab Initio Forces for the Excited Chromophore. *Biophys. J.* 85 (3), 1440-1449.
43. A. Iwamoto, H. Omote, H. Hamada, N. Tomioka, A. Itai, M. Maeda, M. Futai (1991) Mutation in Ser-174 and the Glycine-rich sequence (Gly-149, Gly-150, and Thr-156) in the beta Subunit of Escherichia coli H⁺-ATPase. *J. Biol. Chem.* 266, 16350-16355.
44. D. J. Klionsky, W. S. A. Brusilow, R. D. Simoni (1984) In vivo evidence for the role of the e subunit as an inhibitor of the proton-translocating ATPase of Escherichia coli. *J. Bacteriol.* 160, 1055-1060.
45. S. Fischer (1999) Isolation, Rekonstitution und kinetische Charakterisierung der H⁺-ATPase aus Escherichia coli. *Dissertation*. Biologisches Institut der Universität Stuttgart, 1999.
46. Y. Moriyama, A. Iwamoto, H. Hanada, M. Maeda, M. Futai (1991) One-step purification of Escherichia coli H⁺-ATPase and its reconstitution into liposomes with neurotransmitter transporters. *J. Biol. Chem.* 266, 22141-22146.
47. R. Reuter (1996) Fermentation von Escherichia coli und Optimierung der Isolierung der H⁺-ATPase aus E. coli. *Diplomarbeit*. Universität Freiburg.
48. I. Starke (2014) Kinetische und einzelmolekülspektroskopische Untersuchungen an H⁺-ATPsynthasen aus Escherichia coli und Saccharomyces cerevisiae. *Dissertation*. Fakultät für Chemie und Pharmazie der Albert-Ludwigs-Universität im Breisgau.
49. R. R. Ishmukhametov, M. A. Galkin, S. B. Vik (2005) Ultrafast purification and reconstitution of His-tagged cysteine-less Escherichia coli F1FO ATP synthase. *Biochim. Biophys. Acta* 1706, 110-116.
50. U. K. Laemmli (1970) Cleavage of structural proteins during the assembly of the head of bacteriophage T4. *Nature* 227, 680-685.
51. B. Zimmermann (2005) Die H⁺-ATP synthase aus escherichia coli: Untersuchung der Bewegung der e-Untereinheit während der Katalyse mit Einzelmolekül-Fluoreszenzspektroskopie. *Dissertation*. Fakultät für Chemie und Pharmazie der Universität Freiburg im Breisgau.
52. S. Fischer, P. Gräber (1999) Comparison of ΔpH - and $\Delta\Phi$ -driven ATP synthesis catalyzed by the H⁺-ATPases from Escherichia coli or chloroplasts reconstituted into liposomes. *FEBS Lett.* 457, 327-332.
53. G. Schmidt, P. Gräber (1985) The rate of ATP synthesis by reconstituted CFOF1 liposomes. *Biochim. Biophys. Acta* 808, 45-51.

54. D. Stoeckenius, S. Oesterhelt (1974) Isolation of the Cell Membrane of Halobacterium halobium and Its Fractionation into Red and Purple Membrane. *Methods Enzymol.* 31, 667-678.
55. P.-J. Shiu, Y.-H. Ju, H.-M. Chen, C.-K. Lee (2013) Facile isolation of purple membrane from Halobacterium salinarium via aqueous-two-phase-system. *Protein Expr. Purif.* 89, 219-224.
56. O. Meyer, M. Ollivon, A.-T. Paternostre (1992) Solubilization steps of dark-adapted purple membrane by Triton X-100. *FEBS* 11256, 249-253.
57. R. Seneviratne, S. Khan, E. Moscrop, M. Rappolt, S. P. Muench, L. J. C. Jeuken, P. A. Beales (2018) A reconstitution method for integral membrane proteins in hybrid lipid-polymer vesicles for enhanced functional durability. *Methods* 147, 142-149.
58. G. E. Gerber, C. P. Grey, D. Wildenauer, H. G. Khorana (1977) Orientation of bacteriorhodopsin in Halobacterium halobium as studied by selective proteolysis. *Proc. Natl. Acad. Sci USA* 74, 5426-5430.
59. NanoSciences, Encapsula (2020) <http://www.liposomes.org/2009/01/number-of-lipid-molecules-per-liposome.html> [Online] 10. August 2020.
60. T. Miura, S. Mizushima (1968) Separation by density gradient centrifugation of two types of membranes from speroplast membrane of Escherichia coli k12. *Biochim. Biophys. Acta* 150, 159-161.
61. M. C. Jewett, K. A. Calhoun, A. Voloshin, J. J. Wu, J. R. Schwartz (2008) An integrated cell-free metabolic platform for protein production and synthetic biology. *Mol. Sys. Biol.* 4 (220).
62. M. Osborn, J. Gander, E. Parisi, J. Carson (1972) Mechanism of assembly of the outer membrane of salmonella typhimurium isolation and characterization of cytoplasmic and outer membrane. *J. Biol. Chem.* 247, 3962-3972.
63. J. Wu, J. R. Schwartz (2008) High yield cell-free production of integral membrane proteins without refolding or detergents. *Biochim. Biophys. Acta* 1778, 1237-1250.
64. G. B. Witman (1986) Isolation of Chlamydomonas flagella and flagellar axonemes. *Methods Enzymol.* 134, 280-290.
65. C. Xu, J. L. Prince (1997) Gradient vector flow: A new external force for snakes. *IEEE Proc. CVPR.* 66-71.
66. C. Xu, J. L. Price (1998) Snakes, shapes, and gradient vector flow. *IEEE Trans. image process.* 7, 359-369.
67. S. K. Vogel, Z. Petrasek, F. Heinemann, P. Schwillle (2013) Myosin motors fragment and compact membrane-bound actin filaments. *eLIFE* 2, 1-18.
68. R. Reuter (2004) Struktur- und Funktionsuntersuchungen an der ATP synthase aus Escherichia coli. *Dissertation*, Universität Freiburg.
69. P. T. Wingfield (2001) Protein Precipitation Using Ammonium Sulfate. *Curr. Protoc. Protein Sci.* 3.

References

70. Bioscience, Tosoh. separations.us.tosohbioscience.com (2020) *Principles of Ion exchange chromatography*. [Online] 21. May 2020.
71. J. Tilitsky (2020) https://collab.its.virginia.edu.F1_ATP_synthase. [Online] 21. May 2020.
72. D. A. Skoog (2006) *Principles of instrumental Analysis*. California. Thompson Brooks/Cole. Belmont, Chapter 28.
73. P. Mitchell (1966) Chemiosmotic coupling in oxidative and photosynthetic phosphorylation. *Biol. Rev. Camb. Philos. Soc.* 41 (3), 445-502.
74. G. Kaim, P. Dimroth (1998) ATP synthesis by the F₀F₁ ATP synthase of *Escherichia coli* is obligatory dependent on the electric potential. *FEBS Lett.* 434, 57-60.
75. S. Jain, S. Nath (2000) Kinetic model of ATP synthase: pH dependence of the rate of ATP synthesis. *FEBS Lett.* 476, 113-117.
76. U. Junesch, P. Gräber (1991) The rate of ATP-synthesis as a function of ΔpH and $\Delta\psi$ catalyzed by the active, reduced H⁺-ATPase from chloroplasts. *FEBS Lett.* 294, 275-278.
77. P. Hansma, J. Cleveland, M. Radmacher, D. Walters, P. Hillner, M. Bezanilla, M. Fritz, D. Vie, H. Hansma, C. Prater (1994) Tapping Mode Atomic Force Microscopy in Liquids. *Appl. Phys. Lett.* 64, 1738-1740.
78. D. Walters, J. Cleveland, N. Thomson, P. Hansma, M. Wendman, G. Gurley, V. Elings (1996) Short Cantilevers for Atomic Force Microscopy. *Rev. Sci. Instrum.* 67, 3583-3590.
79. A. Alessandrini, P. Facci (2014) Phase transitions in supported lipid bilayers studied by AFM. *Soft Matter* 10, 7145.
80. B. W. Koenig, S. Kruger, W. J. Orts, C. F. Majkrzak, N. F. Berk, J. V. Silverton, K. Gawrisch (1996) Neutron Reflectivity and Atomic Force Microscopy Studies of a Lipid Bilayer in Water Adsorbed to the Surface of a Silicon Single Crystal. *Langmuir* 12 (5), 1343-1350.
81. T. Nawroth, K. Dose, H. Conrad (1989) Neutron Small angle Scattering of detergent solubilized and membrane bound ATP-synthase. *Physica B: Condens. Matter* 156-157, 489-492.
82. M.-J. Liao, H. G. Khorana (1984) Removal of the Carboxyl-terminal Peptide Does Not Affect Refolding or Function of Bacteriorhodopsin as a Light-dependent Proton Pump. *J. Biol. Chem.* 259, 4194-4199.
83. B. Lorber, J. DeLucas Larry (2001) Large scale preparation of homogeneous bacteriorhodopsin. *FEBS Lett.* 261, 14-18.
84. A. Rath, M. Glibowicka, V. G. Nadeau, G. Chen, C. M. Deber (2009) Detergent binding explains anomalous SDS-PAGE migration of membrane proteins. *Proc. Natl. Acad. Sci.* 106 (6), 1760-1765.
85. Chemindustry (2020) <http://www.chemindustry.com/chemicals/1196265.html>. [Online] 28. May 2020.

86. N. R. Clement, J. M. Gould (1981) Pyranine (8-hydroxy-1,3,6-pyrenetrisulfonate) as a Probe of Internal Aqueous Hydrogen Ion Concentration in Phospholipid Vesicles. *Biochem.* 20 (6), 1534-1538.
87. M. Seigneuret, J.-L. Rigaud (1986) Analysis of Passive and Light-Driven Ion Movements in Large Bacteriorhodopsin Liposomes Reconstituted by Reverse-Phase Evaporation. *Biochem.* 25, 6723-6730.
88. Wikipedia, Bacteriorhodopsin (2020) <https://en.wikipedia.org/wiki/Bacteriorhodopsin> [Online] 29. May 2020.
89. N. A. Dencher, M. P. Heyn (1979) Bacteriorhodopsin monomers pump protons. *FEBS Lett.* 108 (2), 307-310.
90. P. Richard, B. Pitard, J. L. Rigaud (1995) ATP synthesis by the FOF1-ATPase from the Thermophilic Bacillus PS3 Co-reconstituted with Bacteriorhodopsin into Liposomes. *J. Biol. Chem.* 270 (37), 215671-21578.
91. J. Heberle, J. Riesle, G. Thiedemann, D. Oesterhelt, N. A. Dencher (1994) Proton migration along the membrane surface and retarded surface to bulk transfer. *Lett. Nature* 370, 379-382.
92. B. Böttcher, U. Lücken, P. Gräber (1995) The structure of the H⁺-ATPase from chloroplasts by electron cryomicroscopy. *Biochem. Soc. Trans.* 23, 780-785.
93. S. Schenkl, G. Zgrablic, E. Portuondo-Campa, S. Haacke, M. Chergui (2007) On the excitation wavelength dependence of the fluorescence of bacteriorhodopsin. *Chem. Phys. Lett.* 441, 322-326.
94. A. Illanes (2008) *Enzyme biocatalysis: principles and applications*. Dordrecht. Springer.
95. W. W. Christie (2020) Phosphatic acids and related lipids. [Online] 3. July 2020.
96. S. Khan, M. Li, S. P. Muench, J. C. Jeuken, P. A. Beales (2016) Durable proteo-hybrid vesicles for extended functional lifetime of membrane proteins in bionanotechnology. *Chem. Commun.* 52, 11020-11023.
97. J.-F. Le Meins, C. Schatz, S. Lecommandoux, O. Sandre (2013) Hybrid polymer/lipid vesicles: state of the art and future perspectives. *Mater. Today* 16 (10), 397-402.
98. M. Chemin, P.-M. Brun, S. Lecommandoux, O. Sandre, J.-F. Le Meins (2012) Hybrid polymer/lipid vesicles: fine control of the lipid and polymer distribution in the binary membrane. *Soft Matter* 8, 2867-2874.
99. M. L. Jacobs, M. A. Boyd, N. P. Kamat (2019) Diblock copolymers enhance folding of a mechanosensitive membrane protein during cell-free expression. *PNAS* 116, 4031-4036.
100. M. Garni, S. Thamboo, C.-A. Schoenenberger, C. G. Palivan (2017) Biopores/Membrane proteins in synthetic polymer membranes. *Biochim. Biophys. Acta.* 1859, 619-638.

References

101. J. T. Mika, A. J. Thompson, M. R. Dent, N.-J. Brooks, J. Michiels, J. Hofkens, M. K. Kuimova (2016) Measuring the Viscosity of the Escherichia coli Plasma Membrane Using Molecular Rotors. *Biophys. J.* 111, 1528-1540.
102. Z. Lin, R. M. Hill, H. T. Davis, L. E. Scriven, Y. Talmon (1994) Cryo Transmission Electron Microscopy Study of Vesicles and Micelles in Siloxane Surfactant Aqueous Solution. *Lamgmuir* 10, 1008-1011.
103. L. Otrin, N. Marusic, C. Bednarz, T. Vidakovic-Koch, I. Lieberwirth, K. Landfester, K. Sundmacher (2017) Toward Artificial Mitochondrion: Mimicking Oxidative Phosphorylation in Polymer and Hybrid Membranes. *Nano Lett.* 17, 6816-6821.
104. C. Kleineberg, C. Wölfer, A. Abbasnia, D. Pischel, C. Bednarz, I. Ivanov, T. Heitkamp, K. Sundmacher, T. Vidakovic-Koch (2020) Light-driven ATP Regeneration in Diblock/Grafted Hybrid Vesicles. *ChemBioChem.* 21 (15), 2149-2160.
105. R. Seneviratne, S. Khan, E. Moscrop, M. Rappolt, S. P. Muench, L. J. C. Jeuken, P. A. Beales (2018) A reconstitution method for integral membrane proteins in hybrid lipid-polymer vesicles for enhanced functional durability. *Methods.*
106. S. K. Lim, H.-P. de Hoog, A. N. Parikh, M. Nallanim, B. Liedberg (2013) Hybrid, Nanoscale Phospholipid/Block Copolymer Vesicles. *Polymer.* 5, 1102-1114.
107. J. Gaspard, L. M. Casey, M. Rozin, D. J. Munoz-Pinto, J. A. Silas, M. S. Hahn (2006) *Sensors* 16, 390-402.
108. J.-L. Rigaud (1995) Reconstitution of membrane proteins into liposomes: application to energy-transducing membrane proteins. *Biochim. Biophys. Acta.* 1231, 223-246.
109. P. A. Beales, S. Khan, S. P. Muench, L. J. C. Jeuken (2017) Durable vesicles for reconstitution of membrane proteins in biotechnology. *Biochem. Soc. Trans.* 45, 15-26.
110. A. Wiedenmann, P. Dimroth, C. von Ballmoos (2008) $\Delta\psi$ and ΔpH are equivalent driving forces for proton transport through isolated F₀ complexes of ATP synthases. *Biochim. Biophys. Acta.* 1777, 1301-1310.
111. R. I. Kalmbach, I. Chizhov, M. C. Schuhmacher, T. Friedrich, E. Bamber, M. Engelhard (2007) Functional cell-free synthesis of a seven helix membrane protein: in situ insertion of bacteriorhodopsin into liposomes. *J. Mol. Biol.* 371, 639-648.
112. G. Wang, K. Castiglione (2019) Light-Driven Biocatalysis in Liposomes and Polymersomes: Where Are We now? *Catalysts* 9 (12).
113. W. F. Paxton, P. T. McAninch, K. E. Achyuthan, S. H. R. Shin, H. L. Monteith (2017) Monitoring and Modulating Ion Traffic in Hybrid Lipid/Polymer Vesicles. *Colloids Surf. B.* 159, 268-279.

114. N. R. Clement, J. M. Gould (1981) Pyranine (8-hydroxy-1, 3, 6-pyrenetrisulfonate) as a probe of internal aqueous hydrogen ion concentration in phospholipid vesicles. *Biochem.* 20, 1534-1538.
115. Wikipedia, Nigericin (2020) <https://en.wikipedia.org/wiki/Nigericin>. [Online] 05. June 2020.
116. C. L. Kuyper, J. S. Kuo, S. A. Mutch, D. T. Chiu (2006) Proton permeation into single vesicles occurs via a sequential two-step mechanism and is heterogeneous. *J. Am. Chem. Soc.* 128, 3233-3240.
117. W. F. Paxton, D. Price, N. J. Richardson (2013) Hydroxide ion flux and pH-gradient driven ester hydrolysis in polymer vesicle reactors. *Soft Matter* 9, 11295-11302.
118. D. W. Deamer (1987) Proton Permeation of Lipid Bilayers. *J. Bioenerg. Biomembr.* 19, 457-479.
119. S. V. Albers, W. N. Konings, A. J. M. Driessen (2006) Membranes of thermophiles and other extremophiles. *Methods Microbiol.* 35, 161-171.
120. N. Marusic, L. Otrin, Z. Zhao, R. B. Lira, F. L. Kyriallis, F. Hamdi, P. L. Kastiris, T. Vidakovic-Koch, I. Ivanov, K. Sundmacher, R. Dimova (2020) Constructing artificial respiratory chain in polymer compartments: Insights into the interplay between bo3 oxidase and the membrane. *PNAS* 117 (26).
121. M. Seignereut, J.-L. Rigaud (1988) Partial separation of inwardly pumping and outwardly pumping bacteriorhodopsin reconstituted liposomes by gel filtration. *FEBS Lett.* 228 (1), 79-84.
122. L. Ruiz-Perez, C. Hurley, S. Tomas, G. Battaglia (2018) Separating Extreme pH Gradients Using Amphiphilic Copolymer Membranes. *ChemPhysChem.* 19, 1987-1989.
123. B. C. Pressman (1976) Biological applications of ionophores. *Annu. Rev. Biochem.* 45, 501-530.
124. A. Zeng (2013) *Fundamentals and Application of new Bioproduction Systems*. Berlin Heidelberg: Springer.
125. A. Ping-Zeng (2013) *Fundamentals and Applications of new Bioproduction Systems*. Berlin-Heidelberg: Springer, 2013.
126. S. Steigmiller, P. Turina, P. Gräber (2008) The thermodynamic H⁺/ATP ratios of the H⁺-ATPsynthases from chloroplasts and Escherichia coli. *PNAS* 105 (10), 3745-3750.
127. T. Beneyton, D. Krafft, C. Bednarz, C. Kleineberg, C. Woelfer, I. Ivanov, T. Vidakovic-Koch, K. Sundmacher, J.-C. Baret (2018) Out-of-equilibrium microcompartments for the bottom-up integration of metabolic functions. *Nat. Commun.* 9 (1).
128. D. Xu, C. Kleineberg, T. Vidakovic-Koch, S. V. Wegner (2020) Multistimuli sensing adhesion unit for the self-positioning of minimal synthetic cells. *Small* 16 (35), 2002440-2002448.
129. O. I. Lungu, R. A. Hallett, E. J. Choi, M. J. Aikenb, K. M. Hahn, B. Kuhlman (2012) Designing Photoswitchable Peptides Using the AsLOV2 Domain. *Chem. Biol.* 19, 507-517.

References

130. G. Guntas, R. A. Hallett, S. P. Zimmermann, T. Williams, H. Yumerefendi, J. E. Bear, B. Kuhlman (2015) Engineering an Improved Light-Induced Dimer (iLID) for Controlling the Localization and Activity of Signaling Proteins. *Proc. Natl. Acad. Sci. USA.* 112, 112-117.
131. S. V. Wegner, F. C. Schenk, J. P. Spatz (2016) Cobalt(III)-Mediated Permanent and Stable Immobilization of Histidine-Tagged Proteins on NTA-Functionalized Surfaces. *Chem. Eur. J.* 22, 3156-3162.
132. V. Geyer (2013) Characterization of the flagellar beat of the single cell green alga *Chlamydomonas reinhardtii*. *PhD Thesis*. Sächsische Landesbibliothek-Staats- und Universitätsbibliothek Dresden.
133. K. Göpfrich, I. Platzman, J. P. Spatz (2018) Mastering Complexity: Towards Bottom-up Construction of Multifunctional Eukaryotic Synthetic Cells. *Trends in Biotechnol.* 36 (9), 938-951.
134. K. Shin (2019) Artificial cells containing sustainable energy conversion engines. *Emerging Topics in Life Sciences* 3, 573-578.
135. P. W. Holloway (1973) A simple procedure for removal of Triton X-100 from protein samples. *Anal. Biochem.* 53, 304-308.
136. P. Mitchell (2011) Chemiosmotic coupling in oxidative and photosynthetic phosphorylation. *Biochim. Biophys. Acta Bionerg.* 1807, 1507-1538.
137. S. Hoops, R. Gauges, C. Lee, J. Pahle, N. Simus, M. Singhal, L. Xu, P. Mendes, U. Kummer (2006) COPASI - a COMplex PATHway SIMulator. *Bioinform.* 22, 3067-3074.
138. T. Bäck, H.-P. Schwefel (1993) An overview of evolutionary algorithms for parameter optimization. *Evolutionary Computation.* *Evol. Comput.* 1, 1-23.
139. J. A. Nelder, R. Mead (1965) A Simplex Method for Function Minimization. *The Computer Journal* 7, 308-315.
140. S. Y. Yu, T. Azzam, I. Rouiller, A. Eisenberg (2009) pH-Sensitive Polymeric Vesicles from Coassembly of Amphiphilic Cholates Grafted Poly(L-lysine) and Acid-Cleavable Polymer-Drug Conjugate. *J. Am. Chem. Soc.* 131, 10557-10566.
141. S. Fischer, C. Etzold, P. Turina, G. Deckers-Hebestreit, K. Altendorf, P. Gräber (1994) ATP synthesis catalyzed by the ATP synthase of *Escherichia coli* reconstituted into liposomes. *Eur. J. Biochem.* 225, 167-172.
142. M. Tutus, F. F. Rossetti, E. Schneck, G. Fragneto, F. Förster, R. Richter, T. Nawroth, M. Tanaka (2008) Orientation-Selective Incorporation of Transmembrane F₀F₁ ATP synthase Complex from *Micrococcus luteus* in Polymer-Supported Membranes. *Macromol. Biosci.* 8, 1034-1043.

143. R. L. Van der Bend, J. W. B. J. Cornelissen, J. A. Berden, K. Van Dam (1984) Factors defining the functional coupling of Bacteriorhodopsin and ATP synthase in Liposomes. *Biochim. Biophys. Acta.* 767, 87-101.
144. V. B. Borisov, R. Murali, M. L. Verkhovskaya, D. A. Bloch, H. Han, R. B. Gennis, M. I. Verkhovsky (2011) Aerobic respiratory chain of *Escherichia coli* is not allowed to work in fully uncoupled mode. *PNAS* 108 (42), 17320-17324.
145. P. Sharma, K. J. Hellingwerf, M. J. Teixeira de Mattos, M. Bekker (2012) Uncoupling of Substrate-Level Phosphorylation in *Escherichia coli* during Glucose-limited growth. *Appl. Environ. Microbiol.* 78 (19), 6908-6913.
146. M. C. Huber, A. Schreiber, S. M. Schiller (2019) Minimalist Protocell Design: A Molecular System Based Solely on Proteins that Form Dynamic Vesicular Membranes Embedding Enzymatic Functions. *ChemBioChem* 20.
147. A. Carlson, N. Glaser, J. F. L. Meins, S. Lecommandoux (2011) Block Copolymer Vesicle Permeability Measured by Osmotic Swelling and Shrinking. *Langmuir* 27, 4884-4890.

List of figures

Figure 2.1 Overview of the thesis.....	3
Figure 2.2 Scheme of the engineering perspective of the basic principles of energy and co-factor regeneration as well as the assembly to a functional system.....	9
Figure 2.3 Schematic presentation of bacterial ATP synthase (EF _o F ₁).....	14
Figure 2.4 Schematic illustration of Boyer's binding change mechanism for ATP synthase.	15
Figure 2.5 Schematic presentation of the intermediates of the photocycle of bR.	16
Figure 3.1 Schematic diagram of non-his tagged EF _o F ₁ isolation in <i>E. coli</i> (45; 48).....	19
Figure 3.2 Evaluation of the detected luminescence signal to generate the ATP concentration change c_{ATP} ..	25
Figure 3.3 Reaction scheme of the coupled enzymatic test for measurement of ATP hydrolysis.....	26
Figure 3.4 Evaluation of NADH absorption depletion for determination of the kinetic constant $k_{cat,H}$ (s ⁻¹). ...	27
Figure 3.5 Schematic illustration of vesicle preparation using the extrusion method.....	30
Figure 3.6 Evaluation of pyranine absorption A_{405} and A_{450} to generate vesicles internal pH change.	34
Figure 4.1 Isolation of non his-tagged ATP synthase in <i>E. coli</i> (EF _o F ₁ ATP synthase).....	49
Figure 4.2 SDS-PAGE analysis of non his-tagged ATP synthase.	51
Figure 4.3 Isolation of his-tagged ATP synthase in <i>E. coli</i> (EF _o F ₁ ATP synthase).....	52
Figure 4.4 SDS-PAGE analysis of his-tagged ATP synthase.....	53
Figure 4.5 Turnover rates of ATP synthesis as a function of pH _{in} and pH _{out}	55
Figure 4.6 Turnover rates of ATP synthesis as a function of the diffusion potential $\Delta\psi$	57
Figure 4.7 Measurement of ATP synthesis over 27 Days.	58
Figure 4.8 Characterization of ATP synthase with Atomic Force Microscopy (AFM).	59
Figure 4.9 Characterization of ATP synthase vesicles with Dynamic Light Scattering (DLS) and Cryo-TEM. .	61
Figure 4.10 Characterization of isolated bacteriorhodopsin (bR).	62
Figure 4.11 Calibration curve for pH determination using the absorption of pyranine at 450 nm (A_{450nm}) and 405 nm (A_{405nm}).....	64

List of figures

Figure 4.12 Effect of the lipid to protein ratio on bR proton pumping rates.	66
Figure 4.13 Absorbance spectrum of bR before (A) and after solubilization with Triton X-100 (B) and octyl glucoside (C).	68
Figure 4.14 Light-driven ATP synthesis in lipid vesicles (100-150 nm).	69
Figure 4.15 Light-driven ATP synthesis in lipid vesicles over 5 hours.	71
Figure 4.16 ATP production after co-reconstitution with 1 EF _o F ₁ /liposomes and various amounts of bR.	72
Figure 4.17 ATP production in lipid vesicles co-reconstituted with Triton X-100 (0.36 %) solubilized bR compared to bR patches.	73
Figure 4.18 ATP production in lipid vesicles co-reconstituted with different amounts of ATP synthase at constant bR concentration.	74
Figure 4.19 Influence of different light sources on the ATP production rate.	75
Figure 4.20 Influence of valinomycin and different K ⁺ concentrations on the ATP production rate.	77
Figure 4.21 Influence of the ADP concentration on the ATP production rate.	78
Figure 4.22 Influence of the liposome preparation method on the ATP production rate.	79
Figure 4.23 Influence of different buffers on the ATP production rates.	81
Figure 4.24 Freezing and storing of the ATP module leads to little losses in activity.	82
Figure 4.25 Schematic presentation of light-driven ATP production in lipid, polymer and hybrid vesicles. .	84
Figure 4.26 Schematic presentation of different membrane compositions used for co-reconstitution with solubilized bR.	85
Figure 4.27 Size distribution of vesicles made of 0/100 PDMS/PC, 70/30 PDMS/PC, 50/50 PBd/PC and 50/50 PDMS/PBd.	86
Figure 4.28 Detergent destabilization profiles for vesicles made of 0/100 PDMS/PC, 70/30 PDMS/PC, 50/50 PBd/PC and 50/50 PDMS/PBd.	87
Figure 4.29 Size distribution of hybrid vesicles made of 0/100 PDMS/PC, 70/30 PDMS/PC, 50/50 PBd/PC and 50/50 PDMS/PBd.	89
Figure 4.30 Light-driven ATP synthesis in lipid and hybrid vesicles using solubilized bR for co-reconstitution.	90
Figure 4.31 Proton pump activity of solubilized bR in liposomes and hybrid vesicles as measured by pH change upon green light irradiation.	92
Figure 4.32 Proteolytic cleavage of reconstituted bR with proteinase K (ProtK) shows mixed orientation in all lipid and hybrid vesicles.	94
Figure 4.33 Proton permeability of vesicles as measured by pH change after addition of 2.4 mM HCl (A) and 1.6 mM NaOH (B) in the presence of 1.5 nM valinomycin.	96
Figure 4.34 Proton permeability of vesicles as measured by pH change after addition of 2.4 mM HCl (left) and 1.6 mM NaOH (right) to the outer solution in the absence of valinomycin.	98
Figure 4.35 Hybrid vesicles improve long-term stability of the ATP regeneration module.	101

Figure 4.36 Vesicles average diameter (A) and Polydispersity Index (B) stay almost constant over 42 days as determined by Dynamic Light Scattering (DLS).	102
Figure 4.37 Comparison of the size distribution profile of vesicles at day 1 and day 42.....	103
Figure 4.38 Schematic presentation of different membrane compositions used for co-reconstitution with bR patches.	105
Figure 4.39 Size distribution of vesicles made of different mixtures of PDMS and PC before (A) and after (B) reconstitution and removal of detergent using bio beads.	106
Figure 4.40 Size distribution of vesicles made of different mixtures of PBd and PC before (A) and after (B) reconstitution and removal of detergent using bio beads.	107
Figure 4.41 Detergent destabilization profiles for hybrid vesicles made of different mixtures of PC, PDMS and PBd.	108
Figure 4.42 ATP production performance in hybrid vesicles using different reconstitution procedure.	110
Figure 4.43 Light-driven ATP synthesis in hybrid vesicles made of PC and PDMS (A) and PC and PBd (B) co-reconstituted with bR patches.	111
Figure 4.44 Proton pump activity of bR patches in lipid and hybrid vesicles made of PC/PDMS (A) and PC/PBd (B) as measured by pH change upon green light irradiation.	113
Figure 4.45 SDS-PAGE analysis after proteolytic cleavage of reconstituted bR patches with proteinase K (ProtK) shows different orientation in lipid, hybrid and polymer vesicles.	115
Figure 4.46 Proton permeability of vesicles as measured by pH change after addition of 102 mM NaOH to the outer solution.....	116
Figure 4.47 Internal vesicle pH with valinomycin and nigericin after addition of 77 mM NaOH.....	117
Figure 4.48 pH response of vesicles after addition of 77 mM NaOH in the presence of different amounts of valinomycin.	119
Figure 4.49 pH response of vesicles after addition of 77 mM NaOH and 1.5 mM valinomycin in the presence of various concentrations of K^+	120
Figure 4.50 Hybrid vesicles co-reconstituted with bR patches improve long-term stability of the ATP module.	121
Figure 4.51 Scheme of inverted membrane vesicles (IMVs).	122
Figure 4.52 ATP production and NADH consumption in wildtyp IMVs.	123
Figure 4.53 ATP production in overexpressed IMVs.	125
Figure 4.54 Scheme of IMVs encapsulated in water-in-oil droplets.	125
Figure 4.55 Comparison of IMVs kinetic in bulk and in droplets.....	126
Figure 4.56 Schematic presentation of a multistimuli responsive adhesion unit, which responds to light, pH, oxidative stress and the presence of metal ions.....	128
Figure 4.57 Light-driven ATP synthesis of vesicles in the absence (PC) and presence (PC-DGS-NTA) of the functionalized DGS-NTA lipids.....	129
Figure 4.58 Integration of the multistimuli responsive adhesion module with the ATP module. (128)	130

List of figures

Figure 4.59	Scheme of coupling the ATP regeneration module with flagella movement triggered by light.	132
Figure 4.60	Light-driven ATP synthesis in axoneme buffer using a microscope light (5 W) for irradiation.	133
Figure 4.61	Functionalized liposomes were illuminated for different times, generating ATP concentrations up to 330 μ M before being mixed with axonemes for reactivation process.	135
Figure 4.62	Reactivation of axonemes by light-driven ATP module.	136
Figure 4.63	Scheme of coupling the ATP regeneration module with a metabolic module for glucose consumption triggered by light.	137
Figure 4.64	ATP and glucose concentration over time under green light illumination.	138
Figure 4.65	Scheme of light-triggered actin-myosin contraction (filamentation) in droplets.	140
Figure 4.66	Contraction of actin/myosin after incubation with the ATP module under light.	142
Figure A.1	Buffer capacity for different pH (Pipes buffer: pKB = 6.71, cB = 25 mM) as determined by model simulation (Method 1) described above.	163
Figure A.2	pH change inside of vesicles depending on different (A) pKB and (B) buffer concentrations as predicted by model simulation (Method 1).	165
Figure A.3	Determination of permeability coefficients (P) using Method 2.	166
Figure A.4	Determination of permeability coefficients using Method 3 (double exponential fitting).	168
Figure A.5	Calibration curves of pyranine for different membrane compositions.	168
Figure A.6	ATP standard curve for calculation of ATP concentration in IMVs experiments.	169
Figure A.7	Glucose standard curve for calculation of glucose concentration by the fluorescence signal using a high sense glucose assay.	169

List of tables

Table 2.1 Overview of light-driven ATP regeneration modules.	11
Table 3.1 Lipid and hybrid vesicle compositions used for proton pumping experiments with solubilized bR.	31
Table 3.2 Lipid, hybrid and polymer vesicle compositions used for proton pumping experiments with bR patches.	31
Table 3.3 Amount of 10% Triton and SM-2 Bio-Beads used for reconstitution in different lipid, hybrid and polymer vesicles.	32
Table 4.1 Permeability coefficients for different membrane compositions as yield by model simulation (Method 1), coefficients calculated according to Paxton et al. (Method 2) and coefficients derived by double exponential fitting (Method 3).	99
Table A.1 Composition of Luria Media.	151
Table A.2 Composition of culture medium.	151
Table A.3 Composition of T1 media.	152
Table A.4 Composition of T2 media.	152
Table A.5 Composition of amino acid solution.	152
Table A.6 Composition of French Press buffer.	152
Table A.7 Composition of membrane buffer.	153
Table A.8 Composition of solubilization buffer.	153
Table A.9 Composition of buffer A.	153
Table A.10 Composition of LB media.	153
Table A.11 Composition of French press buffer.	154

List of tables

Table A.12 Composition of extraction buffer.....	154
Table A.13 Composition of culture medium.....	154
Table A.14 Composition of sample buffer for SDS-PAGE Analysis.	155
Table A.15 Staining solution Coomassie Blue R250 for SDS-PAGE Analysis.	155
Table A.16 Decolorizing solution for SDS-PAGE Analysis.....	155
Table A.17 Composition of sonification buffer for preparation of dialysis liposomes.	155
Table A.18 Composition of dialysis buffer for preparation of dialysis liposomes.....	156
Table A.19 Composition of reconstitution buffer.....	156
Table A.20 Composition of basic buffer LII for ATP synthesis measurements.....	156
Table A.21 Composition of acidic buffer LI for ATP synthesis measurements.....	156
Table A.22 Composition of measurement buffer for ATP hydrolysis measurements.....	157
Table A.23 Composition of HEPES buffer for proton pumping experiments.....	157
Table A.24 Composition of Laemmli buffer for SDS PAGE analysis of bR fragments.	157
Table A.25 Composition of vesicle buffer for characterization of the ATP module.	157
Table A.26 Composition of measurement buffer for light-induced ATP synthesis.	158
Table A.27 Composition of PIPES buffer for permeability measurements.	158
Table A.28 Composition of HEPES buffer for permeability measurements.....	158
Table A.29 Composition of washing buffer for IMV isolation.....	158
Table A.30 Composition of lysis buffer for IMV isolation.....	158
Table A.31 Composition of membrane buffer for IMV isolation.	159
Table A.32 Composition of measurement buffer for ATP measurement in IMVs.....	159
Table A.33 Composition of HMDEKP buffer for reactivation of isolated flagella.	159
Table A.34 Composition of buffer A for multistimuli sensing adhesion unit.....	160
Table A.35 Composition of MOPS buffer.....	160
Table A.36 Fitted parameter set for calculation of permeability coefficients using Method 1.	165

Publications and list of authorship

Journal Publications

T. Beneyton, D. Krafft, C. Bednarz, **C. Kleineberg**, C. Woelfer, I. Ivanov, T. Vidakovic-Koch, K. Sundmacher, J.-C. Baret (2018) Out-of-equilibrium microcompartments for the bottom-up integration of metabolic functions. *Nat. Commun.* 9 (1).

C. Kleineberg measured ATP production kinetics and NADH consumption kinetics of Inverted Membrane Vesicles in bulk.

L. Otrin, **C. Kleineberg**, L. Caire da Silva, I. Ivanov, M. Wang, C. Bednarz, K. Sundmacher, T. Vidakovic-Koch (2019) Artificial Organelles for Energy Regeneration. *Adv. Biosyst.* 3 (6).

C. Kleineberg wrote the chapter “Light Energy Conversion to ATP” and created the table for comparison of ATP production rates.

C. Kleineberg, C. Wölfer, A. Abbasnia, D. Pischel, C. Bednarz, I. Ivanov, T. Heitkamp, K. Sundmacher, T. Vidakovic-Koch (2020) Light-Driven ATP Regeneration in Diblock/Grafted Hybrid Vesicles. *ChemBioChem.* 21 (15), 2149-2160.

C. Kleineberg carried out the experiments, analysed the results, created the figures, did statistical evaluation of results, partially calculated the permeability coefficients (Method 2) and wrote the manuscript. The article qualified for the **Cover Page** and the Cover picture was designed by **C. Kleineberg**.

D. Xu, **C. Kleineberg**, T. Vidakovic-Koch, S. V. Wegner (2020) Multistimuli sensing adhesion unit for the self-positioning of minimal synthetic cells. *Small* 16 (35), 2002440-2002448.

C. Kleineberg prepared the ATP module, guided the ATP measurements, created figures for SI, helped with the evaluation of data and corrected the manuscript.

Curriculum vitae

R. Ahmad[†], **C. Kleineberg**[†], V. Nasirimarekani, Y. Su, S. Goli Pozveh, A. J. Bae, K. Sundmacher, E. Bodenschatz, I. Guido, T. Vidakovic-Koch, A. Gholami (2021) Light-Powered Reactivation of Flagella: and Contraction of Microtubule Networks: Toward Building an Artificial Cell. *ACS Synth. Biol.*, 10, 6, 1490-1504.

[†] Equal contribution

C. Kleineberg prepared the ATP module, did the ATP measurements, designed the experiment, supported data analysis, created figures for the manuscript and partially wrote the manuscript.

Talks and posters

C. Kleineberg, T. Vidakovic-Koch, K. Sundmacher, ATP regeneration module in an artificial biomolecular energy conversion system, April 17th 2015, MaxSynBio Ceremonial Opening, Berlin, Germany. (Oral presentation)

C. Kleineberg, M. Weiss, L. Silva, C. Bednarz, S. Z. Ali, T. Vidakovic-Koch, I. Ivanov, I. Platzmann, M. Bannwarth, J. Spatz, K. Landfester, K. Sundmacher, Energy Conversion – Light to ATP, October 2016, MaxSynBio Evaluation, Martinsried, Germany. (Poster presentation)

C. Kleineberg, C. Bednarz, T. Vidakovic-Koch, K. Sundmacher, ATP synthase (Co)-reconstitution and activity measurements, May 16th 2017, MaxSynBio Protein Workshop, Dortmund, Germany. (Oral Presentation)

C. Kleineberg, L. Caire da Silva, T. Vidakovic-Koch, M. B. Bannwarth, K. Sundmacher, K. Landfester, Light induced ATP synthesis for synthetic biology applications, May 2017, Dechema, Frankfurt, Germany. (Poster presentation)

C. Kleineberg, L. Peterson, C. Bednarz, T. Vidakovic-Koch, K. Sundmacher, Bottom-up assembly of a light-driven ATP conversion machinery in artificial membranes, July 3^d 2018, MaxSynBio Symposium, Magdeburg, Germany. (Poster and oral presentation)

C. Kleineberg, L. Peterson, C. Bednarz, I. Ivanov, S. Sundmacher, T. Vidakovic-Koch, Reconstitution of membrane proteins into artificial membranes, September 2018, GASB II Conference, Berlin, Germany. (Poster Presentation)